UNIVERSITAT DE BARCELONA

Functional properties and applications of plasma polymerized hexamethyldisiloxane (ppHMDSO) thin films

Francesc Benítez i Porras

ADVERTIMENT. La consulta d'aquesta tesi queda condicionada a l'acceptació de les següents condicions d'ús: La difusió d'aquesta tesi per mitjà del servei TDX (**www.tdx.cat**) i a través del Dipòsit Digital de la UB (**diposit.ub.edu**) ha estat autoritzada pels titulars dels drets de propietat intel·lectual únicament per a usos privats emmarcats en activitats d'investigació i docència. No s'autoritza la seva reproducció amb finalitats de lucre ni la seva difusió i posada a disposició des d'un lloc aliè al servei TDX ni al Dipòsit Digital de la UB. No s'autoritza la presentació del seu contingut en una finestra o marc aliè a TDX o al Dipòsit Digital de la UB (framing). Aquesta reserva de drets afecta tant al resum de presentació de la tesi com als seus continguts. En la utilització o cita de parts de la tesi és obligat indicar el nom de la persona autora.

ADVERTENCIA. La consulta de esta tesis queda condicionada a la aceptación de las siguientes condiciones de uso: La difusión de esta tesis por medio del servicio TDR (**www.tdx.cat**) y a través del Repositorio Digital de la UB (**diposit.ub.edu**) ha sido autorizada por los titulares de los derechos de propiedad intelectual únicamente para usos privados enmarcados en actividades de investigación y docencia. No se autoriza su reproducción con finalidades de lucro ni su difusión y puesta a disposición desde un sitio ajeno al servicio TDR o al Repositorio Digital de la UB. No se autoriza la presentación de su contenido en una ventana o marco ajeno a TDR o al Repositorio Digital de la UB (framing). Esta reserva de derechos afecta tanto al resumen de presentación de la tesis como a sus contenidos. En la utilización o cita de partes de la tesis es obligado indicar el nombre de la persona autora.

WARNING. On having consulted this thesis you're accepting the following use conditions: Spreading this thesis by the TDX (**www.tdx.cat**) service and by the UB Digital Repository (**diposit.ub.edu**) has been authorized by the titular of the intellectual property rights only for private uses placed in investigation and teaching activities. Reproduction with lucrative aims is not authorized nor its spreading and availability from a site foreign to the TDX service or to the UB Digital Repository. Introducing its content in a window or frame foreign to the TDX service or to the UB Digital Repository is not authorized (framing). Those rights affect to the presentation summary of the thesis as well as to its contents. In the using or citation of parts of the thesis it's obliged to indicate the name of the author.

UNIVERSITAT DE BARCELONA

FACULTAT DE FÍSICA

Departament de Física Aplicada i Òptica

FUNCTIONAL PROPERTIES AND APPLICATIONS OF PLASMA POLYMERIZED HEXAMEHTYLDISILOXANE (ppHMDSO) THIN FILMS

Francesc Benítez i Porras

PROGRAMA DE DOCTORAT EN

FÍSICA I TECNOLOGIA DE MATERIALS

BIENNI 1997-99

Director: Joan Esteve i Pujol

Memòria presentada per a optar al títol de Doctor

Barcelona , Novembre de 2015

“Everything happens for a reason”

-popular knowledge-

AGRAÏMENTS

Fer aquesta tesi no ha estat fàcil. Segurament no hi ha ningú que digui que ho ha estat, però en el meu cas el pas del temps ho ha complicat tot més, si cal. Per això vull agrair en aquest preàmbul a totes les persones que al llarg dels anys, d'una manera o altra, ho han fet possible.

En primer lloc, vull agrair al Dr Joan Esteve la seva paciència i suport, que sempre han anat acompanyats de grans consells i tot amanit amb molt bon humor. Més enllà del seu seguiment acadèmic i de la direcció d'aquesta tesi, el seu coneixement em va ajudar quan vaig decidir-me a fer el pas a la indústria privada, ara ja fa uns quants anys. Gràcies a ell he seguit connectat sempre amb la Universitat i amb el Departament de Física Aplicada i Òptica, a través de projectes de recerca dins i fora de l'àmbit de la tesi.

En segon lloc, vull agrair al Dr José Luis Morenza, antic director del Departament de Física Aplicada i Òptica, per haver-me acceptat al Departament i per haver-me encoratjat per no defallir en la finalització de la Tesi. També pel seu suport durant el breu període en què vaig estar sota la seva tutela com a tècnic substitut en processament de materials amb làser.

També vull recordar-me especialment del Dr Manuel Varela, i per extensió de tot el seu grup de recerca, per haver-me acollit en els meus inicis durant gairebé dos anys molt productius, que van concloure amb bona quantitat de publicacions, una tesina i l'assoliment de la suficiència investigadora.

A l'empresa TELSTAR i molt especialment al Miquel Galan pel seu interès i suport financer, per la cessió del reactor prototip de plasma i per la coordinació del Projecte SIDUR, dins del programa CRAFT de la UE, que va permetre finançar gran part de la recerca inclosa en aquesta Tesi.

Vull també agrair especialment a aquelles persones que han contribuit als resultats d'aquesta Tesi amb algunes tècniques de caracterització que no eren del meu àmbit d'expertesa: al Dr Enric Garcia, per les mesures d'el.lipsometria FTIR; al Dr Lorenzo Calvo per les mesures d'XPS, al Dr Ramon Fontarnau (que al cel sia) per la seva increïble i contagiosa passió per la microscopia electrònica; a la Dra Maria Calafat per les mostres de RF i microones (encara que no estiguin incloses aquí) i per la seva gran simpatia; a la Dra Elena Martínez per les mesures de microscratch i per les publicacions conjuntes. Al Jerson Peralta per les mesures dels tractaments de Polycarbonat, encara que no estiguin incloses en aquesta Tesi.

Faig extensiu el meu agraïment a la resta de professores i professors del Departament, que sempre han tingut un moment per atendre'm, ja foren discussions sobre el meu pla de recerca o sobre problemes tecnològics derivats de la meva activitat professional a la indústria.

Greetings and best regards for Prof. Michael Swain, from the Biomaterials Science Research Unit, at Sydney University, for hosting me and teaching me on the use of his wonderful UMIS nanoindenter. Also for showing me your amazing Natural Parks.

Al Dr Salvador Borrós i a J. Porras per l'amable cessió d'ús del seu reactor tubular de polimerització plasma en DC polsat per al recobriment dels eixos d'acer.

Al Jordi Solà i la Maite Fraile per l'ajuda amb tots els tràmits administratius durant aquests anys.

A tots els companys i companyes amb qui he tingut la sort de compartir aquest llarg camí: César, José, Juan Carlos, Alcides, Cristóbal, Ángel, David, Marta, Albert, Mónica, i tants i tants altres…

Als meus companys i responsables durant les diferents etapes professionals a BioSystems, Grífols o STAT, especialment al Dr Sergi Tortosa, el Josep Pagès, l'Enric Martinell, el Jordi Manzano, el Rafel Bru i el Jordi Carrera. Gràcies per la vostra comprensió i pel vostre suport en animar-me a no llençar mai la tovallola.

Als meus amics, que (potser) aviat em podreu dir realment 'Doctor!

I molt especialment, a la meva família. Crec que us farà tanta il.lusió com a mi.

TABLE OF CONTENTS

RESUM **1**

ABSTRACT **9**

CHAPTER 1 – Introduction and Objectives **17**

INTRODUCTION 17

1.1. Plasma Polymerization within Materials Science:
A historical perspective 17

1.2. Fundamental aspects of plasmas and plasma polymerization 20

1.3. Industrial applications of plasma polymerization 43

OBJECTIVES **48**

CHAPTER 2 – Materials and Methods **51**

2.1. Organosilicon monomers: HMDSO 51

2.2. Reactor for plasma polymerization 52

2.3. Protocol for plasma polymerization 61

2.4. Film characterization techniques 65

CHAPTER 3 – Plasma Polymerization of HMDSO **89**

3.1. Introduction and objectives 89

3.2. Results and discussion 92

3.3. Conclusions 118

CHAPTER 4 – Plasma Treatment of ppHMDSO Films ………………… **121**

4.1. Introduction and objectives ………………………………………………… 121

4.2. Materials and methods ………………………………………………… 124

4.3. Results and discussion ………………………………………………… 129

4.4. Conclusions ………………………………………………… 191

CHAPTER 5 – Industrial Applications ……………………………………… **193**

5.1. Introduction and objectives ………………………………………………… 193

5.2. Application I ………………………………………………… 195

5.3. Application II ………………………………………………… 203

CONCLUSIONS ………………………………………………… **223**

BIBLIOGRAPHY ………………………………………………… **227**

LIST OF ACRONYMS ………………………………………………… **243**

RESUM

La **polimerització assistida per plasma** és una tècnica novedosa per a la obtenció de recobriments polimèrics a baixa temperatura sobre qualsevol tipus de substrat: plàstic, metall, semiconductors, fusta, fibra tèxtil o membranes, per citar-ne només alguns. Els recobriments són obtinguts directament a partir de monòmers líquids que s'introdueixen controladament en fase vapor dins una cambra de buit equipada amb un o més elèctrodes que, en aplicació d'una tensió elèctrica constant (DC), alterna (AC) o d'alta freqüència (RF, MW), generen el plasma. L'estat de plasma és un estat gasós altament energètic on la densitat d'electrons, fotons, ions, espècies excitades i fragments moleculars altament reactius és molt abundant. La introducció en el plasma del vapor d'un monòmer orgànic desencadena la creació de fragments moleculars capaços d'iniciar reaccions molt diverses, des de la oligomerització en fase vapor de diferents fragments moleculars per formar molècules més grans o agrupaments nanoscòpics de pols, fins a l'adsorció i reacció sobre qualsevol superfície sòlida per a formar recobriments en capa fina d'alta adherència. Les propietats estructurals, químiques i funcionals d'aquests recobriments venen determinades per la composició de la mescla gasosa precursora i la naturalesa del monòmer, i per diferents paràmetres tecnològics controlables, com ara la pressió, la potència acoplada al plasma, la freqüència d'oscil·lació de la polarització, la posició dels substrats, el flux circulant de gas, etc.. Mitjançant aquests paràmetres tecnològics s'aconsegueix modular el valor de les magnituds que governen els mecanismes fisico-químics responsables del creixement dels recobriments: el temps de residència de les molècules, l'energia disponible per molècula, el grau de fragmentació del monòmer, o la densitat i energia del bombardeig iònic sobre els substrats, entre d'altres.

La polimerització plasma permet obtenir recobriments a partir de virtualment qualsevol tipus de molècula orgànica vaporitzable, fins i tot quan aquesta no sigui la unitat formadora característica de cap polímer generat per mètodes químics

convencionals. La tècnica també permet emprar no només monòmers orgànics sinó també altres tipus de monòmers com els de base silici o els organometàl·lics.

L'ús de monòmers orgànics de base silici permet obtenir propietats amb característiques molt amples, des de les més pròpies d'un polímer elastomèric com la silicona (polidimetilsiloxà, PDMS) a les d'un material inorgànic dur, com el vidre (òxid de silici amorf, SiO_2). Tot i ser de naturalesa aparentment oposada, aquests dos materials comparteixen una base química extraordinàriament similar fonamentada en un esquelet d'enllaços Silici-Oxigen. Durant el treball de desenvolupament d'aquest estudi s'han emprat diferents monòmers de base silici: l'**hexametildisiloxà (HMDSO)**, l'hexametildisilazana (HMDSN) i el tetraetoxisilà (TEOS), però només es presentaran els resultats obtinguts en els dipòsits de polimerització plasma del primer, HMDSO, degut a ser l'únic amb capacitat de generar recobriments de caire polimèric, inorgànic, intermedi o fins i tot amb propietats variables amb la profunditat en un únic recobriment.

En quant a la generació del plasma, la majoria d'estudis publicats opten per fonts d'alta freqüència –radiofreqüència (RF) o microones (MW)-, tot i que existeix la possibilitat d'emprar també fonts de **corrent contínua d'alt voltatge (HV-DC)**, de 500 a 3000 V. Durant el nostre estudi s'han emprat diversos tipus de font, –DC, RF i MW–, però en aquesta memòria es presenten bàsicament els resultats dels estudis en corrent contínua degut a la simplicitat del seu ús en aplicacions industrials, alhora que es determinen els seus avantatges i limitacions, com ara la saturació del creixement del gruix dels dipòsits polimèrics i inorgànics, o l'escalfament dels substrats en funció de la configuració del plasma.

En conseqüència, l'objectiu principal d'aquesta tesi és l'estudi de la **polimerització assistida per plasma en corrent contínua de l'hexametildisiloxà (DC ppHMDSO) amb i sense addició de gasos portadors,** per a l'obtenció de recobriments polimèrics o inorgànics de base silici amb especials propietats funcionals mecàniques, òptiques i protectores contra la corrosió, i l'aplicació pràctica d'aquests recobriments a la solució d'alguns problemes d'interès industrial. El segon gran objectiu és l'estudi de les modificacions de les capes de naturalesa polimèrica ja dipositades mitjançant un segon plasma o **post-tractament sense contingut de monòmer** per tal de

modificar la superfície del recobriment i aconseguir un gradient en profunditat de les propietats del material.

L'estructura i continguts d'aquesta memòria es detallen a continuació.

CAPÍTOL 1 - INTRODUCCIÓ

En aquest capítol es posa en context la polimerització plasma dins l'àmbit de les tècniques de dipòsit de recobriments en capa prima i de la ciència de materials en general i es relaciona amb les seves aplicacions més comuns. També es descriuen els principals aspectes teòrics de la generació i la física del plasma. Finalment es presenten els monòmers de base silici i l'hexametilidisiloxà en particular.

CAPÍTOL 2 - EXPERIMENTAL

En aquest capítol es descriu el reactor de plasma DC emprat en aquest estudi en les seves configuracions cilíndrica i planoparal·lela. A continuació es descriuen les principals tècniques de caracterització estructural (microscopies òptica, SEM i TEM), química (XPS, EDX i FTIR), i funcional (reflectància UV-VIS, el·lipsometria, nanoindentació dinàmica, microscratch, DSA i corrosió) emprades. Finalment es fa esment de les diferents eines de software utilitzades per al processament d'espectres i deconvolució de pics (Essential FTIR, FitiK) o per a les simulacions del flux de gas en el reactor (Cosmos-Flow), propietats òptiques (FT-Calc) i penetració dels ions en el material (SRIM).

CAPÍTOL 3 – POLIMERITZACIÓ ASSISTIDA PER PLASMA d'HMDSO

El tercer capítol presenta els resultats dels estudis de dipòsit d'HMDSO en plasma DC. En primer lloc es demostra que els ritmes de dipòsit i l'homogeneïtat dels recobriments depenen de paràmetres com la posició i orientació dels substrats respecte el plasma, la pressió, i el flux de monòmer. Aquests paràmetres es consideren en relació amb l'energia dissipada al plasma, d'acord amb el **model de Yasuda**, que defineix un paràmetre compost Y=W/(FM), on W és la potència efectivament acoplada al plasma, F és el flux de monòmer i M és la massa molecular del monòmer. Aquest paràmetre reflecteix l'energia disponible per molècula en la zona del plasma i permet distingir dos règims de característiques diferents: el règim de creixement deficient en energia, per a Y baixos, i el règim deficient en monòmer,

per a Y alts. No només els ritmes de dipòsit depenen del règim de creixement, sinó també les propietats dels materials dipositats.

En el **règim deficient en energia**, la densitat d'energia disponible al plasma és insuficient per activar totes les molècules i el grau de fragmentació és baix. La creació de radicals es produeix principalment per impacte electrònic provocant l'abstracció d'hidrogen atòmic i de grups metil, doncs aquests són els enllaços més febles de l'estructura de l'HMDSO; l'adsorció i reacció constant de molècules senceres i lleugerament fragmentades sobre la superfície dels substrats, afegida al bombardeig de fotons i ions, genera cadenes polimèriques similars a les del PDMS, amb alt contingut orgànic sobre un esquelet d'enllaços siloxà, però amb un grau d'entrellaçament tridimensional entre cadenes (cross-linking) superior a la del polímer convencional de silicona. L'estequiometria del material dipositat s'apropa a la del monòmer ($SiO_xC_yH_z$, amb $x<1$, $y>1.5$, $z>4$), amb un lleuger augment de la proporció d'oxigen i una disminució de la proporció de carboni i hidrogen. Els recobriments resultants tenen una densitat d'entre 1,10 i 1,35 g/cm^3 i els ritmes de dipòsit s'estanquen o fins i tot disminueixen en augmentar el flux i la pressió de treball.

En el cas del **règim deficient en monòmer**, les molècules de monòmer pateixen un grau de fragmentació superior, que s'incrementa amb valors encara més alts del paràmetre Y. En aquest règim l'energia mitja disponible per molècula és suficient per a trencar els enllaços Si-O de manera generalitzada, i en la composició de les capes dipositades disminueix el pes relatiu de carboni i hidrogen, alhora que augmenta el d'oxigen. El contingut de carboni és encara important, però els grups metil poden arribar a desaparèixer gairebé per complet i els àtoms de carboni es troben en altres configuracions. La densitat del material dipositat pot arribar fins a 1.75 g/cm^3 per als valors d'Y més alts d'entre les condicions assajades.

Els **ritmes de dipòsit** i la **homogeneïtat** dels gruixos dipositats són característiques de màxima importància per a l'aplicació en processos industrials de qualsevol tècnica de dipòsit. L'estudi d'aquests valors demostra que amb els plasmes DC es poden obtenir recobriments polimèrics transparents fins als 3 μm amb ritmes de dipòsit propers als 100 nm/min, cosa que demostra una eficiència del procés similar o superior a les fonts de plasma de RF. Els dipòsits en substrats grans (a partir

de 20 mm) presenten recobriments amb variacions significatives en el gruix degut al factor hidrodinàmic que intervé en el transport de les molècules de monòmer i dels fragments i radicals. La homogeneïtat dels dipòsits millora per a baixes pressions i fluxos menors, però el gruix obtingut és també menor. A fluxos mitjans i alts, és possible obtenir recobriments a les cares anterior i posterior dels substrats, tot i que les propietats d'ambdós són diferents degut a la diferència en el bombardeig iònic. Es demostra també que la configuració d'elèctrodes planoparal·lela produeix recobriments més homogenis que la configuració cilíndrica, i per a substrats plans la homogeneïtat és excel·lent.

L'addició de gasos portadors com ara l'Ar, el N_2, l'O_2 o l'aire comporta canvis importants en les característiques dels recobriments dipositats. L'addició d'argó augmenta la densitat del plasma i el grau d'ionització i de manera efectiva incrementa el paràmetre *Y*. L'argó no s'incorpora a les capes, però pot incrementar el ritme de dipòsit (en el règim deficient en energia) o el grau de fragmentació (en el règim deficient en monòmer), i en general augmenta la densitat i el cross-linking. L'addició de nitrogen genera major absorció i pèrdua de transparència dels recobriments (lleuger aspecte groguenc), mentre que el nitrogen s'incorpora al material en quantitats reduïdes (<5%). Els canvis més substancials es produeixen amb l'addició d'oxigen o d'aire. En ambdós casos, la part orgànica del monòmer és consumida per l'oxigen i desapareix en forma de CO_2 i vapor d'aigua, majoritàriament. Si la quantitat d'oxigen és suficient, el grau d'oxidació és gairebé total i s'obtenen recobriments transparents de propietats similars a l'òxid de silici amorf (SiO_x), amb densitats que arriben als 2.0-2.1 g/cm^3. Els ritmes de dipòsit per a les capes més inorgàniques (SiO_x) es redueixen substancialment fins a ser de l'ordre dels 10 nm/min.

La caracterització de les **propietats mecàniques** dels recobriments indica que en tots els casos la duresa i el mòdul elàstic són molt superiors a les del PDMS. Les dureses per a capes polimèriques sense addició d'oxigen es troben en el rang de 800 MPa a 1.3 GPa, i el mòdul de Young sobre els 10-16 GPa, en comparació als 100-150 MPa i 20-100 MPa per a la duresa i mòdul de Young del PDMS. Amb l'addició de gasos portadors les dureses s'incrementen i és amb l'addició d'oxigen quan arriben al seu valor màxim, sobre els 6.6 GPa. Amb una mescla precursora amb un ratio O_2:HMDSO de només 3:2, s'aconsegueixen propietats molt properes a les del vidre.

Aquest ratio és força més baix que el reportat a la literatura per a altres reactors amb plasma RF o MW, possiblement degut a l'intens bombardeig iònic existent en el plasma DC.

La caracterització de les **propietats òptiques** indica que els índex de refracció en el rang visible per a les capes polimèriques poden variar, entre 1.4 i 1.6 depenent del contingut en carboni i de la densitat i porositat de les capes. En el cas de les capes més inorgàniques obtingudes amb l'addició d'oxigen els índexs de refracció s'acosten molt als de l'òxid de silici amorf, situant-se en el rang 1.45-1.48.

La caracterització de **l'energia superficial** mostra que les capes polimèriques presenten una baixa energia superficial que les fa totalment hidrofòbiques, amb un angle de contacte entre 100 i 115°. L'addició d'oxigen crea grups silanol a la superfície que incrementen la part polar de l'energia superficial fins a reduir l'angle de contacte de l'aigua a 30-35° per a les capes més oxidades.

Finalment, la caracterització de **l'estabilitat tèrmica** i **química** de la protecció contra la corrosió demostra que els recobriments polimèrics de ppHMDSO són altament estables davant de temperatures fins a 450 °C i d'entorns altament corrosius (KOH and NaOH 1M). Es presenten també resultats d'estabilitat amb el temps que demostren que l'únic efecte perceptible és l'adsorció reversible de vapor d'aigua, fet que redueix l'angle de contacte amb el temps. Aquest efecte es reverteix sotmetent els recobriments a tractaments de temperatura o buit.

CAPÍTOL 4 – TRACTAMENT PLASMA DE LES CAPES ppHMDSO

En aquest capítol es presenten els resultats de l'estudi del procés de modificació per post-tractament amb plasma de les capes polimèriques ppHMDSO obtingudes mitjançant els processos de polimerització descrits en el capítol 2. Aquests post-tractaments permeten obtenir recobriments amb **gradients de composició** amb la profunditat. S'analitza principalment l'efecte de diferents paràmetres com la pressió, el tipus de gas i el temps de tractament en la composició i profunditat de la zona modificada. Es demostra que la penetració del tractament depèn principalment de la densitat i porositat de les capes i que per a gasos no reactius (Ar, N2) la modificació es produeix per increment dels enllaços entre cadenes o **CASING**. En el cas de gasos amb contingut d'oxigen, es produeixen reaccions de combustió que

eliminen gairebé totalment els grups orgànics i produeixen oxidació addicional del silici, molt possiblement per condensació de grups silanol formats en passos anteriors. La oxidació completa de la superfície s'assoleix de forma relativament ràpida (4-10 min) però la penetració del tractament s'alenteix a mida que augmenta la profunditat.

Després de discutir els mecanismes fisico-químics mitjançant els quals es produeix la modificació es conclou que el principal paràmetre determinant és el coeficient de difusió dels àtoms d'oxigen, per sobre de l'energia dels ions incidents, i que aquest deu dependre significativament de l'estructura i densitat de cada capa. Molt possiblement, el coeficient de difusió disminueix amb el temps durant el tractament de plasma degut a la densificació de les primeres capes atòmiques sota la superfície

El capítol conclou amb els resultats de la caracterització de les propietats funcionals dels recobriments modificats, on es destaca la baixa **recuperació hidrofòbica** que presenten els tractaments d'oxidació sobre ppHMDSO en comparació amb la ràpida recuperació del PDMS tractat amb els mateixos processos. Finalment es discuteixen els mecanismes que podrien explicar la diferència substancial en la recuperació hidrofòbica en tractaments plasma sobre polímers convencionals i sobre ppHMDSO.

CAPÍTOL 5 – APLICACIONS INDUSTRIALS

En el cinquè capítol es presenten dos exemples reals d'aplicacions industrials dels recobriments polimèrics de ppHMDSO que aprofiten propietats diferents. En el primer exemple, s'aprofita la superior duresa, elasticitat i baixa fricció de les capes polimèriques i la seva transparència en el visible respecte els polímers convencionals per a la protecció contra el ratllat en l'ús habitual d'embellidors d'interruptors elèctrics injectats en ABS. En el segon exemple es fa ús de la baixa energia superficial i l'alta estabilitat química per disminuir la capil·laritat en les arestes dièdriques de les cubetes d'un rotor de PMMA, que presenta un problema de contaminació creuada entre reaccions adjacents.

ABSTRACT

Plasma Polymerization is a novel technique for the preparation of polymer-like thin film coatings at low temperatures onto almost any type of substrates: plastic, metal, semiconductors, wood, textile fibers or membranes, to cite just a few. The films can be grown directly from liquid monomers that are introduced in the vapor phase into a vacuum chamber equipped with one or more electrodes that generate the plasma after a high voltage in continuous current mode (DC), low-frequency (AC) or high frequency (RF) is applied. The plasma state is a high-energy gas state in which the density of electrons, ions, excited species and radical fragments is abundant. The introduction of an organic monomer vapor into the plasma triggers the formation of molecular fragments capable of initiating multiple reactions: in the gas phase, recombination of radicals, oligomerization of high-weight molecules and aggregation into nanoscopic dust can occur, whereas adsorption and reaction onto any solid surface will result in the growth of highly adherent thin films. The structural, chemical and functional properties of these coatings are determined by the composition of the precursor gas mixture and the type of monomer, and also by several technological parameters that can be fine-tuned, such as the pressure, plasma power, frequency of change of electrode polarization, substrate location, flux of gas, etc… By controlling these technological parameters it is possible to modulate the value of the magnitudes that govern the physico-chemical mechanisms which are responsible for film growth: residence time of molecules, available energy per molecule, degree of monomer fragmentation, density and energy of ion bombardment on the substrates, and gas transport in the reactor, among others.

Plasma polymerization allows to grow films from virtually any kind of organic molecule which can be evaporated at low temperatures (<80 °C) and introduced in the reactor at sufficient flow rates (> 1sccm), even when that molecule would not be the characteristic repeating unit of any conventional polymer synthesized by other

physical or chemical means. The technique is also applicable to other types of monomers (non-carbon based), such as organosilicon or organometallic molecules.

The use of organosilicon monomers allows to obtain films with a wide spectrum of properties, from those frequently attributed to an elastomeric polymer such as silicone (polydimethylsiloxane, PDMS) to those associated to a hard inorganic material, such as glass (amorphous silicon dioxide, silica). Regardless of their apparently opposed nature, these two materials share an extremely similar chemical backbone based on silicon-oxygen chemical bonds. During the investigations conducted in our study, different organosilicon monomers have been employed for plasma polymerization: **hexamethyldisiloxane** (**HMDSO**), hexamethyldisilazane (HMDSN) and tetraethoxysilane (TEOS), but the only results presented within the scope of this Thesis are those obtained for ppHMDSO films. This is due to the fact that HMDSO is the only monomer allowing the growth of polymer-like films, inorganic-like films, intermediate stoichiometry films and even graded films with properties varying with depth in a single plasma process.

With respect to power sources for plasma generation, most published works choose high frequency electrical power sources, such as radiofrequency (RF) or microwaves (MW), although plasma polymerization can also be carried on with **direct-current high-voltage** sources (HV-DC), from 500 V to 3000 V. In our investigations, these three types of sources have been employed, as can be found in our related publications, but again only results with the DC plasma source will be presented due to their simple design and use in industrial applications. A main objective of this Thesis is to establish its limitations, such as the limited film thickness attainable or the excessive heating of substrates, depending on the reactor configuration and the operating parameters.

As a consequence, the scope of this Thesis covers two main objectives: first, the **study of DC plasma polymerization of hexamethyldisiloxane (DC ppHMDSO) with and without addition of carrier gases** in the precursor mixture, in order to obtain polymer-like or inorganic silica-like coatings with specific mechanical, optical and corrosion protective functional properties, for further application to solving some practical problems of industrial interest; secondly, **the study of modifications**

produced by a different non-additive post-treatments in a polymer-like ppHMDSO film, in order to obtain a film with graded properties varying with depth.

The structure and contents of this Thesis dissertation are outlined in the remaining of this section.

CHAPTER 1 – INTRODUCTION AND OBJECTIVES

This chapter puts in context plasma polymerization with respect to thin film deposition techniques and within materials science in general. It also describes the main theoretical aspects of the generation and physics of the plasma state and plasma polymerization mechanisms. A brief introduction to industrial applications of plasma polymerization is also included.

CHAPTER 2 - MATERIALS AND METHODS

This chapter describes the DC plasma reactor used in this study in its cylindrical and parallel plate configurations. After that, it also covers the main structural characterization techniques (optical microscopy, SEM and TEM), chemical (XPS, FTIR and EDX) and functional (reflectance UV-VIS, ellipsometry, nanoindentation dynamics, microscratch, DSA and corrosion) that were used.

CHAPTER 3 – PLASMA POLYMERIZATION OF HMDSO

The third chapter presents the results for plasma polymerization of HMDSO in a DC plasma. First, it shows that deposition rates and coatings homogeneity depend on certain parameters such as the location and orientation of the substrates with respect to the plasma, the pressure, and the monomer flow. These parameters are related to the energy dissipated in the plasma, according to **Yasuda's model**, which defines a composite parameter Y=W/(FM), where W is the effective power coupled to the plasma, F is the monomer flow and M the molecular mass of the monomer. This parameter reflects the available energy per molecule within the plasma region and allows to distinguish three different characteristic regimes: the energy-deficient regime, for low Y values, and the monomer-deficient regime for high Y values. A grey zone in the middle is defined as a transition regime. Thus, not only the deposition rates depend on the applicable growth regime, but also the properties of the deposited materials.

In the **energy deficient regime**, the energy density available in the plasma is insufficient to activate all monomer molecules, and, consequently, the fragmentation rate is low. Free radicals are mainly produced by electronic impact causing the cleavage of atomic hydrogen and methyl groups, as these are the weakest bonds in the HMDSO molecule. The adsorption and constant reaction of monomer molecules and slightly fragmented ones on the surface of the substrate, added to the bombardment of photons and ions, generates polymer chains similar to those in PDMS, with a high organic content over a siloxane scaffold, but with a higher dimensional cross-linking than the conventional silicone polymer. The stoichiometry of the deposited material resembles that of the monomer ($SiO_xC_yH_z$ with x <1, y> 1.5, z> 4) with a slight increase in the oxygen and a decrease in the carbon and hydrogen proportion. As a result the coatings have a density between 1.10 and 1.35 g/cm^3 and deposition rates saturate or even decrease when monomer flow and working pressure increase.

In the **monomer deficient regime**, monomer molecules experience a higher degree of fragmentation, which increases at higher values of the *Y* parameter. In this regime, the average energy available per molecule is enough to break the Si-O bonds at higher rates. Thus, the relative proportions of carbon and hydrogen in the deposited layers decrease, while oxygen concentration increases. Carbon content is still important, but the methyl groups can disappear almost completely as carbon atoms are increasingly incorporated to other groups. The density of the deposited material can reach up to 1.75 g/cm^3 for the higher *Y* values of the tested conditions.

The **deposition rates** and **homogeneity** of deposited films are features of outmost importance for the applicability of any deposition technique to industrial processes. The study of these values shows that using DC plasmas, transparent polymer coatings up to 3 μm can be obtained with deposition rates up to 100 nm/min, demonstrating similar or superior process efficiency as compared to RF plasma sources. Deposition in large substrates (from 20 mm) present coatings with significant thickness variations due to the hydrodynamic factor involved in transporting monomer molecules, fragments and radicals. The homogeneity of films improves for lower pressures and lower flows, but the obtained thickness is also lower. At medium to high flows, it is possible to obtain coatings on both sides of the substrates, although

the properties in both sides are different due to the substantial difference in the amount of ion bombardment. It also demonstrates that the parallel plate configuration of electrodes produces more homogeneous coatings than the cylindrical configuration, and when flat substrates are used, the homogeneity is excellent.

Addition of carrier gases, such as Ar, N_2 or O_2 results in significant changes in the properties of the films. When Ar is used as a carrier gas, the plasma density and the ionization ratio increase, and also does the *Y* parameter. Ar is not incorporated to the films, but it can increase deposition rates (in the energy-deficient regime) or monomer fragmentation (in the monomer-deficient regime), and, as general rule, the density and cross-linking of the films is increased. N_2 addition results in slightly yellow coatings, although nitrogen concentration in the films is found to be less than 5%. The most significant changes occur when oxygen or air are added to the precursor flow. In both cases, the organic part of the monomer is consumed by oxygen in a combustion-like process that forms volatile CO_2 and H_2O vapor, mainly. At high oxygen/monomer ratios, the degree of oxidation is almost complete and transparent coatings with properties close to those of silica (SiO_x) are obtained, with densities as high as 2.0-2.1 g/cm^3. Deposition rates drop down to 10 nm/min for SiO_x-like films with higher amounts of oxygen.

The characterization of **mechanical properties** of the films indicates that for all plasma polymerized films the elastic modulus and hardness values are higher than conventional PDMS. Hardness values for films from pure monomer range from 800 MPa to 1.3 GPa, and Young's modulus reach 10-16 GPa, as compared to 100-150 MPa and 20-100 MPa for hardness and elastic modulus for PDMS.

Addition of carrier gases result in increased values for hardness, with oxygen containing precursor mixtures producing the best results with hardness values up to 6.6 GPa; at an Oxygen:monomer ratio of 3:2 the properties of the deposited films are already close to those of fused silica. Surprisingly, this ratio is lower than those reported in the literature for RF or MW plasmas, which is probably due to the higher ion bombardment on the growing films achieved in DC plasmas.

Characterization of **optical properties** was conducted in the visible spectrum. The refractive index varies between 1.4 and 1.6 depending on the carbon content and the

density and porosity of the films. For films deposited with addition of oxygen the values of the refractive index are close to those of fused silica, in the range 1.45-1.48.

Characterization of the **surface energy** shows that polymer-like films have a low surface energy, which makes them hydrophobic, with a contact angle between 100 and 115°. Addition of oxygen creates silanol groups at the surface, which increases the polar component of the surface energy until de contact angle is reduced to 30-35° for the most oxidized films.

Finally, characterization of **thermal stability and corrosion protection** indicate that polymer-like films are highly stable up to 450°C, and also in highly corrosive conditions (KOH and NaOH 1M). Some results on aging are also presented and demonstrate that the only effect of aging is physical adsorption of water vapor, which results in a decrease of the contact angle over time. This effect is reverted if the films are baked.

CHAPTER 4 – PLASMA TREATMENT OF ppHMDSO FILMS

This chapter contains the results of the study of plasma post-treatment of ppHMDSO films deposited by the methods and conditions described in chapter 3. These post-treatments allow to obtain coatings with **graded properties** that vary with depth. The effect of operational parameters such pressure, type of gas and treatment time in the composition and depth of the modified region are analyzed.

It will be shown that the penetration of the treatment depends on the density and porosity of the films. For non-reactive gases (Ar and N_2) the modification is effected by increasing the amount of links between polymeric chains (CASING mechanism). When pure oxygen or oxygen containing treatments are applied, combustion reactions consume almost all organic groups and the silicon atoms in the film are further oxidized, probably by condensation of silanol groups created during removal of organic groups. Complete oxidation of the surface is accomplished in less than 10 min, but further progression of the oxidation is slowed down as the oxidized region increases in depth. The discussion of the mechanisms that lead to the modification suggests that the main parameter that explains the results is the diffusion coefficient of oxygen atoms, rather than the energy of impinging ions. This coefficient may be highly dependent on the structure and density of the films prior to the plasma

treatment. It is also hypothesized that the diffusion coefficient may be decreased as the first atomic layers are densified by the plasma treatment.

The last part of this chapter is devoted to the characterization of the functional properties of the modified films. The most interesting property is the low **hydrophobic recovery** demonstrated by the oxidation post-treatments in ppHMDSO films as compared to the fast hydrophobic recovery of PDMS treated under the same conditions. The mechanisms that could explain this substantial difference in the hydrophobic recovery of plasma-treated conventional polymers and plasma-treated ppHMDSO are discussed at the end of this chapter.

CHAPTER 5 – INDUSTRIAL APPLICATIONS

Chapter 5 contains two real examples of industrial applications where polymer-like ppHMDSO films solve real problems, by taking advantage of one specific property. In the first example, the superior hardness, elasticity and low friction of polymer films, together with their low absorption in the visible spectrum, are applied to increase the scratch resistance of ABS plastic protectors for home switches. The second example shows how the low surface energy and high chemical stability of ppHMDSO films allows to decrease the capillary phenomena at dihedral surfaces defined by the wells of PMMA cuvettes for chemistry analyzers.

CHAPTER 1

INTRODUCTION

1.1. PLASMA POLYMERIZATION WITHIN MATERIALS SCIENCE: A HISTORICAL PERSPECTIVE

From a certain perspective, the History of mankind is also the story of our ability to give form to the materials provided by nature in order to produce tools, goods, shelter and energy that would allow us to achieve a much more productive and comfortable day-to-day life. From the *Paleolithic*, or “Early Stone Age”, to the *Neolithic*, the “New Stone Age”; from the *Bronze* Age to the *Iron* Age, all these historical periods refer to the capacity of our ancestors to master different materials. It could be argued that over the last century we have subsequently entered the *Concrete Age*, the *Silicon Age* or even the *Plastic Age*.

Materials Science is therefore an ancient discipline that only recently has been recognized as an interdisciplinary field that involves physics, chemistry and engineering. Most interesting is the fact that Materials Science allows us not only to understand, transform and employ *natural* materials but also to create new *artificial* ones, quite often by mimicking biological life’s ability to do so.

Thin film technology is a field within materials science that goes one step further. It allows fabricating composite materials that have different properties *at* the surface and deeper *below* it, within the bulk. By employing thin film techniques it is possible to obtain coatings with thicknesses well below the human eye’s perception, yet thick enough to provide a beneficial combination of surface and bulk properties not achievable with the bulk material alone. Just as an example, a chrome or aluminum thin film on top of a plastic surface provides the appealing finish of a polished metal

part, but much lighter, much cheaper, and much easier to produce in serial manufacturing of large quantities.

Gold beating in the 18th Dynasty of Ancient Egypt (1543 – 1292 BC) could be considered as the oldest thin film technology documented.[1] Samples from this period have been found to be even below 1 μm in thickness. The extraordinary malleability of gold enables it to be rolled and hammered into leafs of just a few microns or even less, which would then be usually applied on top of wood, bronze or copper by means of a small amount of wax or resin. The resulting gilded objects (statues, crowns, coffins) would just appear as if made of pure gold. From Egypt, the craft spread throughout ancient cultures and is still in use nowadays.

Thin film deposition by vacuum coating techniques is a much more recent development.[2] The first findings on deposition of materials in a vacuum date from the mid 1800s. They originated rather unintendedly from the study of electrical discharges in vacuum, which was a hot topic for physicists studying electricity and electromagnetism. In 1852 W.R. Groove noticed the deposits formed on a polished silver surface that was the anode of a DC discharge in vacuum, and similar findings were published by M. Faraday in 1854. But it was A. Wright, professor at Yale University, who first recognized that this effect, *sputtering* as it would be termed a few years later, could be a useful technique to deposit metals on glass to form mirrors and study their properties. Since Wright was not very specific in his experimental description, T. Edison successfully patented the first system for vacuum coating in 1894, after ten years of litigation, although the US Patent Office recognized Wright's

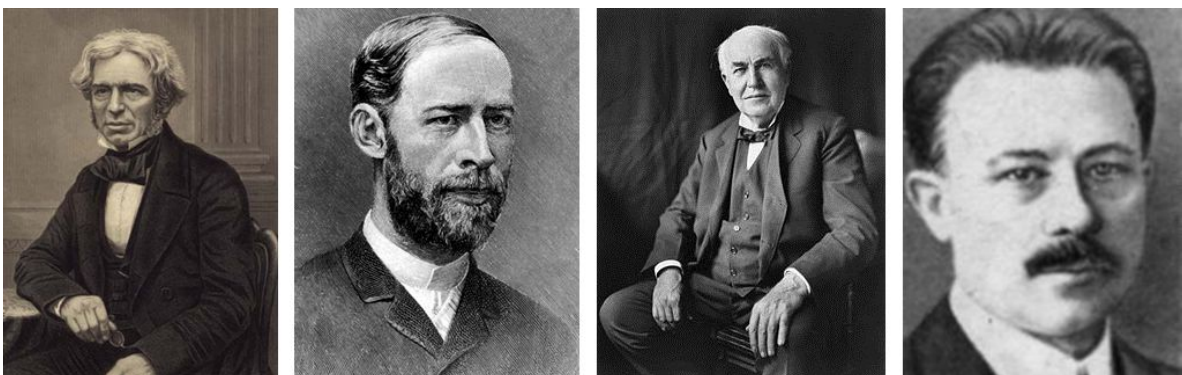

FIGURE 1.1. Pioneers in vacuum coating. From left to right: Michael Faraday, Heinrich Hertz, Thomas A. Edison, Martin Knudsen.

work as prior art.[3] In all these early original works it is not clear whether the processes described by Wright and Edison were really due to sputtering or arc vaporization of material. Surprisingly, thermal evaporation in vacuum was studied later than sputtering and arc vaporization. Works on evaporation of heated material in vacuum were first published by H. Hertz in 1882 but he did not pay any attention to the deposited materials, but only to evaporation rates. Thermal evaporation was also covered by Edison in his 1884 patent application, but apparently it was not applied to any equipment. In 1887 Nahrwold reported the deposition of platinum by sublimation in vacuum and he is credited to be the first scientist to use the technology effectively for the deposition of thin films. Finally, in 1909 Knudsen proposed his well-known "Cosine Law of Distribution" for vapor emerging from a point source. The development of reactor chambers, vacuum pumps, pressure gauges and power sources continued steadily during the first half of the Refth century, but it was with the explosion of microelectronics in silicon integrated circuits in the 1960's that vacuum coating technologies blossomed and progressed to generate a variety of efficient deposition and etching techniques which soon after expanded to other fields and applications.

Many of the techniques developed for thin film deposition and materials processing take place in a special state of matter called ***plasma***. The term *plasma* derives from Greek's πλάσμα, meaning "that wat is made". Faraday was a pioneer in the study of luminous discharges at low gas pressure,[4] back in 1831, which he called ***glow discharges,*** but the association of the term "plasma" is generally attributed to Langmuir,[5] who used it in 1929 to describe an ionized gas formed around tungsten filaments in vacuum, when he was investigating on how to expand the lifetime of a lighting bulb for General Electric.(1)

The term ***polymer*** derives from the ancient Greek word πολύς (*polus*, meaning "many") and μέρος (*meros*, meaning "parts"), and refers to a macromolecule whose structure is composed of multiple repeating units. The units composing polymers derive from molecules of low relative molecular mass. Although the term was coined in 1833 by Jöns Berzelius, his definition is completely different from the modern

(1) Langmuir was aware of how an electric field in an ionized gas carries electrons and ions and was reminded of the way that blood plasma carries red and white blood cells[5].

definition of polymers as covalently bonded macromolecular structures, which was proposed in 1920 by Hermann Staudinger.[6] Natural polymers can be found among the most important biomolecules: polysaccharides, (such as cellulose), proteins and nucleic acids are all excellent examples of polymers with extraordinary biochemical properties. Synthetic polymers started being developed in the early 1900's: Bakelite in 1907, PolyVinyl-Chloride (PVC) in 1927, PolyStyrene (PS) in 1930 and Nylon in 1938 where among the first ones to be synthesized.

Plasma polymerization can be defined as the formation of polymeric materials under the influence of plasma. Almost simultaneously as the history of sputtering and thermal evaporation started, some studies detected that organic compounds formed solid deposits under the effect of electrical discharges in vacuum. Similarly to sputtering, these coatings were not identified as potentially useful but rather as undesirable by-products; in contrast, it took more than eight decades, in the 1960's, to recognize this process as a useful means of synthesizing polymers. This was most likely due to the fact that the concepts of polymers and polymerization were not well-developed.[7] Until the mid 1980's, plasma polymerization was just studied as another method of polymerization, without recognizing the unique properties that could be achieved with these new type of materials such as their higher stability, insolubility and adhesion to any substrates. Although it is possible to use plasma polymerization as a mechanism to obtain materials close to the conventional polymers, it can also be employed to achieve a wide range of properties, from mostly polymer-like to inorganic-like,(2) or even with graded properties, just by controlling different process parameters. Therefore, plasma polymerization should be considered as a method for forming a new type of materials rather than just another method of preparing conventional polymers.

1.2. FUNDAMENTAL ASPECTS OF PLASMAS AND PLASMA POLYMERIZATION

Since a plasma is basically an ionized gas, a complete description of the physical model needs to deal with the properties and interactions of gas molecules in a

(2)When only an inorganic deposit is sought, plasma deposition is usually referred to as plasma enhanced chemical vapor deposition (PECVD).

vacuum reactor and also with the interactions between the electric field and the charged particles and the sequence of processes generated thereafter.

1.2.1. Gas Physics

The interaction among all particles in the gas phase and between these particles and the surfaces in the reactor will greatly influence the deposition rates and the chemical properties and structure of films deposited in plasma polymerization processes. It is therefore important to understand the basic equations governing these phenomena, which are described by the kinetic theory of gases.[1,7]

Number of molecules in a closed reactor

In a vacuum reactor, the amount of gas molecules can be related to the pressure, P, and the reactor volume, V, by the ideal gas law,

$$PV = nRT, \qquad (Equation\ 1.1)$$

where n is the number of moles of gas, R the gas constant, and T the absolute temperature. One mole of gas contains 6.02×10^{23} molecules, Avogadro's number (N_A), and at 1 atm it occupies 22.4 liters. Equation 1.1 is simple and yet it has some important implications in all vacuum processes, including plasma polymerization, such as:

- At a given pressure the total number of gas molecules is independent of the molecular weight and the number of atoms per molecule, i.e. the number of Ar, O_2, or $Si_2OC_6H_{18}$ molecules is the same in a pure gas of each one at the same pressure.
- In a closed system, if molecules are dissociated the pressure will increase.
- In a closed system, if molecules are deposited on the surfaces, they will be removed from the gas volume and the pressure will drop.
- In a closed system, the pressure variation depends on the balance between fragmentation rates and deposition rates.

Molecular velocity

For a real gas, Maxwell established the law governing the distribution of molecular velocities and derived the average velocity, $\bar{c}$, and the most probable velocity, α, as:

$$\bar{c} = (8\ RT/\pi M)^{1/2} = 1.46 \times 10^4\ (T/M)^{1/2}\ \text{cm/s}, \qquad (Equation\ 1.2)$$

$$\alpha = (2\,RT/M)^{1/2} = 1.29 \times 10^4\,(T/M)^{1/2} \quad \text{cm/s}, \qquad (Equation\ 1.3)$$

thus, for Ar at 25°C the average velocity of molecules will be as high as 39850 cm/s.

Collisions between molecules

For collisions between like molecules in a gas, the number of collisions per second, Z, in a volume V (cm^3), at pressure P (mbar) and temperature T (K) for a gas sphere of radius d is given by

$$Z = 1.09 \times 10^{41} \cdot d^2 \cdot M^{-1/2} \cdot P^2 \cdot V^2 \cdot T^{-3/2} \qquad (Equation\ 1.4)$$

Mean free path

The mean time between collisions is the reciprocal of the amount of collisions per second, and the mean free path, λ, is the distance traveled by a molecule between successive collisions. If λ_1 is the mean free path at 1 mbar, the mean free path at a different pressure P (torr) is inversely proportional to pressure:

$$\lambda_p = \lambda_1/P \qquad (Equation\ 1.5)$$

For oxygen, λ_1 is 65 μm and the mean free path at 0.1 mbar is 0.65 mm.

Collisions of gas molecules with surfaces

According to the classical kinetic theory of gas, the number of molecules $\hat{n}$ striking a unit surface at a certain pressure P (mbar) and temperature T (K) is given by

$$\hat{n} = 1.62 \times 10^{23} \cdot P/(M \cdot T)^{1/2} \ \text{molecules}/(\text{s·cm}^2) \qquad (Equation\ 1.6)$$

From equations 1.4 and 1.6 it is easily derived that the number of gas-gas collisions is proportional to P^2, whereas the number of gas-surface collisions is proportional to P. In fact, the ratio ϕ of total gas-gas collisions ($Z{\cdot}V$) to gas-surface collisions ($\hat{n}{\cdot}A$) in a reactor of volume V and area A is given by

$$\phi = 1.15 \times 10^{20} \cdot (V/A) \cdot P \cdot V^2 \cdot T^{-1} \cdot d^2 \qquad (Equation\ 1.7)$$

Equation 1.7. has a practical implication to understand the mechanisms of film growth, that is: larger molecules with larger diameters, higher pressures and larger reactor volumes increase gas-phase reactions with respect to gas-surface ones.

Monolayer formation time

From the flux of collisions $\hat{n}$ between gas molecules and surfaces the time required for molecules impinging on a certain surface to form a monolayer of adsorbed molecules, τ_{mon}, can also be calculated. Assuming a certain sticking coefficient, *s*, and a certain surface density, d_{sur}, the monolayer formation time is given by

$$\tau_{mon} = d_{sur}/(s \cdot \hat{n}) \qquad (Equation\ 1.8)$$

For a surface density of 10^{15} nucleating sites, a sticking coefficient of 1, a temperature of 298 K and a pressure of 0.1 mbar, one monolayer of a monomer of 162 amu would form on any surface in just 31 μs .

Flow rate and pumping rate

The flow rate *F* in a reactor at stable pressure reflects the amount of gas molecules entering and leaving the reactor per unit time. It is expressed as the volume occupied by the flowing molecules at standard temperature and pressure, per unit of time, and it is usually measured in standard cubic centimeters per minute (sccm). One sccm is equivalent to 7.44×10^{-7} moles or 4.48×10^{17} molecules entering and leaving the reactor every second.

If the vacuum pump in a reactor is closed and the inlet of gas is left open, the pressure in the reactor will increase at a constant rate, from which the input flow rate of gas can be calculated as

$$F = 60 \cdot (V_R/P_0) \cdot \frac{dP}{dt} \ \text{(sccm)} \qquad (Equation\ 1.9)$$

where V_R (cm^3) is the volume of the reactor and P_0 is the standard pressure; *P* and P_0 need to be expressed in the same units and dP/dt should be the average pressure change per second.

Residence time

If the vacuum outlet is opened again the reactor pressure decreases until the pressure is stabilized. At that point, the input flow rate *F* and pumping throughput of gas *Q* are equal. The residence time τ_{res} is the average time spent by a molecule in a reactor before it is pumped out and it is equal to the time needed to renovate all the

molecules in the reactor. The residence time can be calculated as the time employed to pump out all the gas molecules from the reactor if the pumping throughput could be kept constant at the same value achieved for the equilibrium pressure. If pressure is expressed in (mbar), reactor volume in (liters), temperature in (K) and flow rate in (sccm), the residence time is given by

$$\tau_{res} = 1.62 \times 10^4 \cdot (P \cdot V)/(T \cdot F) \ \text{(s)} \qquad (\textit{Equation 1.10})$$

For a flow rate of 1 sccm in a 100 L reactor at a pressure of 0.1 mbar and 25°C, the residence time will be 543 s. In a practical approach, the residence time is usually controlled by changing the pumping speed and the flow rate simultaneously and maintaining the pressure. According to Equation 1.10, larger reactors, higher pressures and lower flow rates will favor long residence times, which will increase the amount of interactions of molecules with other molecules, with charged and energetic species and with the surfaces inside the reactor. This has a decisive effect on plasma polymerization.

Flow regimes

For systems with a net flow of gas, the mean free path defines the boundaries between different flow regimes which are characterized by an individual or a collective behavior, depending on the amount of collisions between molecules. Criteria for distinguishing between the different flow regimes are based on the magnitude of the Knudsen number, K_n, which is defined as the ratio of the mean free path to a characteristic dimension of the system (chamber diameter or length).

At low gas pressures, where $K_n > 1$, free *molecular flow regime* occurs, which is very accurately described by the kinetic theory of gas. The main free path in this regime is large when compared to the characteristic dimensions of the reactor, and molecule-surface interactions predominate.

At higher pressures, where $K_n > 0.01$, the amount of molecule-molecule collisions in the gas phase increases, the mean free path diminishes and the *viscous flow regime* is established. The theory of fluid mechanics offers the best picture to explain how molecules flow in these conditions. At low gas velocities the flow is mainly *laminar* with layered, parallel gas flow lines and with laminar flow velocity close to zero at the

walls of the reactor and higher towards the central axis. For higher flow velocities, the layers cease to be parallel and can create swirls, especially around obstacles in their way. This is known as the *turbulent flow*.

It is worth noting that the boundaries between these regimes are diffuse and in the middle, where $1>K_n>0.01$, the flow is neither completely molecular nor viscous. It is also to be noted that some parts of the reactor may be at a different regime, e.g. close to the inlet of processing gas and near the outlet leading to the vacuum pumps.

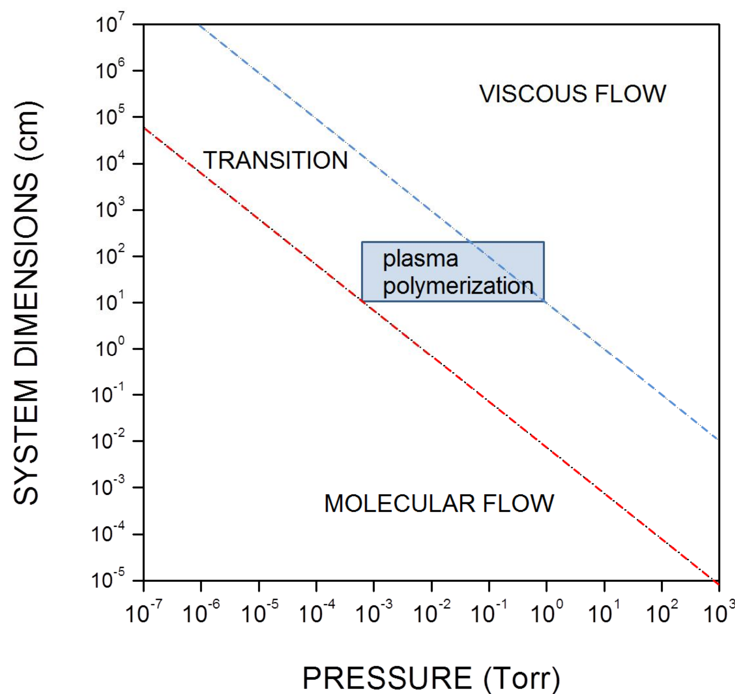

FIGURE 1.2. Boundaries for the different flow regimes. Plasma Polymerization takes place in a transient regime which is neither molecular nor completely viscous.

Plasma polymerization processes take place usually somewhere in between the molecular and the laminar viscous regimes as shown in Figure 1.2.

1.2.2. Plasma Physics

Plasmas are naturally present in the Universe: the sun and the rest of the stars consist entirely of plasma; the earth's ionosphere, the space between galaxies and, closer to us, lightning, polar auroras and most fires(3) are also good examples of

(3) There is some debate about whether fire can be considered a plasma or not. Von Engel proposed a simple method to settle down the question: a flame is placed between two parallel plates and an electric field is applied. If the flame is deviated towards the cathode, it can be considered as a plasma.

natural plasmas. Plasma can also be artificially created in the laboratory by combustion, electric discharge, controlled nuclear reactions or other means. Even in some consumer products we may find plasmas, such as in the almost extinct plasma TV sets, in common fluorescent tubes or in the old-fashioned neon tubes.

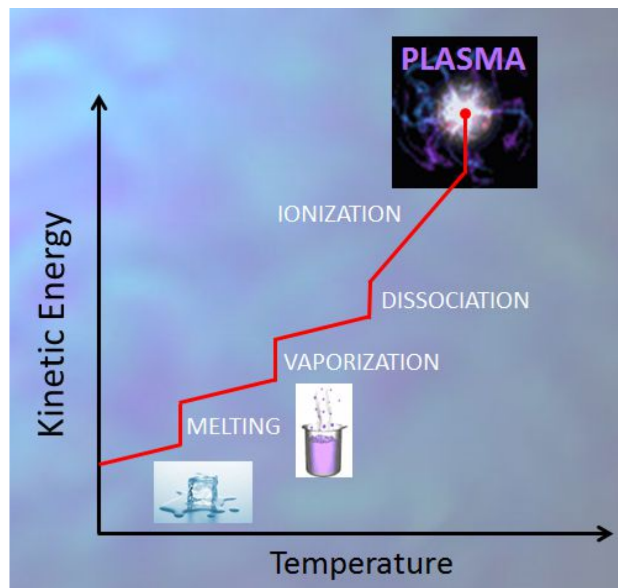

FIGURE 1.3. A plasma state can be achieved by increasing the temperature of a gas beyond several thousand degrees. It is considered as "the fourth state of matter" above less energetic states of solid, liquid and gas.

The simplest definition of plasma would be an ionized gas. A more complete definition would include also its complex composition: electrons, ions (both positive and negative), neutral molecules and atoms either in the ground or excited states and photons. In addition, plasmas posses important properties such as quasineutrality, electrical conductivity and a collective fluid behavior of electrons. Plasma is also commonly referred to as "*the fourth state of matter*" [(4)]. Such a reference originates from the comparison with the remaining three physical states: solids, liquids and gases. The main difference between these states is the kinetic energy of the atoms and molecules: the higher the energy the more freely can molecules depart from their neighbors. Kinetic energy of neutral molecules is increased by different mechanisms of energy absorption and it is macroscopically perceived as an increase in temperature. When the energy of molecules is further increased, spontaneous

[(4)]The expression "the fourth state of matter" is attributed to Crookes, who first used it in a pioneer paper in Phyllosophical Transactions, vol. 1, p.135 (1879)

dissociation of molecular fragments or atoms will occur. At many thousand degrees centigrade, the collisions of these fast particles would produce ionization of the atoms. The onset of ionization is the door to the plasma state (Figure 1.3). As a reference, the ionization energies for oxygen and nitrogen are in the range of 13-15 eVs. The energy required to produce the ionization of an atom can be provided by fast particle (high T) collision or by photon absorption. A charged particle with kinetic energy of 1 eV has an equivalent temperature of 11600 K, which is given by $T = E / k_B$, where k_B is Boltzmann's constant.

Plasma species and degree of ionization

As mentioned, all plasmas are composed of charged particles (electrons, ions) and neutral ones, with respective densities n_e, n_i and n_0. The plasma is electrically neutral in average and therefore $n_e = n_i << n_o$.

The degree of ionization, f_i, represents the fraction of ionized atoms or molecules with respect to the total amount, and it is also an important characteristic of plasma. The degre of ionization is simply defined as

$$f_i = n_e /(n_e + n_0) \qquad (Equation\ 1.11)$$

Plasmas for material processing and thin film deposition have low degrees of ionization which may range from 10^{-7} to 10^{-2}. The density of charged particles can be calculated from the ideal gas law (Eq. 1.1): at 0.1 mbar, $n_0 \sim 10^{15}$ cm^{-3}, hence electron density for these plasmas will be in the range 10^8 to 10^{13} cm^{-3}.

Electron temperature, ion temperature and plasma temperature

Plasmas at low pressures do not achieve complete thermalization of all particles, which means that the temperature of electrons, T_e, ions, T_i, and neutrals, T_n, can be extremely different. This non-equilibrium situation is also possible because the mechanisms by which electrons, ions and neutrals gain and dissipate energy can be different. For example in the presence of an electric field, both electrons and ions can gain energy from the electric field, whereas neutrals cannot. In addition, electrons can gain much higher energies from the electric fields because they do not lose significant fractions in inelastic collisions, whereas ions and neutrals do.

Depending on the difference in the energy of electrons, ions and neutrals, plasmas can be further classified between thermal plasmas, if $T_e = T_i = T_n$, and non-thermal or 'cold' plasmas, if $T_e >> T_i >> T_n$. Most artificial plasmas are non-thermal plasmas and all glow discharges employed for plasma processing of materials have average electronic temperatures between 10^4–10^5 K, ion temperatures between 300 – 1000 K and neutral temperatures at room temperature or slightly higher.

Figure 1.4. illustrates the electron density and electron temperature for different natural and artificial plasmas.

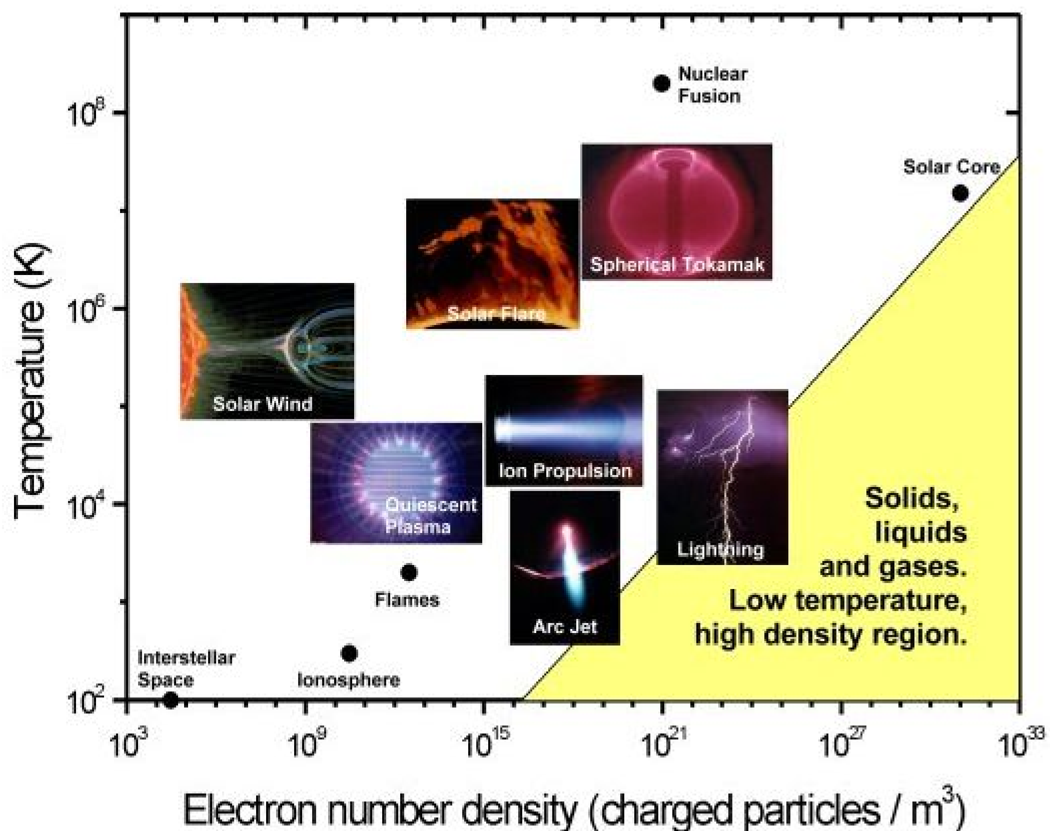

FIGURE 1.4. Density of charged particles (electrons) and equivalent temperature for different natural and artificial plasmas.

Energy transfer by particle collision

Theoretically, energy transfer by particle collision can occur in atom-atom, electron-atom, electron-ion, electron-electron, ion-ion and ion-atom. When the relative energy of the colliding particles is large, an inelastic collision occurs and part

or all of the kinetic energy will be absorbed into potential energy of electrons in the target atom, except for ion-ion and electron-electron collisions in which only elastic collisions are possible due to high repulsive forces.

For elastic collisions between an electron and a slow neutral, and an ion and a slow neutral, by conservation of energy and momentum, it can be shown that the fractions of energy Q_e and Q_i lost by the electron and the ion respectively depend on their relative masses with respect to the neutral and are given by[8]

$$\mathrm{Q}_e = 4 \cdot m_e/m_n \qquad (\textit{Equation 1.12})$$

$$\mathrm{Q}_i = 2 - \left(2\, m_n/(m_n + m_i)\right) \qquad (\textit{Equation 1.13})$$

where m_e and m_n are the mass of the electron and the neutral atom or molecule respectively. According to Equations 1. 11-12, when electrons and ions collide elastically with slow moving neutrals, electrons do not lose a significant amount of energy due to the extreme difference in mass between an electron and an atom or molecule, and therefore electrons will continue to gain energy until they suffer an inelastic collision. On the contrary, ions and neutrals can lose a significant fraction of their kinetic energy with each collision with another neutral or ion, either in elastic and inelastic collisions.

For inelastic collisions, conservation of energy requires that the energy before and after the collision be the same. Thus, for particles of mass m_1 and m_2 and initial velocities v_1 and v_2:

$$\tfrac{1}{2} m_1 v_1^2 + \tfrac{1}{2} m_2 v_2^2 = \tfrac{1}{2} m_1 v_1'^2 + \tfrac{1}{2} m_2 v_2'^2 + \Phi \qquad (\textit{Equation 1.14})$$

where Φ is the energy absorbed by the collision. If Φ is higher than the ionization energy, collision will lead directly to ionization; if Φ is less than the ionization energy but more than the excitation energy, the atom will be activated and an electron in the atom will be promoted to a higher energy level where it will stay for a short time (10^{-8} to 10^{-9} s), after which it will decay to the ground state and emit the excess energy as a photon. If metastables exist (excited states with longer decay times) ionization could be possible even if Φ is less than the ionization threshold.

Types of collisions

In general, electron-neutral collisions leading to dissociation, excitation and ionization are by far the most frequent ones but other types of collisions can lead to additional reactions. These have been clearly summarized by Ohring[1] as follows:

Electron collisions

1.	**Ionization**	$e^- + A \rightarrow A^+ + 2e^-$	$e^- + A_2 \rightarrow A_2^+ + 2e^-$
2.	**Excitation**	$e^- + A_2 \rightarrow A_2^* + e^-$	$e^- + AB \rightarrow (AB)^* + e^-$
3.	**Dissociation**	$e^- + AB \rightarrow A^* + B^* + e^-$	
4.	**Dissociative ionization**	$e^- + AB \rightarrow A + B^+ + 2e^-$	
5.	**Dissociative attachment**	$e^- + A_2 \rightarrow A^+ + A^- + 2e^-$	
6.	**Recombination**	$e^- + A^+ \rightarrow A$	

Atom – molecule – ion collisions

7.	**Symmetrical charge transfer**	$A + A^+ \rightarrow A^+ + A$
8.	**Asymmetric charge transfer**	$A + B^+ \rightarrow A^+ + B$
9.	**Metastable-neutral (*Penning* ionization)**	$A^* + B \rightarrow A + B^+ + e^-$
10.	**Metastable – metastable ionization**	$A^* + B^* \rightarrow A^+ + B + e^-$

Energy transfer by photon absorption

Photons are capable to produce direct photodissociation, photoexcitation and photoionization provided that their energy is higher than the respective thresholds for dissociation, excitation and ionization. Taking into account that the energy of a photon of wavelength λ is given by hc/λ, where h and c are Planck's constant and the velocity of light respectively, the wavelength of photons capable of photoionization is written as follows:

$$\lambda(nm) \leq 1239.8/\phi \qquad (Equation\ 1.15)$$

where ϕ is the ionization energy in eV.

1.2.3. Plasma Generation

In order to reach the plasma state and to sustain it, the energy required for ionization must be input into the atoms and molecules from an external source. Due to the high energies involved, raising the temperature of the gas is not a realistic alternative to produce plasmas in the laboratory. The most practical sources to couple this energy in a controlled manner are electric fields and lasers. We will focus our attention only on plasma generation by electric fields, i.e. an electrical discharge in a gas. Among the several types of electrical discharges (Townsend, corona, arc, glow discharge, etc…) glow discharge is by far the most frequently used in plasma polymerization.

It is well-known that when two electrodes are immersed in a gas and an electric field is generated by an applied voltage a luminous discharge is initiated at the interspace between the electrodes, provided that the voltage is sufficiently high. The onset of the discharge is characterized by a sudden increase in the intensity of current which suggests that the otherwise isolating gas has undergone electrical breakdown allowing the flow of charge carriers. A simple explanation follows on how this effect is produced.[9–11] A small amount of free electrons in a gas can exist due to different reasons such as random ionization by energetic cosmic rays or random collisions between neutral atoms. These primary electrons are accelerated in the presence of an electric field towards the anode, gaining energy in their way. As shown in the previous section, electrons will not lose much energy due to inelastic collisions and therefore can accumulate a sufficient amount to induce ionization when an inelastic collision with a neutral atom or molecule takes place. In this process, charge conservation demands that an ion and an additional electron are generated. The resulting two electrons will continue to be accelerated towards the anode, whereas the new positive ion will be dragged towards the cathode. The electrons will repeat this process as many times as possible until they are collected at the anode and the ions will impinge on the surface of the cathode where they will lose their energy through a cascade of collisions that will release secondary electrons(5). This sequence

(5) Sputtered material will also be generated but this is not substantial to our model on how the plasma is generated and sustained.

of events repeats increasingly and extremely fast until the avalanche of collisions is sufficiently large to cause the gas to breakdown.

The voltage and pressure at which the onset of the discharge takes place are gas dependent and can be calculated by applying the condition that electrons need to be able to gain sufficient energy to overcome the ionization potential. The relationship between the breakdown voltage, V_B, the gas pressure, P, and the interelectrode distance, d, is known as Paschen's Law:

$$V_B = \frac{A\,Pd}{ln(Pd) + B} \quad \text{(V)}, \qquad \textit{(Equation 1.16)}$$

where A and B are gas dependent constants. Paschen's curves relate the breakdown voltage V_B needed to sustain a plasma to the product of $P{\cdot}d$. Figure 1.5 shows different Paschen curves for commonly used gases. For most gases, a plasma can be sustained in small to medium reactors (up to 50 cm interelectrode spacing) at typical working pressures of 0.01 to 0.5 mbar with less than 1kV. At higher pressures, collisions are too frequent and the electrons cannot gain sufficient energy unless the electric field is increased; at very low pressures, the production of secondary electrons is not sufficient to compensate for electron loses and the glow is not sustainable.

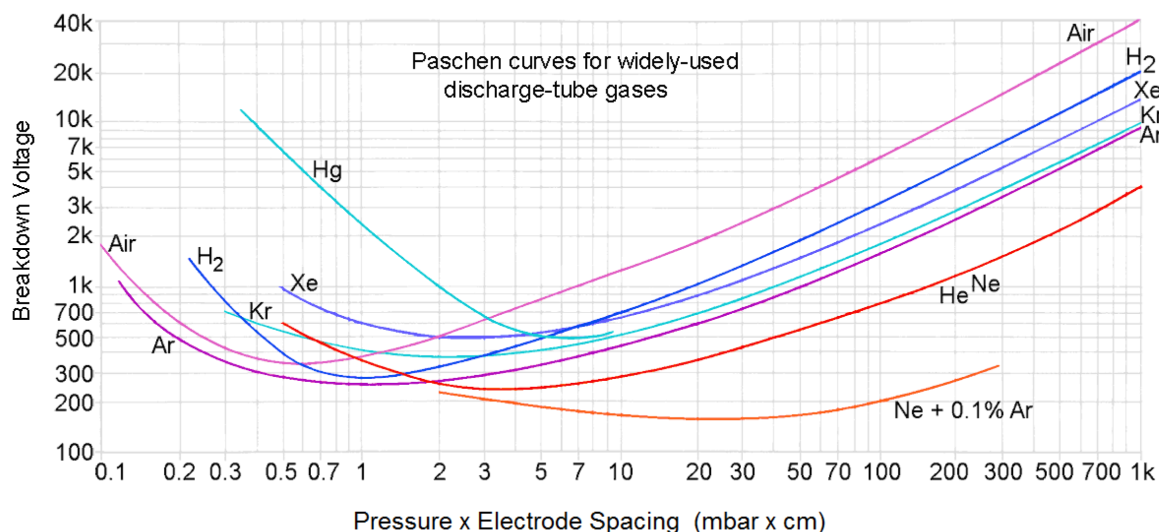

FIGURE 1.5. Paschen curves for commonly used simple gases. Adapted from [12].

DC Glow Discharge

Glow discharges are characterized by the appearance of several luminous and dark zones between the cathode and the anode. The relative size of these zones varies with pressure and with the interelectrode distance. The existence and characteristics of these regions (luminous intensity and width) have been studied for several gases and conditions, but the exact mechanisms leading to their formation are not yet completely understood.[8–12] Here we will follow the model described by Boenig in [9], which is illustrated in Figure 1.6.

In a DC Glow Discharge, up to eight distinctive characteristic regions have been observed, four glowing regions and four dark regions, that is, from cathode to anode:

- Aston Dark Space
- Faraday's Dark Space
- Crookes Dark Space
- Anode Dark Space
- Cathode Glow
- Negative Glow
- Positive Column
- Anode Glow

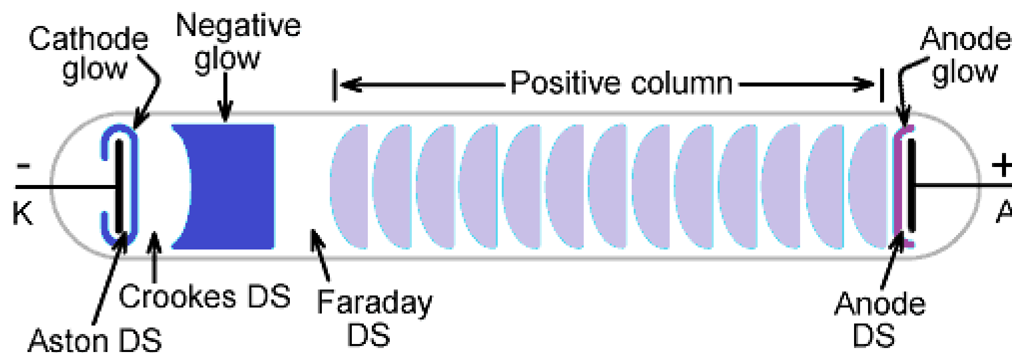

FIGURE 1.6. Luminous and dark regions in a DC Glow Discharge. Adapted from [9].

The *Aston dark space* is a very thin layer in contact with the cathode which contains mainly low energy secondary electrons just emerging away from the surface of the cathode and high energy ions accelerated towards it. In this area electrons do not have sufficient energy to produce excitation and ionization of atoms, therefore no photons are emitted. Next to it we find the *cathode glow*, which is a very luminous layer that wraps around the cathode. De-excitation of positive ions through neutralization by electron attachment and recombination of dissociated fragments in

polyatomic molecules are the likely mechanisms responsible for the emission of photons in this region.[13,14] The next region to follow is the *cathode dark space* or *Crookes dark space*. This region is of maximum importance because most of the discharge voltage is dropped across it, which means that positive ions gain the energy employed to bombard the cathode, and electrons gain energy to move away from the cathode towards the anode, all of it occurring in this region. Next comes the *negative glow* which is also of great interest because most ionization processes are believed to occur in this region, where electrons have sufficient energy to start exciting and ionizing molecules. For a fixed electric field (given by a fixed applied voltage and interelectrode separation) the location of the negative glow is an approximate indication of the average energy of electrons; the closer to the cathode, the least energetic electrons are. In the *Faraday's dark space*, primary electrons that lost their energy and secondary electrons that were created in the ionization processes within the negative glow region do not have sufficient energy, since this has been consumed in inelastic collisions producing ionization. In addition, the field is too small to accelerate them to energies above ionization or excitation thresholds, and this region remains dark. In the *positive column*, the field starts increasing and electrons can be accelerated again to produce excitations by collision, mainly, which produces a fainter glow. The positive column is usually the largest glow in the plasma. Faraday's dark space, positive column, anode dark space and anode glow may actually be suppressed in many applications as the distance between the electrodes becomes smaller, where they collapse and disappear, which indicates that they are not indispensable for sustaining the plasma.

Plasma sheaths

An important characteristic of plasmas are the plasma sheaths. When a floating substrate or electrode is in contact with the plasma, the flux of energetic faster electrons arriving at the surface will be much larger than the flux of less energetic slower ions. This causes a potential to develop close to the surface, called the *sheath potential* or *sheath drop*, which forms a barrier capable of reflecting the more mobile electrons. When connected to an external current source, the sheath potential adjusts itself so that the flux of electrons to the wall equals the electron current that is drawn from the wall by the external circuit. If the wall is electrically isolated, the electron

flux is reduced to the point where it is equal to the ion flux, so that the quasi-neutrality of the plasma can be maintained. Figure 1.7 shows a schematic illustration of a typical discharge plasma which is in contact with surfaces that are either cathodes or anodes, or electrically isolated (floating). The plasma potential Vp forms with respect to the most positive surface (anode). The potential of a floating surface relative to the plasma potential is known as the floating potential, V_f. For a Maxwellian energy distribution, the floating potential is given by[8]

$$V_f = \frac{kT_e}{2e} \ln\left(\frac{\pi\, m_e}{2\, m_i}\right) \quad \text{(V)} \qquad \textit{(Equation 1.17)}$$

This is the differential potential with respect to the plasma potential and it has very important implications for the growth of films on floating substrates: film growth will be modified or assisted by bombardment with ions having kinetic energies of up to $-e(V_p - V_f)$.

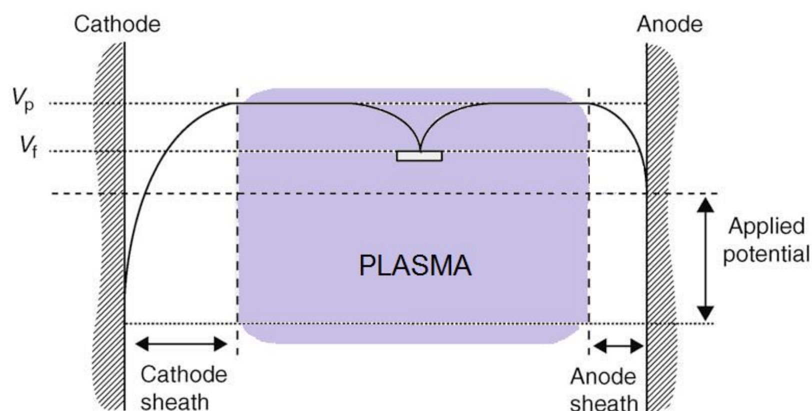

FIGURE 1.7. Luminous and dark regions in a DC Glow Discharge. Adapted from [10].

Plasma power sources and discharge types

Besides the classical DC discharge, plasmas for materials processing can be created by a broad variety of power sources, each having its own features and benefits: magnetron DC, pulsed-DC discharge, alternating current (AC), capacitively coupled radio-frequency (CC-RF), inductively coupled radio-frequency (IC-RF), microwaves (MW), atmospheric pressure barrier discharges or electron-cyclotron-resonance (ECR). All of them are used for different applications, either in industry or academia. For plasma polymerization in industrial applications CC-RF discharges, and, to less

extent, DC, AC and MW discharges are almost exclusively employed, but MW plasmas do not deal too well with metallic substrates.

For RF discharges the operating frequency is generally 13.56 MHz as it is within a commonly reserved band assigned for industrial applications in Europe and the US. At this high frequency, only electrons can follow the temporal variations of the applied potential. A fraction of the ionizing electrons will be repelled from the electrode toward which they are accelerated as the cycle changes. Thus wall losses decrease and electrons remain in the discharge longer to make additional ionizing collisions. These two effects allow sustaining the plasma at typical operating pressures one order of magnitude lower than in DC plasmas. In addition, the discharge can be sustained between non-conducting electrodes, which is in theory a great advantage when depositing dielectric materials. Figure 1.8 shows two simple RF reactors, capacitively coupled and inductively coupled. In both cases power is supplied by a high-frequency power source through a matching network, but in the capacitively coupled reactor the electrodes are placed inside the reactor, whereas for the inductively coupled one no electrodes are required. Inductively coupled discharges are very popular in the laboratory but they are not applied in real industrial applications for materials processing(6). The main reason is that a non-conducting reactor is required, usually a quartz bell, and glass reactors cannot be easily deployed and operated in an industrial environment as they would not be acceptable for safety reasons.

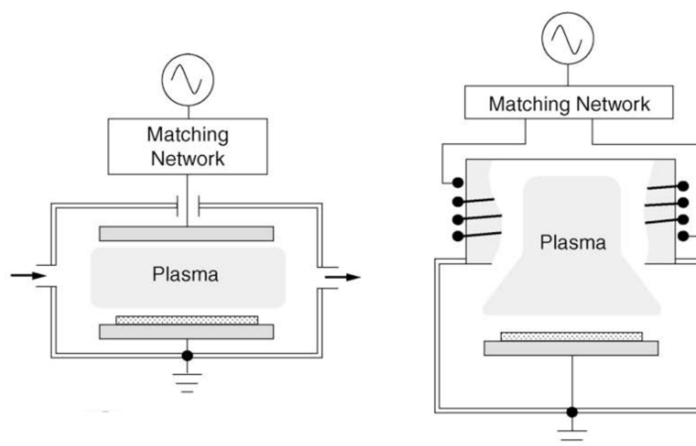

FIGURE 1.8. Luminous and dark regions in a DC Glow Discharge. Adapted from [10].

(6) ICP find applications in analytical techniques such as ICP-OES.

1.2.4. Polymer Formation by Plasma Polymerization

The first documented description of plasma polymerization was published by Goodman in 1960 in a work titled "*The formation of thin polymer-films in the gas discharge*" and it was published in "*Polymer Chemistry*".[15] This is illustrative of the fact that during the first two decades after Goodman's work plasma polymerization was considered just as an exotic means of synthesizing polymers, following the same mechanisms described in the preceding decades for conventional polymerization. The efforts to elucidate the specific mechanisms of plasma polymerization were pioneered by Yasuda[7] and completed by Inagaki and Hegemann[16–19] during the last four decades. Their work has allowed to establish a different and more complete perspective of plasma polymerization.

Mechanisms of plasma polymerization

In order to understand the different mechanisms taking place during plasma polymerization, it is convenient to discuss the processes leading to non-plasma polymers first, from a chemical perspective. Conventional polymerization can be described by two basic mechanisms: *step-growth* polymerization and *chain-growth* polymerization.

In step-growth polymerization, a polymer is formed by the stepwise repetition of the same chemical reaction over and over again, and by-products such as water are formed at each step. Polymerization can proceed indefinitely as far as sufficient monomer is added and water needs to be removed constantly to avoid slowing down the reactions. Long chains can react with other chains producing larger ones and the reaction does not have a terminating step other than the consumption of all the reactants.

In chain-growth polymerization, long-chain molecules are formed by the addition of monomer units at the end of the chains, without the formation of any by-products. After addition of a new unit, the elongated chains themselves retain the reactive group at the new end group. Termination steps can be accomplished when the reactive end group is neutralized, usually by hydrogen incorporation, by an impurity or by combination with another long chain instead of a monomer. Therefore, polymerization takes place in three steps: initiation, propagation and termination.

Chain-growth polymerization is also referred to as *addition* polymerization and it can be further divided into *radical* and *ionic* polymerization.

In radical polymerization, propagating reactions are initiated by radical species at the polymer chain ends; in ionic polymerization, the addition step takes place between a chain with an ionic group at the end and a neutral monomer, where the resulting longer chain regenerates the charge at the new end. The initiation of ionic polymerization usually requires the activation of starting chains by a strong anion or cation initiator. This can be also achieved by ionizing radiation such as UV, γ-rays or electron beams, in which case the adequate term would be *radiation* polymerization.

These different mechanisms can be summarized as follows:

STEP-GROWTH

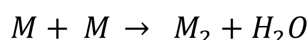

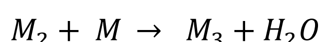

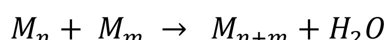

CHAIN-GROWTH

Radical

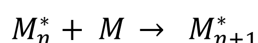

Ionic

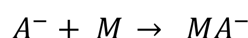

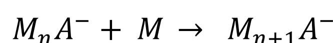

Radiation

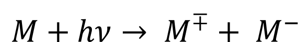

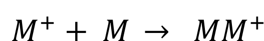

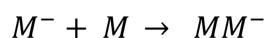

The mechanisms of plasma polymerization have been explained by all these mechanisms and additional ones. First it was proposed by several authors that chain growth by the ionic mechanism was the responsible process for polymer formation,

and that plasma was only a tool to generate the required ions.[20–23] After that, the radical mechanism was proposed by many other works.[24–27] Finally, Yasuda proposed that chain-growth polymerization mechanisms are not possible, neither ionic nor radical, because the proportion of monomer molecules to activated chains does not allow chain-growth polymerization to proceed in the gas phase. Therefore he expanded the view to a new mechanism exclusive of plasma polymerization, which he called *atomic* polymerization:[28] monomers entering the plasma gain energy from electrons, ions and pre-existing radicals and are dissociated into activated small fragments and even atoms, if sufficient power is available. These activated fragments are recombined and grow into large molecular weight ones, which can happen either in the gas phase or at the surface of a substrate. When atomic polymerization occurs, the structure of the polymers formed thereby can be significantly different from that of the precursor monomer: the higher the energy available in the plasma, the higher the fragmentation degree of the monomer and much less will the deposited polymer resemble the structure of the monomer.

A few years later, Yasuda completed his atomic polymerization model to propose a more complete model called *Competitive Ablation and Polymerization* (CAP), first,[29] and, secondly, the *Rapid Step-Growth Polymerization* (RSGP) mechanism.[30]

Mechanisms of film deposition: CAP and RSGP

Rather than explaining the growth of plasma polymers by a single mechanism, as in conventional polymerization, modern approaches to the problem accept that plasma polymerization is a more complex process that involves several pathways that can interact and affect each other.

The CAP mechanism was the first one of such complex models. It proposes that the properties of a plasma polymer film result from the competition between etching and deposition processes. This implicitly depends on the effect of energetic particle bombardment on the surfaces, which is an extremely important process in DC plasmas and was neglected in conventional polymerization models. The RSGP model proposes that recombination of reactive species and cyclic reactivation of already reacted products play a decisive role, in addition to the ablation and deposition processes. It further suggests that activated species may be monofunctional (denoted

as M·), such as free radicals, or difunctional (·M·). In the case of monofunctional reactive species, a single reaction would be a termination process. However, in the presence of plasma, the product of a reaction can be reactivated and recycled to be available for further reaction. The complete RSGP model is illustrated in Figures 1.9 and the activation and recycling processes (1) and (2) are illustrated in Figure 1.10.

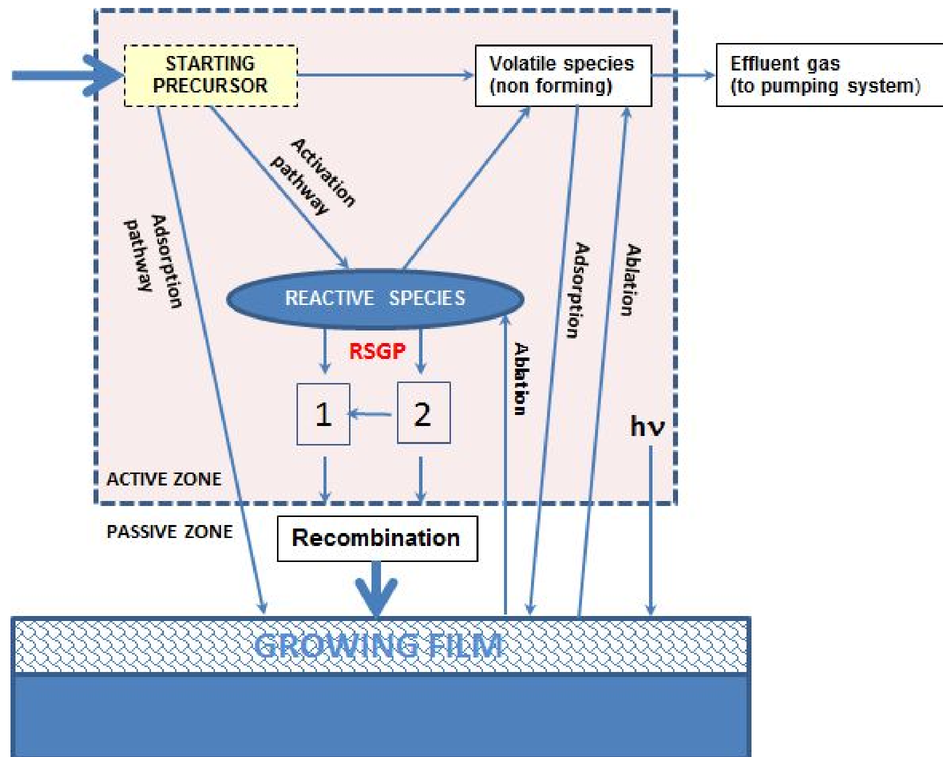

FIGURE 1.9. Schematic representation of Rapid Step-Growth Polymerization integrated in the overall film deposition process. Numbers 1 and 2 represent activation and recycling reactions. Adapted from [17].

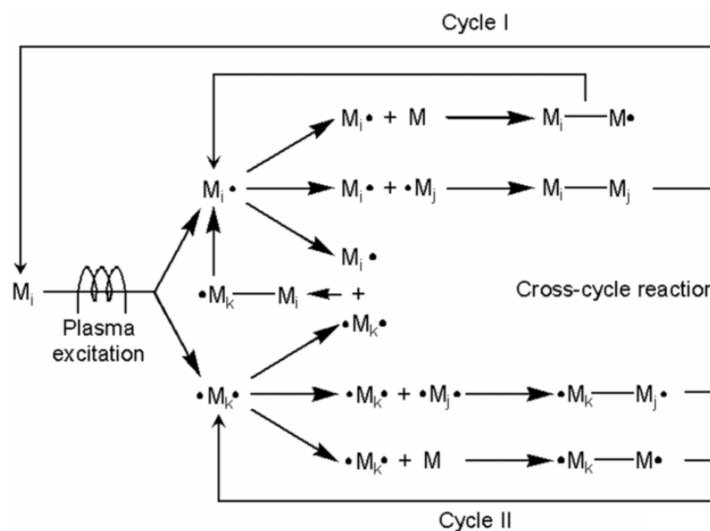

FIGURE 1.10. Reaction schemes of bicyclic step-growth mechanism of plasma polymerization. Adapted from [7].

Figure 1.9 also illustrates several steps that take place in the overall process:

- transport of the reactants from the gas inlets to the reaction zone,
- reactions in the active zone that form the reactive fragments and by-products,
- transport of the reactants and their products from the gas phase to the substrate,
- adsorption of these species on the substrate surface,
- surface diffusion, chemical reactions and incorporation of these species on different growth sites,
- irradiation by UV photons,
- desorption of the volatile by-products of surface reactions.
- transport of the by-products away from the reaction zone.

It is important to remark that the location of the substrate (onto which the growing film develops) with respect to the active zone can have a significant impact on the properties and structure of the films, since the equilibrium among the different processes (activation, ablation, adsorption, desorption, ion bombardment and UV irradiation) can be different at different locations.

Effect of operational parameters on plasma polymerization

The RSGP model assumes that the gas precursors travel through the plasma active zone (the glowing plasma and the plasma/sheath boundaries) where radical formation takes place within the gas phase. After exiting the active zone and entering the passive zone (plasma sheath and surface growth region) recombination of radicals and deposition of stable products develops. The different processes that reach a quasi-equilibrium (radical formation, ablation, recombination and deposition) are dependent on operational parameters such as flow rate, total pressure, power coupled to the plasma, molecular weight of the monomer and substrate location. The effect of any of these parameters alone can be rather useless in determining growth rates or film properties and would produce irreproducible results when scaling the processes from one reactor to another. Instead, the critical parameter is the energy $\bar{E}$ invested per particle in the active plasma zone, which is given by

$$\bar{E} = \frac{W \cdot \tau_{res}}{P \cdot V_{act}} \quad \text{(J/s)} \qquad (\textit{Equation 1.1.8})$$

where W is the power effectively coupled to the active plasma zone, τ_{res} is the residence time of monomer molecules in the same zone, P is the reactor pressure and V_{act} is the volume of the active zone. The residence time is not an operational parameter itself, but a physical value derived from the gas flux and the reactor volume. In addition, the residence time in the reactor chamber is higher than the residence time in the plasma zone, since the flux of molecules through the active region is the same as the overall gas flux, but the volume of the active region is smaller. The residence time in the plasma region can then be calculated by

$$\tau_{res} = \frac{P \cdot V_{act}}{P_0 \cdot F} \quad \text{(s)} \qquad (\textit{Equation 1.18})$$

and therefore combining Eq 1.18 into Eq 1.17 the energy per molecule can be more conveniently expressed as

$$\bar{E} = \frac{W}{P_0 \cdot F} \quad \text{(J/molecule)} \qquad (\textit{Equation 1.19})$$

P_0 is a constant (the atmospheric pressure at standard conditions) and therefore the energy per molecule $\bar{E}$ is proportional to the composite parameter W/F. A variation of the composite parameter includes the mass of the monomer and it is known as the *Yasuda parameter*,

$$Y = W/FM \quad \text{(J/kg)} \qquad (\textit{Equation 1.20})$$

Depending on the amount of energy transferred by the plasma to each molecule, as determined by Y parameter, polymerization can proceed in three different regimes: *monomer-deficient regime*, *competition regime* and *energy-deficient regime*.

In the monomer-deficient regime, there is sufficient energy to convert all molecules that transit through the active plasma zone to an activated or radical form and deposition rates increase almost linearly as additional molecules are fed in at increasing flow rates. Deposition rates in the monomer-deficient regime will also increase with increasing pressures up to the point where the energy per molecule is not sufficient to convert all the monomer. If pressure or flow are further increased, deposition rates will start decreasing. Only if additional power is supplied, deposition rates will increase again and the deflection point will be shifted to higher flow rates.

In the energy-deficient regime, a fraction of the molecules can travel through the active plasma zone without being activated and they will be pumped out from the

reactor without contributing to the deposited mass; if the flow of molecules is increased in this regime, the average energy per molecule will be decreased and the deposition rates will also decrease as no additional energy will be available to produce more radicals.

The thresholds for these regimes are reactor dependent and geometry dependent and they can only be determined empirically.

Types of plasma polymers

Depending on the growth regime, usually two types of plasma polymers are obtained, according to Yasuda's classification:[14] Type-A and Type-B. Type-A plasma polymers are obtained in the energy-deficient regime and they are characterized by the deposition of oligomers retaining most of the chemical structure of the precursor molecule. The properties of Type-A plasma polymers are consequently very similar to those of their conventional equivalent polymer. Type-B plasma polymers are deposited in the monomer-deficient regime where extensive fragmentation of the monomer takes place and therefore they usually exhibit interesting properties such as good adhesion to any kind of substrate and high chemical and temperature stability, which makes them highly insoluble in common solvents and heat-resistant up to a few hundred degrees centigrade.

There is obviously a diffuse limit between Type-A and Type-B plasma polymers. Films with intermediate properties can be prepared in a broad grey zone corresponding not only to the conditions where the competitive regime takes place but also due to the different intensities of ion bombardment that can be effected by placing the substrates and the orientation of the growing film in a convenient way with respect to the plasma and the electrodes.

1.3. Industrial applications of plasma polymerization

A worldwide search at the European Patent Office (EPO) database offers a first perspective on the impact of plasma polymerization in industry. There are 371 patents which explicitly mention "plasma polymerization" in their title. If the search is extended to the abstract, the number of patents increases to 2,193. As a comparison, the number of publications indexed by Scopus which explicitly mention

"plasma polymerization" in their titles and abstracts reaches 1,025 and 4,043 respectively. This indicates that the ratio of scientific publications to patents is between 2-4 papers per patent.

Large corporations such as Volkswagen, Bosch, Coca-Cola, LG, Intel, Sony, Hitachi, Canon, Novartis, Bayer, Minolta, Procter&Gamble, Leybold, Shimadzu, or research institutions such as NASA, Fraunhoffer Institute or UCLA all have their own explicit patents on plasma polymerization. If we examine the activity markets that these companies cover we can find automotive, food, consumer electronics, microelectronics, pharmaceutical, optics and analytical instrumentation industries which is the best indication that plasma polymerization has become an extended technique to provide materials with unique properties that can be applied to solve challenging problems.

This broad range of applications arises due to the different functional properties derived from the versatility of structures and chemical compositions that can be achieved by employing different reactors, precursor molecules and operating parameters.

Plasma polymerization of organosilicon monomers is a more reduced field, but it has tremendous potential due to several interesting properties:

- flexibility to prepare mostly polymer-like or mostly silica-like coatings,
- excellent corrosion protection due to chemical stability of the pp-films,
- excellent thermal stability,
- excellent adhesion to any substrate with low internal stress,
- increased hardness and elastic modulus as compared to any conventional bulk polymer,
- flexibility to obtain a wide range of values for the surface energy, from hydrophilic to hydrophobic,
- excellent gas barrier properties,
- low-k dielectric properties,
- high transparency and refractive index close to that of glass.

Each one of these properties has found applications in important fields. Table 1.1 relates different properties and the corresponding applications as described in the literature.

PROPERTY	APPLICATION	REFERENCES
Chemical stability	Corrosion protection of metals	[31–43]
Chemical stability	Biocompatible coatings	[44–53]
Low surface energy	Hydrophobic treatment of textiles	[54–65]
Low surface energy	Protection of archeological objects	[66–70]
Low surface energy	Superhydrophobicity and self-cleaning surfaces	[71,72]
Mechanical properties	Protection of plastic substrates	[73–83]
Gas barrier propertires	Food Packaging	[84–90]
Selective permeability	Gas and humidity sensors	[91–97]
Thermal stability	Fire retardants	[98–101]
High adherence	Adhesion promoting coatings	[102–105]
UV absorption	UV aging protection	[106]
Dielectric properties	Microelectronics encapsulation	[107–111]
Refractive Index and high transparency	Optical coatings (antireflective, etc...)	[112,113]

TABLE 1.1. Properties and related applications of plasma polymerization of organosilicon monomers as described in the relevant bibliography.

1.3.1. Commercial systems for plasma polymerization

In industrial processes the design of reactors for plasma polymerization is greatly conditioned by the geometry and presentation of the parts to be coated. Three main configurations are available: continuous roll-to-roll reactors, flat batch reactors and volumetric reactors.

Continuous roll-to-roll reactors are high-throughput reactors that allow to coat rolls of materials. They are extensively used in the web-converting and food-packaging industries to provide high barrier properties by plasma polymerization of SiO_x coatings or hydrophilic modifications by plasma treatment to increase surface wettability for quality ink printing. When only plasma treatment is required, they are usually employed at atmospheric pressure. If plasma polymerization is required, the web coater needs to be completely or partially placed in a vacuum. In web or roll-to-roll coating, the material to be coated needs to be flexible enough to be presented in rolls, which is usually the case for textiles, fibers and plastics. The part to be coated is presented flat and stretched in front of the active plasma zone and it is scrolled at a certain speed to allow continuous deposition (Figure 1.11).

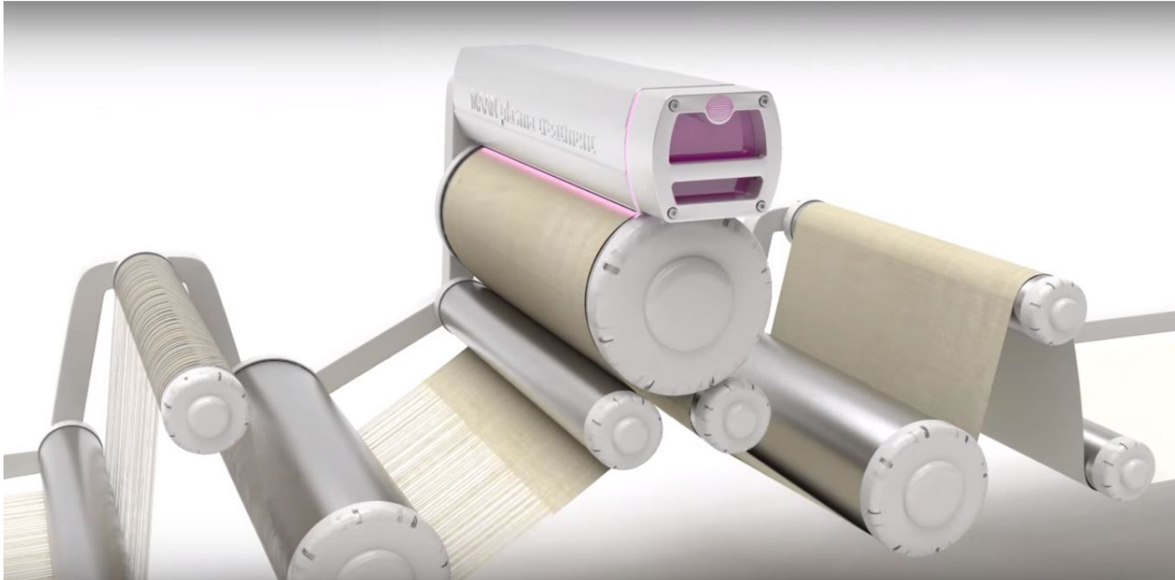

FIGURE 1.11. Continuous roll-to-roll plasma treatment / plasma deposition system used to coat fibers and textiles. (Adapted from MAAN Plasma Treatment).

For flat individual parts that cannot be coated continuously, such as optical lenses or electronic components, large area batch coaters are usually employed. These reactors include parallel plate electrodes that define a clear plasma zone where the components are placed.

For complex 3D parts, such as most consumer products, volume reactors are necessary (Fig. 1.12). The materials to be coated are fixed onto piece holders called ”satellites”, which are part of a loading/unloading rotating system, called “planetary system”. During the coating process, the satellites rotate within the plasma region and on their own axis, to cover even complex surfaces uniformly. This has been proved to be the best approach to ensure a perfectly uniform and conformal coating.

1.3.2. Protection of metallizations on plastic parts

The most extended industrial application is, by far, plasma deposition of polymer films to protect aluminum metallizations evaporated or sputter-deposited on plastic parts. This is applied to a wide range of products: car headlights, halogen reflectors, bottles of perfume, cell phone covers, lipstick tubes, food packaging films, etc… Until very recently, the complete coating cycle for such parts comprised several processes: first, an adhesion promoter was applied, usually a chemical lacquer which evens out small defects at the surface of reflective parts and prepares the part to receive the

FIGURE 1.12. Commercial vacuum metallization and plasma polymerization reactor with a rotating planetary system for homogeneous coating deposition.

metallic coating; second, the part was dried and cured; third, a metallic coating was applied in vacuum, by evaporation or sputtering; fourth, the part was removed from the vacuum chamber and a second lacquer was applied and cured, to protect the metallization from corrosion. Overall, this was a rather lengthy procedure which produced large amounts of liquid residues and volatile organic compounds (VOCs). An industry driver for change was the enact of the European Directive 1999/13/EC which aimed at reduction in usage of organic solvents and to update existing plants to environmentally cleaner processes not later than 30/10/2007. As of today, most metallizing processes are conducted in completely in vacuum. This is possible by substituting the lacquering steps by plasma polymerization steps.

FIGURE 1.13. Consumer products make use of metallization processes to achieve appealing surface finishing on plastic parts and protective plasma polymer coatings to avoid damage or scrathes in day to day use.

OBJECTIVES

The scope of this Thesis is the study of plasma polymerization of an organosilicon monomer, *hexamethyldisiloxane* (HMDSO), in different configurations of a DC plasma reactor with the following objectives:

- To elucidate **if plasma polymerization of HMDSO is feasible in DC a plasma** reactor at significant deposition rates and to understand the requirements and limitations of such a process.

- To investigate the **sctructural properties and stoichiometry** of ppHMDSO films prepared **without the addition of carrier gases**, aiming at the obtention of polymer-like SiO_xC_y:H films, and to understand the effect of different operational parameters on the structure of the films.

- To investigate the **structural properties and stoichiometry** of ppHMDSO films prepared **with the addition of carrier gases**, aiming at the obtention of inorganic-like SiO_x films, and to understand the effect of different operational parameters on the structure of the films.

- To investigate the **functional properties of polymer-like and inorganic-like** ppHMDSO films, and to understand how these properties depend on different operational parameters.

- To investigate the **plasma post-treatment of polymer-like ppHMDSO** films with different gases and treatment conditions in order to obtain films with graded properties.

- To investigate the **functional properties of plasma post-treated ppHMDSO** films, and specifically the hydrophobic recovery.

- To study the **applicability of films** with optimized properties to solve real challenges in industrial applications.

CHAPTER 2

MATERIALS AND METHODS

In this chapter we describe the experimental set-up and protocols employed for the plasma deposition and plasma treatment of ppHMDSO films. We also introduce the main properties of the HMDSO monomer and compare it with other available monomers. The second part of this chapter is devoted to the analytical techniques employed for the characterization of the structural, chemical and functional properties of the films. In addition, a short reference is made to several software tools employed to analyze the data.

2.1. ORGANOSILICON MONOMERS: HMDSO

Different liquid organosilicon monomers are available for plasma polymerization. Selecting the right organosilicon monomer can depend on the target application. As an example, it is well-known that tetraethoxisilane (TEOS) is preferred in the microelectronics industry for the deposition of SiO_2 films by thermal CVD, since its central Si atom is already surrounded by four oxygen atoms in the same configuration as SiO_2. The structure of HMDSO is clearly convenient for deposition of polymer-like films, since it is the repeating unit in poly(dimethylsiloxane), PDMS, commonly known as silicone. The choice of HMDSO monomer to deposit silica-like films is not obvious: there are six methyl groups that need to be etched and additional oxygen needs to be incorporated in order to replicate the stoichiometry of silica. From that chemical perspective, other monomers such as TEOS or tetramethyldisiloxane (TMDSO) could be a better choice. In our case, we selected HMDSO through a decision matrix with the following criteria: toxicity and environmental hazard, capacity of

generating polymer-like and silica-like materials, vapor pressure at 20°C to allow high evaporation rates, and cost. Table 2.1 summarizes some relevant data that helped us making the choice for HMDSO.

Overall, it is clear that HMDSO offers the best compromise between lower toxicity, cost, evaporation rate and versatility. Some physical and chemical properties of HMDSO are summarized in Table 2.2 and the 3D model of the molecule is illustrated in Figure 2.1, which allows to visualize the relative size of atoms, bond distance and dihedral angles.

	HMDSO	TEOS	TMDSO
VAPOR PRESSURE @30°C	73 mbar	4.8 mbar	272 mbar
COST (500 mL)	39.90 €	48.40 €	350.00 €
TOXICITY (*)	32500 mg/kg	6270 mg/kg	3000 mg/kg
POLYMER-LIKE DEPOSITION	Yes	Difficult	Yes
SILICA-LIKE DEPOSITION	Good	Best	Better

TABLE 2.1. Comparison of organosilicon monomers based on different practical criteria. Data from GELEST and SIGMA-ADLRICH catalogues and MSDS. (*) Toxicity tested in guinea pigs as maximum level before symptoms.

HEXAMETHYLDISILOXANE	
CAS NUMBER	107-46-0
FORMULA	$C_6H_{18}OSi_2$
MOLECULAR MASS	162.38 g/mol
DENSITY	0.764 g/cm^3
REFRACTIVE INDEX	1.377
MELTING POLINT	-59ºC
BOILING POINT	101ºC
VAPOR PRESSURE @ 30°C	73 mbar

TABLE 2.2. Physical properties of HMDSO.

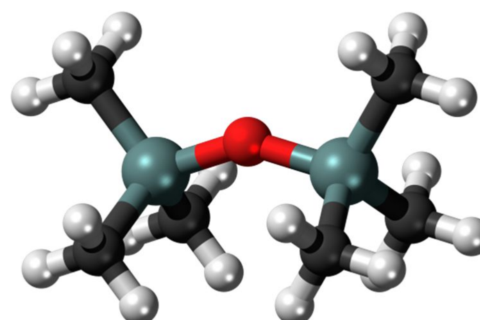

FIGURE 2.1. 3D model of HMDSO.

2.2. REACTOR FOR PLASMA POLYMERIZATION

A prototype commercial reactor designed by Telstar Industrial SA was employed in all the investigations conducted within the scope of this Thesis (Figure 2.2). This

industrial prototype provides means for three different processes: plasma treatment, aluminum metallization and plasma polymerization in one vacuum cycle, as corresponds to a typical industrial headlight coating process. The main subsystems of the reactor are: the vacuum chamber, the vacuum system, the gas handling system, the power source system, the automated-safety-control system and the process monitoring system, as illustrated in Figure 2.3.

FIGURE 2.2. Prototype industrial reactor for DC plasma polymerization designed and assembled by Telstar.

Vacuum chamber

The reactor body consists of a main stainless-steel cylindrical vacuum chamber of approximately 70 cm of base diameter and 70 cm of height. The theoretical reactor volume is therefore 269.400 cm^3, which is a rather large volume for research reactors, but a medium to small one for industrial applications. A frontal viewport equipped with a transparent shutter in front of a 120 mm diameter - 15 mm thick pyrex glass window allows to observe the plasma process. Different orifices on top of the reactor and at the base allow to introduce powered wiring or sensor wiring (e.g. thermocouple wiring) through bulkhead vacuum connectors. The chamber can be vented by introducing air via a high flow porous polyethylene filter with a mean pore size of 3 μm, in order to prevent dust or particulates from entering the reaction chamber. Once vented, the reactor can be opened easily by a main front door which is vacuum tight due to a long elastomeric seal fitting its contour. Different threaded

holes at the base and top of the chamber allow to fix different configurations of substrate holders and electrode holders. In the latter case, the powered electrode/s need to be conveniently isolated from any grounded by means of plastic or ceramic spacers.

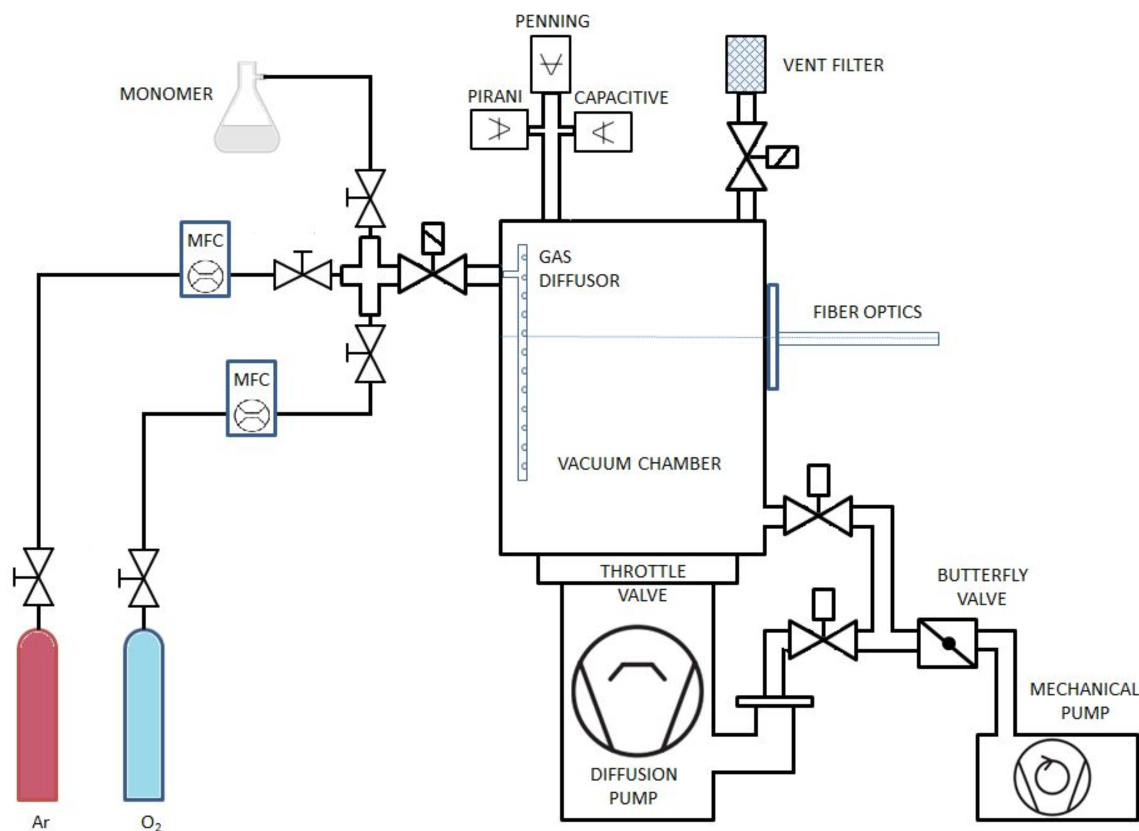

FIGURE 2.3. Schematic drawing illustrating the Reactor Chamber, the Vacuum System and the Gas Handling System.

Vacuum system

The vacuum system is equipped with a high throughput pumping system consisting of a mechanical rotary pump, capable of a maximum pumping speed of 40 m^3/h, a diffusion pump (2000 l/s) and an intermediate trap where liquid nitrogen can be introduced to avoid reflux of oil molecules from the pumps (not used in this study). When the reactor is cleaned, baked and pumped overnight, the ultimate pressures achieved by the mechanical and diffusion pumps are respectively 1×10^{-3} mbar and 1×10^{-6} mbar. The mechanical pump can suck directly from the chamber to produce a primary or medium vacuum (down to a few μbar) or from the

base of the diffusion pump. The different paths are opened and closed by means of pneumatically actuated valves. The diffusion pump is connected to the main chamber by a large throttle valve which is pneumatically actuated. The system pressure is measured by a Pirani gauge, a capacitive gauge and a Penning gauge. The Pirani gauge can only be calibrated for one type of gas, which is by default a low mass diatomic gas. For high molecular weight monomers it can produce falsely elevated pressure values. Even if recalibrated for a higher molecular weight molecule, when the plasma is activated in the presence of a monomer, the Pirani gauge can lead to inconsistent results due to monomer fragmentation, which creates a multiplicity of species with additive partial pressures. The automated safety control system gets feedback from the Pirani gauge to control the onset and deactivation of high voltage plasma power and therefore it cannot be bypassed. For that reason, in this Thesis pressure values for plasma processes are always referred to the readings from the capacitive or penning gauges.

Gas handling system

Different gases can be introduced into the reaction chamber through microleak valves and one mass flow controller (MFC). Microleak valves are preferred for monomer introduction since MFCs are calibrated for simple mono- or diatomic gases and they would need recalibration for complex gases. In addition, special heated MFCs are required for condensing gases, such as HMDSO. Therefore, only carrier gases (O_2, Ar, N_2) were controlled by MFCs. Microleak valves can also be calibrated by a simple method described in the next section. Carrier gases are pumped in from high pressure gas bottles equipped with a regulator manometer. A differential pressure is required for the carrier gas to flow into the chamber, which was provided by setting the manometer to 2.0 bar absolute pressure. For HMDSO flow, liquid monomer was held in a glass Kitasato flask which was connected to the inlet microleak valves by a PVC tube. The differential pressure required to introduce the monomer vapor in the chamber was created by the vapor pressure generated by evaporation at the liquid-gas interface. Monomer evaporates until equilibrium is reached at a partial pressure equal to the monomer vapor pressure at the corresponding temperature, which is sufficiently high to generate the pressure difference required for the monomer vapor to flow into the chamber. The system was prepared to heat monomer

reservoir and gas line to a constant pressure, e.g. 30°C, but since lab temperatures where stable at 22°C and monomer flows where measured during each deposition process (as described in the next sections), the monomer reservoir and line were normally left unheated, hence at room temperature. The gases are premixed prior to entering the vacuum chamber, where they are dispersed by a shower like that can be positioned at different locations to optimize the flow of precursor species through the active plasma zone.

Electrical Power Source

A high voltage direct current source capable of providing up to 4000V and 200 mA (800 W) is installed at the base of the reactor, below the vacuum chamber. The voltage output of the source is generated by a high voltage transformer and a 4-diode bridge that rectifies a 50Hz input signal. The voltage waveform is therefore a 50 Hz AC-rectified DC without filtering. Filtering is avoided because it makes use of capacitors that can accumulate charge at high voltages and therefore it could cause powerful destructive arc discharges besides posing a potential serious hazard for the operators.

Automated and safety control

The open/closed door sensors, the signals from the Pirani and Penning gauges, the actuation of all valves and the activation of high voltage and evaporation sources are interphased to a programmable logic controller (PLC) for safety reasons. Pumps, valves and electrode power can be actuated from a central command panel at the front of the reactor, but only certain workflows are permitted to avoid hazardous situations, as for example, applying a high voltage discharge to the powered electrode when the door is open, or actuating the throttle valve to communicate the diffusion pump with the reactor chamber, if the pressure value is not below a certain threshold and the mechanical pump is not pumping from the base of the diffusion pump.

Process monitoring system

In order to monitor the plasma process several magnitudes are measured and simultaneously recorded by a self-coded software application written in Vbasic 6.0. Thus, the evolution of the vacuum pressure, discharge intensity, discharge voltage, and temperature at the anode during all the coating process can be analyzed

afterwards. All the corresponding sensors produce voltage signals that are measured by four multimeters with integrated RS-232 interfaces so that the signals can be transmitted by serial protocol to a PC and visualized and recorded by our own software.

In addition, an optical fiber connected through an orifice at the frontal viewport allows to collect the light emitted from the center of the reactor and to deliver it into a miniature spectrophotometer (OceanOptics S2000). The spectral emission is then processed and captured by the OOIBase32 Software, which allows to configure the gain, integration time, averaging, smoothing and darkness subtraction in order to achieve high quality spectra with a peak resolution ~1nm.

2.2.1. Electrode Configuration

Three main configurations were assayed: the central electrode configuration (or cylindrical configuration), the horizontal parallel-plate configuration and the vertical parallel plate configuration. Substrates were placed at different distances from the power electrode (cathode), and for the parallel-plate configurations also within the plasma region and outside the plasma region (afterglow or remote location). Figure 2.4 illustrates these three different geometries. In the cylindrical configuration, the precursor gases where injected from the side of the reactor; in the parallel plate ones, different gas diffusors where tested to direct the gas outlet towards and through the plasma zone (e.g. left-two-right in the horizontal geometry and up –down in the vertical one).

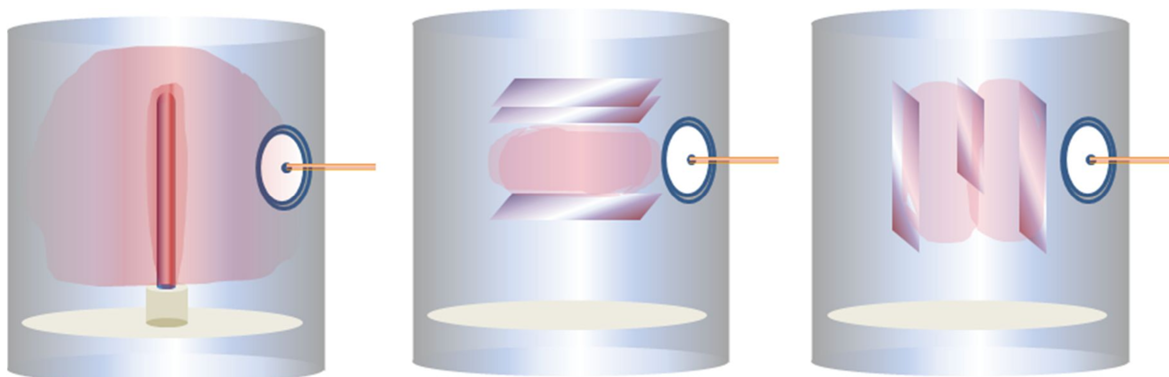

FIGURE 2.4. Different electrode geometries generate different active plasma zones. From left to right: cylindrical central electrode configuration; horizontal parallel plate configuration; vertical parallel plate configuration.

2.2.2. Vacuum characterization

Prior to studying plasma polymerization, a minimum characterization of the vacuum performance of the reactor was conducted in order to: 1) determine the exact reactor volume; 2) measure the residual leak rate of the vacuum system, including outgassing from reactor walls in order to quantify the residual gas contribution; 3) estimate monomer flow rates and their relation with equilibrium pressures and microleak valve setting.

Calculating reactor volume

The reactor volume is a constant value of the system that is used to calculate some process-related magnitudes, such as flow rate or residence time. A calculation of reactor volume based on the measured dimensions of the reactor should provide a first rough estimation, but the geometry of the reactor does not correspond to a perfect cylinder and some additional dead volume is also housed below the chamber in the area leading to the pumping system. Therefore, in order to confirm that the geometrical calculated volume was consistent with the real volume, a simple experiment to obtain a more accurate value was conducted as follows. First, the exact volume of a 10 L glass flask with a rubber stopper was measured by filling the flask with water and weighing. The flask was then dried overnight and connected to the reactor chamber by a short press-fitted 10mm I.D. PVC tube through one of the available microleak valves. The solenoid valve for the gas inlet was completely closed and the reactor was pumped down below 0.1 mbar with the mechanical pump. The valve was then opened allowing for the air molecules in the flask to expand to a larger volume, and the increase in pressure at the reactor chamber was measured after 15 s of stabilization time. Assuming that the pressure inside the reactor before opening the valve was negligibly small, the volume of the reactor was derived from the simple equation:

$$P_0 V_{flask} = P_1 (V_{flask} + V_{reactor}) \qquad (Equation\ 2.1)$$

where P_0 is the atmospheric pressure and P_1 is the reactor pressure after communicating both volumes. The volume thus calculated was 275.200 cm^3, which is in very good concordance (less than 2.2 % error) with the geometrically calculated value of 269.400 cm^3.

Measuring the leak rate and outgassing of the reactor

The background flow of gas due to leaks or outgassing in the reactor can be estimated with good precision by a simple method consisting in: a) evacuating the chamber, b) closing the pumping outlet and allowing the gas molecules to flow in through system leaks or to desorb from the reactor walls, and c) registering the increase in pressure due to the increasing number of molecules. Within a certain range, the differential pressure is constant, and the increase in pressure due to leaks is linear with time. Although the contribution of outgassing is not completely linear, the flow rate due to outgassing+leaks can be calculated using Equation 1.9. Given the volume of our reactor previously measured, the equivalent flow leak rate is

$$F_{leak} = 16300 \cdot dP/dt \quad \text{(sccm)} \qquad (\textit{Equation 2.2})$$

Figure 2.5 shows an example of residual flow rate after leak detection and correction, for 1 day of pumping, and again after adding 2 h of reactor baking with an Ar plasma, when the plasma eventually heats the gas and all surfaces and promotes desorption. In our system, in the best conditions, the effect of leaks plus the outgassing is below 0.1 sccm.

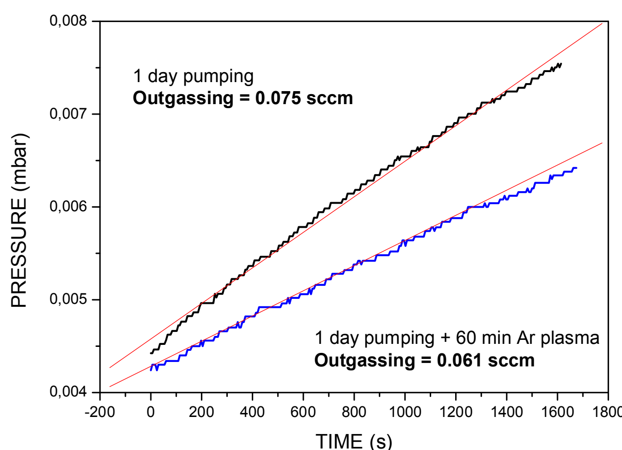

FIGURE 2.5. Evolution of pressure with time due to leaks through connectors and outgassing from the reactor walls. The estimated equivalent flow rates are below 0.1 sccm.

Measuring the flow rates and equilibrium pressures

Measuring the actual flow rates of the monomer follows the same approach as the leak rates. In this case, after a certain time the mechanical pump can be connected

again to evaluate also the final equilibrium pressure achieved when the pumping flow through the outlet equals the inlet flow rate. Figure 2.6 (left) shows the pressure evolution for three different positions of the microleak controlling the monomer flow. Figure 2.6 (right) shows the dependence between monomer flow rate and equilibrium pressure.

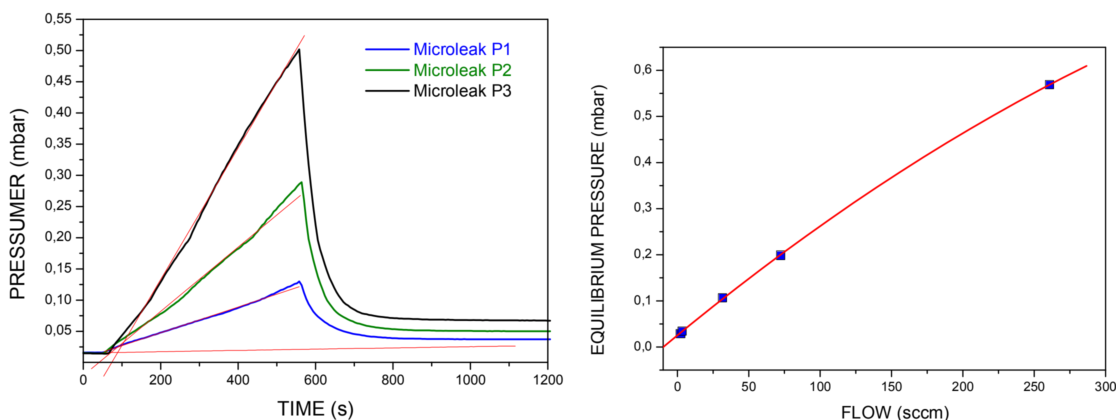

FIGURE 2.6. Evolution of pressure with time due to leaks through connectors and outgassing from the reactor walls. The estimated equivalent flow rates are below 0.1 sccm.

Adjusting the residence time

After measuring the relation between flow rates and equilibrium pressures, we realized that it might be necessary to allow the system to vary the residence time of monomer molecules without modifying the equilibrium pressure. By applying Equation 1.10 the residence time in our system could be calculated as

$$\tau_{res} = 15113 \cdot (P/F) \text{ (s)} \qquad (Equation\ 2.3)$$

where P is the equilibrium pressure in mbar and F the monomer flow in sccm. In our system, for a flow of 30 sccm an equilibrium pressure of 0.1 mbar was initially established, which means that the residence time of the monomer molecules in the chamber was originally around 50 s. According to the literature, this was a rather short residence time for plasma polymerization. In order to achieve some control on the value of the residence time, the pumping throughput of the mechanical pump needed to be also a variable parameter and therefore we installed a butterfly valve to restrict the conductance to the pump and limit the effective flow into it. Figure 2.7

shows the effect of the aperture of the valve on the effective pump-down curves of the system.

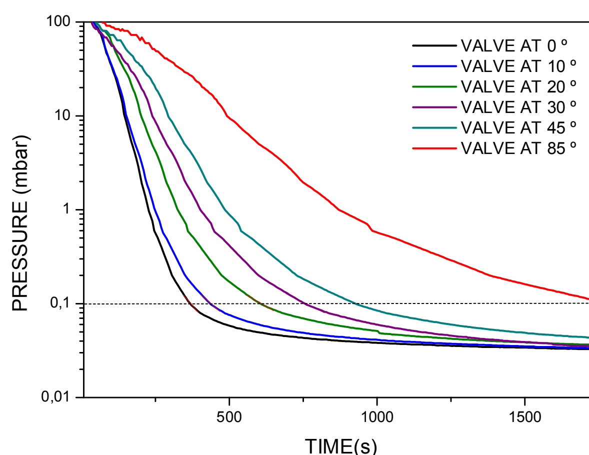

FIGURE 2.7. Pump down curves for different angular positions of the butterfly valve.

In most of the experiments we employed a 45° configuration which allowed to set an approximate monomer flow of 15 sccm at 0.1 mbar, which is equivalent to a residence time of 100 s.

2.3. PROTOCOL FOR PLASMA POLYMERIZATION

This section describes the complete protocol with detailed steps employed to prepare plasma-deposited polymer films on our reactor. The protocol consists of several preparative steps, the plasma polymerization process itself and the unloading of the chamber, described as follows:

STEP 1. Cleaning and preparing the substrates

For metal, glass and silicon substrates, the cleaning procedure starts with brushing the surfaces with a small toothbrush using powder detergent and water, and rinsing abundantly with deionized water. The substrates are then immediately introduced in a small glass beaker with trichloroethylene and placed in an ultrasound shaking bath for 2 minutes, then trespassed to another beaker with acetone for 2 additional minutes of ultrasound shaking and finally to a last beaker with ethanol for the last 2 minutes. The substrates are extracted and dried with a dry-nitrogen gun while holding one edge in contact with absorbing filter paper. This protocol proved to be much more effective than ultrasound cleaning alone.

For plastic substrates, the surfaces where not cleaned with any liquid solvent and only dried nitrogen was blown onto the surface in order to remove any dust particles. All the substrates were handled with gloves and tweezers throughout the process.

STEP 2. Aluminum metallization

For some of the glass substrates, Al metallization was conducted in high-vacuum (less than 10^{-5} mbar) in a separate PVD reactor. The substrates were placed on holders 12 cm above a tungsten filament, where small pieces of U-shape Al wire were held. Evaporation took place by heating the filament at high currents (1-2 A). The onset of Al melting could be seen through the glass reactor walls, and the current was held until the transparent substrates turned completely opaque. The as-obtained Al films were in the range 40 – 80 nm.

STEP 2. Kapton tape masking

In order to detect a clear step indicative of the thickness of the film, adhesive, temperature-resistant Kapton tape was used to mask small areas in all the substrates.

STEP 3. Weighing of the substrates

Prior to film deposition, the substrates were weighed in a Mettler Toledo AT621 Delta Range analytical balance, with a resolution of 10 μg, located at the Departament de Química Organica de la Universitat de Barcelona.

STEP 4. Preparation and loading of the chamber

Before any deposit, the surfaces of the electrodes were wrapped up with pure Al foil (no laminated material) in order to expose always a fresh metal area. This simple step avoids deposition of thick isolating coatings over time that would modify the intensity of the discharge and would introduce contaminants in the plasma due to sputtering and desorption. After that, all substrates were loaded into the chamber at their assigned positions and orientations, holding them in place with different fixtures, or with no fixtures in the anode polymerization of the horizontal parallel plate configuration.

STEP 5. Pump down, residual leakage, flow rate and equilibrium pressure

Once the chamber was loaded with all the substrates, the front lid was closed and the rough vacuum solenoid valve was actuated from the front panel. The volume of the chamber was left to pump down to a pressure of 0.1 mbar, which was usually accomplished in less than 10 min, and then the large throttle valve was actuated and

the diffusion pump was allowed to pump down for 30 min, in order to reduce the amount of adsorbed water and other contaminants. After that the throttle valve was closed and the residual leak and outgassing flow rates were verified. If these were sufficiently low, the monomer vapor was introduced and the flow rate was registered. After 300 s, the roughing valve was opened and the mechanical pump was connected again directly to the vacuum chamber and the pressure was left to equilibrate, which usually takes between 5-10 min. If the equilibrium pressure was different than the targe one, the monomer inlet microleak set point would be slowly tuned until the required pressure was achieved, and then the system would be pumped done (only mechanical pump) and the cycle repeated again to remeasure the flow rate.

STEP 6. Plasma polymerization

Once the pressure and the flow of monomer had been stabilized to the expected values, the plasma could be established by applying a high negative voltage to the central powered electrode. The onset of plasma could be easilty distinguished as a sudden increase in the system pressure; conversely, when the plasma was extinguished a sudden drop in the system pressure was detected. During plasma polymerization, several optical emission spectra could be captured for further analysis. Frequent visual control of the plasma was necessary in order to ensure that arcing or local glows did not develop, which could produce unexpected effects on the properties of the deposited films.

STEP 7. Chamber pump down, chamber vent and extraction of samples

After the required deposition time is finished, the plasma should be exinguished by manually turning off the switch control at the front panel. Re-assesment of the monomer flow rates could be achieved by closing the roughing valve if necessary, otherwise, the inlet electrovalve should be closed and the monomer flow would be stopped. The system should be pumped down for 2-3 minutes and then the vent electrovalve should be open for 3-5 seconds without closing the roughin valve, in order to allow a certain amount of fresh air to flow in fast, diluting any residual gases and increasing the pumping efficiency. This step (pump-down + partial vent) was performed at least 3 times to ensure that all process gases had been pumped out to acceptable levels. After that the roughing valve would be closed and the vent valve

open until the pressure inside the chamber equals the atmospheric pressure. At that point the lid opens without any intervention and the substrates can be removed.

STEP 8. End of protocol. Analysis of registered data

After the procol is completed, coated samples and process records for Pressure, Voltage, Current Intensity, Temperature and OES spectra were available for further characterization and data analysis (Figure 2.8)

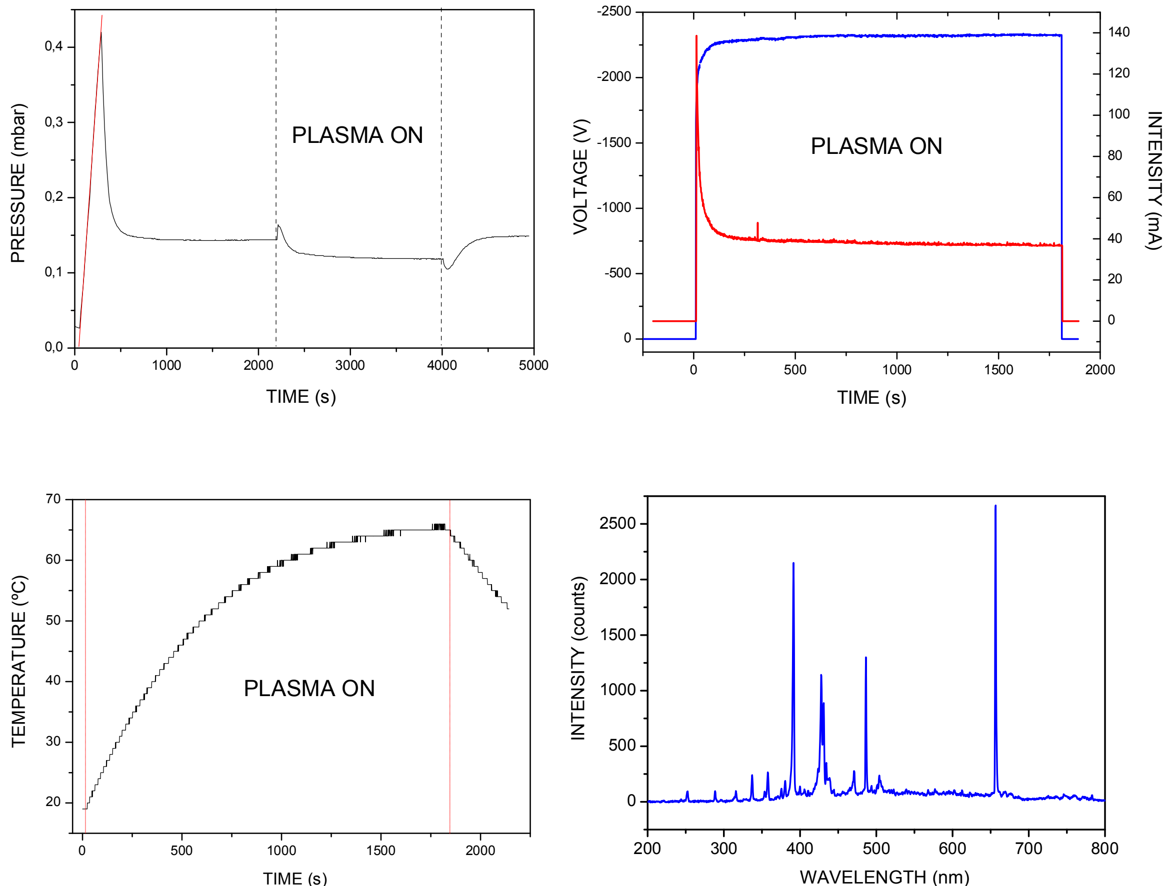

FIGURE 2.8. Output registers for each plasma polymerization run. **(TOP-LEFT)** Pressure register. **(TOP-RIGHT)** Voltage and Current Intensity. **(BOTTOM-LEFT)** Temperature register. **(BOTTOM-RIGHT)** Emission spectrum.

The steps already described do not include any pre-treatment or post-treatments. If pre-treatments were required, they would be performed usually after the leakage rate evaluation in Step 5, by introducing a controlled flow of Ar, O_2 or air. The pre-treatments were employed as an activation step of surfaces prior to polymerization and they should not last longer than 30 s. Post-treatments would be performed before steps 6 and 7, and the chamber should be pumped down before introducing the treatment gas,

2.4. FILM CHARACTERIZATION TECHNIQUES

Once the films have been deposited, different analytical techniques are available to characterize the structural properties, the stoichiometry and the functional properties of the films. A brief description of these techniques follows, with some remarks if special provisions need to be made in order to overcome any difficulties for the optimal performance of certain techniques.

2.4.1. Physical structure and morphology

Analytical Precision Balance

The first measurement made with all fresh-coated samples was a simple weight measurement which, in combination with thickness measurements, allowed us to easily estimate the density of the coatings. High resolution analytical balances measure the mass laid on a measuring plate by counteracting the gravitational force exerted by the unknown mass with an electromagnetic force restoration sensor. Such a sensor makes use of an electromagnet to generate the necessary counter-force and the output value is calculated by measuring the force needed to achieve balance.

These measurements were performed in a Mettler Toledo AT621 Delta Range analytical balance, with a resolution of 10 μg (5-digit resolution). The balance was located at the Departament de Química Organica de la Universitat de Barcelona.

Mechanical Profilometry

After weighing all the samples, Kapton tape protectors were removed and defined steps between substrate and coating were revealed. The height of these steps corresponds to the thickness of the film and they can be measured by mechanical stylus profilometry. In these profilometers the sample is laid or fixed on a stage which is scanned beneath a a diamond-tipped stylus. The stylus is mounted on an arm that translates the surface topography into vertical displacements which are measured by a linear variable differential transformer (LVDT) sensor. The LVDT generates a voltage output that is digitized and transformed to relative displacements. Stylus profilometry achieves a resolution up to 0.1 nm and a maximum height range of 130 μm. It is important to note that for soft substrates, the contact force of the stylus tip may scratch and deform the surface, producing lower than expected results. In our

case, we employed a contact force of 0.1 mN which, from our experience in nanoindentation, poduced a deformation below 10 nm and goood repoducibility.

Stylus profilometry was performed in a a Dektak 3030 profilometer located at the Departament de Física Aplicada i Òptica de la Unviersitat de Barcelona.

Scanning Electron Microscopy (SEM)

The surface morphology of the films was inspected by a conventional scanning electron microscope (SEM). Although this type of microscopes are highly automated and easy to operate, the principles on which scanning electron microscopy are based are not simple[1,114]: the electrons thermoionically emitted from a heated filament are accelerated towards an anode by a high voltage difference (1 to 50 keV); the anode has a central orifice from where high energetic electrons scape and an electron beam is generated; the beam is focused and deflected to scan the desired area by a series of electromagnetic lenses and coils. SEM generates high contrast images by irradiating the surface of the sample held in high vacuum with a highly focused electron beam (typically 0.5-2 nm in waste diameter). The image is formed by sequentially scanning all the spots in a certain area, the 'rastered' area and collecting electrons emitted from that area. Upon impinging on the surface, the fast electrons lose their energies in a series of scattering inelastic collisions. This excites the electrons in the atoms of the lattice within a tear-drop shaped volume of an approximate depth up to 1 um. The excitation processes can be relaxed by the emission of X-rays, energetic electrons or low energy electrons, called *secondary electrons*. Some electrons are also backscattered directly by elastic collisions without losing significant energy. Depending on the collected species, different analytical techniques or imaging modes are derived. SEM in usually employed in the secondary electron emission mode. Secondary electrons have low energies (< 50 eV) which implies that they are generated from a subsurface depth of a few angstroms. The electrons are attracted by a positive voltage towards a scintillator-photomultiplier combined sensor. The signal generated by the photomultiplier at each point is composed as a two-dimensional intensity distribution, that is, the SEM image.

A practical problem in SEM is that the samples need to be conductive, otherwise negative charge build-up generates as electrons reach the surface, deflecting future

incoming electrons and distorting the image. In order to avoid this effect, non-conducting samples need to be coated with a thin metal or carbon sputtered layer. In our case, in order to allow the samples to be characterized by the combined Energy Dispersive X-ray (EDX) spectroscopy, the applied coating was sputtered gold, since it is an external element not included in the stoichiometry of the films.

All SEM images included in this Thesis were obtained in a Leica Stereoscan 360 SEM located at the Centres Científics i Tecnologics de la Universitat de Barcelona.

Transmission Electron Microscopy (TEM)

TEM is also a type of electron microscopy that requires a high vacuum for an electrom beam to travel and impinge on a certain sample, but it differs from SEM in the fact that electrons traverse the whole sample to be analyzed, and therefore the sample needs to be *electron transparent*, which in practice means extremely thin (100 nm – 1 μm). Therefore, TEM is mostly used to obtain cross-section images of the films, so that electrons traverse the thinnest dimension.

If we compare TEM and SEM with optical microscopies, TEM would be the electronic equivalent to transmission optical microscopy (for transparent samples), whereas SEM would be the more similar to epi-illumination (for opaque samples). Another major difference between TEM and SEM is that TEM can generate the image from the whole analyzed area, in contrast to SEM which generates it point by point. A clear advantage of TEM over SEM is the higher resolution, typically one order of magnitude better. The main disadvantage is the cumbersome sample preparation in order to achieve the thin necessary thickness.

The working principle of TEM is similar to SEM in what respects to electron beam generation and differs in interaction with the sample and image collection. The interaction with the sample is equivalent to a transmission optical imaging system such as a slide projector. The transmitted beam forms an image that is magnified by a final projector lens onto a phosphor viewing screen. This is the *bright-field* or *conventional* TEM image, which discards scattered or diffracted electrons with a set of apertures. Those parts of the sample where electrons have been deflected appear dark, whereas less denser regions have higher transmittance and appear as bright zones in the TEM image. Other modes gathering the scattered beams such as the

dark-field and *lattice-imaging* modes are possible, but where not employed to obtain the images presented in this Thesis. The magnification achievable by TEM is enormous due to the short equivalent wavelength of electrons and can reach easily $\times10^6$ to $\times10^7$.

Sample preparation in TEM was conducted as follows:

- ppHMDSO films on Al-coated glass slides where cut with a diamond saw into 3×2 mm slides,
- the slides were glued with a polymeric glue (M-bond) by facing together the coated sides and they were held in compression at 100°C for 4h until the glue was completely cured,
- glued sandwiches were mirror polished with a disc grinder and sand paper until the thickness was down to 0.5 to 1 mm,
- the sandwich was dettached with acetone, and the process repeated until a thin layer is left, of 0.1 mm approximately,
- the sample was dettached, rinsed with acetone, dried and glued again on a special copper disc holder,
- the sample was finally ion-milled in an ion milling system until a hole was produced at the center. The area to be inspected by TEM is the surrounding area, which is thin enough for electrons to be transmitted.

An important tip for analyzing plasma polymers with electronic microscopes, and especially with the TEM, is that, unlike crystalline denser materials, the accelerating voltage and intensity of the electron beam needs to be reduced in order to avoid damaging the sample. Also the exposure time needs to be kept small and frequent movement is necessary to avoid 'burning' the film[115]. Our films were analyzed with accelerating voltages of only 150 keV, when typical values for inorganic materials are around 300 keV.

All TEM images included in this Thesis were obtained in a Philips CM30 transmission electron microscope, located at the Centres Científics i Tecnologics de la Universitat de Barcelona.

2.4.1. Stoichiometry and chemical structure

Fourier Transform Infrared Spectroscopy (FTIR)

FTIR is the most popular technique for the analysis of the chemical bonds in organic and also in some inorganic materials. It is based in the principle of photon absorption by matter, similarly to UV or Vis absorption spectroscopy. Most materials show characteristic absorption patterns in the mid-infrared range of the spectrum (2.5 to 25 μm). The physical principle responsible for IR absorption is the exchange of dipolar momentum due to the absorption of electromagnetic radiation of a determined energy. Considering molecules as classic oscillators, where the interatomic distance and the angle subtended by the atoms can change, characteristic oscillation frequencies can be calculated for diiferent bonds and groups. If the frequency of the incoming photons matches that of the characteristic oscillation, a resonant absorption will take place: the photon will transfer its energy to excite the vibrations in the molecules and it will be 'lost' from the rest of the photons in the transmitted beam and consequently the intensity at that frequency will decrease.

Molecules can vibrate in many different modes (Figure 2.9). Some of them are IR-active and others are Raman active. In order to detect a certain vibration mode in IR it must be associated with changes in the dipole. Taking as an example the methylene group (=CH_2), the main modes of vibration are:

- *Stretching*: a change in the length of a bond, such as C-H or C-C.
- *Bending*: a change in the angle between two bonds, such as the H-C-H angle in a methylene group
- *Rocking*: a change in angle between a group of atoms, such as a methylene group and the rest of the molecule.
- *Wagging*: a change in angle between the plane of a group of atoms, such as a methylene group, and a plane through the rest of the molecule,
- *Twisting*: a change in the angle between the planes of two groups of atoms, such as a change in the angle between two methylene groups.
- *Out-of-plane*: a change in the angle between any one of the C-H bonds and the plane defined by the remaining atoms of the ethylene molecule.

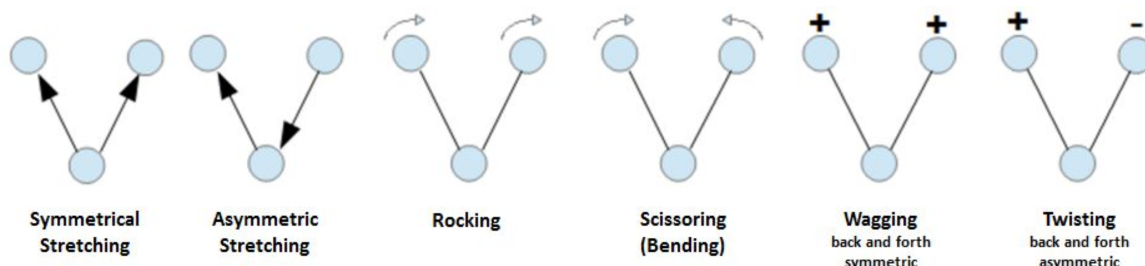

FIGURE 2.9. Schematic representation of the main modes of intramolecular vibration.

In a rocking, wagging or twisting vibration the bond lengths within the groups involved do not change, but the angles do. Rocking is distinguished from wagging by the fact that the atoms in the group stay in the same plane.

Working with the mid-infrared is not easy, since most materials absorb many frequencies in that part of the spectrum. Therefore, very special optics is required,

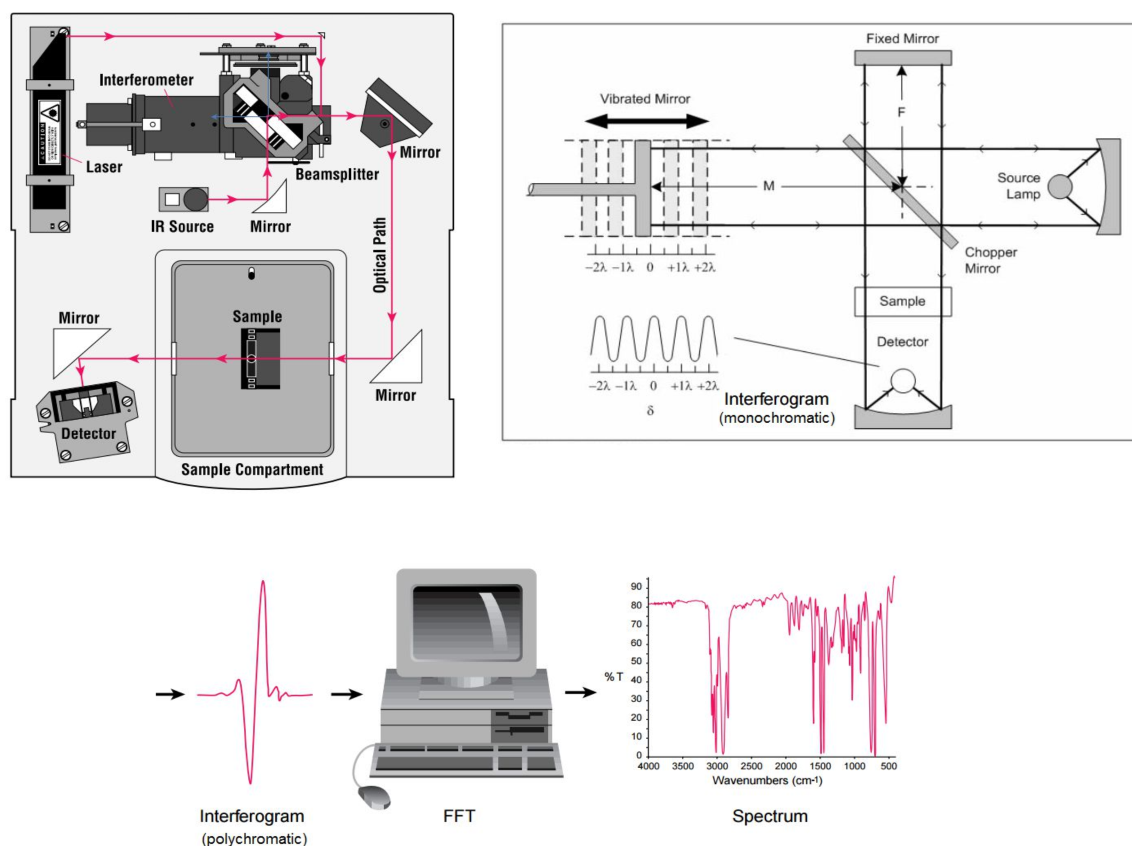

FIGURE 2.10. Example of an FTIR spectrophotometer **(TOP-RIGHT)**, with the detailed schematic for an interferometer **(TOP-LEFT)**. The interferogram for a monocromatic source would show a sinusoidal waveform, whereas for a polychromatic source it generates a complex interferogram that needs to be Fourier-Transformed by a computerto the space of wavelength and intensity.

involving mainly mirrors (ideally gold mirrors) and IR-transparent materials, such as ionic salts (e.g. KBr or NaCl). Water and CO_2 are also specific problems in IR measurement, since they are quite difficult to avoid and they are strong absorbers of some of the frequencies. Most interferometers (Figure 2.10) employ a beamsplitter which takes the incoming infrared beam and divides it into two optical beams. One beam reflects off of a flat mirror which is fixed in place. The other beam reflects off of a flat mirror which is on a moving mechanism which allows this mirror to move a very short distance (typically a few millimeters) away from the beamsplitter. The two beams reflect off of their respective mirrors and are recombined when they meet back at the beamsplitter. Because the path that one beam travels is a fixed length and the other is constantly changing as its mirror moves, the signal which exits the interferometer is the result of these two beams "interfering" with each other. Since the IR beam is a polychromatic beam, the resulting signal is the addition of the interferences generated for each individual frequency, and therefore they have different periods and different intensities. This addition, which is in the space of Intensity vs Time, is called an interferogram and has the unique property that every data point which makes up the signal is a function of the moving mirror position and has information about every infrared frequency which comes from the broadband polychromatic source. This means that as the interferogram is measured, all frequencies are being measured simultaneously. Thus, the use of the interferometer results in extremely fast measurements. Obviously, the measured interferogram signal can not be interpreted directly, because the analysis requires an Intensity vs Frequency spectrum in order to make an identification. Decoding is accomplished via a Fourier transformation, which is performed by the computer. The desired spectral information is calculated by dividing for a background reference spectrum. The Transmittance vs Frequency spectrum is thus obtained.

Transmittance spectra can further be converted to absorbance by a logarithmic transformation and, hence, the absorption coefficient at every wavelength could in principle be calculated. After baseline subtraction, the absorption bands are gaussian or lorentzian shaped, with their area being a measure of the absorption intensity and, therefore, of the number of bonds involved in such absorption. Absorption band frequencies have been extensively published for all kind of chemical groups within different molecules. Still, peak shifting and band broadening are common deviations

and they provide indication about complex chemical environments, with different bond distances usually involved.

Different modes of interaction between the beam and the sample are possible, and the right one needs to be applied to each sample. Transmission modes are usually employed for powders or films on IR transparent substrates. In this mode, the beam is transmitted through the sample or through a pellet generated by compressing the sample with an ionic salt (KBr or NaCl). But for thin films on absorbing solid substrates this procedure is not possible. The most common method is to employ an attenuated total reflectance accessory (ATR), as shown in Figure 2.11. An ATR accessory operates by measuring the changes that occur in a totally internally reflected infrared beam when the beam comes into contact with a sample. An infrared beam is directed onto an entry face of an optically dense crystal, such as diamond, with a high refractive index at a certain angle. The internal reflectance creates an evanescent wave that extends beyond the surface of the crystal into the sample held in contact with the crystal. This evanescent wave protrudes only a few microns (0.5 μm - 5 μm) beyond the crystal surface and into the sample. Consequently, there must be good contact between the sample and the crystal surface. In regions of the infrared spectrum where the sample absorbs energy, the evanescent wave will be attenuated or altered. The attenuated energy from each evanescent wave is passed back to the IR beam, which then exits the opposite end of the crystal and is passed to the detector in the IR spectrometer. The system then generates an infrared spectrum.

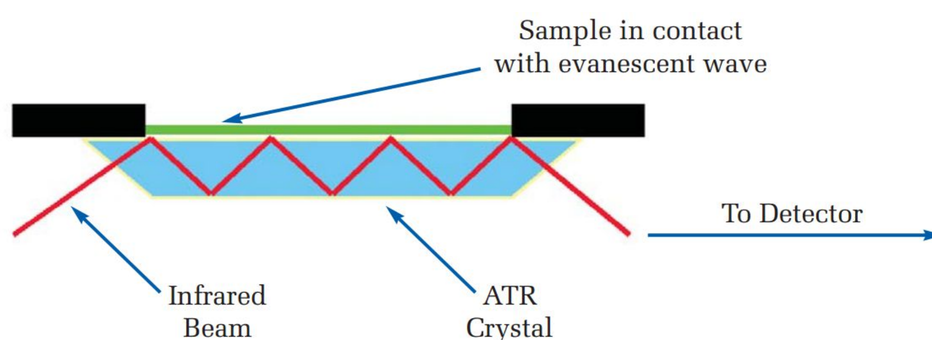

FIGURE 2.11. Illustration of an Attenuated Total Reflectance (ATR) accessory showing the main beam and the sample in contact with the evanescent wave. Adapted from [116].

Without the aid of modern ATR systems, we envisioned an alternative way to measure our spectra with the aid of a reflectance accessory consisting in a set of

deflecting mirrors, with extremely good results. All ppHMDSO coatings were deposited on Al-coated glass slides and therefore reflections on the surface of the sample absorbed the characteristic IR bands, and at the same time the sample acted as another mirror that redirected the beam towards the entrance of the spectrophotometer. This method is usually called *reflection-absorption* FTIR or even *transflection* FTIR.

With this approach we consistently measured spectra of good quality, and even the spectra of monomers could be obtained by allowing a liquid film to be formed on the surface of a fresh Al-coated substrate and taking the measurement before the liquid could evaporate. This method for liquid measurement has not been reported to the best of our knowledge and it is a simple, elegant method to obtain qualitative spectra from liquid samples.

Even more interesting, when the incident angle in reflectance absorption is changed, some modes are enhanced which respect to the normal reflectance or normal absorption. This method can be used to distinguish between certain overlapped bands.

Some of the spectra obtained in this Thesis have been measured with a diamond ATR already integrated in a system from Thermo Scientific, the Nicolet iZ10, at the Centres Científics i Tecnologics de la Universitat de Barcelona. Prior to that all samples had been measured with a Thermo Scientific Nicolet 5ZDX, installed at the Departament de Física Aplicada i Òptica de la Universitat de Barcelona. Both normal reflectance and angular reflectance were employed, and all spectra were obtained by averaging 32 scans with a resolution of 4 cm^{-1} and a spectral range between 4000 and 400 cm^{-1}, except for the ATR, which was limited to 525 cm^{-1}

X-Ray Photoelectron Spectroscopy (XPS)

XPS is a widespread technique for the chemical analysis of solid samples. Its basic principle[117] is irradiating a sample with energetic X-rays, since X-rays are a powerful ionizing radiation, and analyzing the so-called photoelectrons emitted by the atoms in the target sample. The energy of these electrons is not arbitrary, but depends on the energy of the incident X-ray and on the energy of the specific electronic transition required for the photoelectron to escape from the attraction of the nucleus of a

certain atom. Thus, if the energy of a photon is $h\nu$ the kinetic energy of the escaping photoelectron will be given by

$$E_{kin} = h\nu - E_B \qquad (Equation\ 2.4)$$

where $h = 6{,}63 \cdot 10^{-34}$ J·s is Planck's constant, E_B is the energy of the bound state of the electron, which has specific characteristic values for each element. If the energies of the emitted photoelectrons are analyzed by an electrostatic energy analyzer a spectrum showing the relative intensities of photoelectrons emitted with different bond energies is generated. The analyzer's software automatically identifies the electron orbitals of atoms from where all different peaks generate and their intensity can be employed to calculate the relative atomic concentration (stoichiometry) of each element in the film. Since the incident energy is higher than 1 keV, ionisation of the deep energy levels in the valence band is produced.

From the instrumental side, an ultra-high vacuum is required because the photoelectrons have to travel a long path until the electron analyser, and therefore the samples are introduced in the chamber and analyzed on the following day. The radiation source consist of Mg or Al anticathodes that generate X-rays as they are bombarded by accelerated electrons coming from a filament. The interaction of the incident electrons with the anticathode produces a group of X-ray lines, from which only the corresponding to K_α line is filtered for the measurements. Our samples were analyzed with the Mg and Al K_α lines (1253.6 eV and1486.6 eV, respectively). After photoelectrons are generated, they are directed by means of electrostatic lenses to the entrance of an electron energy analyzer, where they follow different paths depending on their kinetic energy (Figure 2.12).

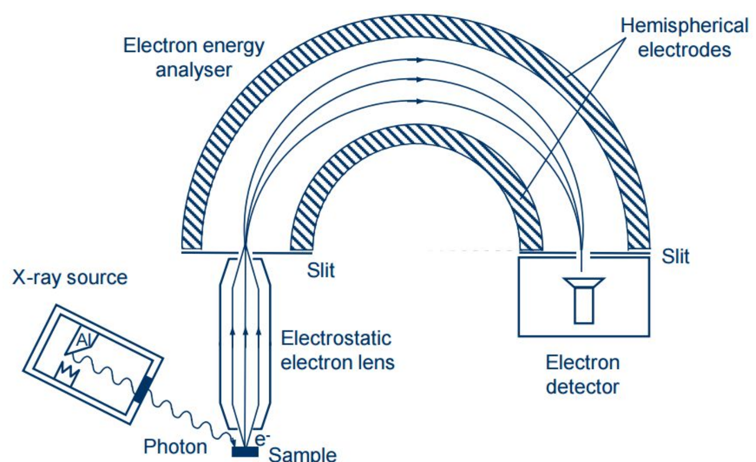

FIGURES 2.12. Simplified schematic representation of an X-Ray analyzer .

An XPS spectrum consists of sharp lines characteristic of each element superposed to a background of radiation. The different proportions of the areas defined by every line indicate the stoichiometry and the background increases at low kinetic energies, due to electrons with energy-loss, whereas characteristic spectral lines are due to the electrons with full energy. Some factors contribute to line broadening: broadening of the radiation line, the uncertainty in the bond energy and the detection band of the instrument.

An important feature of XPS analyis is that chemical shift affecting the lines arises due to the influence of the atomic environment of the probed elements. This allows XPS spectrum to provide also information about the nature of the chemical bonds, and not only the originating element. This bond information can be retrieved by deconvoluting the high-resolution peaks.

In addition, depth chemical profiles can be obtained by combining step-by-step sputtering with an ion gun and collecting spectra at each step, and therefore at different depths. For our samples, an Ar+ with an energy of 4 keV was employed.

The XPS measurements were performed in our investigations by a Perkin-Elmer PHI 5500 Multitechnique spectrometer, which was located at the Centres Científics i Tecnològics de la Universitat de Barcelona. The spectra were analyzed with the PhiMultipak v5 software, which allowed to correct all spectra with respect to the C1s binding energy of 284.6 eV. Deconvolution of high resolution peaks was made with the PhityK freeware package.

Energy-Disperive X-Ray Spectroscopy (EDX)

EDX is conceptually the reverse technique from XPS. In EDX, the samples are irradiated with energetic electrons and the emitted X-rays are detected by the analyzer. EDX analyzers are usually not a stand-alone equipment and it is coupled as an accessory to an SEM which already provides the necessary vacuum and electron source.

In EDX, an electron from the outer shell fills the whole that has been left by another electron and emits its excess energy as an X-ray. An X-ray analyzer generates the corresponding intensity vs wavelength spectrum.

Since EDX is an SEM-coupled technique, two practical considerations must be made: first, for non-coductive materials it is necessary to select a conductive coating to be sputter-coated. We needed to avoid C coatings, since they would interfere in our chemical analysis, and therefore we employed Au, which contribution was clearly distinguished in the spectra. Secondly, the depth of penetration of electrons is dependent on their energy and can exceed 1μm, which means that the contribution of the substrate material can add to the spectra. Therefore, we adjusted the accelerating voltage of the electron beam to sense only the required thickness. EDX spectra for ppHMDSO films were obtained at 7 kV acelerating voltage, 2.78 A for filament intensiy and 3 nA probe intensity, which were found to be the optimal conditions.

All EDX spectra included in this Thesis were obtained by a Link Inca EDX analyzer coupled to a Leica Stereoscan 360 SEM located at the Centres Científics i Tecnològics de la Universitat de Barcelona.

2.2.4.Functional Properties

For ppHMDSO films, our main interest was to test the optical and mechanical properties, the surface energy and the thermal and chemical stability. Electrical and gas barrier properties, which are also of great interest for certain applications, were left out of the scope of this Thesis. Optical properties were measured with UV-VIS reflection spectrophotometry and IR Ellipsometry; mechanical properties were tested by the Nanoindentation and Microscratch techniques; surface energy was measured by Drop-Shape Analysis (DSA), and chemical and thermal stability were measured by specific in-house made set-ups.

UV-VIS Reflection Spectrophotometry

In order to characterize the refractive index of the films, reflectance spectra were collected on ppHMDSO films deposited onto Al-coated glass substrates, and a reflectance measurement set-up was prepared, as illustrated in Figure 2.13.

A Y-shape fiber optics was employed to couple reflected light from the sample into a miniature spectrophotometer (OceanOptics USB2000). One end of the Y fiber was illuminated by a broadband halogen source and the symmetrical end was coupled to

the entrance slit of the spectrophotometer. The terminal end was placed in close contact with the sample, at normal incidence.

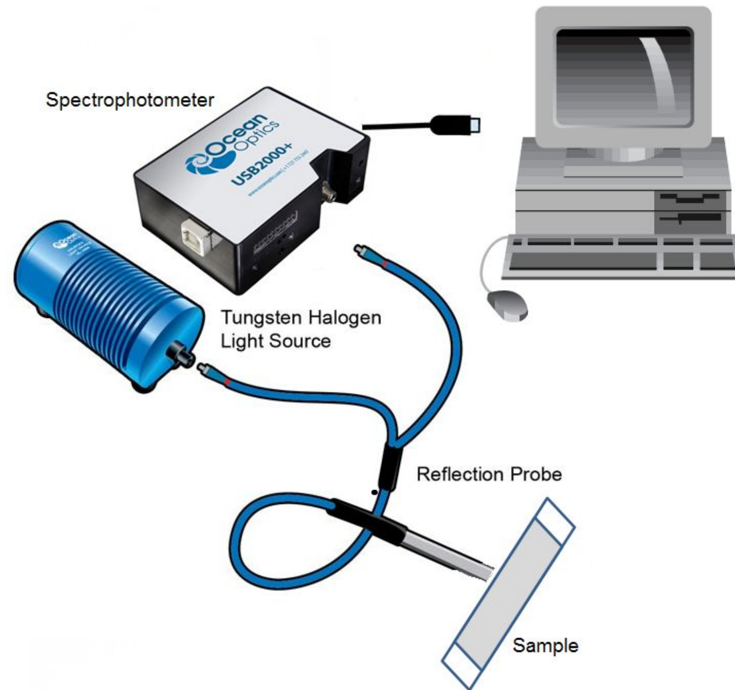

FIGURES 2.13. Measurement set-up for reflectance spectroscopy.

The spectra show a typical intereference-fringe pattern with several maxima and minima. From the wavelength positions of the maxima and minima the thickness and the refractive index of the film can be derived. For thin non-absorbing films on absorbing substrates the total reflected intensity in normal incidence is given by [118]

$$I = |r|^2 = \frac{r_{01}^2 + r_{12}^2 + 2r_{01}r_{12}\cos 2\beta}{1 + (r_{01}r_{12})^2 + 2r_{01}r_{12}\cos 2\beta}, \qquad (Equation\ 2.5)$$

where

$$\beta = \frac{2\pi n d}{\lambda}, \qquad r_{01} = \left(\frac{1-n}{1+n}\right)^2, \qquad r_{12} = \left|\frac{n - \tilde{n}_{Al}}{n + \tilde{n}_{Al}}\right| = 1 - \frac{4nn_{Al}}{n^2 + n_{Al}^2 + 2nn_{Al} + k_{al}^2}$$

r_{01} and r_{12} being the reflected amplitude coefficients at the air-film interface and at the film-substrate interface, respectively, λ the wavelength of a maximum/minimum and d the thickness of the film. The intensity is maximum for $\cos 2\beta = 1$ and minimum

for cos2β=-1. Hence, considering Equ. 2.5 the difference between maxima and minima is given by

$$\Delta I = I_{\max} - I_{\min} = \frac{4r_{01}r_{12}(r_{01}^2 + r_{12}^2)}{(1-(r_{01}r_{12})^2)^2} \qquad \text{(Equation 2.5)}$$

By measuring the difference of envelopes, ΔI_{meas} The correct value of n may be easily found graphically (Figure 2.14) as the intersection of $\Delta I = \Delta I_{meas}$ and a plot of ΔI vs n. Only intersections >1 must be considered. In order to undertake these calculations, an assignation for n_{Al} and k_{Al} must be done. For Al thin films evporated on glass, values of n_{Al}=0.93 and k_{Al}=6.33 at 578 nm have been reported.[119] In any case, small deviations in n and k do not produce signifficant variations in ΔI. Once n has been calculated, the thickness d may be obtained from the position of the maxima and minima:

$$\lambda_{max} = \frac{2nd}{k}, \qquad \lambda_{min} = \frac{4nd}{2k-1} \qquad \text{(Equations 2.6)}$$

Usually the calculation of n is undertaken if the thickness d can be measured independently, but the method applied here gives consistent results both for n and d.

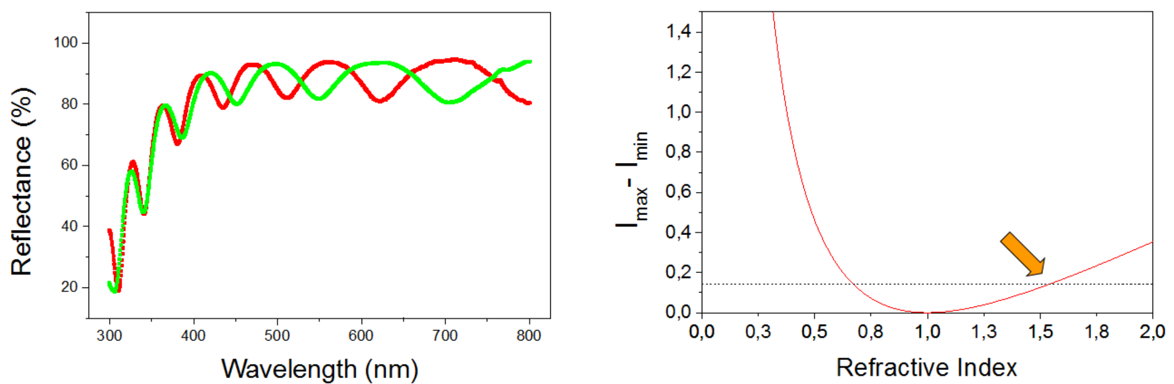

FIGURES 2.14. (LEFT) Reflectance spectra of two films with different thickness grown with the same conditions; a A typical interference fringes pattern develops. The maxima/minima location depends on the product *nd* (optical thickness). **(RIGHT)** The difference between I_{max} and I_{min} only depends on *n*, and can be found graphically).

Ellipsometry

Although ellipsometry was not the primary tool employed in this Thesis for optical characterization, some of the films for the SiOx-like depositions and post-treatments

were also characterized by IR ellipsometry as a means to confirm that the optical properties were consistent with chemical modifications leading to the formation of silicon oxides. FTIR Phase Modulted Ellipsometry was carried out with an ISA Jobin-Yvon Ellipsometre in the polarizer-modulator-sample-analyzer configuration. The spectral range was restricted to 900 – 3500 cm^{-1} by the detector specifications. The angle of incidence of the beam was set to 72.3° with respect to the normal, and the interferogram accumulation was set to 30 scans with a resolution of 4 cm^{-1}. This equipment is located at the Departament de Física Aplicada i Òptica de la Universitat de Barcelona.

In addition, for the post-treated samples, optical properties in the UV-Vis were also measured by ellisometry in order to detect the thickness and optical parameters between the surface modified region and the underneath unmodified region. In this case, the spectra were collected using a microspot beam in a Sopra GES5 Ellipsometer at 75.3° (silicon Brewster angle), and the film thickness and refractive index were calculated following the Forohui-Bloomer model.[120] This analyzer is located at the Laboratoire de Genie Electrique de Tolouse, at the Univesité Paul Sabatier.

Nanoindentation

Indentation methods are based on the ability of a hard material to penetrate a test sample. They are somehow similar to stylus profilometers, but they do not allow any relative movement between the tip and the surface under test. The stylus employed to apply the load on the sample is the indenter, usually a diamond tip for pyramidal shapes and tungsten carbide for conical or spherical shapes.

The hardness of a certain material, H, is defined by the relation between the applied load, P, and some deformation on the surface of the material, such as the residual area of the imprint after the indenter is removed or the projected area of the indenter at maximum penetration depth. Thus, hardness is given by

$$H = P/A \qquad \text{(Equation 2.7)}$$

which has units of force per unit area, usually expressed as MPa for soft materials or GPa for harder ones. Nanoindenters allow to apply extremely low loads, increasingly, up to a maximum load of a few mN or even μN, and to monitor the penetration depth

at each step. The unloading process is also carefully controlled and registered. For this reason, it is usually referred to as the depth-sensing nanoindentation technique. In contrast to classical indentation techniques (Brinell, Rockwell, etc…) the contact area is not determined by the residual print once the indenter is removed, but it is calculated indirectly from the depth measurement and the geometry of the indenter.

The force and penetration depth measurements are usually presented by plotting the penetration depth, *h*, as a function of the applied load, *P*, or viceversa. In this Thesis we have applied the former convention, as the controlled parameter is the applied load. The corresponding graph is known as the *Load-Unload Displacement Curve* (Figure 2.15). Hardness and elastic modulus can be calculated from the load-unload displacement curves by means of the analysis method described by Oliver and Pharr.[121] In this method, several data points from the unloading part of the curve are employed to fit the slope of the curve (*dP/dh*), which is known as the *stiffness* of the contact. The slope of the curve is then extrapolated to the depth axis and various corrections are applied in order to determine the plastic depth h_p. After the plastic depth is determined, the corresponding contact area can be calculated from the form factor of the indenter and hardness values will be obtained from Equation 2.7. The reduced Young's modulus, E_r, can also be calculated by applying the relation derived by Sneddon[122] for the contact between rigid and elastic materials:

$$\frac{dP}{dt} = \frac{2}{\sqrt{\pi}} E_r \sqrt{A} \qquad (Equation\ 2.8)$$

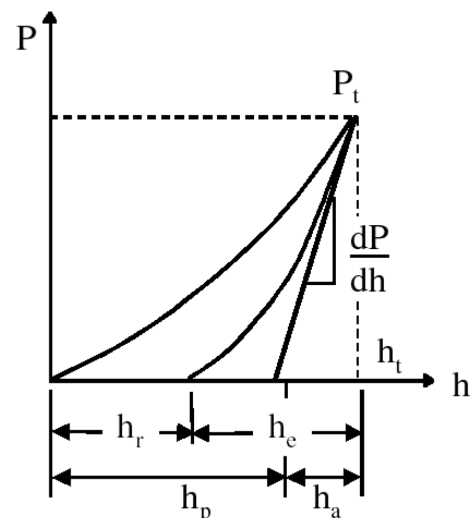

FIGURE 2.15. Example of a Load-Unload Displacement Curve The maximum penetration depth (h_t), the maximum applied load (P_t), the residual penetration (h_r), depth and the elastically recovered depth (h_e), are measured by the system. The extrapolated plastic deformation (h_p), and elastic deformation (h_a) are extrapolated from the slope of the unloading curve at maximum penetration depth.

Nanoindentation measurements have been performed in two different instruments: NanoTest 550 (MicroMaterials Ltd, Wrecham, UK) and UMIS-2000 (CSIRO, Sydney, Australia), located at the Departament de Física Aplicada i Òptica de la Unversitat de Barcelona, and at the Biomaterials Science Research Unit of the University of Sydney, respectively.

There are important differences between both nanoindenters, the main one being the axis of actuation. Whereas the diamond indenter in the Nanotest is mounted on a pendulum and actuates on the horizontal axis, the UMIS nanoindenter is mounted on a vertical stage, which allows to apply forces in the vertical axis. This has a first significant advantage for the UMIS system: samples can be laid flat on the sample stage, whereas for the Nanotest, they have to be glued to the stage.

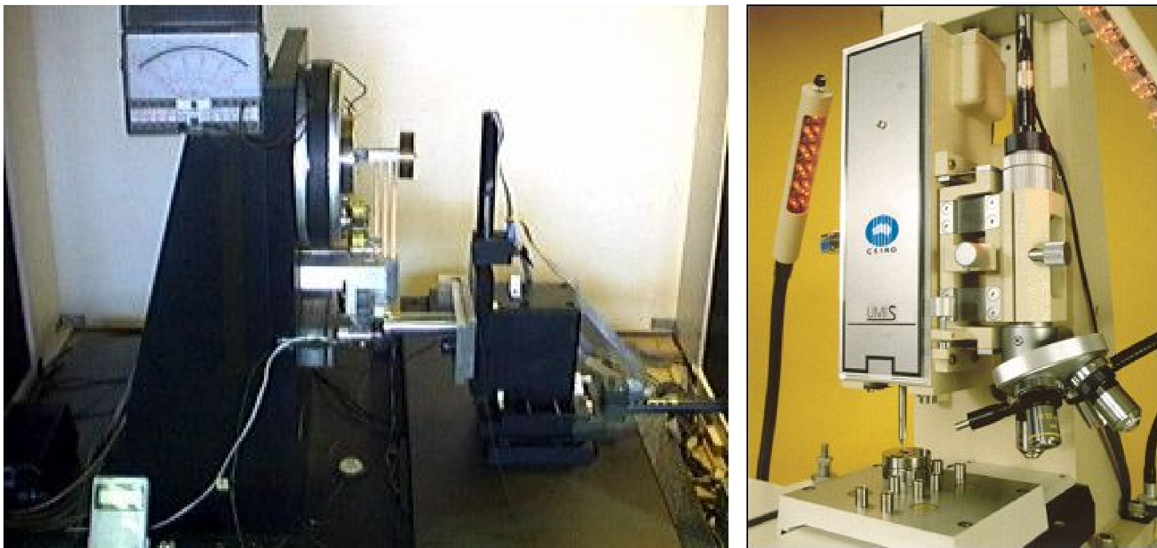

FIGURE 2.16. Nanoindenters employed for mechanical characterization. **(LEFT)** Nanotest, by Micromaterials; **(RIGHT)** UMIS-2000, by CSIRO.

The principles of operation that allow the application and measurement of loads and displacements are quite different for both systems (Figure 2.17). The Nanotest system is based on a pendulum that has the indenter at one end and a coil at the other. The coil effects a controlled calibrated force on the axis of the pendulum which is transformed in the horizontal displacement of the indenter; the penetration depth is measured by a parallel plate capacitor where one of the plates moves along with the pendulum. Further details can be found in [[123]].

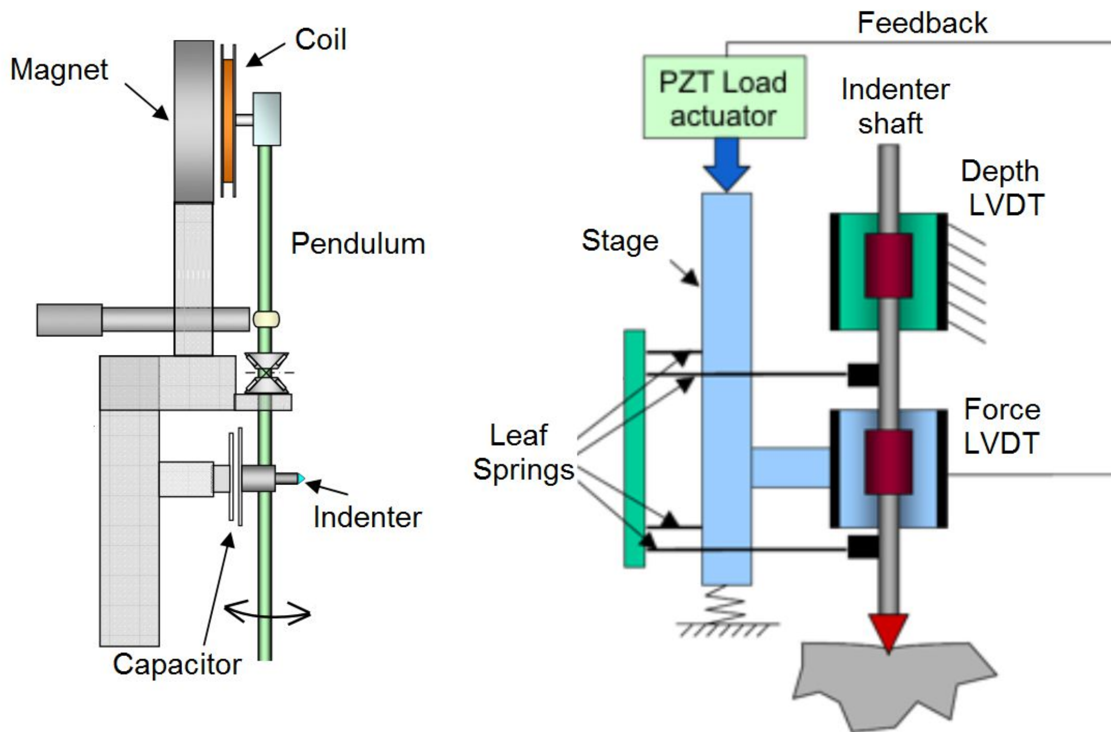

FIGURE 2.17. Schematic representation of the operating principles for the Nanotest **(LEFT)**, and UMIS **(RIGHT)** systems.

The UMIS-2000 system is based on an indenter attached at the bottom end of a metal shaft, which is attached to a carriage stage by a series of carefully machined leaf springs. The carriage is driven by the expansion of a piezo-electric device and when the indenter contacts the specimen, the springs deflect. This deflection is measured using a force LVDT (linear variable differential transformer). A feedback system ensures precise control over the application of the force, and a second LVDT measures the displacement of the indenter shaft relative to the carriage.

The UMIS-2000 indenter allows a minimum contact force of only 2μN and a force resolution of 500 nN, whereas for the Nanotest system these values are one order of magnitude higher.

In the UMIS, the samples are usually bonded with melted wax, although heavier samples can be left laying on the measuring sample holders, which are magnetically attached to the base of the instrument. The system includes an optical microscope to allow visualizing the target area for analysis and also to inspect the footprints left by indentations. The sample stage is motorized, which, in combination with the

microscope, allows for precise positioning of the indentation spots. A set of up to 50 spots can be located and preset so that the instrument will carry out as many indentations in the exact locations. This is extremely useful to have as many replicates as possible, since microhardness differences can be signifficant from one spot to another, due to surface impurities or dust. Also any tilt in the sample can be compensated by locating three reference points; the software calculates automatically the associated reference plan.

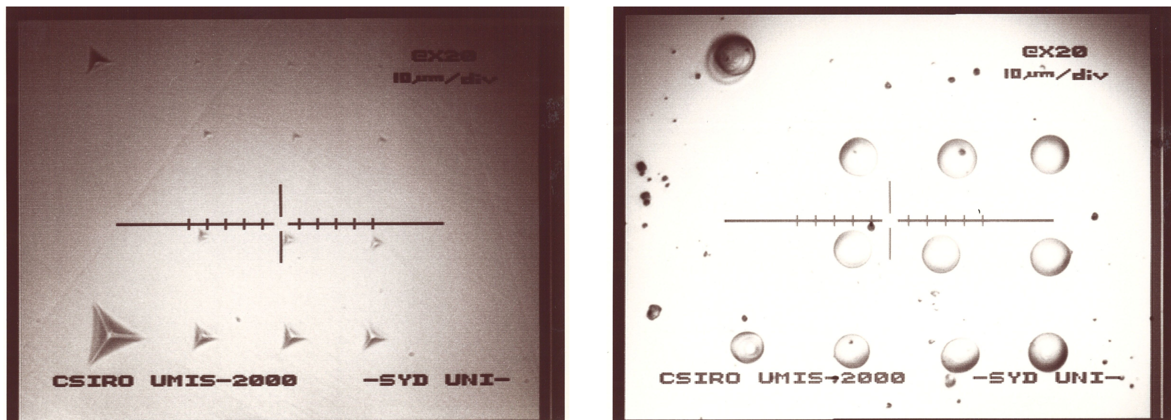

FIGURE 2.18. Optical images captured by the micrscope coupled to the UMIS-2000 Nanoindenter. Several indentation spots are visible. **(LEFT)** Residual print after indentations with a Berkovic indenter at different applied maximum loads. **(RIGHT)** Equal indentations with an spherical indenter of 20 μm tip diameter.

Different shaped indenters were used to characterize the samples included in this Thesis. The Berkovic indenter was used to calculate the mechanical parameters (H and E_r), whereas the Corner Cube indenter was used to distinguish properties among plasma post-treated films. Spherical indenters (1 μm and 20 μm) were also employed, since the evolution of the estimated hardness as a function of the penetration depth can be calculated from a load-unload cycle with partial unload at eatch sampling step. The hardness value at each step was calculated following the method by Swain and Field.[124,125]

Microscratch

Microscratch testing is used to assess the adhesion and the wear resistance of coating/substrate systems. The Nanotest 550 instrument is also equipped with a

second pendulum capable of actuating a much higher force, up to 20 N, and measuring higher depths, up to 80 μm.

Microscratch measurements were performed with a Rockwell diamond indenter with a tip radius of 100 μm. The scratches were produced along a scratch distance of 2 mm, starting at 0 mN of normal load and increasing at a constant rate of 32.5 mN/s, up to a maximum of 3000 mN. A friction sensor was added to the diamond suport in order to measure tangential forces, so that real-time monitoring of the penetration depth of the diamond into the coating and the frictional force experienced by the diamond along the scan were registered. A failure and dettachment of the coating is detected by a sudden increase in the friction force and its associated noise. The force at which such a failure occurs is defined as the critical load (L_c).

After the scratch is produced, the samples can be removed for further inspection with optical microscopy or profilometry, in order to measure the dimensions of the tracks.

Drop Shape Analysis (DSA)

The measurement of static contact angles of liquids on surfaces can be accomplished by a very simple method. A small drop (ideally 2-10 μL) is laid on top of the surface to be analyzed and a cross-sectional image is taken. The image is then analyzed by software and the angle θ between the liquid and the flat surface is measured (Figure 2.19). This simple technique is known as Drop Shape Analysis (DSA). Materials and surfaces with a contact angle for water, $\theta < 90°$, are *hydrophilic*; materials with a high contact angle, $\theta > 90°$, are called *hydrophobic*. The contact angle of a liquid on a material can be used to determine the surface energy of the solid material, γ_{SG}. According to Young's equation,

$$\gamma_{LG} cos\theta = \gamma_{SG} - \gamma_{SL} \qquad (Equation\ 2.9)$$

where γ_{LG} is the surface tension between the liquid and the gas and and γ_{SL} is the free energy of the interface between the solid and the liquid; q is the contact angle.

The energy of adhesion between two phases consists of a dispersive component, σ_d, (derived from the London interactions) and a non-dispersive component, σ_p, (also known as the *polar* component) of the interactions.

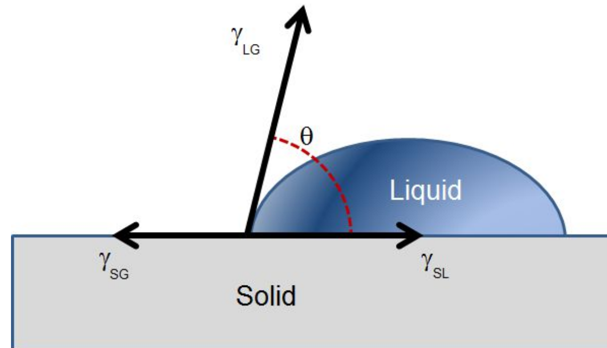

FIGURE 2.19. Representation of the components that define static contact angle according to Young's equation.

There are a few methods for determining the polar and dispersive components of surface energy of solids. All of them rely on measuring the contact angle for different liquids (at least two) with known polar, σ_l^p, and dispersive, σ_l^d, components. The results presented in this Thesis have been obtained by measuring the contact angles of water, formamide and diiodomethane, and applying the Owens-Wendt-Kaelble method.[126,127]

In this method, a plot of $y = \frac{1}{2}(1 + cos\theta) \cdot \frac{\sigma_l}{\sqrt{\sigma_l^d}}$ versus $x = \left(\sigma_l^p / \sigma_l^d\right)^{1/2}$ is generated adding the pairs of values (*x,y*) for each liquid, and a linear fit *y=mx+b* is calculated. The polar and dispersive components can then be directly estimated from the slope and the y-axis intercept as

$$\sigma_s^p = m^2, \quad \text{and} \quad \sigma_s^d = b^2 \qquad \textit{(Equations 2.10)}$$

The measurements of contact angles and surface energies were conducted in a DSA-10 (Krüss GmbH, Germany) and a Digidrop (GBX, France)

Corrosion resistance

A simple, home-made test set-up was assembled for mesuaring corrosion resistance (Figure 2.20. A white LED was employed to illuminate the surface of a

miniature solar cell. The current generated by the solar cell was registered by a Mastech 345 digital multimeter and sent to a PC by an RS-232 interface. When an opaque sample is placed on top of the solar cell, the intensity drops to virtually zero.

Since corrosion protection is often required for metals, and specially for metallizations on plastics, Al-coated polycarbonate and glass samples were prepared and subsequent ppHMDSO coatings were applied.

In order to test the corrosion protection of Al, the samples were placed on top of the solar cell and 20 uL drops of different concentrations of strong alkaly solutions of KOH and NaOH where dispensed on top of the substrates. When the Al films get in contact with the corrosive solutions, a chemical reaction takes places and the coating is disolved. This is detected as a sudden increase in the intensity registered by the software and the time required for film disolution is determined.

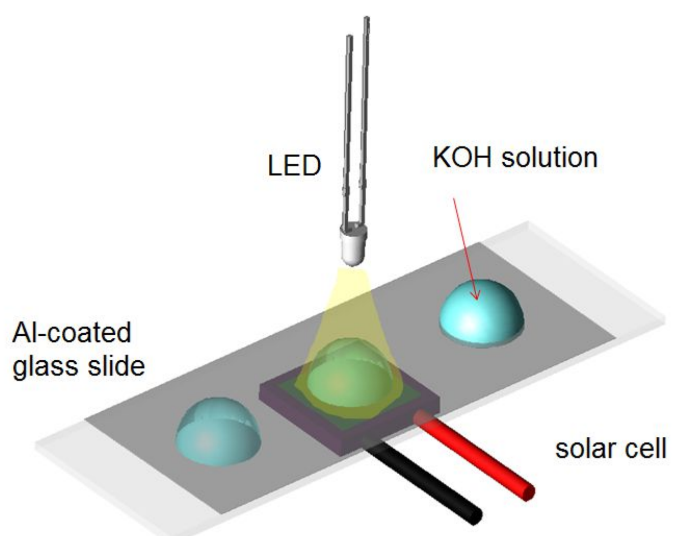

FIGURE 2.20. Experimental set-up for measurement of the corrosion time in Al-coated samples.

CHAPTER 3

PLASMA POLYMERIZATION OF HMDSO

3.1. INTRODUCTION AND OBJETIVES

According to Scopus database, plasma polymerization and plasma enhanced chemical vapor deposition (PECVD) of hexamethyldisiloxane have been a subject of attention for almost 900 publications worldwide over the last five decades. From these publications, plasma polymerization employing a DC plasma or 50Hz AC plasma source has been reported by only a handful of papers[128–136] and only three groups have published works on DC plasma polymerization of HMDSO, to the best of our knowledge.(7)

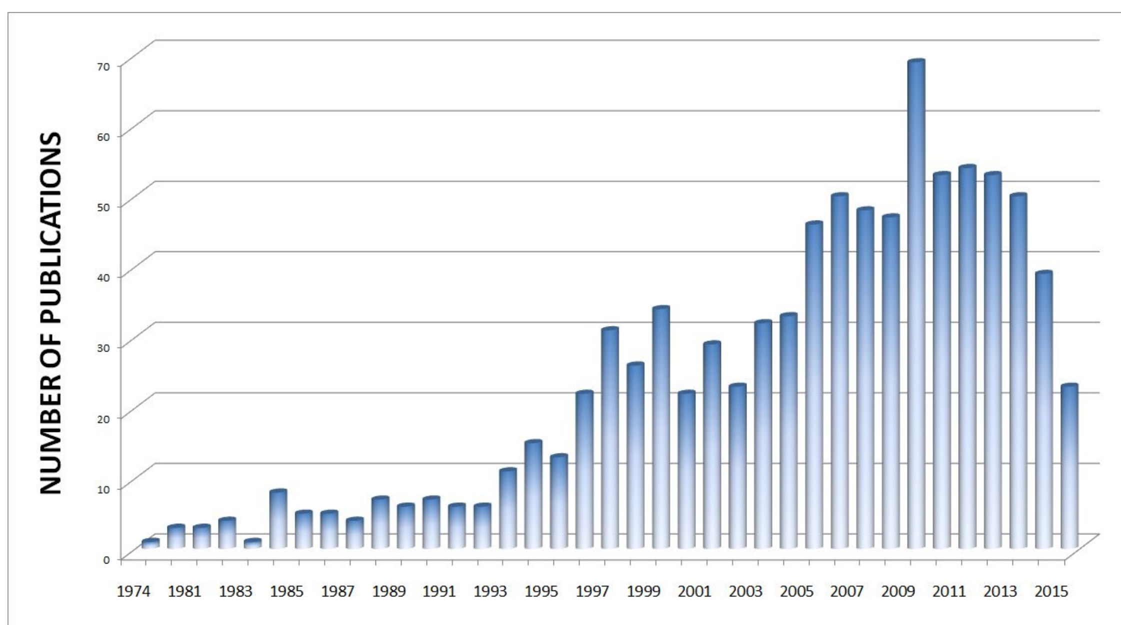

FIGURE 3.1. Number of yearly publications devoted to the plasma polymerization or PECVD of HMDSO, as indexed by Scopus database.

(7) A group from University of Cincinnati leaded by professor W.J. van Ooij, a group from University of Campinas (Brazil) leaded by M.A. Bica de Moraes, and a group from Chemitz, Germany.

Sustaining a DC plasma between two metallic electrodes is in principle easy and requires rather simple equipment, yet the reasons for the apparent lack of interest in the application of this process to plasma polymerization are diverse: first, it has been generally accepted that only metal samples can be coated in DC plasmas and that after a certain limiting film thickness further growth would be inhibited by the formation of an insulating film on the surface of the electrodes [7,137,138]; secondly, most attempts of retaining the structure of hydrocarbon monomers in DC plasmas ended up in the growth of carbon-like films due to extensive ion bombardment[128,138], i.e. no polymerization was achieved; third, the higher ion energy and ion bombardment, as compared to high frequency plasmas, can induce excessive thermal load on the parts to be coated; and last, DC plasma is asymmetrical by nature and the deposits on top of or near the vicinity of the cathode and anode may be significantly different from each other[139], which poses difficulties to obtaining coatings with homogeneous properties.

Certainly, the formation of insulating films on top of the electrodes is the main drawback of DC plasma polymerization and it will result in arching either at the cathode, at the anode or at any grounded surface, for longer deposition times. Ions and electrons can accumulate on the dielectric layers up to the point where electrical breakdown may occur; also, if the walls of the reactor are made of stainless still, the plasma will be distorted and local glows will generate preferentially at the least resistive path for the flow of electrons, due to the different thickness deposited at different locations. Arcing often results in unpredictable film properties due to unstable plasma parameters, increased temperature, inhomogeneous film growth and evaporation of material that redeposits on the substrates and alters the composition and properties. Therefore, arcing should be avoided by all means. Nonetheless, although arcing and sparking are usually not a problem in RF or MW reactors, it is known that microarcing can also occur in them[140].

Achieving controlled reproducible properties with DC plasma polymerization is challenging, but could be interesting for industrial applications due to the simplicity of the equipment, the availability of increased ion bombardment with respect to high-frequency techniques and the possibility to combine it with other techniques such as sputtering, without employing additional sources.

In this chapter we will present the results obtained for plasma polymerization of HMDSO and we will demonstrate that the same range of structure, composition and functional properties of the films can be achieved in a DC discharge as in the results published for high-frequency plasmas (RF, MW, ECR).

As mentioned in the introduction, HMDSO is an especially useful monomer because it allows to vary the properties of the deposited films from polymer-like to completely silica-like[(8)]. In other words, we can potentially achieve films with the properties of cross-linked silicone (PDMS) or with the properties of silica glass (SiO_2) starting from the same precursor molecule (HMDSO) and depending on the degree of preservation of the original structure of the monomer. Shifting from one to another is possible by fine-tuning the parameters involved in the plasma deposition mechanisms.

Plasma polymerization is a very complex physico-chemical process which is not yet completely understood and many operational parameters can have an influence on the properties of the films: starting gas mixture composition (with or without carrier gas), total pressure, power, monomer flow, residence time of monomer molecules, deposition time, substrate material, surface area ratio between electrodes, geometry of electrodes and reactor, location of gas inlets, location and orientation of substrates, etc. It is not possible to test all relevant parameters and combinations within the scope of this Thesis.

Therefore, the objectives of this Chapter are:

- To study the effect of different operational parameters on the growth rate and properties of ppHMDSO films: plasma pressure, deposition time, reactor geometry, substrate location, precursor mixture.
- To stablish the best reactor configuration and operational parameters for the deposition of homogeneous polymer-like and silica-like films.
- To characterize the composition and functional properties of polymer-like and silica-like films obtained from ppHMDSO and to relate these properties to the deposition parameters.
- To understand the basic physico-chemical mechanisms leading to the deposition of polymer-like and silica-like films.

[(8)] For the deposition of the inorganic material, many publications prefer to use the term Plasma Enhanced Chemical Vapor Deposition (PECVD) as an extension of the thermal Chemical Vapor Deposition (CVD) process.

- To establish and understand the limitations and possible applications of the technique.

3.2. RESULTS AND DISCUSSION

Our plasma polymerization reactor can be set up with two main configurations: the cylindrical and the planoparallel plasma geometries, as described in Chapter 2. Both configurations have advantages and disadvantages and may be employed depending on the application requirements: size and geometry of the part to be coated, and desired thickness, homogeneity and composition of the film. In addition, some variations can be employed to optimize the deposited films, such as: position and distribution of the gas inlets and the gas flow, increasing or decreasing the surface area, relative position of the electrodes, and location and orientation of the substrates with respect to the plasma and to the gas flow.

We have studied the deposition of organic and inorganic films from HMDSO in both configurations aiming at characterizing and understanding the effect of different parameters on the deposition rates and the properties of the deposited films. In real industrial applications, the deposition rate is a key figure that affects cycle time and drives costs up or down, which can make *the* difference between a successful technology and a rejected one.

3.2.1. Films deposited from pure HMDSO

3.2.1.1. Deposition rates and thickness homogeneity

First in our study, the effect of monomer pressure and cathode-substrate distance was analyzed in order to establish the optimal working range for growth of transparent polymer-like films. Al-coated microscope glass slides (75×25×1 mm) were positioned at 5, 10, 15, 20 and 25 cm from the central cathode. The substrates were faced perpendicularly to the cathode and they were kept in place by grounded holders. The substrates were slightly rotated as to avoid shadowing effects among each other (Figure 3.2). The range of pressures between 0.05 mbar and 0.3 mbar was studied. Higher and lower pressures are still possible, but at lower pressures deposition rates were too low to grow sufficient thickness in a reasonable process

time and at higher pressures arcing often occurred within 10 min of plasma which generates locally uncontrolled fast polymerization. If arcing occurs anywhere near the substrates, powder particles incorporate into the growing films and result in a milky appearance due to scattering of light.

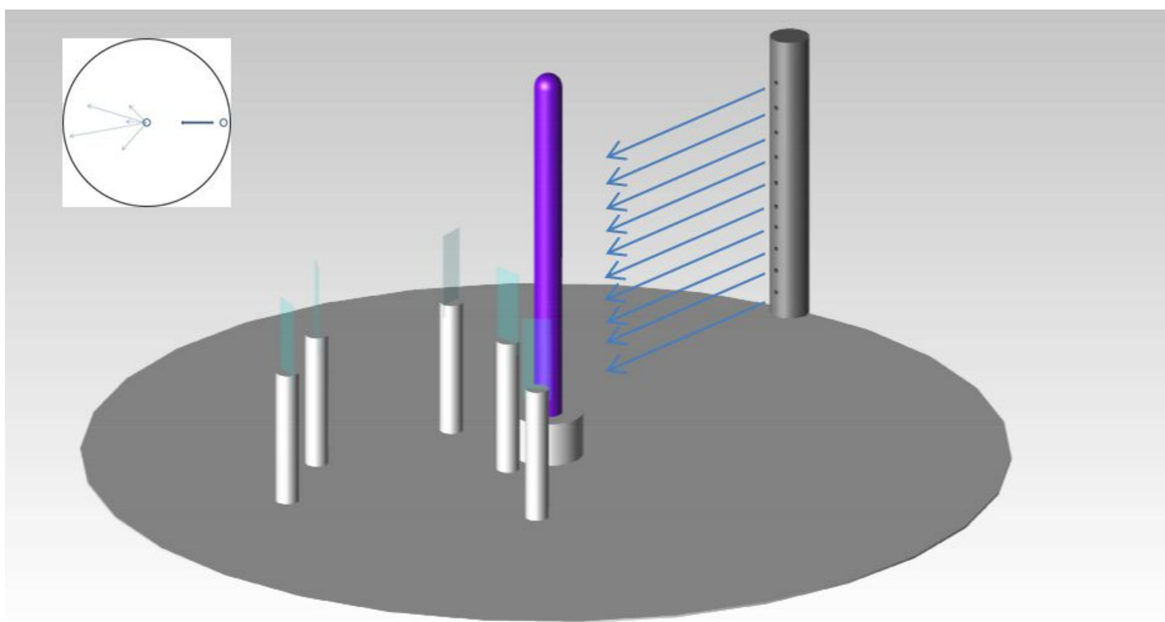

FIGURE 3.2. Cylindrical configuration for plasma polymerization. The substrates are placed perpendicular to the central cathode at a distance of 5, 10, 15, 20 and 25 cm, and monomer is injected into the plasma from the left side by a linear distributor**. (TOP LEFT IMAGE INSERT)** Zenithal view of the substrate layout with respect to the cathode and gas inlet.

The deposition rates at each position can be easily calculated as the ratio of the thickness of the film and the deposition time. The evolution of deposition rates with pressure is shown in Figures 3.3 and 3.3. As pressure increases, deposition rates also increase and maximum deposition rates seem to be found at around 0.20 mbar, and start decreasing at higher pressures with the operational parameters in this configuration. It is also noteworthy to mention that the difference in deposition rates between the substrates placed at the closest (5 cm) and farthest (25 cm) distances from the cathode seem to be slightly reduced at lower pressures. This effect was studied by Yasuda et al[13,14] and it is probably related to the facts that, first, at lower pressures the mean free path of reactive molecules generated within the glow near the cathode is higher and thus the probability of these reactive species to reach farther substrates is increased, and second, the different glowing layers around the

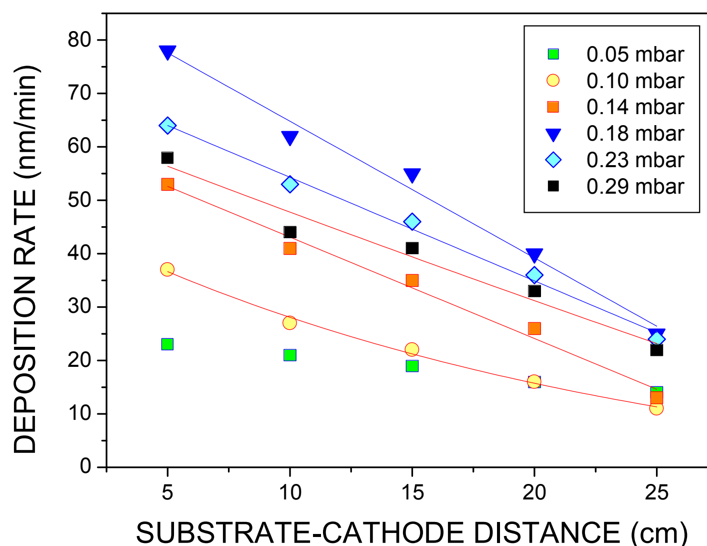

FIGURE 3.3. Deposition rates as a function of substrate-cathode distance for different monomer pressures.

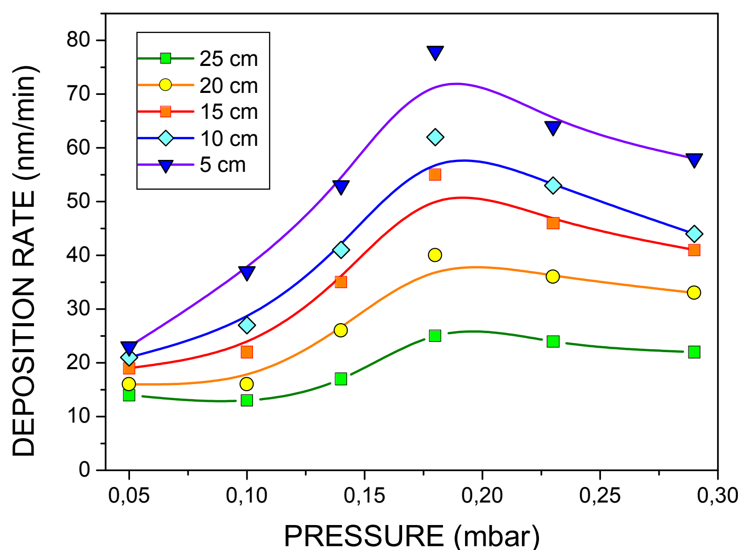

FIGURE 3.4. Deposition rates as a function of monomer pressure for at different locations in the reactor.

cathode (cathode glow and negative glow) are extended in size away from the cathode as pressure is decreased. A similar drop in the deposition rates with the distance from the cathode was found by van Ooij et al. for DC plasmas[128] and by Li[141] for RF plasmas.

Both studies concluded that the maximum deposition rate was achieved at the cathode surface and those substrates at the anode or floating within the plasma only achieved around one order of magnitude lower deposition rates. We have also found the same trend, but in our DC plasma only conductive substrates can be effectively

placed at the cathode(9), otherwise any dielectric substrate blocks the emission of secondary electrons and disturbs the electric field, and as a consequence the cathode does not glow where the dielectric material covers its surface.

Deposition rates for ppHMDSO films reported in the literature together with the experimental conditions in which they were obtained are summarized in Table 3.1. In comparison, our maximum deposition rates of almost 80 nm/min rank middle-class in efficiency among these processes. Almost all the studies analyzed employed a pressure range which is in the same range of our study (0.1 – 0.3 mbar); the power and monomer flow are more variable depending on the specific reactor configuration. For the dependence of the deposition rates on pressure, different trends have been reported, and they show that also the maximum deposited rates are extremely dependent on reactor configuration. Deposition rates may either increase within all the pressure range studied,[128] reach a maximum and then decrease,[141–144] or reach a plateau.[145]

Max rate (nm /min)	Reactor Type / position	Pressure (mbar)	Power (W)	Flow (sccm)	Reference
0.5	DC Floating Back	0.25	13	1.2	Van Ooij, WJ[128]
1.2	DC Anode	0.25	11	1.2	Van Ooij, WJ[128]
5.0	DC Floating Front	0.25	12	1.2	Van Ooij, WJ[128]
6.0	RF inductively	0.08	15	2	Alexander, MR[146]
32	DC Cathode	0.25	10	1.2	Van Ooij, WJ[128]
45	RF inductively	---	100	---	Rau, C[145]
90	RF capacitive	0.30	300	90	Hegemann, D[76]
100	Microwave	0.10	50	76	Vautrin, C[142]
140	RF capacitive	0.10	50	---	Sahli, S[143,144]
400	RF capacitive	0.23	60	2	Li, K[141]
530	Microwave	0.25	90	2	Walkiewicz-Pietrzykowska, A[147]
1000	DC cathode	1.00	30	2	Heyner , R[148]

TABLE 3.1. Maximum deposition rates reported in different plasma reactors, DC, RF and MW.

The explanation for this apparently arbitrary behavior in the dependence of deposition rates on pressure was given by Yasuda[7] and has been generally accepted thereafter with some adaptions by Friedrich and Hegemann.[18,17,19,149,62,16] They all share the basic concept that the amount of deposited material is dependent on the

(9) This was confirmed by placing small Si substrates on the cathode in the parallel plate configuration.

energy available per molecule. In its simplest form, this can be expressed by employing the composite or "Yasuda" parameter *Y*:

$$Y=W/FM, \qquad (Equation\ 3.1)$$

where *W* is the input power (in Watts), *F* is the flow rate of monomer (in sccm) and *M* is the molecular weight (in g/mol); *Y* has units of J/g.

Depending on the amount of energy transferred by the plasma to each molecule, polymerization can proceed in three different regimes: *monomer-deficient regime*, *competition or transition regime* and *energy-deficient regime*. These regimes are explained in section 1.2.4.

If we reanalyze our deposition rates in view of the assumptions of Yasuda's model, by expressing deposition rates (*DR*) as a function of monomer flow and Yasuda's parameter the influence of these regimes is even more clear (Figures 3.5 and 3.6). Since in our system flow rate and pressure are almost proportional between 0.1 and 0.3 mbar (see Figure 2.6 in Chapter 2) the evolution of deposition rates looks similar for *P* and *F*, and the evolution is inversed for *Y*. For a better analysis of the deposition rates as a function of the composite parameter, ideally, we should be able to control independently the power, the flow rate and the pressure, but this is not completely possible in our reactor, as explained in Chapter 2. Since the available power is approximately fixed (between 77-88 W) both graphs (*F* vs *DR* and *Y* vs *DR*) show that, for the lower range of pressure and monomer flow rates the addition of molecules into the system results in an increase in the deposition rates. The Yasuda's parameter plot shows that this situation corresponds to the monomer deficient region, where the amount of available molecules is the limiting factor. In this region, when the flow rate increases, the amount of molecules and the deposition rates are directly correlated. Due to the variation in the efficiency of the pumping throughput of the mechanical pump, in this area the Y parameter is significantly decreased when pressure is increased from 0.05 to 0.1 mbar. Between 0.1 and 0.23 mbar there seems to be a transition between increasing deposition rates and decreasing deposition rates. This behavior suggests that the system is crossing through the transition regime which leads to the energy-deficient regime. A similar transition has been shown for the plasma polymerization of tetramethyldisiloxane at low powers[7], which probably means that the available power is low for the size of the active area in

the cylindrical configuration and for the required high flow due to the size of the reactor.

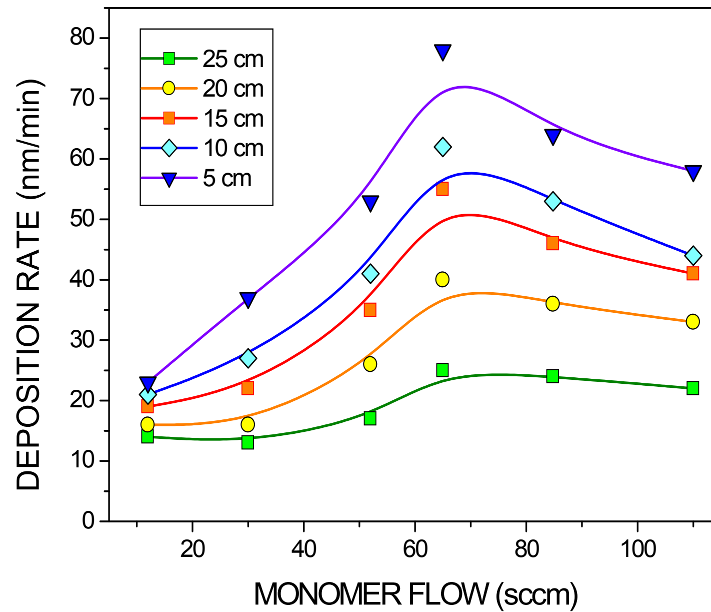

FIGURE 3.5. Deposition rates as a function of substrate-cathode distance for different monomer pressures.

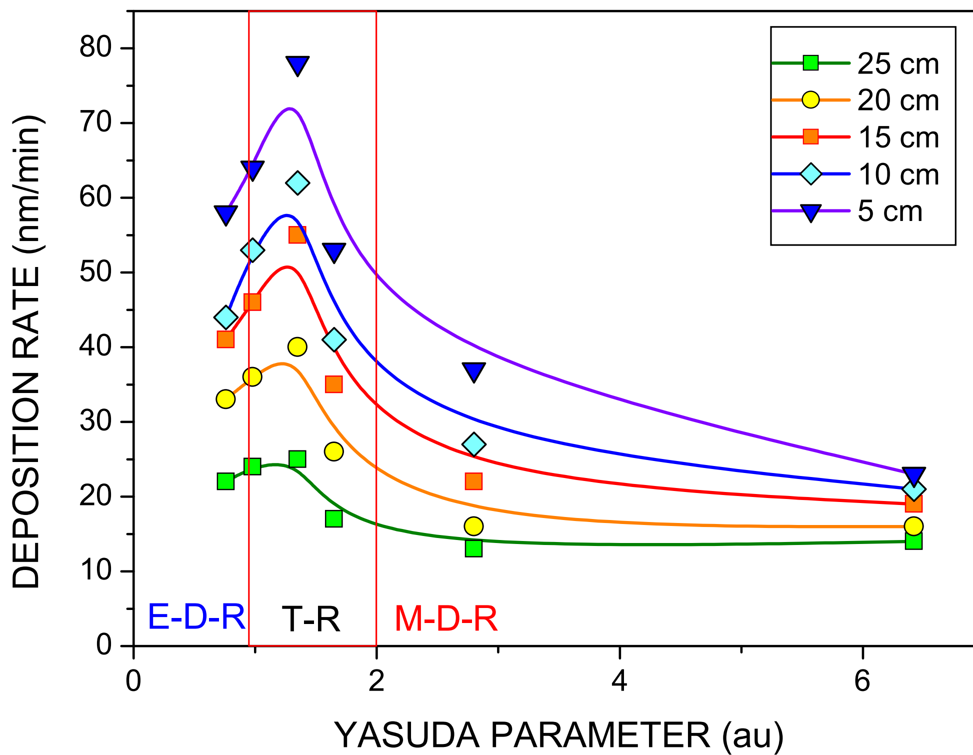

FIGURE 3.6. Deposition rates as a function of monomer pressure for different locations in the reactor. Approximate suggested limits for the energy-deficient regime (EDTR), transition regime (TR) and monomer-deficient regime (MDR) have been indicated.

The operational parameters involved in Figures 3.3 to 3.6 are summarized in Table 3.2.

Flow (sccm)	Pressure (mbar	Residence Time (s)	Power (W)	Y=W/F	REGIME
12	0.05	63	77	6.42	Monomer Def
30	0.1	50	84	2.80	Monomer Def
52	0.14	41	86	1.65	Transition
65	0.18	42	88	1.35	Transition
85	0.23	41	83	0.98	Energy Def
110	0.29	40	84	0.76	Energy Def

TABLE 3.2. Summary of operational parameters employed in Figures 3.5 to 3.6 .

According to the model, in principle it should be possible to further increase deposition rates by applying higher power to the discharge. It should also be possible to achieve it by working at lower flows and higher pressures, in order to increase the residence time of the molecules. We have applied this approach with success by reducing the pumping throughput and the energy-deficient regime was displaced to higher pressures: at 50% lower flow rates, deposition rates increased with pressure up to 0.3 mbar instead of 0.2 mbar.

Thickness homogeneity

The total thicknesses deposited on each substrate by the cylindrical configuration at 0.10 mbar of pure HMDSO monomer plasma and 30 min of deposition time are shown in Figure 3.7. From these data, two observations can be made: first the average thickness for each substrate decreases almost linearly with the distance to the cathode and secondly, all films show a variation in thickness of 20-25%, as indicated by the error bars. This variation is measured only at the central part of the substrates, a few millimeters away from the edges; close to the edges, thickness variations are still higher. Thickness distributions in all substrates show characteristic 'flame-like' patterns (Figure 3.8) which were already described by Yasuda[150,151] for plasma polymerization in a tubular reactor and were attributed to a fluidodynamical effect by the sudden disruption of the aerodynamic flow of reactive species around edges. We confirmed this assumption by simulating the gas flow in a simplified model of our reactor and setting the following parameters: P=0.2 mbar and F=60 sccm. In these

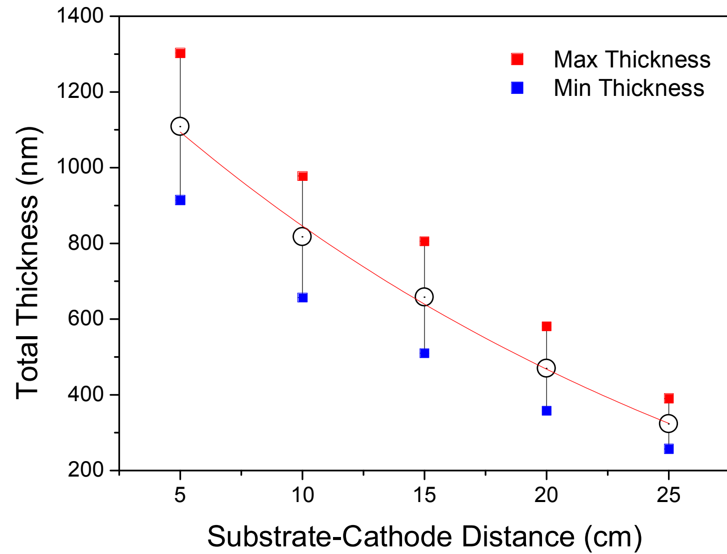

FIGURE 3.7. Total thickness deposited by a cylindrical plasma on substrates placed as shown in Figure 3.2. The error bars indicate the maximum and minimum thickness measured for each sample.

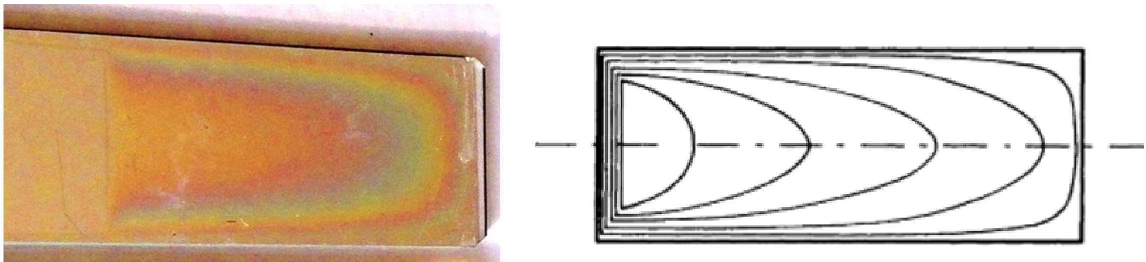

FIGURE 3.8. (LEFT) Flame-like deposition pattern in our cylindrical reactor and in a tubular reactor employed by Yasuda **(RIGHT)**, from [132]. The edges create a sudden disruption in the flow path of the reactive species that behave like a fluid.

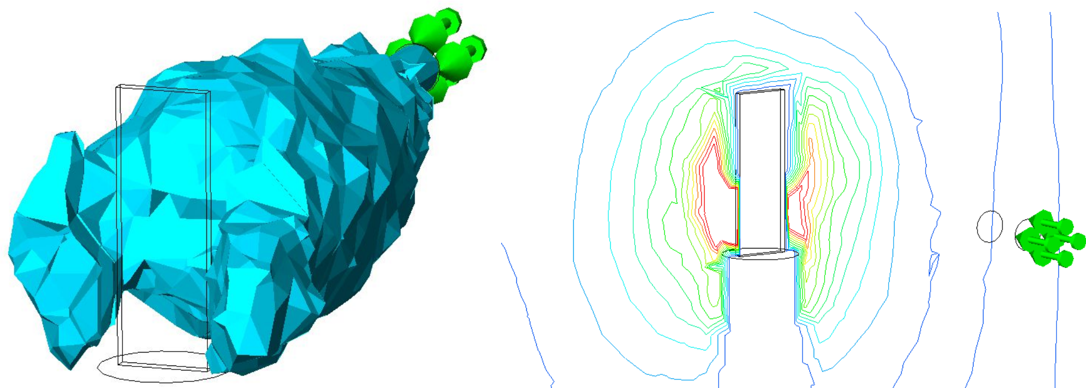

FIGURE 3.9. CFD simulation of a gas flowing around the edges of a substrate, from an inlet at 25 cm. F=60 sccm; P=02 mbar. The gas flow behaves like a fluid.

conditions, the gas flow lines (iso-surfaces for fluid velocity) gather close to the edges and 'wrap' the substrates (Figure 3.9).

Although this fluid-like behavior may be detrimental to some applications that require highly homogeneous coatings, it may also pose some interesting benefits with respect to depositing conformal films in complex 3D shapes. The fluidic behavior of gas flow in a reactor is a complex phenomenon out of the scope of this Thesis, but reactor design for industrial applications needs to take into account the transport of species as much as any consideration with respect to the plasma generation. This effect can be illustrated by measuring the coating thickness on the front surface of the substrate –i.e. the face that is oriented to the cathode- and on the rear surface (Figure 3.10). In contrast to deposition techniques that work with pressures in the molecular flow regime of gas, where no deposition is achieved at the backside of substrates, in plasma polymerization the viscous flow behavior is demonstrated by the growth of films at the 'dark' side of the substrates due to transport of activated fragments that polymerize therein.

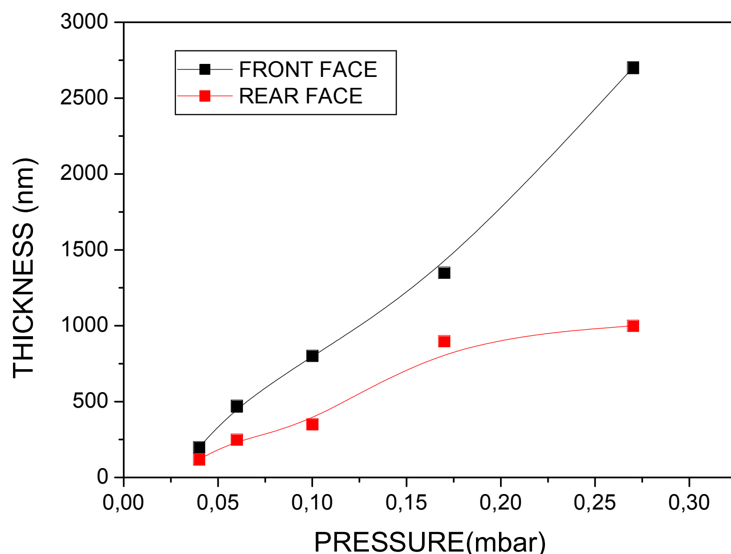

FIGURE 3.10. Thickness measurements at the front face and at the rear face of a substrate (75x25x1 mm) for different working pressures.

Deposition in a parallel-plate electrode configuration

The cylindrical configuration shows that the plasma activated reactive species can reach all surfaces in the reactor, but the homogeneity is the samples may not be adequate for some applications, unless the rotating planetary system introduced in Chapter 1 is available. In order to improve deposition homogeneity, a parallel-plate

electrode configuration was set up. In this configuration three 25x30 mm stainless-steel electrodes are laid out according to the set-up illustrated in Figure 2.4. The central powered electrode acts as a cathode and the top and bottom electrodes act as grounded anodes. The top anode is separated from the cathode at a distance of 10 mm, whereas the bottom electrode is held at different distances from 7 to 20 cm. Figure 3.11 is an image of several films deposited on Al-coated glass substrates placed directly on the surface of the bottom anode. No interference fringes were observed in any of the films, indicating excellent homogeneity. This was confirmed by mechanical profilometry, which showed thickness variations of less than 20 nm for large areas (up to 70x25 mm corresponding to a standard microscope glass slide).

FIGURE 3.11. Films with homogeneous thickness deposited on a parallel-plate electrode configuration.

Remote deposition

The parallel-plate configuration confines the plasma glow well within the projection of the electrodes, in contrast to the cylindrical configuration where the plasma glow occupies the whole volume of the reactor, since the grounded walls are actually the anode. One advantage of the parallel-plate configuration is that the substrates can be placed outside of the active plasma zone. The rates are typically 50 to 10% of those found for the substrates placed within the glowing plasma. Still, deposition rates are extremely variable in the remote configuration, and completely dependent on gas transport. This is exemplified by the surprising finding that deposition rates in substrates placed in close proximity to the outlet of gas that leads

to the vacuum pumping system may be higher than substrates located closer to the active area. It is also an indication that reactive radicals are long-lived and can travel by drag or diffusion to any region of the reactor.

3.2.1.2. Structure and composition of the films

Density

The density of the films can change significantly depending on the growth regime and on the location of the substrates. The lowest densities are achieved at the back face of substrates, in the energy-deficient regime. Densities as low as 1.10 g/cm^3 have been measured; the highest densities are achieved in the monomer-deficient regime at the front face of substrates placed in close proximity to the cathode. Densities as high as 1.65 g/cm^3 have been achieved, and up to 1.75 g/cm^3 on small silicon substrates placed on the surface of the cathode (cathodic polymerization).

Surface morphology

At first sight, the surface structure of the films is that of a smooth pinhole-free film. SEM characterization shows that all films are extremely smooth when deposited at the anode surface in a pressure range between 0.05-0.25 mbar. Only films deposited under two different conditions break this trend (Figure 3.12): films deposited at the cathode envelopes show a slightly higher surface roughness that can only be perceived by tilting the viewing angle at the SEM, and films deposited at high pressures (above 0.3 mbar at high flows and above 0.5 mbar at low flows) where a granular structure can be clearly distinguished already with the optical microscope or by visual inspection, since they show a characteristic milky appearance specially on the area close to the edges. SEM shows that for the second type of films, scattering by globular structures around 0.2-2.0 μm is the likely cause of this effect.

If a discharge is generated still at very high pressures (>1 mbar) and high powers (>300 W), the plasma is no more stable and powder particles are formed (Figure 2.12), which might be interesting for certain applications (e.g. superhydrophobicity).

As a conclusion, if films are grown within the optimal conditions a smooth continuous surface is observed and completely transparent films are obtained.

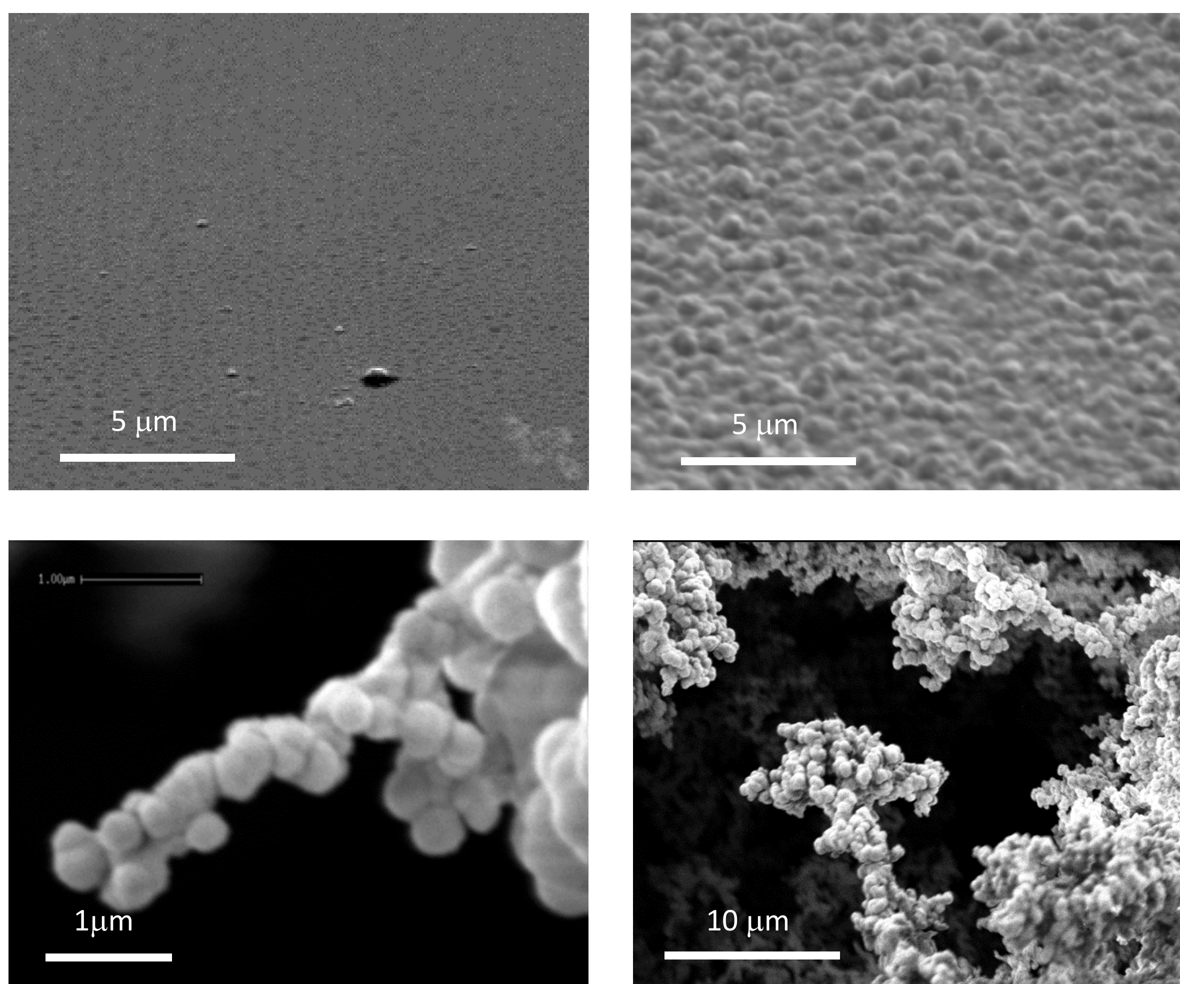

FIGURE 3.12. Films showing some structure are formed either at the cathode **(TOP LEFT)** or at the **anode (TOP RIGHT)** at pressures above the optimal range. **(BOTTOM LEFT AND RIGHT)** Powder particles and structures formed at very high pressures and powers.

Chemical structure

The chemical bonds present in the films were studied by FTIR. Figure 3.13 compares the FTIR spectra of pure liquid monomer, conventional PDMS polymer and a typical ppHMDSO film deposited at low values of the composite parameter (energy-deficient regime), and Table 3.3 summarizes the main absorption frequencies for ppHMDSO films[133,136].

Wavenumber (cm^{-1})	Mode
3650	OH stretching in free SiOH
3400	OH stretching of H-bonded OH
2958	CH_3 asymmetric stretching
2900	CH_3 symmetric stretching
2125	SiH stretching
1409	CH_3 asymmetric bending in $Si(CH_3)_x$
1354	$-CH_2$ scissor vibration in $Si-CH_2-Si$
1258	CH_3 symmetric bending in $Si(CH_3)_x$
1070-1020	SiOSi asymmetric stretching
890	CH_3 rocking in $Si(CH_3)_2$
837	CH_3 rocking in $Si(CH_3)_3$
795	CH_3 rocking in $Si(CH_3)_2$, SiOSi bending
758	CH_3 rocking in $Si(CH_3)_3$

TABLE 3.3. Main IR absorption bands in ppHMDSO films.

The most relevant absorption bands existing in the monomer spectrum and their related bond vibrations are: 2960 cm^{-1} (asymmetric stretching in CH_3 groups), 2900 cm^{-1} (symmetric stretching in CH_3 groups), 1260 cm^{-1} (symmetric bending of methyl groups bonded to Si), 1070 cm^{-1} (Si-O-Si asymmetric stretching), 837 and 760 cm^{-1} (rocking of CH_3 in $Si-(CH_3)_3$). All these vibrations are easily derived from the structure of the monomer molecule.

The absorption bands in the ppHMDSO film which were not found in the monomer are: 2870 cm^{-1} (CH_2 symmetric stretching), 2120 cm^{-1} (Si-H stretching), 1455 cm^{-1} (CH_2 asymmetric bending), 1400 cm^{-1} (stretching of the CH_2 group in $Si-CH_2-CH_2-Si$), 1355 cm^{-1} (stretching –or scissor vibration– in $Si-CH_2-Si$), 795 cm^{-1} (rocking of CH_3 in $Si(CH_3)_2$). Besides, a significant broadening of the Si-O-Si band (1130-930 cm^{-1}) is found in ppHMDSO films. From the appearance of $Si-CH_2-CH_2-Si$ bonds it can be suggested that the formation of such bridges is one of the main polymerization mechanisms of HMDSO.

The absorption bands in conventional PDMS are similar to those of ppHMDSO except for the fact that the peak at 837 cm^{-1} is almost negligible, which indicates that the amount of $Si-(CH_3)_3$ terminal bonds is very low; on the contrary, the amount of $Si-(CH3)_2$ bonds is extremely high in PDMS. This can be explained by the fact that PDMS

is a polymer consisting in large chain of repeating units of dimethylsiloxane. It is therefore clear that in these conditions, ppHMDSO corresponds to a plasma-polymer with shorter cross-linked chains than those found in PDMS.

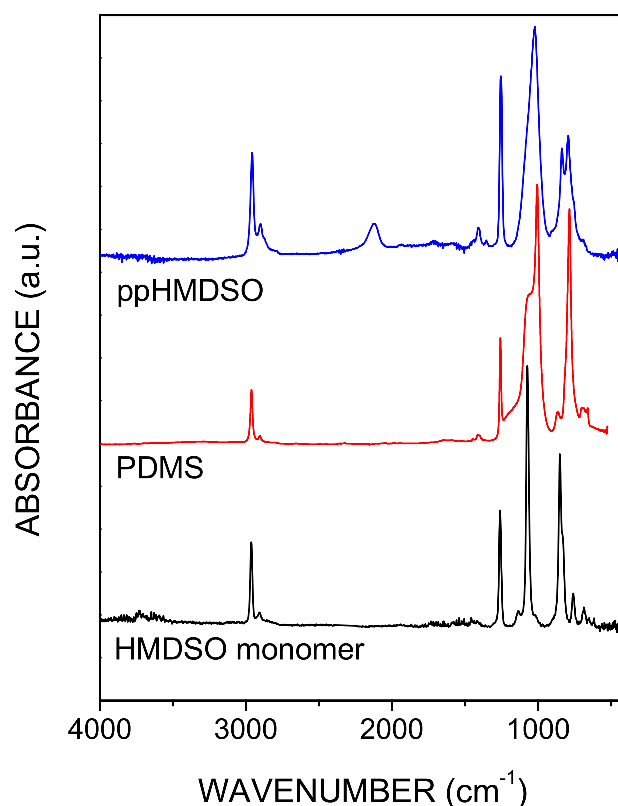

FIGURE 3.13. FTIR spectra of HMDSO monomer, PDMS and ppHMDSO film deposited under energy-deficient conditions (low Y parameter).

Films grown with different conditions show some variations with respect to the film in Figure 3.13. Figure 3.14 shows several spectra for films deposited at increasing *Y* parameter, starting from the monomer-deficient regime and leading into the energy-deficient regime.

The effect of the growth regime can be clearly observed in these spectra: ppHMDSO films grown in the energy-deficient regime show polymer-like spectra, characterized by the high content in organic-related groups, such as $Si-(CH_3)_3$ and $Si-(CH_3)_2$, whereas for films grown in the monomer-deficient regime the intensity of methyl-associated peaks is substantially decreased, specially the peaks at 1260 cm^{-3} and 2960 cm^{-3} which are unequivocally related to the concentration of methyl groups. In addition to the decrease in methyl groups, a general broadening of all bands is

observed. Broadening is generally associated to a more diverse chemical environment which can only be explained by increasing activation of monomer molecules, which leads to fragmentation, deposition and ablation, all occurring at the same time, as suggested by the RSGP model. OH incorporation was also increasingly detected in the monomer-deficient regime as indicated by the broad band at 3200-2700 cm-1

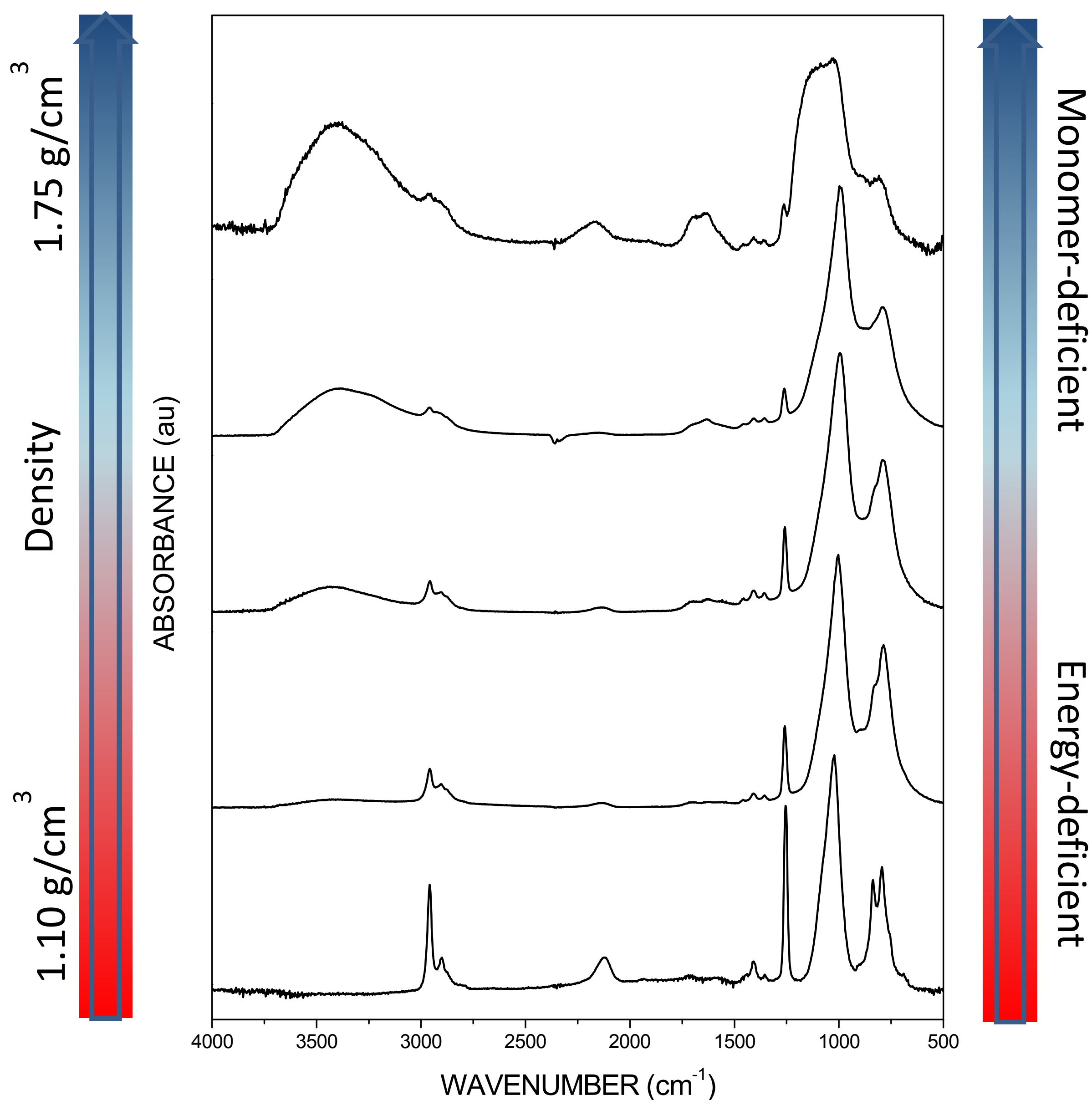

FIGURE 3.14. FTIR spectra of ppHMDSO films deposited at different conditions in the energy-deficient and in the monomer-deficient regimes. A clear drop in the intensity of methyl and tri-methyl associated frequencies is observed. In parallel, density increases with additional energy input per molecule.

In order to elucidate if the decrease in methyl-related peaks is associated to a high decrease in the concentration of C in the films, XPS measurements were conducted. The stoichiometry of the HMDSO monomer is $SiO_{0.5}C_6H_{18}$; the stoichiometry derived from XPS does not allow to determine the H content, but still, it can be assumed to be somewhere between 2 to 3 times the amount of C.

The lowest oxidation and highest carbon content has been found on the back side of substrates in the cylindrical configuration, and in some locations in the remote configuration. The closest sample to monomer stoichiometry was determined as $SiO_{0.60}C_{2.12}$:H , whereas the sample with the lowest carbon content was a silicon substrate placed on top of the cathode in a parallel-plate configuration. It was determined as $SiO_{1.03}C_{1.31}$:H

The stoichiometry of the films shows a smaller difference between low-carbon denser films and high-carbon films. This is probably due to the fact that carbon is not completely removed, but the Si-CH_3 methyl group is transformed to Si–CH_2.

3.2.2. Films deposited with the addition of carrier gases to HMDSO

3.2.2.1. Addition of Argon

When Ar is used as a carrier gas, the plasma density and the ionization ratio increase, and also does the Y parameter. Ar is not incorporated to the films, but it can increase deposition rates (in the energy-deficient regime) or monomer fragmentation (in the monomer-deficient regime), and, as general rule, the density and cross-linking of the films is slightly increased.

3.2.2.2. Addition of Nitrogen and air

N_2 addition is similar to the addition of Ar (higher plasma density, more intense glow and slightly higher deposition rates in the monomer deficient regime), but it has also an undesirable effect: the coatings deposited in N_2 show some absorption in the blue region of the spectrum and appear as slightly yellowish. XPS shows that although nitrogen relative concentration in the films is found to be less than 5%, films with such an amount are considerably yellowish. Addition of air also produces the same

colored appearance, but in this case the stoichiometry is also changed to a more oxidized state.

3.2.2.3. Addition of Oxygen

The most significant changes occurred when oxygen was added to the precursor flow. The main operational parameter in this case is the ratio between O_2:HMDSO. The addition of oxygen is intendedly directed to depositing SiO_x-like coatings. With the addition of oxygen, even at small ratios, the density of the plasma is significantly increased and the bombardment on all surfaces is also increased, due to the generation of negative ions which can also reach the anode surface with high energies. Different concentrations were assayed within the ratio O_2:HMDSO from 0 to 1.5. Higher oxygen concentrations are also possible, but the deposition rates dropped enormously to less than 3 nm/min. With an O_2:HMDSO ratio of 1.5, deposition rates were found to be between 10 nm/min to 5 nm/min, depending on the distance to the cathode, but two additional effects occurred: first, temperatures raised beyond 200 °C and in the parallel plate configurations the electrodes were deformed; secondly, a highly isolating dense coating is deposited on the surface of the electrodes and the plasma is difficult to maintain further than 20 -30 min. Therefore, at a ratio of 1.5, the maximum achievable thickness is lower than 300 nm; as a comparison, films as thick as 3 μm have been deposited at a ratio of 0 (pure monomer).

Density

The density of samples increased from 1.70 g/cm^3 with the addition of only 15% of O_2 to the precursor mixture, and reached up to 2.11 g/cm^3 at 60%.

Chemical structure

In order to assess the degree of oxidation accomplished by the addition of oxygen, the chemical structure of the films was double checked by FTIR, EDX and Ellipsometry analysis.

Figure 3.15 shows the FTIR spectra of films prepared with 0, 15, 35, 45 and 60% of oxygen in the plasma gas (corresponding to O_2:HMDSO ratios of 0, 0.17, 0.53, 0.82 and 1.50), at a constant pressure of 0.12 mbar ($P = P_{O2} + P_{HMDSO}$) . Both normal and 60°

incidence reflection spectra have been displayed in order to emphasize the higher sensitivity of the oblique incidence to changes in the 1200-900 cm^{-1} broad band.

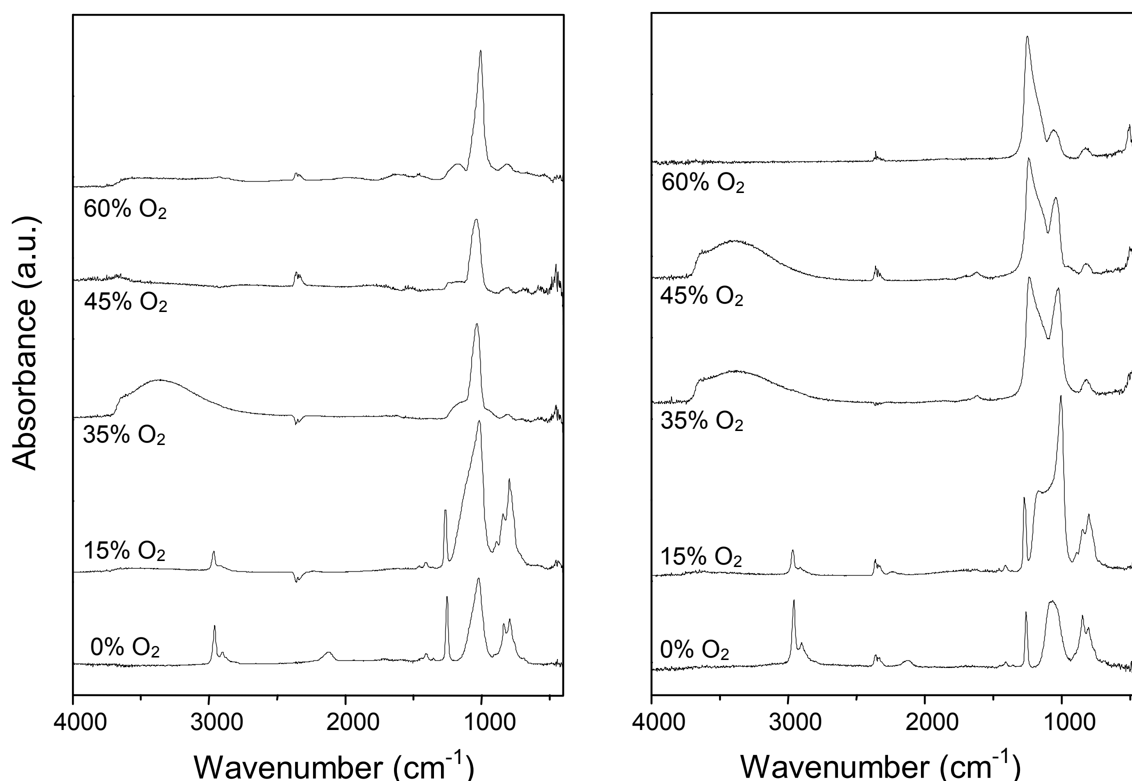

FIGURE 3.15. FTIR spectra of films prepared with increasing oxygen content in the plasma gas. **(LEFT)** Reflection at normal incidence, **(RIGHT)** reflection at 60º incidence.

From the analysis of the most intense methyl-related peaks (1260 cm-1 and 2960 cm-1) it is clear that no CH_3 bonds are detected beyond 35% of oxygen in the plasma gas and therefore the carbon content of the film must be significantly reduced although not completely removed. The spectrum obtained at 60% oxygen is of special interest: its three distinctive absorption bands correspond to different Si–O vibrational modes[133]. The band approximately 820 cm^{-1} is associated to the symmetrical stretching mode of the Si–O–Si bond; the double band at higher wavenumbers (a prominent peak at 1010 cm^{-1} and an adjacent shoulder at 1180 cm^{-1}) corresponds to the asymmetrical stretch of the same bond. Two general trends in SiOx films grown by PECVD from diverse monomers (TEOS, HMDSO) have been reported: first, the more defined the shoulder appearing at 1180 cm^{-1} ;the more stoichiometric (SiO_x, with x~2) the deposited oxides are; and secondly, that a narrow

width of the peak at 1010 cm^{-1} is also related to quasi-stoichiometric SiO_2 films [134]. Consequently, according to these spectra, films obtained from gas mixtures with oxygen relative concentrations over 60% are expected to have properties similar to those of SiO_2 films. As in the case of ppHMDSO films from pure monomer deposited in the monomer-deficient regime, some samples present an additional broad absorption band in the range 3400-3650 cm^{-1}, corresponding to OH bonds. This bond is supposed to play a role in Si-O bond formation by condensation of adjacent Si-OH bonds [152].

Figure 3.16 shows the FTIR spectra of films prepared with 0, 45 and 60% of oxygen. The spectrum of SiO_2 has been overlapped in red to each of the SiOx-like films. It is clear that the stoichiometry of the last film (60% O_2) is almost identical to that of fused silica, at least as far as EDX can detect. Surprisingly, even the film at 45% of oxygen content is close to the EDX signal generated by a fused silica sample.

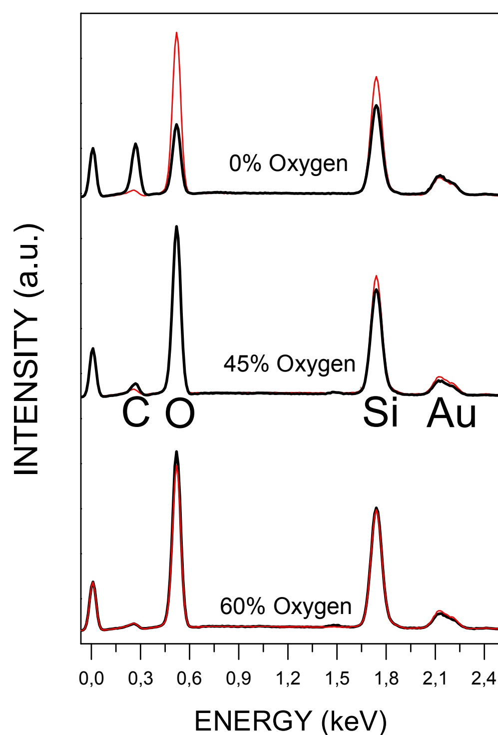

FIGURE 3.16. EDX spectra for samples deposited at 0%, 45% and 60% of oxygen content. The signal corresponding to a fused silica sample has been overlapped in red to aid in the comparison.

The chemical analysis by FTIR and EDX strongly supported the conclusion that the addition of oxygen to the precursor mixture leads to silica-like films already at 45%-

60% of oxygen content. In order to confirm the chemical analysis, ellipsometric measurements were made for the films grown at 15, 35 and 45% of oxygen. The stoichiometry of the films was derived by means of a simple calculation based on the results obtained from ellipsometry(10). As a general rule, the quality of the fitted model is defined by the estimator ξ; the closer to unity, the better the quality of the fit.

Figure 3.17 shows the measured ellipsometric angles Ψ and Δ along with the best fit obtained with the proposed model. Table 3.3 displays the best fitted volume fractions for three different samples. The corresponding value of ξ^2 is also included. The resulting stoichiometries confirm that the higher the oxygen content in the precursor feed the closer the stoichiometry mimics that of SiO_2. Fig 3.17 also shows the simulation obtained for a pure a-SiO_2 film on Al, whose optical behavior is very similar to that of a film obtained from 45% oxygen.

O_2/O_2+HMDSO	χ^2	**SiO_2 content**	**SiO content**	**H_2O content**	**Void**	**Formula**
15 %	1.21	50%	43%	5%	2%	$SiO_{1.53}$:C:H
35 %	1.09	58%	27.6%	10%	4.4%	$SiO_{1.68}$:C:H
45 %	1.04	91%	9%	0%	0%	$SiO_{1.91}$:C:H

TABLE 3.3. Estimated composition of the films after fitting ellipsometric measurements. The film at 45% oxygen content shows an almost perfect fit with a pure a-SiO2 film.

(10) The measured ellipsometric data were fitted by assumig a simple model: the optical behavior of the samples cam be compared with that of a system consisting of a thin layer deposited onto a semiinfinite substrate. After measuring the ellipsometric angles ψ and Δ, the optical response of the films was simulated using the Bruggeman effective medium approximation for a mixture of SiO_2, SiO and H_2O, with certain volumic fraction. A void fraction was also included in the model to account for the porosity of the film. As a substrate for this simulated system, the measured dielectric function of an Al evaporated film similar to the samples was used. A fitting procedure based on the least-squared method and the quality of the film given by an statistical estimator was conducted. Further details can be found in [134]

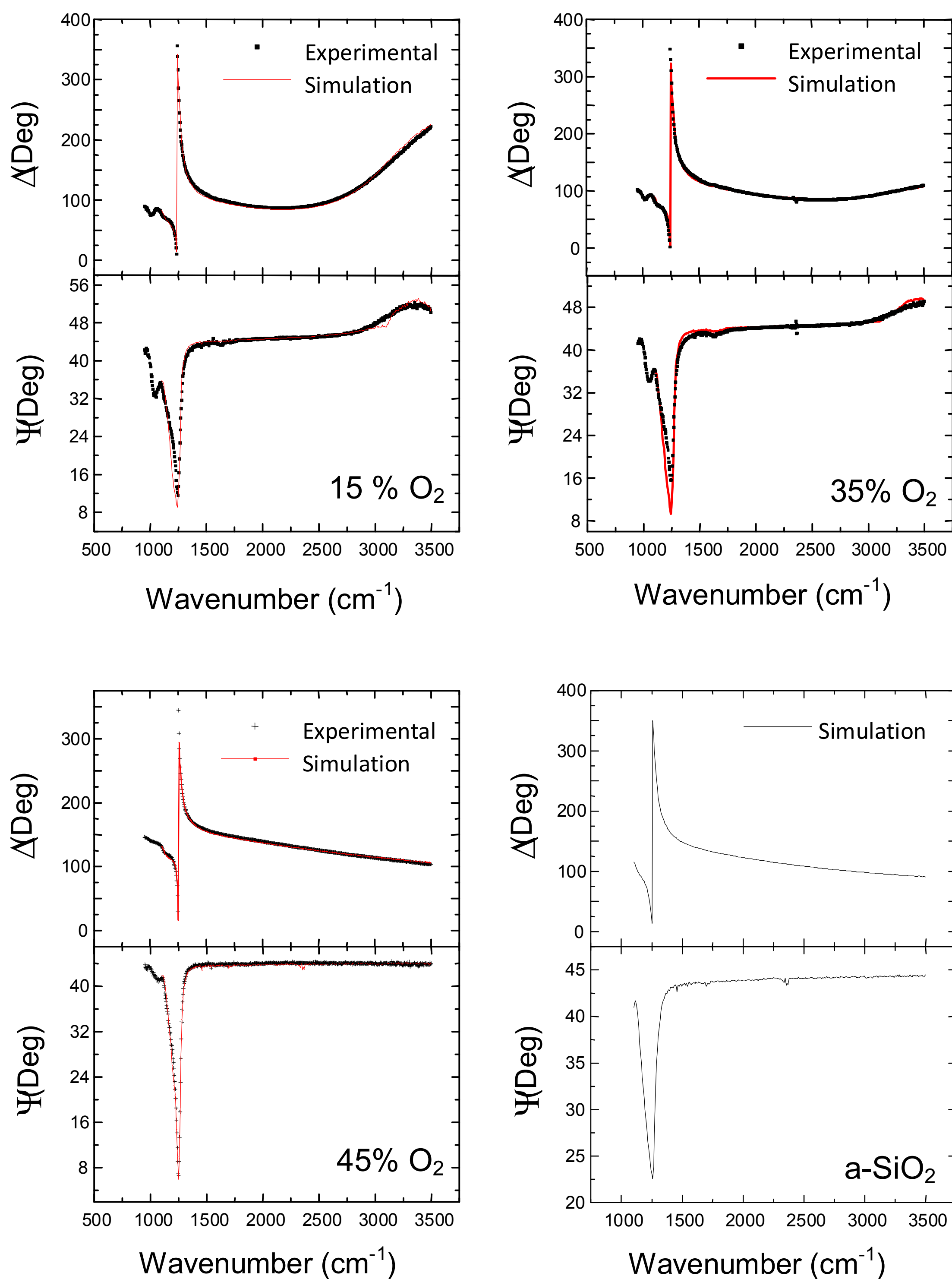

FIGURE 3.17. Measured ellipsometric angles Ψ and Δ for films deposited from 15% **(TOP LEFT)**, 35% **(TOP RIGHT)**, and 45% **(BOTTOM LEFT)** of oxygen in the gas feed. The additional plot corresponds to a simulation of an a-SiO2 film on Al **(BOTTOM RIGHT)**. The calculated best fits are superimposed to the experimental data..

Therefore, in light of the data gathered by three different methods, we can conclude that SiO_x-like films with structure and composition close to that of fused silica can be otained by PECVD of O_2:HMDSO mixtures in our DC reactor. The required oxygen proportions are much lower than those reported in the literature for RF or MW reactors [153].

3.2.3. Functional properties of ppHMDSO films

Functional properties of all polymer-like and silica-like films were characterized aiming at possible applications: mechanical properties were sought for scratch-protection and increased hardness; optical properties such as high transmittance in the visible for cosmetic application of the coatings without changing the appearance of the coated parts; surface energy was analyzed aiming at hydrophobic or hydrophilic behavior, depending on the deposition parameters. Finally, the thermal and chemical stability of the films was also tested.

Mechanical characterization: hardness and elastic recovery

The characterization of mechanical properties of the films indicates that for all plasma polymerized films the elastic modulus and hardness values are higher than conventional PDMS. Hardness values for films from pure monomer range from 800 MPa to 1.3 GPa, and Young's modulus reach 10-16 GPa, as compared to 100-150 MPa and 20-100 MPa for hardness and elastic modulus for PDMS.

Addition of carrier gases result in increased values for hardness, with oxygen containing precursor mixtures producing the best results with hardness values up to 6.6 GPa; at an oxygen:monomer ratio of 3:2 the properties of the deposited films are already close to those of fused silica. Surprisingly, this ratio is lower than those reported in the literature for RF or MW plasmas, which is probably due to the higher ion bombardment on the growing films achieved in DC plasmas.

Figure 3.18. shows the Berkovic indenter load-unload displacement curves for five different representative samples: a medium-density ppHMDSO film, a film deposited with the addition of 50% of N_2 to the precursor mixture, two SiOx-like films deposited at 35% and 45% of oxygen in the precursor mixture, and a fused silica calibrator. The

nitrogen-containing sample is added as a comparison, since a certain improvement in hardness is also achieved by N_2 addition, but to a lesser extent than O_2.

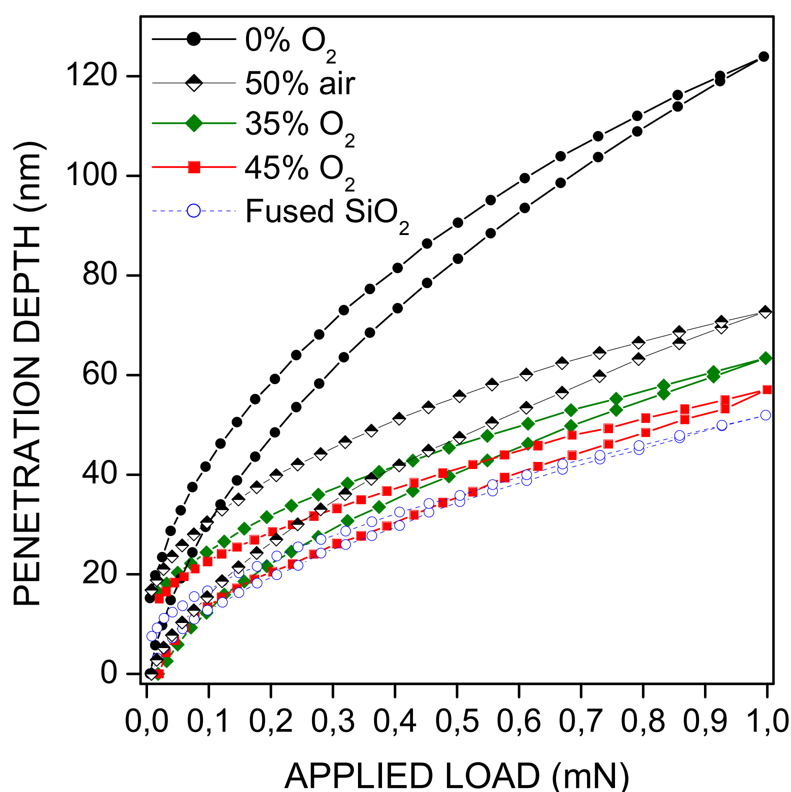

FIGURE 3.18. Berkovic indenter Load-unload displacement curves for samples deposited with the addition of O_2 and N_2 as carrier gases. The curves for ppHMDSO from pure monomer and a fused silica calibrator are also included.

Optical characterization: refractive index and absorption

Characterization of optical properties was conducted in the visible spectrum. The refractive index varies between 1.4 and 1.6 depending on the carbon content and the density and porosity of the films. For films deposited with addition of oxygen the values of the refractive index are close to those of fused silica, in the range 1.45-1.48. But more interesting for the applicability of the films to cosmetic applications is the absorption coefficient. Figure 3.19 shows the absorption coefficient in the visible range for films deposited with and without the addition of carrier gases. The yellowish color of films deposited from N_2 containing mixtures is revealed as an increase in the deep-blue region of the spectrum. On the other hand, addition of

oxygen seems to produce the most transparent film, whereas the addition of Ar results in the same absorbance as for films from pure monomer.

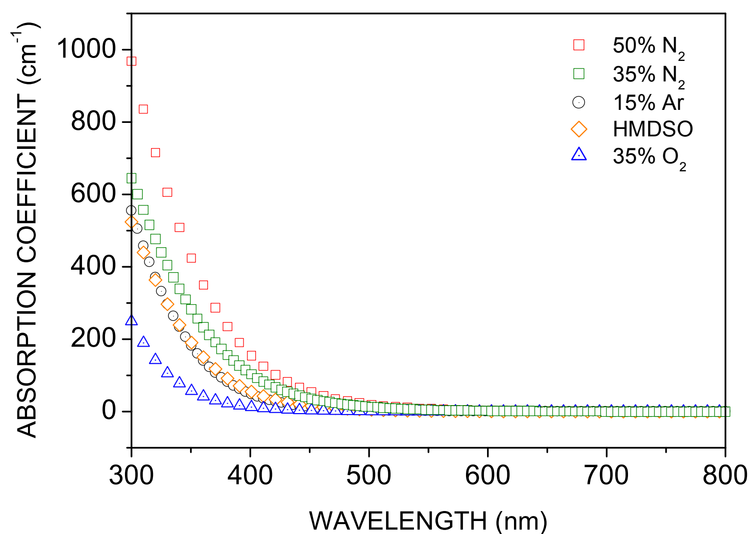

FIGURE 3.19. Absorption coefficient in the near-UV/VIS calculated from the envelopes of the interference fringes in reflectance mode .

Water contact angle

Characterization of the surface energy may be an important issue when dealing with corrosion protection, biocompatible or optical-quality coatings. For these applications, different requirements must be met, from highly hydrophobic to hydrophilic (haze droplet preventing).

Figure 3.20 shows cross-sectional views of water drops on a ppHMDSO film from pure monomer (LEFT) and with the addition of 60% oxygen (RIGHT). Values for the contact angle range from 110° for films deposited from pure monomer to 35° for films deposited at high oxygen concentrations. The likely mechanism for increased wettability is that the addition of oxygen creates silanol groups at the surface, which increases the polar component of the surface energy until de contact angle is reduced to 30-35° for the most oxidized films.

It is also worth mentioning that films showing some optical scattering (and therefore globular structures on the surface) produce contact angles as high as 140°, which is probably due to the effect of surface roughness, which acts as an

enhancement of the hydrophobic properties of the material by reducing the effective contact surface of the droplet.

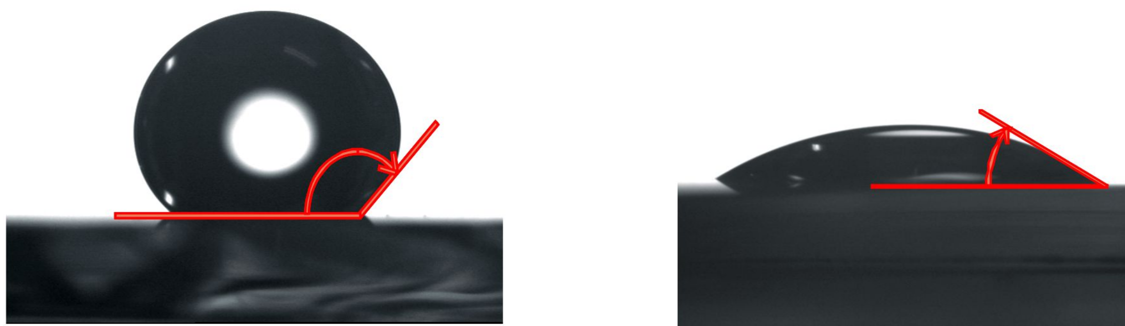

Figure 3.20. Drop-shape analyzer images showing a highly hydrophobic surface **(LEFT)** deposited from pure HMDSO, and a hydrophilic surface **(RIGHT)** generated by addition of oxygen to the precursor mixture.

Aging, thermal stability and chemical stability

Finally, characterization of aging, thermal stability and corrosion protection indicate that polymer-like films do not age significantly, are highly stable up to 450°C, and are also resistant to corrosive conditions (KOH and NaOH 1M).

Figure 3.21 shows FTIR spectra of a polymer-like film as-deposited, the same film after 2 years of storage in ambient atmosphere and after baking in vacuum for 125 min. The broad bands at 3200-3600 cm^{-1} correspond to free OH groups that can be removed by the action of heat and vacuum, but without affecting the remaining structure. Thus, ppHMDSO films demonstrate good thermal stability and no aging, other than the reversible adsorption of water molecules.

Figure 3.22 shows the result of a simple test for testing corrosion resistance. The time needed for a concentrated solution of KOH (1M) or NaOH (1M) to dissolve a thin film of Aluminum is greatly delayed by the protective effect of a thin film of ppHMDSO of just 80 nm. The dissolution of the films is detected as a sharp increase in the intensity generated by a small solar photocell. Therefore, ppHMDSO films are excellent candidates to enhance the protection of metals in harsh environments.

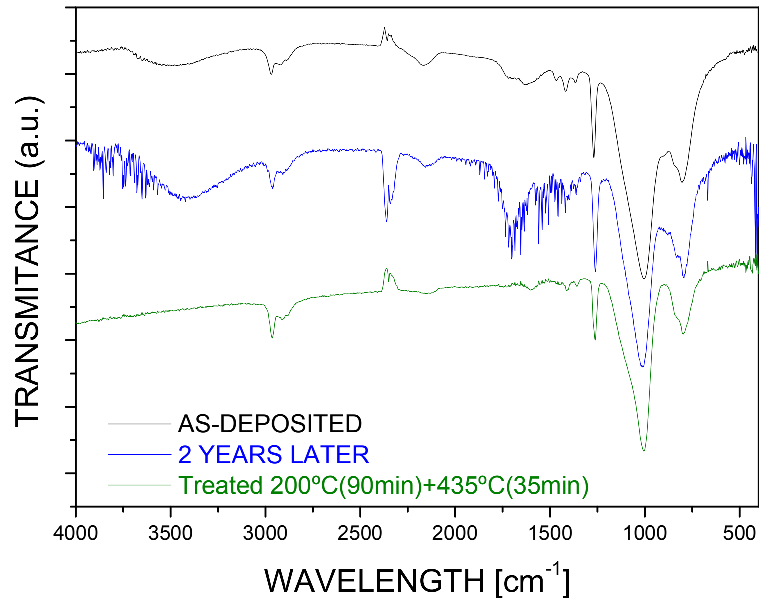

FIGURE 3.21. FTIR spectra showing the same ppHMDSO film as-deposited, 2 years after aging in ambient atmosphere, and after a 125 min heat treatment in vacuum. Increase by aging and removal by baking of the OH absorption bands at 3200-3600 cm^{-1} is revealed.

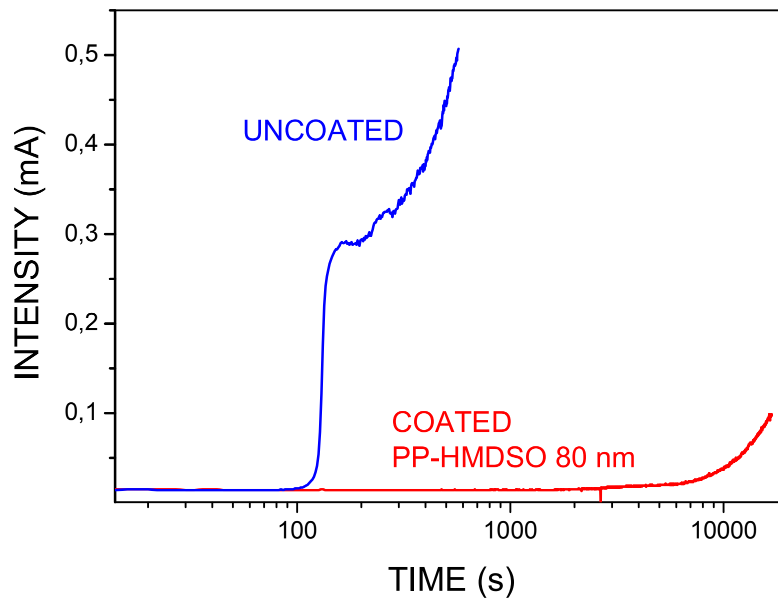

FIGURE 3.22. Corrosion test: the uncoated Alu film is dissolved in NaOH 1M in around 100 s, whereas a thin film of just 80 nm of ppHMDSO delays the corrosion this time by 2 orders of magnitude.

3.3. CONCLUSIONS

- Plasma polymerization of hexamethyldisiloxane can be successfully achieved in a DC plasma reactor provided that the reactor, anode and cathode surfaces are clean in order to avoid arcing. Plasma polymerization in the direct configuration can be sustained up to 60 min if these conditions are met.

- Polymer-like films have been grown to thickness up to 3 μm. Higher thickness may be possible but the plasma is highly instable when the dielectric film grows thick on the electrodes.

- Deposition rates are highly dependent on the composite parameter, Y. Higher values of Y result in higher deposition rates. Deposition rates up to 200 nm/min have been achieved for short deposition times, but these rates decrease with time as the intensity of the glowing plasma is diminished by the isolating film growing on all surfaces.

- Conformal films are achieved more easily at higher pressures, where the mean free-path of the molecules is smaller and the gas behaves like a fluid.

- Uniform films with static substrates are achieved more easily at lower pressures, where the mean-free path of the molecules is higher and the interactions in the gas phase smaller.

- Loss of transparency with a characteristic milky appearance is produced by scattering of globular like structures incorporated in the growing film. This can happen due to ultra-fast polymerization rates in the energy-deficient regime and at higher pressures. The same effect is observed when local glows are generated near the substrates due to arcing or plasma instability. At very high pressures and high powers, powders can be generated in the gas phase.

- The properties of DC ppHMDSO thin films are dependent on many different operational parameters (pressure, residence time of molecules, deposition time, starting gas mixture composition, power, electrodes surface area, geometry, substrate location) but the most important parameter is the composite parameter, $Y=W/(M*F)$, which relates de energy available per monomer molecule, and allows to define three regimes: monomer-deficient regime, transition-regime and energy-deficient regime

- The character of the films may be varied from polymer-like to inorganic-like by varying the composite parameter and the relative amount of oxygen in the precursor mixture. Polymer-like films with high C/Si and low O/Si ratios are mainly produced in the energy-deficient regime and at low oxygen concentrations; inorganic-like films with low C/Si and high O/Si rations are obtained in the monomer-deficient regime and at high oxygen concentrations.

- The addition of oxygen results in the deposition of silica-like films in any regime, but it is more efficient in the high energy regime. Silica-like films can be obtained at oxygen/monomer ratios of 1.0 - 1.5, but they can only be grown up to 300 nm in thickness.

- Inorganic films grown at high Y values are generated by cleavage of organic groups, which can be produced in the gas phase or by ion/solid interaction, due to ion-bombardment during film growth.

- When the cleavage of organic groups and high fragmentation of the monomer are produced already in the gas phase by electron impact or charge exchange, inorganic films will develop independently of the location of the substrate. Films with inorganic-like properties can be also obtained by locating the substrates in high ion bombardment locations, especially at or in proximity to the cathode.

- In the monomer deficient regime, monomer molecules are highly fragmented. Films grown in the monomer deficient region have lower organic content, hence their refractive index is lower, their hardness and elastic modulus higher.

CHAPTER 4

PLASMA TREATMENT OF ppHMDSO FILMS

4.1. INTRODUCTION AND OBJECTIVES

In Chapter 3, it has been shown that the stoichiometry and structure of ppHMDSO films may be varied from a polymer-like ($SiO_xC_yH_z$, also named organic-like film due to the high content of C and H) to a silica-like film (SiO_x almost C-free) by adding an adequate amount of O_2 to the precursor mixture in the plasma. The structural and stoichiometric differences of the organic-like and silica-like films also result in different values for most functional properties.

For certain applications, a combination of functional properties may be required which cannot be provided by a single homogeneous film, but only by a graded film (a film with properties varying along its depth) or by a multilayer coating.(11) For example, in order to produce a scratch protective hard coating onto a plastic substrate, a graded layer could be prepared with a softer polymer-like structure at the film/substrate interface and a harder denser silica-like structure at the surface. This would create a smooth transition from the properties of the soft plastic substrate to those of a glass-like scratch-resistant surface, which would result in a lower stress to the film, a better adhesion to the substrate and a lower damage to the plastic part by ion bombardment.

Some publications suggest an effective way to produce a graded film and to tune its structure and functional properties[154–156] (e.g. Figure 4.1). The method consists in slowly varying the proportion of HMDSO and O_2 during the growth time of the

(11) Graded films are generated from a starting mixture of precursors by varying one or more of the plasma parameters during the deposition time, including the ratio of gas precursors in the mixture. Multilayer films would be achieved by changing, in addition to any of the parameters, at least one of the chemical components of the precursor mixture, so that the elementary composition is different between layers.

deposit, usually by starting with a flux of pure HMDSO and ending with a large amount of oxygen. This would require an accurate control of the rate of change for the gas flux for each gas. While this is a very effective method to obtain a graded film, for a manually-driven gas control such procedure is almost impossible in a reproducible manner.

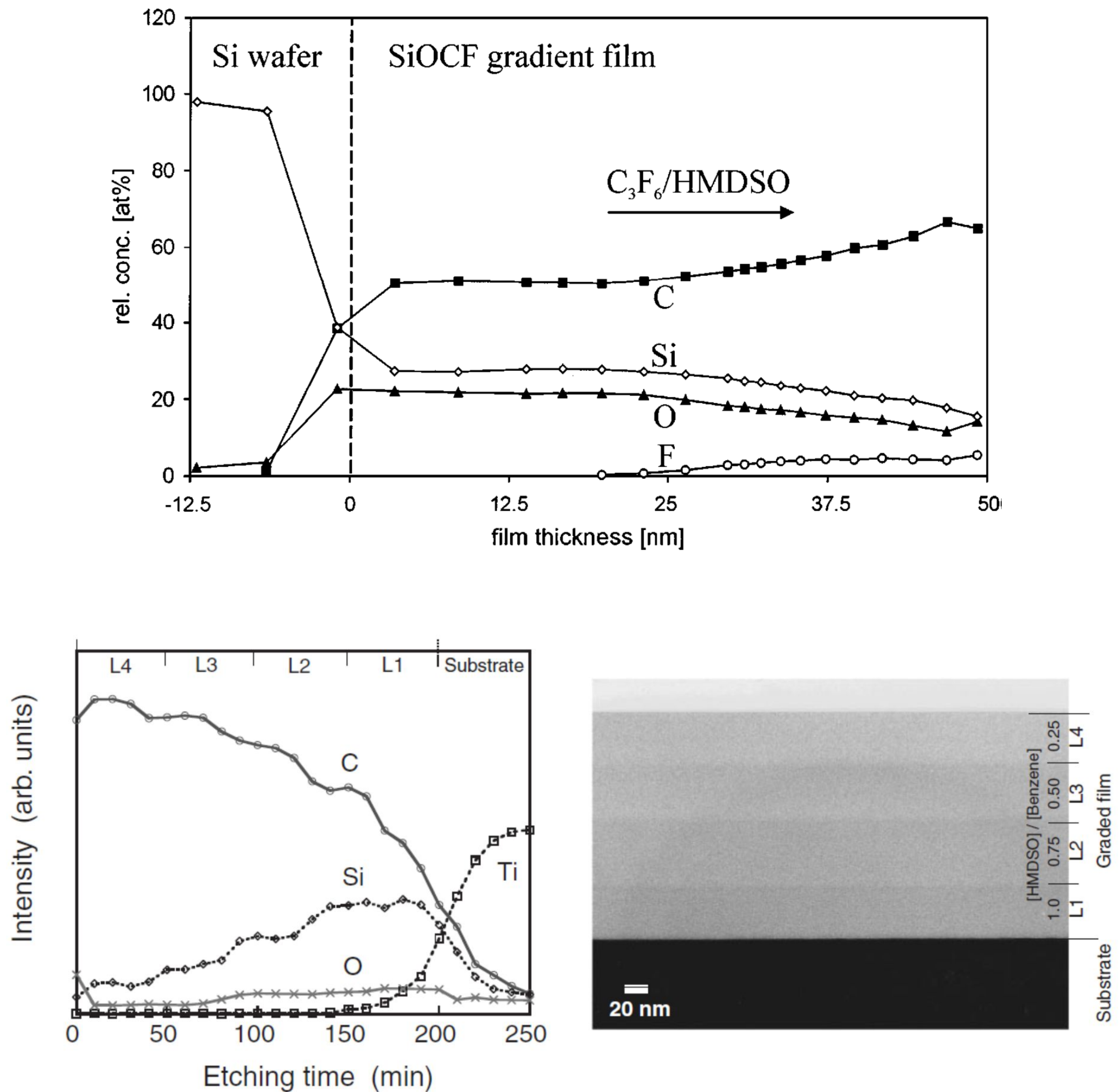

FIGURE 4.1. (TOP) Example of a graded film grown on a Si wafer from an HMDSO/C_3F_6 precursor mixture where the elemental composition varies with depth (from Ref. [155]). **(BOTTOM)** Example of a graded film grown from an HMDSO/Benzene mixture, aiming at a DLC/SiOxCyHz transition to release internal stress and improve adhesion (from Ref. [156]). In both cases, the variation of stoichiometry with depth can be assessed by XPS or, much less often, by TEM.

The surface of any polymer can be modified by treatment in different plasmas, and specifically in an O_2 plasma.[16] A ppHMDSO film can be considered also as a type of polymer substrate, but a denser one and with a higher degree of cross-linking than its conventional counterpart, polydimethylsiloxane (PDMS). Therefore, in principle, the same approach used to modify the surface of a bulk polymer could be employed to modify a thin film polymer. But rather than trying to control the relative concentrations of gases in the precursor mixture, for certain applications it may be sufficient and more convenient to first deposit a polymer-like film from 100% HMDSO or HMDSO/Ar mixtures and to effect an ulterior surface modification by a post-treatment in an O_2 plasma. A graded film is thus also obtained with a similar functionality as in the first method. This is especially useful when the required enhanced property is only a surface property, for example in the case of wettability, which only depends on the very first few nanometers at and under the surface. It may also be the best choice for systems without an automated control of gas inlets to generate a varying mixture of gas over time in a reproducible way. Finally, it may also be advantageous for remote plasma systems and for DC plasma systems, since the deposition rate for SiO_x films may be much smaller than for ppHMDSO, and therefore it may be more efficient to deposit a thicker polymer-like film and post-treat it afterwards.

While there is a certain corpus of publications devoted to the plasma modification of polymers by bombardment of energetic species, the amount of bibliography dedicated to the plasma post-treatment of plasma-polymerized organosilicon films is very limited.[133,136,152,157–163] In the latter case, the higher density and higher degree of cross-linking of plasma polymers can account for important differences in the penetration of the treatment, but also in the recovery during aging of the original properties of the surface prior to the plasma treatment. A more complete explanation about these differences will be left for discussion later on in this chapter.

It is the aim of this Chapter to report the results and discussion on the modification of ppHMDSO films by plasma post-treatment, which was for the first time published in our original work "*Improvement of Hardness in plasma polymerized hexamethyldisiloxane coatings by silica-like surface modification*" and only preceded by a related work on the plasma post-treatment of a different organosilicon film

(tetraethoxysilane, TEOS), by Vallée and colleagues.[163] A second publication from our group, in cooperation with R. Clergeraux and his plasma processing group, entitled "*Comparison between continuous and microwave oxygen plasma post-treatment on organosilicon plasma deposited layers: Effects on structure and properties*"[136] included further studies on the post-treatment of ppHMDSO with different plasma sources.

Based on our extended experimental results and on the available bibliography generated since our first report, we will try to answer five important questions:

1) What is the depth of the modified region and how does it depend on different parameters: time of treatment, plasma pressure, type of gas, plasma frequency (DC/RF), substrate position and starting film density.
2) What is the chemical composition of the modified region (stoichiometry and chemical structure) and its dependence on the same parameters.
3) How is the modification effected: physico-chemical mechanisms.
4) What are the functional properties of the resulting graded films, as compared to the untreated ones: water contact angle, hardness, refraction index.
5) How do functional properties change in time and how much recovery of the initial surface energy can be expected for a post-treated plasma-polymerized film after a certain elapsed time (the so-called 'hydrophobic recovery').(12)

4.2. METHODOLOGY

4.2.1. Preparation and choice of samples

In order to study the plasma post-treatment process, ppHMDSO films with medium thickness, e.g. 150 – 600 nm, are the preferred choice, because the effect of the modified region may be detected more easily by the different characterization techniques. If a thinner film is selected (e.g. 50 nm) the modified region could easily reach the interface with the substrate and the effect of different parameters on the thickness of the modified region could rapidly saturate. If a much thicker film is selected (e.g. >1000 nm) the sensitivity to detect the contribution of a modified region of just 50 nm, for example, would decrease for certain techniques, such as

(12) In polymer industries, this and other time-dependent effects such as creeping are usually referred as with the expression 'polymers are alive'.

normal incidence reflection FT-IR spectroscopy,[133] which gathers signal from the complete thickness,(13) thus minimizing the influence of the modified region in the overall spectrum (see Figure 4.2).

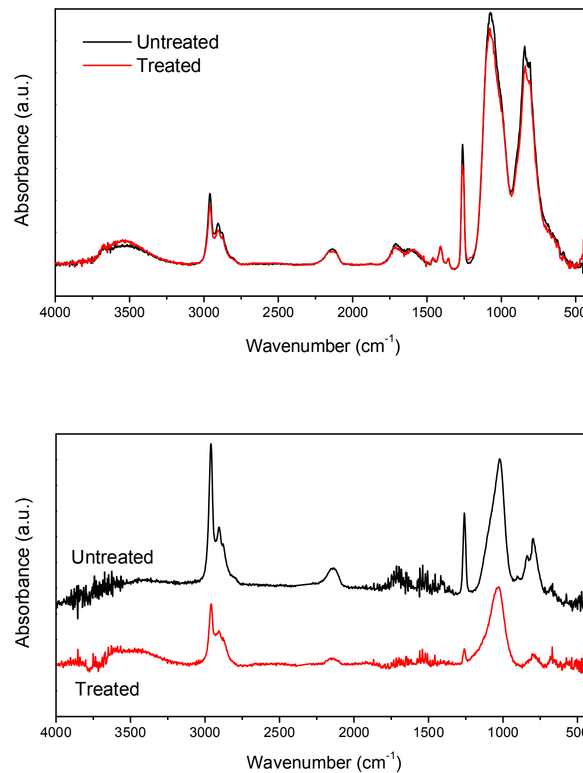

FIGURE 4.2. (TOP) A 1500 nm plasma-polymerized film treated for 20 min in an oxygen plasma reveals a very small change in the FT-IR reflection spectrum, at normal incidence. (BOTTOM). In contrast, the same treatment generates a clear change in a 400 nm thick film at at 45° incidence.

In addition to the absolute thickness of the samples selected for post-treatment, additional precautions must be foreseen due to the fact that in this two-step process (film deposition + plasma post-treatment) we would like to analyze ideally only those differences which could be attributed to the technological parameters related to the plasma post-treatments, but not to any pre-existing variations between untreated samples, ensuring that only one parameter in the post-treatment is varied at a time. Therefore, special care must be taken to select untreated samples which are as similar as possible between them prior to plasma post-treatment. Whenever possible, this was achieved by placing several substrates within the plasma reactor in equivalent positions, or, alternatively, by cutting larger substrates into smaller pieces,

(13) This limitation would be overcome by the use of ATR FT-IR, but this technique was not available during most of the experimental development of this thesis.

in order to apply different post-treatments to the resulting replicas. In the first case, it was necessary to ensure that the reactor-dependent 'hydrodynamic factor' and the transport of reactive species did not induce different growth rates on different substrates within the same plasma batch; in the second case, we needed to guarantee adequate thickness homogeneity throughout the film, e.g. less than 10% variation (Figure 4.3).

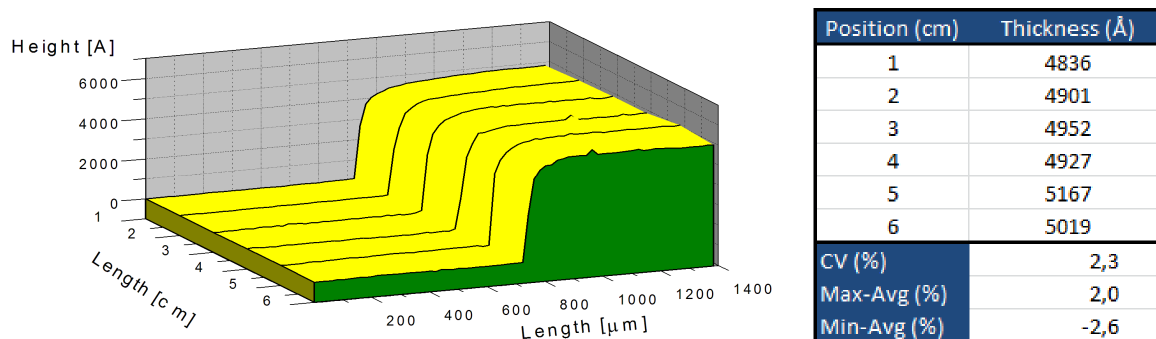

Position (cm)	Thickness (Å)
1	4836
2	4901
3	4952
4	4927
5	5167
6	5019
CV (%)	2,3
Max-Avg (%)	2,0
Min-Avg (%)	-2,6

FIGURE 4.3. Thickness homogeneity of a 500 nm ppHMDSO film deposited on a glass slide. Different measurements with mechanical profilometry across a step produced on the film along the main length of the substrate indicate good homogeneity (less than 3% CV) within at least 60 mm. Such a sample is a good candidate to be cut into several smaller pieces in order to apply different post-treatments and to study the effect of the variation of a given plasma parameter.

Finally, in order to control the density of the films to obtain reproducible results, we prepared ppHMDSO films with low, medium and high densities by adapting the necessary plasma parameters as derived from our previous experience in ppHMDSO deposition (see Chapter 2), as follows:

- *Low Density samples*: 1.21-1.32 g/cm^3, deposited in the energy-deficient regime, with $SiO_{0.66}C_{1.94}$:H average stoichiometry. ~400-500 nm thick films were grown on Al-coated glass substrates and Si wafers placed in the afterglow region of the plasma (remote plasma deposition 2 cm below from the boundary defined by the electrode projection) at high pressure (0.3 mbar) and high monomer flow (45 sccm), in a parallel plate DC plasma with 15 cm distance between electrodes, during 8 min of plasma polymerization.
- *Medium Density samples*: 1.43-1.51 g/cm^3, deposited in the energy/monomer competitive regime, with $SiO_{078}C_{1.67}$:H average stoichiometry. ~400-500 nm thick films deposited within the glow discharge on Al-coated glass substrates

and Si wafers placed at the anode, 15 cm apart from the cathode, in a parallel plate DC plasma at medium monomer flow (15 sccm) and medium pressure (0.1 mbar), during 10 min of plasma polymerization.

- *High Density samples*: 1.62-1.75 g/cm^3, deposited in the monomer-deficient regime, with $SiO_{0.96}C_{1.38}$:H average stoichiometry. ~400-500 nm thick films deposited within the glow discharge on Al-coated substrates and Si wafers placed at the anode 10 cm apart from the cathode in a parallel plate DC 50% Ar/50% HMDSO plasma at low flow (4 sccm) and low pressure (0.06 mbar), during 24 min of plasma polymerization.

All the post-treatments were effected by placing the samples in the same locations where they were deposited, even when the reactor was opened between the plasma deposition and the plasma post-treatment to cut the samples or to remove part of them in order to apply different treatment conditions.

4.2.2. Choice of substrates

Substrate choice has a small effect on the properties of the growing film itself, but has some implications with regards to the available characterization techniques: size limitations apply for FT-IR reflectance at oblique incidence in our Nicolette spectrophotometer without ATR, and can only be performed on large size substrates such as microscope glass slides with the oblique incidence reflectance accessory; in XPS and in SEM-EDX, different charge build-up may develop due to different substrate conductivities, which can result in necessary corrections of the spectra or different current settings for the electron probe, respectively; hardness as measured by Nanoindentation is modified by the substrate if the penetration depth is more than 1/10th of the total film thickness;[47] DSA is the only technique with no technical limitations with respect to the choice of substrate.

Therefore, all plasma polymerized films for ulterior plasma modification have been deposited on two different types of substrates to facilitate their characterization: Al-coated glass slides and intrinsic Si wafers.(14) For the study of hydrophobic recovery, 1mm-thick PDMS substrates have also been employed.

(14) The substrates were prepared as described in Chapter 2: microscope glass slides were cleaned in detergent with an abrasive brush, rinsed in an ultrasonic bath with trichlorethylene, acetone and methanol successively, rinsed again in two different recipients with deionized water, dried out with N_2 and coated with an 80 nm film of

4.2.3. Technological parameters

The following technological parameters have been varied and their effect on the induced modifications has been studied:

- Type of gas,
- Post-treatment time,
- Plasma Pressure,
- Substrate position and orientation within the plasma,
- Discharge-associated parameters:
    - plasma source frequency (DC, RF, MW),
    - plasma power (in RF and MW),

4.2.4. Characterization techniques

Literature about the study of plasma treatment of bulk polymers is abundant and states that the depth of the modified thickness could be easily within 100-200 nm for moderate time/intensity treatments and up to 2μm for lengthier treatments.[164] Since plasma-polymerized films have a higher degree of cross-linking and density, in principle it is expected that the penetration of ions would be lower and the diffusion of reactive species slower than for bulk polymers. As a consequence, an expected rough estimation of the modified thickness could be anything around 1 or 2 orders of magnitude smaller for plasma polymers than for conventional polymers for similar plasma treatment conditions.

In chemical cross-linking and also in plasma treatment of conventional polymers, the main 'chemical' technique used for determination of the modified crosslinked thickness is gel fraction analysis.[9,165] This technique relies in finding a suitable solvent for the polymer backbone. If such a solvent exists, the sample is dissolved, filtered, and the insoluble fraction F_{cross} is weighed; the ratio between the sample prior and after solubilization is then calculated and multiplied by the original thickness of the polymer sample in order to obtain the modified thickness. This classical technique assumes that the nature and extent of the induced modification is constant throughout the modified region, -which could be reasonable for certain

evaporated Al in high vacuum PVD. Si wafers were cleaned alike, but no Al film was evaporated on top. PDMS substrates were not cleaned, but a short Ar plasma pretreatment was used to remove contaminants and activate the surface.

materials and treatment conditions, but does not apply in many cases-; it is also a cumbersome technique and impractical for the modification of ppHMDSO thin films, which are insoluble and have an extremely low weight.

In order to look for the answers to the relevant questions, different analytical techniques have been employed: XPS, TEM, Ellipsometry, FT-IR Spectroscopy Nanoindentation and Drop Shape Analysis. All of them, except for DSA, allow some direct or indirect insight about the thickness of the modified depth, while XPS and FT-IR can add some information about the chemical modifications effected on the surface and subsurface of the film. Nanoindentation and DSA allow an objective characterization of the functional properties, and DSA is sensitive to chemical changes or rearrangements occurring at the surface over time by the hydrophobic recovery mechanism. Detailed explanations about all these techniques may be found in Chapter 2.

4.3. RESULTS AND DISCUSSION

4.3.1. Measurement of the penetration depth of plasma treatment

Our first goal was to assess that the selected characterization techniques were indeed capable of detecting any changes after plasma treatment in ppHMDSO thin films, –since these films are much denser, less porous and have a higher degree of cross-linking than conventional polymers–, and to evaluate the depth of modification after different plasma treatments with varying parameters.

4.3.1.1. Depth of penetration by XPS depth profiling

Figure 4.4 shows an example of an XPS depth profile[(15)] for a 150 nm untreated ppHMDSO sample deposited onto a Si substrate. The evolution with depth for the concentrations of C, O and Si is monitored (H is not detected by XPS). The depth profile shows three distinctive regions: a polymer-like film with constant

[(15)] Depth profiling by XPS allows to measure not only the relative atomic concentrations of atoms at different sputtered depths, but also the neighboring chemical environment in which they are embedded. Therefore, it is the analytical tool employed for depth characterization in almost all prior literature in order to assess the chemical variations within a graded film, and it is also the choice for our study. Other suitable analytical techniques for depth profiling are AES, SIMS, GD-OES or neutron reflectometry, but when the chemical environment of the atoms is also sought, XPS outperforms all the rest.[166]

stoichiometry $SiO_{0.66}C_{1.6}$:H; the film-substrate interface, which is detected as a region with a composition varying from that of the film to that of the substrate; and the Si substrate. It is worth noting that the interface between the ppHMDSO film and the Si substrate seems to be thicker and more gradual than anticipated. This has also been found often in prior literature and is attributed to a technical artifact related to the inability of the ion gun in the XPS analyzer to cleanly etch a sufficiently flat area,(16) which generates a mix up of signals coming from different depths.[50,51] The apparent thickness of the interface generates an additional uncertainty when transforming the sputtering times to sputtering rates or depths. There are three simple methods in order to do so: 1) use theoretical values found in bibliography or tabulated by the instrument manufacturer or related handbooks, 2) employ sufficiently thin films so that the interface between the film and the substrate can be reached in a reasonable number of sputtering steps and the empirical average sputtering rate can be readily calculated as the ratio between the film thickness and the elapsed time, or 3) whenever the film-substrate interface cannot be reached or is not detectable due to the chemical similarities between the film and the substrate, measure the sputtering crater by interferometry or mechanical profilometry and estimate the sputtering rate as in 2).

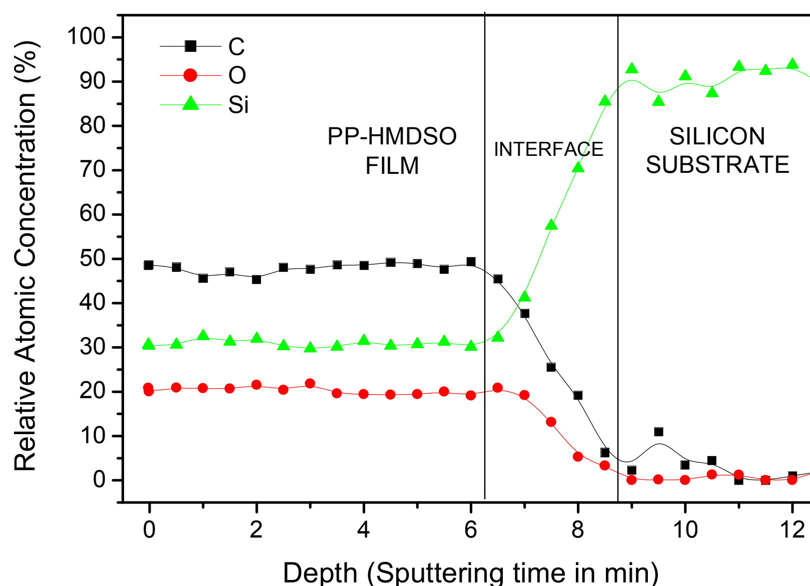

FIGURE 4.4. XPS depth profile for a 150 nm untreated ppHMDSO film deposited onto a Si substrate.Three distinctive regions can be observed which correspond to the ppHMDSO film, the film-substrate interface, and the Si substrate. The x-axis can be transformed from sputtering time to depth by using the empirical time needed for the ion gun to etch the complete film and reach the substrate. In this case, the etch rate would be estimated about

(16) This could be improved by rotating the sample during ion etching to achieve a flat crater [166,167],

We noticed significant differences between the theoretical and empirical rates, depending on the instrument and the density of the films (5 nm/min up to 20 nm/min), and therefore we chose to rely on the empirical approach to calibrate the depth axis. We selected the sputtering point where the concentration is midway between that of the film and that of the substrate as the sputtering time when the film has been completely etched and the substrate has been reached. The sputtering rate thus calculated was 20 nm/min for the film in Figure 4.4, corresponding to complete etching of 150 nm of ppHMDSO in 7.5 min.

Figure 4.5 shows an example of an XPS depth profile prior an after an O_2 DC plasma treatment applied for 4 min at 0.1 mbar on the same sample profiled in Figure 4.4. After plasma treatment, a new region *at* and *below* the surface of the film can be detected where the stoichiometry has been altered significantly. Thus, the XPS depth profile suggests the existence of four main regions instead of three: a chemically modified surface region with a depth of about 40 nm;(17) an inner region of about 80 nm that remains apparently unaffected by the plasma treatment; the film-substrate interface where the detected stoichiometry (not necessarily the real one) changes gradually across 50 nm from that of the film to that of the substrate; and, finally, the Si substrate.

We will focus our interest in the first region, the so-called “modified” region. In this case, the XPS profile shows that the chemical composition at the outermost surface layer of the film is about $SiO_{1.9}C_{0.4}$:H and evolves in about 40 nm to the composition of the original film $SiO_{0.68}C_{1.6}$:H. It is clear that XPS is also a technique for chemical characterization, but the discussion about the chemical changes occurring at the modified region will be left for later on in this chapter. Here XPS is used only to demonstrate how the depth of modification by the plasma treatments can be effectively estimated with this technique. These modifications are easy to detect by XPS depth profiling provided that a minimum change in stoichiometry be involved (such as in an oxidation process). However, the modified zone will not be as easily detected by XPS when only additional cross-linking is generated, with no associated

(17) The criterion used to determine the depth of penetration of the treatment is as follows: the modified area ends where two consecutive sputtering cycles produce a concentration within ±3% of that of the unmodified film, since the imprecision in assigning atomic concentration values can be as high as 2.5%.

change in the relative atomic concentration, as is the case with non-reactive gases such as Ar or N_2.

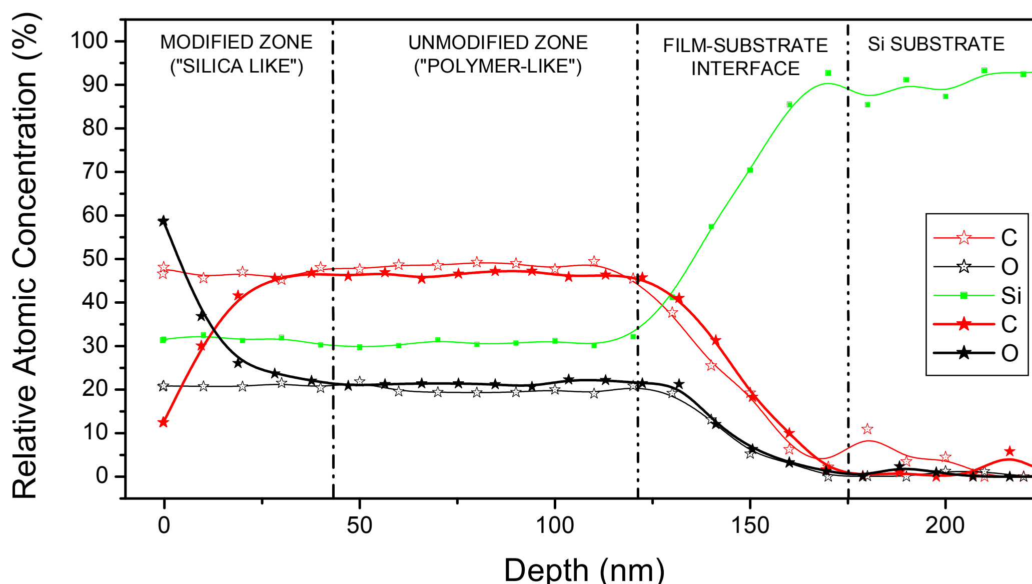

FIGURE 4.5. XPS depth profile for the same film as in Fig 3.4. after 4 min of O_2 DC plasma treatment. A new distinctive region appears at the surface of the film, where the C content is significantly decreased while the O content is increased.The depth profiles of O and C for the untreated film are superimposed as a reference.

4.3.1.2. Depth of penetration by TEM

In order to confirm the existence of a modified region without a clear stoichiometric change, we employed TEM to detect the extent of the modified region in a direct visual way, as first demonstrated by Vallée.[163] Since the transmission of an electron beam through any material is sensitive to density gradients, TEM can be a useful tool to detect if a density change is created by the plasma treatment, either in a reactive or non-reactive gas.

Figure 4.6 shows a cross-sectional image of a 400nm PP-HDMSO film grown onto an Al-coated glass substrate and post-treated with a DC O_2 plasma for 20 min at 0.1 mbar. Five different regions can be distinguished within the cross-sectional view:

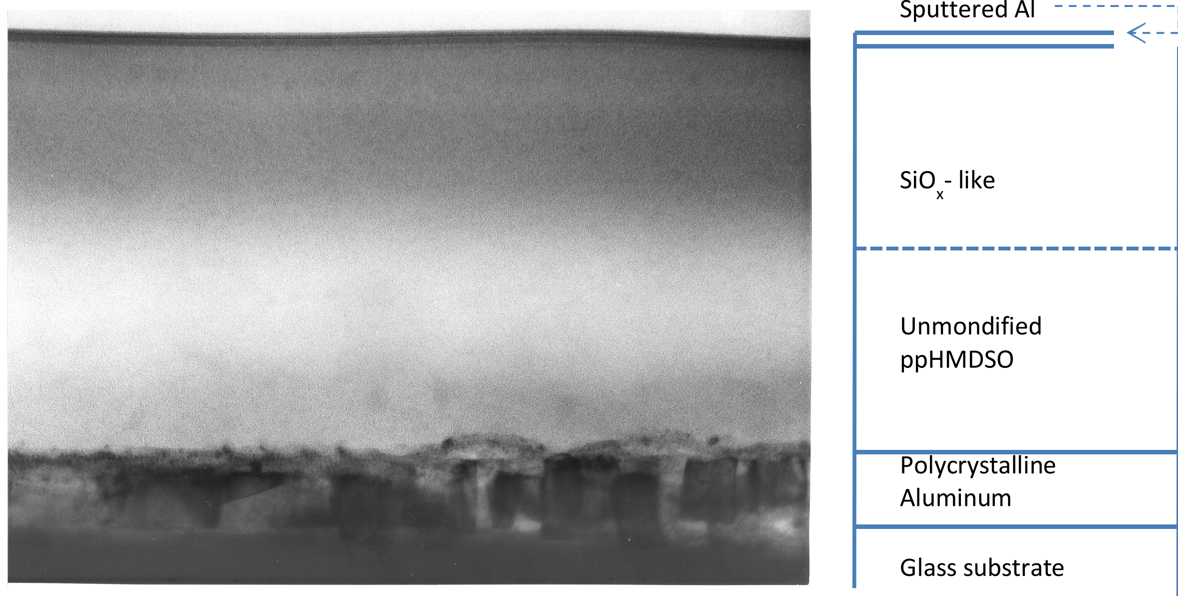

FIGURE 4.6. TEM cross-sectional micrograph for a a 400 nm thick ppHMDSO film deposited onto a PVD Al-coated glass, and post-treated by a DC O_2 plasma for 20 min at 0.1 mbar.

1) A very thin dense layer at the surface of the film, 5-10 nm thick, attributed to Al or Al-oxide sputtered from the cathode and redeposited at the surface of the film during plasma post-treatment.

2) A darker region beneath the surface, up to 120-160 nm, attributed to the oxidized silica-like region, which is an amorphous layer with a higher density than that of the original untreated film.

3) A lighter region, 220-260 nm thick, attributed to the unaffected polymer-like region of the original ppHMDSO film.

4) The Al coating, 50-60 nm thick polycrystalline film evaporated on the substrate.

5) The Glass substrate, with an optical density slightly higher than that of the silica-like region of the film.

According to the micrograph, in this case the modified region could extend up to 160 nm, which seems concordant with the depth predicted from the XPS profile for the same sample (see Figure 4.7). The XPS analysis also confirms the presence of a thin Al-containing layer at the surface, although this is not observed after all plasma treatments.

We believe that it is a protocol-dependent artifact, as the cathodes are always wrapped in an Al envelope to protect them from continued erosion and to avoid the formation of a thick organic coating that would generate arching. Since the process is split in two separate steps[(18)] (plasma polymer deposition and plasma post-treatment), the effect of replacing the Al envelope on the cathode after film deposition and prior to plasma treatment determines whether the source of sputtered material is the organic deposit already generated by plasma polymerization or the Al envelope itself. In the former case, the sputtered material is similar in composition to the ppHMDSO film and therefore indistinguishable; in the latter case a thin Al-containing layer is detected. In addition to this, the sputtered Al layer is only observed when the DC plasma source is used, but not with the RF or MW sources, probably due to the much higher energy of the positive ions impinging on the cathode in a DC discharge. In this case, the composition for the unmodified polymer-like region is within the normal range for ppHMDSO films, $SiO_{0.7}C_{1.5}$, but the stoichiometry at the surface is non-conclusive due to the sputter-deposited Al contaminating layer.

As mentioned before, for plasma treatments with non-reactive gases, XPS does not detect a significant change in stoichiometry and therefore it is not effective in detecting the modified region. Therefore we tried to detect the modified region for Ar plasma treatments by TEM, but the contrast between the modified and unmodified regions seems to be much smaller than for O_2 plasma treatments (Figure 4.8). This may be explained by the fact that cross-linking is already high in ppHMDSO films and non-reactive plasma treatments do not generate a sufficient increase in cross-linking and density in order to produce a stronger contrast by TEM. In this case, whereas XPS depth profiling does not allow to detect the modified depth, TEM suggests a higher density within a modified region below the surface of 40 – 80 nm of thickness, but the lack of contrast does not allow to resolve the penetration depth clearly. It is also important to note that in this case the higher-contrast dense Al layer on top of the polymer film is not observed.

[(18)] The process is splitted so that the thickness of the ppHMDOS film can be measured and the substrates can be cut into several pieces before applying the post-treatment.

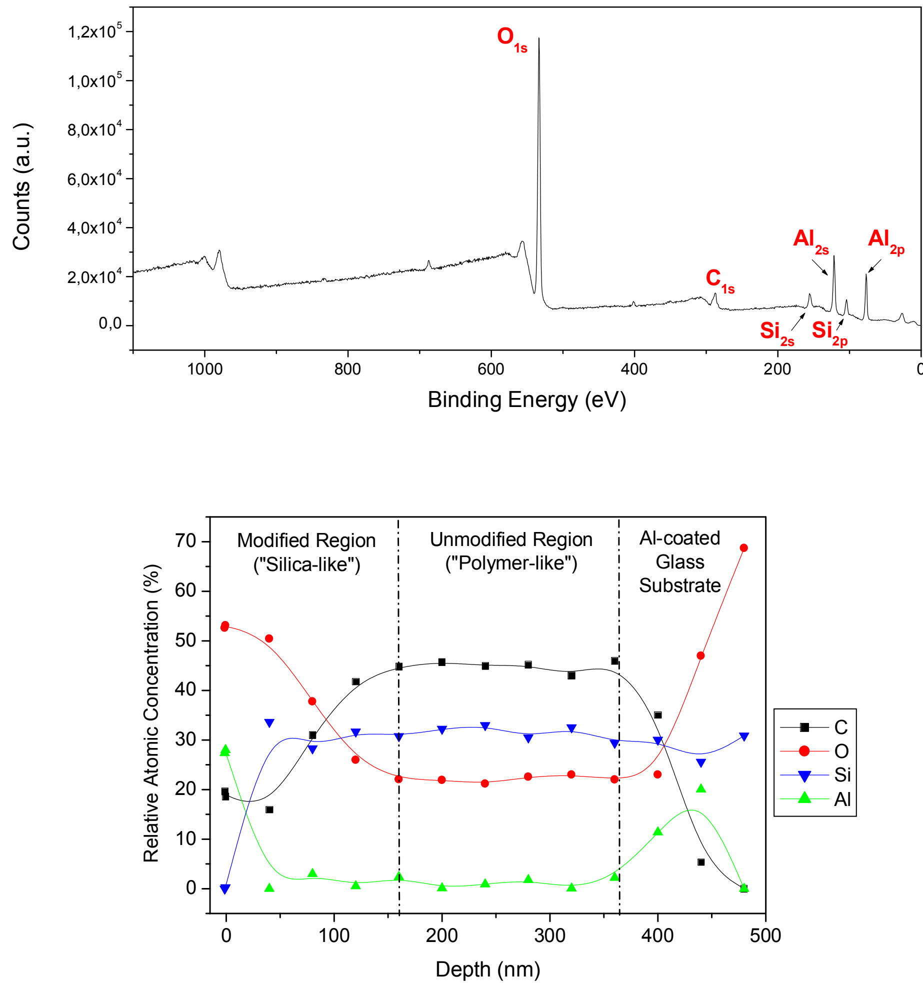

FIGURE 4.7. XPS survey scan of the surface (TOP) and depth profile (BOTTOM) for the same post-treated film as in Figure 4.6. Note the presence of a peak at the surface due to an Al layer sputtered from the cathode, and a second peak due to a different Al film encountered under the ppHMDSO film, which indicates that the sputtering raster has reached the Al-coated glass substrate.

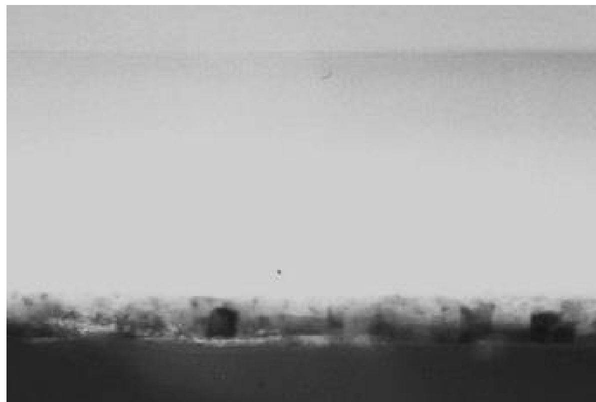

FIGURE 4.8. TEM micrograph for a cross-section of a 400 nm thick ppHMDSO film deposited onto a PVD Al-coated glass, and post-treated in a floating holder by a DC Ar plasma for 20 min at 0.1 mbar.

4.3.1.3. Depth of penetration by indirect techniques: FTIR spectroscopy and ellipsometry

Among the different analytical techniques employed in this study, XPS and TEM are the only ones that allow a direct measurement of the depth of penetration of the plasma treatment, but they both have some limitations, specially for non-reactive plasma treatment, where the main changes are additional cross-linking and a slight change in density. In addition, both XPS and TEM are destructive techniques that may not allow small samples to be re-analyzed by other techniques, and, last but not least, these techniques are time and cost consuming.

There are other non-destructive optical techniques that may allow us to detect the extent of such changes and to estimate the penetration of the plasma treatment, such as ellipsometry and FTIR spectroscopy. They have the advantage of being much faster and cheaper, plus allowing the samples to be reused in further analysis. Their main drawback is that some assumptions are needed to derive the penetration depth, what makes their estimates indirect and only as accurate as the model behind them.

Estimation of penetration depth by FT-IR Spectroscopy

FTIR can be used as to determine the penetration depth of the plasma treatment[152] taking into account that the absorbance at a given wavelength is proportional to the concentration of the absorbing compound (or chemical bond), according to the Beer-Lambert law.[(19)] Although this relationship holds, having a percentage of reduction or increase at a given frequency only means that the concentration of that absorbing bond has varied, but has no necessary direct correlation with the stoichiometry of the film (as XPS does). Figure 4.9 shows the effect of two different plasma treatments (10 and 20 min of O_2 DC plasma treatment) on the FTIR spectra of a 400 nm thick ppHMDSO film, in absorbance units. The corresponding relative absorption values with respect to those of the untreated film for the three most distinctive organic absorption bands of ppHMDSO ($-CH_3$ asymmetric stretching, symmetric bending of $-CH_3$ in $Si-(CH_3)_x$, and Si–H stretching) are calculated and displayed in Table 4.2.

[(19)] There is no consensus in relevant literature on how to display FTIR graphs. Both Transmission vs Wavenumber and Absorbance vs Wavenumber (or Wavelength) are commonly used. For qualitative analysis both choices are equally useful, but only Absorbance can be linearly related to the concentration of the aborbing bond vibrations by the Beer-Lambert law.

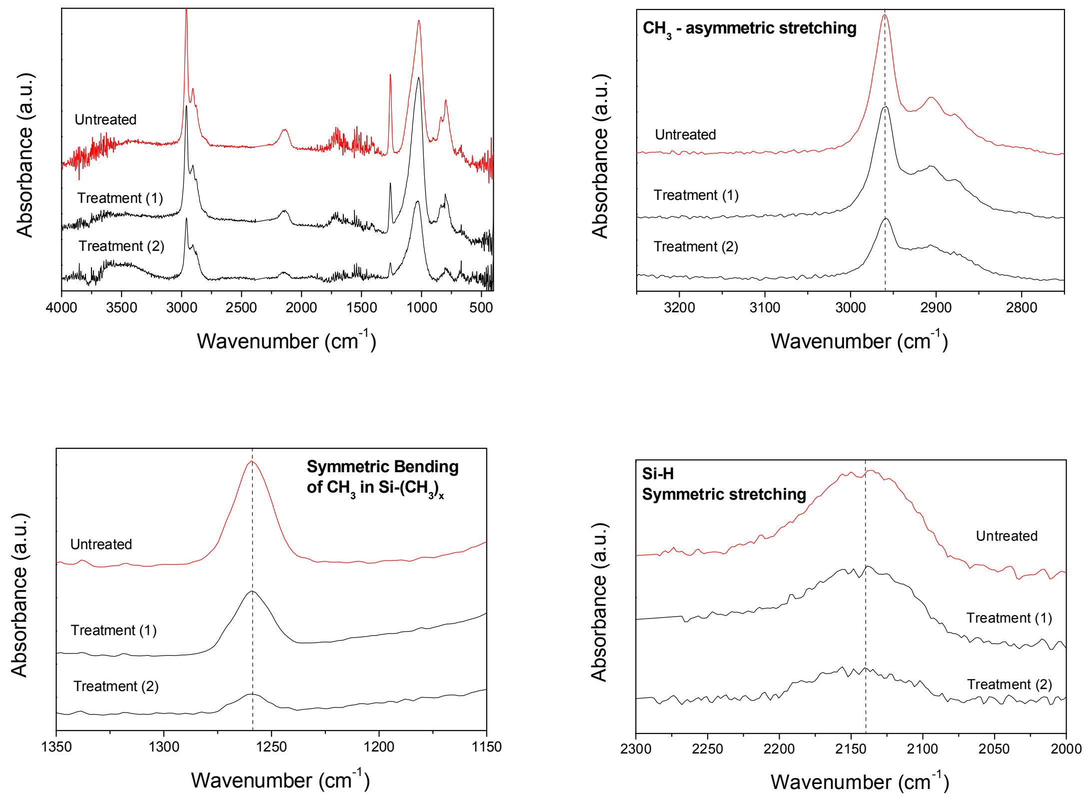

FIGURE 4.9. (TOP LEFT) FTIR reflection spectra of a 400 nm thick ppHMDSO film deposited onto a PVD Al-coated glass, and post-treated by a DC O_2 plasma for 10 min (Treatment 1) and 20 min (Treatment 2) at 0.1 mbar. **(TOP RIGHT)** Detailed zoom of the -CH_3 asymmetric stretching peak centered at 2960 cm^{-1}. **(BOTTOM LEFT)** Detailed zoom of the Si-$(CH_3)_x$ symmetric bending peak centered at 1260 cm^{-1}. **(BOTTOM RIGHT)** Detailed zoom of the Si-H peak centered at 2140 cm^{-1}.

Relative Absorbance (%)			
	@ 1259 cm^{-1}	@ 2135 cm^{-1}	@ 2960 cm^{-1}
Untreated Sample	100,0	100,0	100,0
Treatment I	66,0	72,7	79,0
Treatment II	19,6	32,6	43,5

TABLE 4.2. Relative absorbance for the FTIR peaks plotted in Figure 4.9 with respect to the untreated film.

In order to use FTIR to estimate the penetration depth of the treatment, two previous considerations must be made: first, not all bonds can be indistinctively used, since the amount of change in absorption for different bonds is different –as shown in Table 4.2–, and therefore making estimations based on different peaks would lead to

inconsistent results without taking into account the chemical nature of each specific peak;[20] secondly, if the relative concentrations of the bond absorptions need to be transformed into penetration depths, some assumptions need to be maid about the profile of concentration vs depth. In our case, we have used as an example the relative concentrations calculated for the absorbance of the Si–H bond, which is a terminal bond with relatively easy cleavage and an IR peak which does not overlap with other peaks, to calculate the depth of penetration of the treatment for seven different gradient profiles:

- constant concentration with 100% cleavage,
- constant concentration with 50% cleavage,
- linear increase starting at 100% cleavage,
- exponential increase starting at 100% cleavage for two different rates,
- exponential increase starting at 50% cleavage for two different rates.

Figure 4.10 shows these seven different profiles fitted to match the total concentration of remaining Si-H bonds after 10 min O_2 DC plasma treatment of a 400 nm thick ppHMDSO film, 72.7%, and Table 4.3 shows the penetration depths calculated with each model profile[21] for 10 min and 20 min treatment.

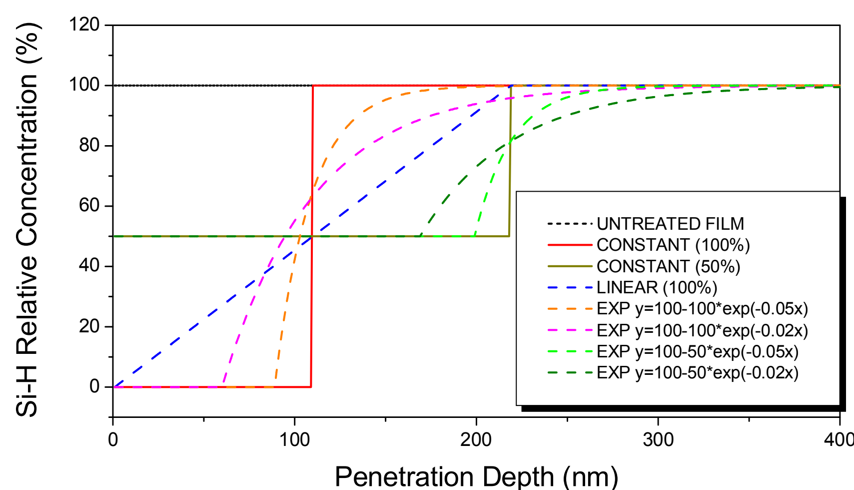

FIGURE 4.10. Different depth profiles for the Si-H bond absorption that would match the total bond concentration, 72.7%, for a 10 min DC plasma treatment in O_2 at 0.1 mbar on a 400 nm thick ppHMDSO film.

[20] The differences in the calculations by chosing one peak or another need to be related to the chemical modifications occurring on the film upon bombardment of energetic species and to the different bond energies holding the organic groups together, (Si-H, Si-C, C-H, Si-O) and will be discussed in the next pages.

[21] The same criterion applies as with XPS: the penetration depth is consideres as the depth at which only <3% of the Si-H bond has bean removed.

	PROFILE 1	PROFILE 2	PROFILE 3	PROFILE 4	PROFILE 5	PROFILE 6	PROFILE7
Treatment I	109	218	218	159	235	255	309
Treatment II	270	>400	>400	321	395	>400	>400

TABLE 4.3. Calculated depths (in nm) from the absorption of the Si-H bond, for the same plasma treatments as in Figure 4.9.

From these calculations, it is clear that only those profiles that predict a penetration depth smaller than the thickness of the film are compatible with the absorption measured by FTIR. Profiles 1 and 4 (constant concentration with 100% cleavage, and exponential increase starting at 100% cleavage) seem to provide the most realistic estimations, although the penetration depths are still larger than for XPS. Apart from the possible inaccuracy of the measurement of absolute absorbances in solids by FTIR, one possible explanation is that the depth axis in XPS is calibrated with a constant etching rate calculated for the average film, whereas the graded film is inhomogeneous and may be more difficult to etch at the beginning, up to a factor of 1.5.[168] This would mean that the thickness of the modified region may be underestimated and the thickness of the unaltered region overestimated by XPS.

Estimation of penetration depth by Ellipsometry

Although some authors argue that the depth of plasma treatment cannot be simulated by ellipsometric models to represent any real physical value,[152] we attempted to evaluate the post-treated layer thickness from calculations on ellipsometric data, similarly to Vallée and co-workers.[163] The multilayer stack used for these simulations, was derived directly from the TEM cross-sectional structure shown in Fig 3.6, except by the use of a different substrate, as follows:

- the roughness was not taken into account but in the case of the DC process a thin aluminum oxide layer was added;
- the bottom layer corresponding to the untreated film was simulated as a dielectric material *M1* of thickness *d1*. The refractive index and extinction coefficient of *M1* were described according to a Forouhi-Bloomer dispersion function[169,170] by five parameters(22) and a simulation of a single homogeneous

(22) These five parameters are n_∞, E_g, A, B, C, but only n_∞ (refractive index at high frequencies) and E_g (band gap energy) have physical significance.

layer was carried out to fit the data from measurements of the untreated material. The fitted values of *M1* were thus determined and would be used afterwards in the multilayer fit;

- the top layer was simulated as an unknown dielectric material *M2* related to the post-treated layer. Although this layer should not be uniform in composition but gradient-like, we made the hypothesis of a uniform layer to simplify the simulations. Thickness *d2* was unknown and material *M2* was optically described by the same dispersion functions and parameters as *M1*.
- the substrate was simulated as crystalline silicon instead of Al-coated glass.

The simulations were used to determine *d2* and the list of parameters for materials *M1* and *M2*.

In Table 4.4, the evolution of the modified depth, *d2*, estimated by fitting the multilayer model to the experimental ellipsometric data is compared to the depth calculated from XPS depth profile measurements, for one set of samples with varying treatment time. For milder post-treatments (shorter times), the ellipsometric calculations seem to be in good agreement with the depth profile performed by XPS, but for more aggressive post-treatments (longer times) the ellipsometric simulations result in smaller penetration depths than the XPS. This could be explained by the fact that for treatments of a few nanometers in depth, the approximation of a modified region with homogeneous properties may work closely to reality, but for longer times the modified region should be probably simulated as a group of 2-4 layers with different properties to account for a graded profile, which could produce a more accurate depth estimation.

Treatment Time (s)	Depth by Ellipsometry (nm)	Depth by XPS (nm)
120	23	25
240	38	42
600	62	87
1200	91	129

TABLE 4.4. Comparison between depth of treatment for different treatment times in an O_2 DC plasma, as estimated by ellipsometry and measured by XPS.

4.3.2. Chemical composition and depth of the modified region

The chemical processes involved in the plasma treatment of ppHMDSO films are substantially similar to those of the plasma polymerization processes studied in Chapter 3. There are two main pathways involved, depending on whether there is oxygen in the treatment or not: when oxygen is available, either intended or unintendedly, we are dealing with a reactive plasma treatment. Oxygen atoms will lead to an oxidation process where the organic groups (–H, $–CH_3$, $–CH_2$, –CH) will be etched, oxidized and removed by the vacuum system as volatile species, while additional oxygen will be incorporated into the film as Si-O-Si or Si-OH bonds. When oxygen is not involved (i.e. non-reactive plasma treatment), the energy released by ion and electron bombardment, and UV photons, will etch –H and $–CH_3$ groups and create reactive sites that will bond to neighboring sites thus inducing a higher degree of cross-linking. In both cases, the surface roughness of the films will also be increased.

4.3.2.1. Non-reactive plasma treatment of ppHMDSO

Non reactive plasma treatments are the most difficult to analyze, since changes induced by the energetic ions are not easily detected by XPS, TEM or even FTIR. Our experiments with Ar and N_2 plasmas show that the most significant differences can be found for films with a lower density. In addition to the density of the films, it is extremely important to avoid oxygen and water vapor as much as possible, otherwise the treatment will produce some degree of oxidation even with a 1% oxygen background. For that reason, in all cases the background pressure needs to be low enough (at least 3 decades below the working pressure) and different purges with Ar or N_2 may be necessary to avoid oxygen contamination, prior to starting the plasma treatment, although for reactors without a load lock system some trace amounts of oxygen and water vapor are inevitable due to adsorption at the inner reactor walls and surfaces at reactor opening and ulterior desorption during plasma treatment.

Argon plasma treatment

All the films referenced herein were treated with post-treatments of 10 min, 20 min and 30 min Ar plasmas at 0.1 mbar by placing the samples at the same

location with respect to the plasma where the film deposition had taken place, i.e. in the closer afterglow region for low density films and on the grounded electrode plate (anode) for the medium and high density films, but at different distances between the powered and grounded electrodes (20 cm and 15 cm, respectively). Only some differences between treated and untreated samples were observed in the IR spectra for the medium density film and almost no differences for the low and high density films, which was rather unexpected, especially for the low density films. In order to check if this could be due to the lack of Ar^+ ion bombardment when placing the samples in the afterglow region, the low density films were duplicated and the treatments repeated by placing the samples on the anode surface within the plasma, so that they would be receiving additional ion bombardment. In this case, the changes in the post-treated low-density sample were even larger than for the medium-density film, indicating the important role of ion bombardment.

Figure 4.11 (top) shows the FTIR spectra for the low density film prior to plasma treatment and after plasma treatments, with all samples located on the anode surface during post-treatment. Figures 4.11(mid) and 4.11(bottom) show the equivalent FTIR spectra for the medium and high density films, respectively.

The chemical modifications induced by the plasma were identified by detecting changes in $Si–CH_3$, $Si–CH_2$, Si–H, Si–O–C, $Si–CH_2–Si$ and Si–OH related peaks. Since $Si–CH_3$, Si–OH and Si–H are terminal groups, i.e. chain extension cannot proceed further from these bonds, they are related to a lower degree of cross-linking and to a lower density polymeric film; furthermore, $Si–(CH_3)_3$ is really the end of the chain extension for Si in any direction; on the other hand, Si–O–C, Si–Si, $Si–CH_2–Si$ and $Si–CH_2–CH_2–Si$ bonds are an explicit result of cross-linking (non-existing bonds in HMDSO molecule or linear PDMS chains), and could either produce a further propagation of the chain or be left as radical sites and therefore extremely prone to linking to another neighboring site. The quantification of $Si–CH_2$ related bands is difficult if not impossible, since they are either too weak or masked by stronger bands at similar wavenumbers (usually $–CH_3$ related peaks). The same difficulty applies to the Si–O–C related peaks, which are masked by the strong vibration bands of the Si–O–Si siloxane backbone. In addition, changes and deformations in the baseline levels may have a strong effect on the accuracy of comparisons between low-intensity

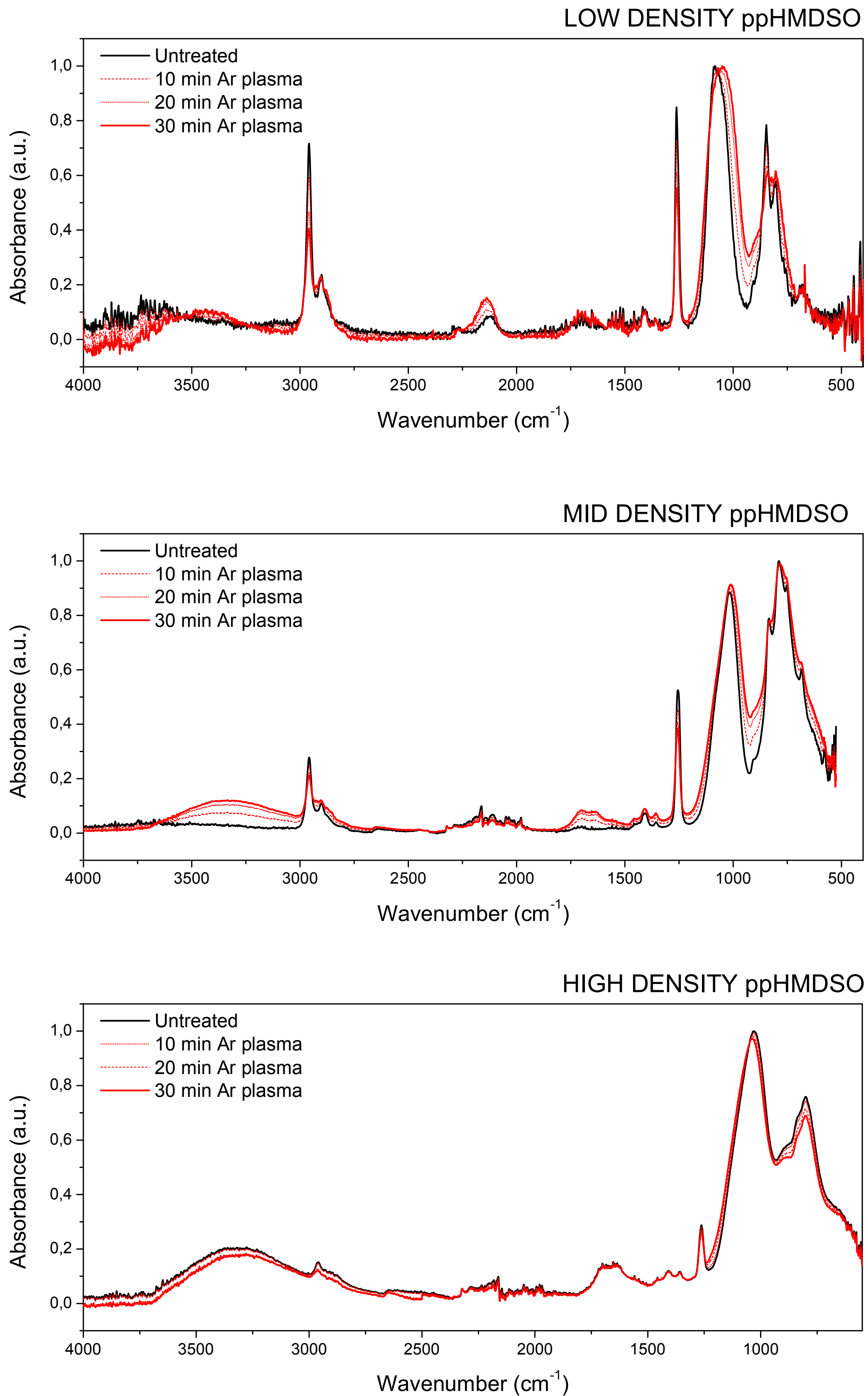

FIGURE 4.11. FTIR spectra for low, medium and high density ppHMDSO films post-treated in a DC Ar plasma at 0.1 mbar for 10 and 20 min**.**

peaks. A closer look at Figure 4.11 allows us to find evidence for additional cross-linking for the Ar plasma treatment in the low and medium density films:

- A decrease in the intensity of the methyl-related peaks, and specially for the strong Si–$(CH_3)_{n=1,2,3}$ symmetric bending band around 1260 cm^{-1} and a slight shift of this band to higher wavenumbers with increasing treatment time indicate that some methyl groups have been lost. The shift has been reported to be related to the amount of methyl groups which are bonded to the silicon atom,[153,171] with higher wavenumbers being indicative of methyl group etching in Si–$(CH_3)_3$ structures; this leaves Si–$(CH_3)_2$ or Si–$(CH_3)_1$ and one or two free sites to form new bonds with the central Si atom, respectively.
- An increase in the band around 2130 cm^{-1} is indicative of additional Si–H bonds created after some methyl groups have been substituted by H. H atoms are released by etching of organic groups and subsequent decomposition by electron impact and are always available due to the inability of mechanical/diffusion pumps to pump them out. This can be observed in the OES spectrum of the Ar plasma in the presence of any organic compounds.
- A slight increase in the peaks at 800 cm^{-1}. and 1400 cm^{-1} corresponding to bending vibrations of Si–CH_2–Si and Si–CH_2–CH_2-Si bonds are direct indicators of additional cross-linking.[143,145]
- Broadening of the complex absorption bands at 800-900 cm^{-1} are also indirect signals of additional cross-linking.[128]
- An increase of absorbance around 900-960 cm^{-1} and the broad band appearing between 3200-3400 cm^{-1} are related to the incorporation of Si-OH groups. While the band at 900-960 cm^{-1} is covalently linked as Si-OH, the band at 3200-3600 cm^{-1} is linked by H-bridge and can be removed by vacuum or annealing.[172]
- Finally, a shift in the big absorption band around 1000-1100 cm^{-1} to lower wavenumbers can be correlated to a higher density.[128,172]

For the high density film, the methyl content is already much lower before any plasma treatment, as shown by the small relative absorbance of the band at 1260 cm^{-1}. The differences after plasma treatment are not significant, except for a small increase in the absorption band around 800 cm^{-1}. This increase may be related

to a higher oxidation of the film or to additional Si–CH_2–Si bonds, but in any case it is clear that the effect is much smaller than for the low and medium density films.

Finally, XPS stoichiometric analysis did not produce significant differences between treated and untreated samples (see Table 4.5), indicating that the amount of C remains basically unaltered during non-reactive plasma treatment. Since there is a certain amount of CH_3 groups which are necessarily etched by collision with energetic species, most of this C needs to be redeposited in a short time via recombination with the freshly created reactive sites in the film, if the composition is to remain unaffected. In addition, there may be a slight oxidation of the films, but it is not clear whether this is produced during or after plasma treatment, since there is a small amount of free (unbound) OH groups in the films, as indicated by the presence of the FTIR band at 3200-3400 cm^{-1}, in principle these groups should not contribute significantly to the XPS signal, since they should be removed by the vacuum system, wherein samples are left overnight prior to XPS measurements. Still, the measurements suggest a small additional oxidation, but this trend is smaller than the quantification error of the technique and therefore cannot be considered as conclusive.

	UNTREATED	10 min Ar Plasma	20 min Ar Plasma	30 min Ar Plasma
Low Density	$SiO_{0.63}C_{1.94}$:H	$SiO_{0.66}C_{1.86}$:H	$SiO_{0.65}C_{1.90}$:H	$SiO_{070}C_{1.89}$:H
Medium Density	$SiO_{0.80}C_{1.67}$:H	$SiO_{0.83}C_{1.68}$:H	$SiO_{0.88}C_{1.63}$:H	$SiO_{0.86}C_{1.60}$:H
High Density	$SiO_{0.91}C_{1.28}$:H	$SiO_{0.92}C_{1.26}$:H	$SiO_{0.94}C_{1.28}$:H	$SiO_{0.93}C_{1.20}$:H

TABLE 4.5. Stoichiometry of untreated and Ar plasma treated films as calculated from XPS survey scans.

Nitrogen plasma treatment

Nitrogen plasma treatment is substantially equal to Ar plasma treatment in terms of cross-linking enhancement but N_2-treated samples acquire a slight yellowish color after plasma treatment, although this color is more faint than the case where N_2 is added *during* plasma polymerization. No traces of Si–N or N–H bonds could be found in FTIR spectra, but probably because these vibration bands (920 and 1170 cm^{-1}

respectively) are overlapped with much stronger Si-O bands. XPS survey scans indicated a small amount of N atomic concentration (<5 %) at the outermost surface of the treated films, as shown in Figure 4.12. Also some amount of sputtered Al is detected as two small peaks in the vicinity of Si peaks. We did not investigate if the incorporated N atoms are effectively bonded to Si or C, but still the slight change in stoichiometry and color indicates that N_2 treatments can be considered as mid-way between non-reactive and reactive plasma treatments.

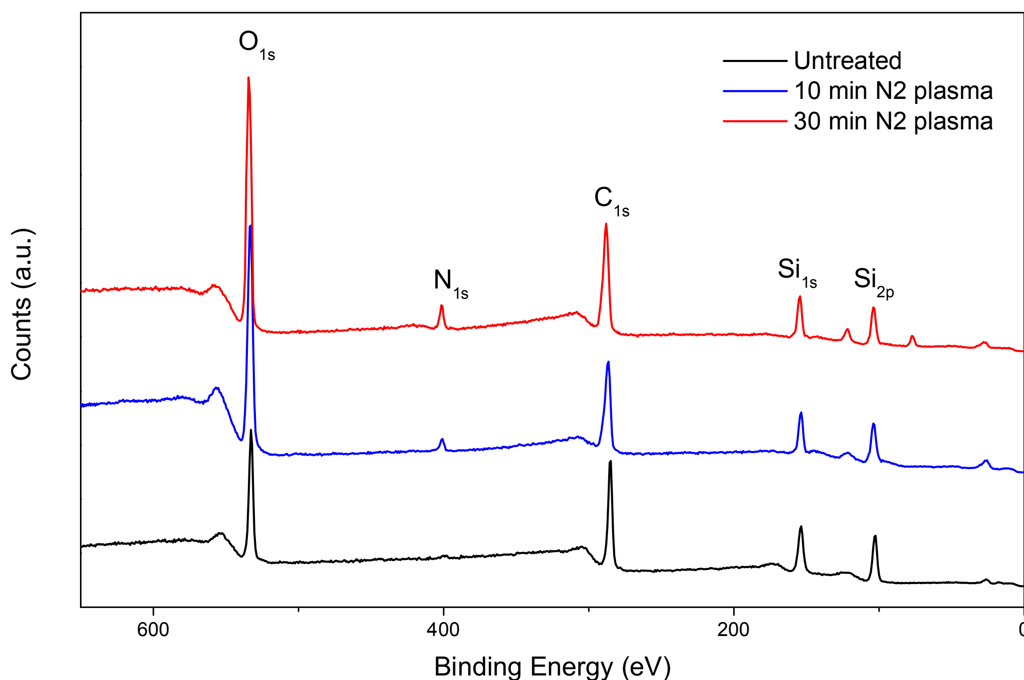

FIGURE 4.12. XPS survey spectra of the surface of medium-density ppHMDSO films post-treated by a DC nitrogen plasma at 0.1 mbar at different treatment times.

4.3.2.2. Reactive (oxygen) plasma treatment of ppHMDSO

Oxygen plasma treatments produce chemical modifications which show some similarities to the oxidation processes described for plasma polymerization of precursor mixtures of oxygen and HMDSO. An oxygen plasma post-treatment can be employed to achieve partial oxidation of the plasma-polymer film, thus modifying the functional properties in a beneficial way for applications that may require increase of hardness, increase of wettability, decrease of water vapor permeability or increase of adhesion strength with respect to pure ppHMDSO films. For organosilicon

compounds, this modification is often referred to as a "mineralization" process, since most organic groups will be removed and a silica-like material will be generated. As mentioned in the previous section, even Ar or N_2 plasma treatments can result in some degree of oxidation due to small amounts of water vapor and oxygen outgassing from the reactor walls or from previous deposits. Other reactive plasma treatments can be effected with NH_3 or N_2O, but these are not within the scope of this thesis.

In opposition to Ar plasma treatment, O_2 plasma treatment produces a strong modification of the stoichiometry of the films and a concentration gradient in depth which can lead to a complete depletion of the carbon content of the films, at least on the first 50-100 nm.

Effect of treatment time on the oxidized region

Figure 4.13 shows the oxygen and carbon relative atomic concentrations with respect to the unmodified film from XPS depth profiles for ppHMDSO films post-treated in an oxygen plasma at different treatment times. The plasma treatments were effected in 450 nm thick medium-density ppHMDSO films (1.44 g/cm^3) deposited on Si substrates located on the anode surface of a DC parallel plate HMDSO plasma and post-treated at the same location. The post-treatment parameters were 0.1 mbar O_2 pressure and treatment times of 30s, 120s, 240s, 300s, 600s and 1800s. The normalized concentrations of atomic oxygen and carbon were derived from peaks for the O1s and C1s photoelectrons. From these profiles, the depth of the modified region seems to reach up to 140-150 nm after 30 min of treatment. The profiles also indicate that C was virtually eliminated from the surface of the films after only four to ten minutes of plasma treatment, whereas the O concentration was almost tripled, from $SiO_{0.71}C_{1.89}$:H to $SiO_{1.91}$:C:H, which is close to the stoichiometry of silica (SiO_2). Therefore, the first nanometers at and below the surface seem to be almost fully oxidized. Furthermore, this silica-like region progresses with longer treatment times to a thicker depth, although the fully oxidized region is half the thickness of that of the modified region for 30 min treatment time. It is not clear whether the modified depth would extend at longer treatment times or would saturate, but these longer times were not explored due to the temperature increase of the substrates, which produces thermal damage on plastics and would make the

process impractical for industrial applications, which are our main driver. However, some authors have extended the treatment times in the afterglows of microwave plasmas and expanding thermal plasmas[152,160] and claim to have reached full oxidation and oxidized depths of up to 500-700 nm in 2 hs.

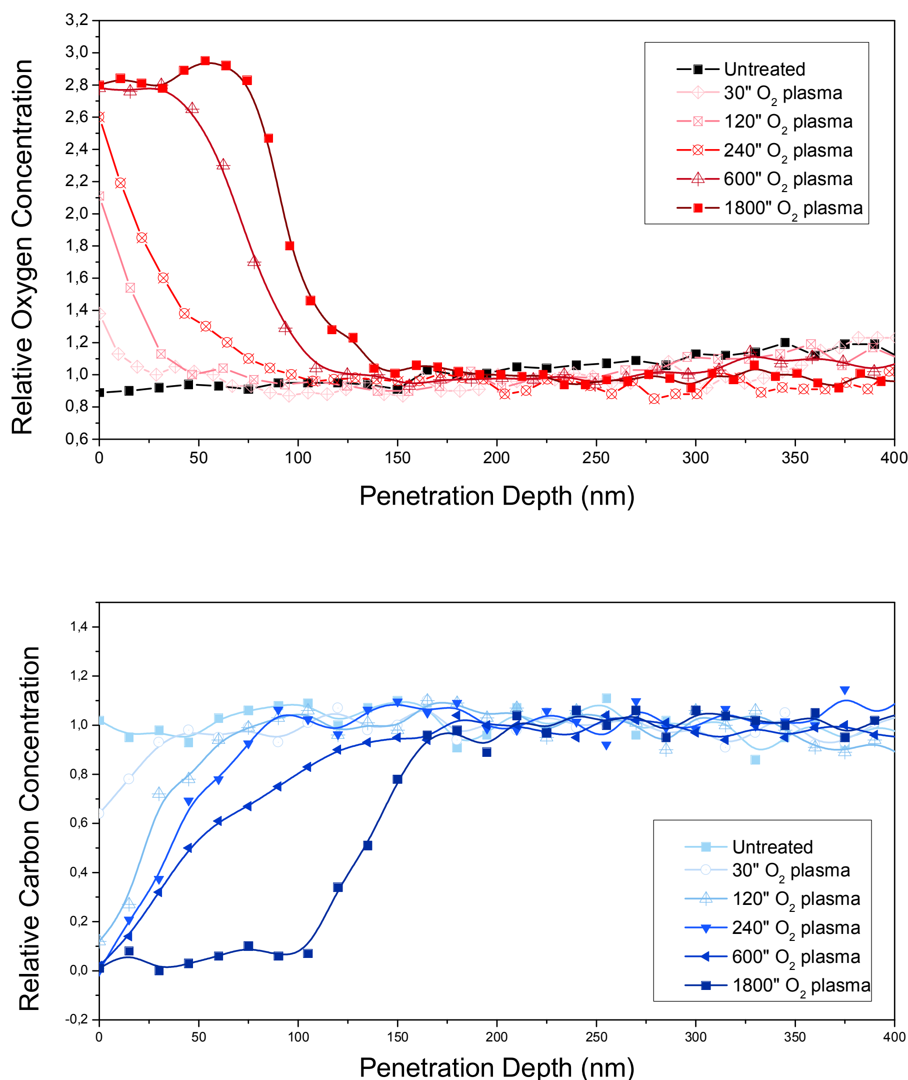

FIGURE 4.13. Relative concentration of Oxygen and Carbon with respect to the untreated film as a function of depth calculated from XPS depth profiles for the O_{1s} and C_{1s} peaks, for a medium density ppHMDSO film post-treated in a DC oxygen plasma at 0.1 mbar.

In addition to the stoichiometry, XPS provides additional information about the chemical environment of the modified region, since the binding energies of photoelectrons escaping from Si atoms can be used to determine the degree of oxidation. The difference in the coordination state of Si to O can thus be obtained by

deconvoluting the peaks from spectra generated at different depths. In a HMDSO monomer molecule, Si is bonded to one oxygen atom and three methyl groups; in fused silica and quartz, Si is surrounded by four oxygen atoms; in ppHMDSO films and plasma post-treated films, Si will be in an oxidized state between those of HMDSO and SiO_2. The binding energies for Si2p electrons assigned to the different oxidation states

	Si I	Si II	Si III	Si IV
Structure	R (top), R – **Si** – O, R (bottom)	R (top), R – **Si** – O, O (bottom)	O (top), R – **Si** – O, O (bottom)	O (top), O – **Si** – O, O (bottom)
Binding Energy	100.5 eV	101.7 eV	103.0 eV	104.1 eV

TABLE 4.6. Binding energies for Si2p photoelectrons for different oxidation states.

of Si (Si^{I}, Si^{II}, Si^{III}, Si^{IV}) has been reported in several references[157,173,174] and are summarized in Table 4.6. Figure 4.14 shows the deconvoluted Si2p peaks from photoelectrons generated at the surface and at 300 nm deep from an oxygen plasma-treated ppHMDSO film. As expected, the oxidation state of Si is much higher close to the surface than deep into the film. Si is almost completely oxidized at the surface, with most electrons coming from Si^{III} and Si^{IV} states, whereas deeper inside the main contributors are SiC and Si^{II} bonds. This is in line with the stoichiometry calculated before for the surface and inner regions of the plasma treated ppHMDSO film.

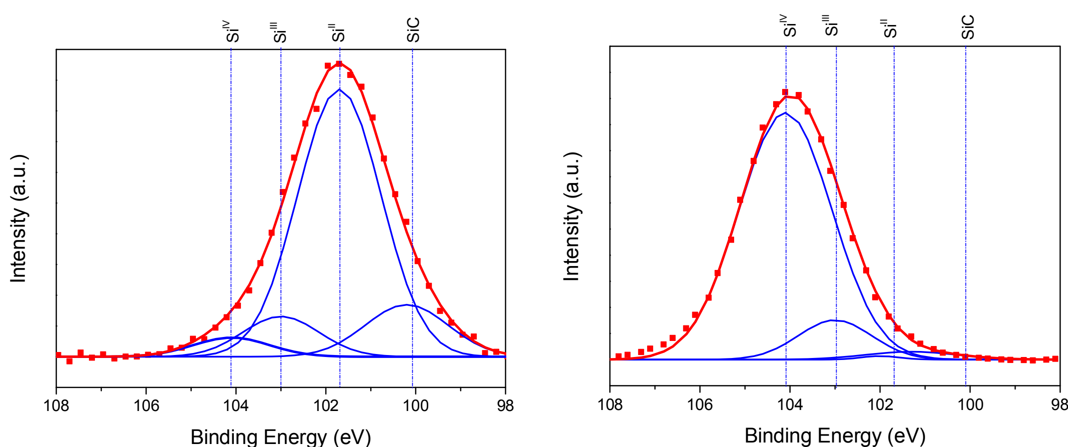

FIGURE 4.14. Si2p XPS deconvolution for the corresponding to the unmodified ppHMDSO at 300 nm below the surface **(LEFT)** and the oxidized region, at 10 nm below the surface **(RIGHT)**.

A complementary view of the chemical changes induced by the oxygen post-treatment can be obtained from the IR absorption spectra for the modified films, which are shown in Figure 4.15.

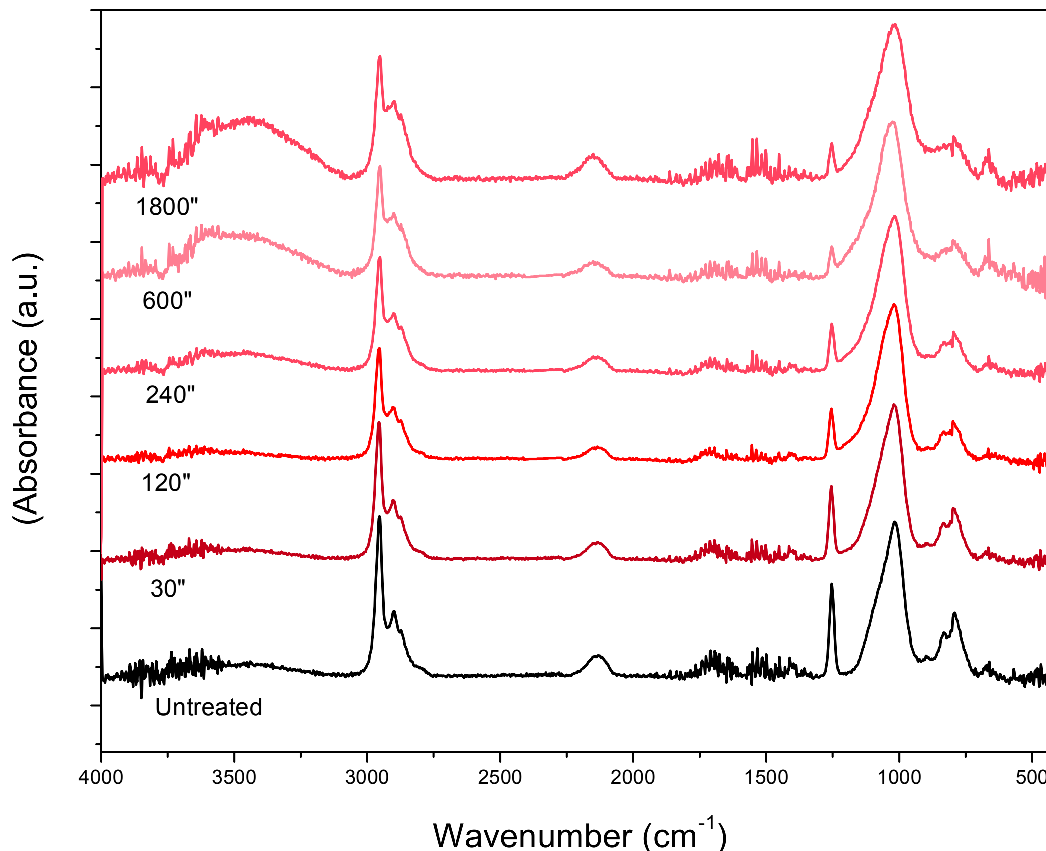

FIGURE 4.15. FTIR spectra of treatments effected on medium density ppHMDSO films by a DC oxygen plasma at 0.1 mbar at different treatment times.

The ablation of –CH_3 groups is clearly distinguishable but not complete, as can be assessed by substracting the spectrum of the untreated film to those of the modified films (Figures 4.16 and 4.17). This reveals a reduction of the Si–$(CH_3)_{1,2,3}$ symmetric bending and Si-CH_3 asymmetric stretching bands appearing at 1260 cm^{-1} and at 2960 cm^{-1}, respectively. Still, the removal of organic groups of the film is not complete, even after 30 min of treatment. In addition, some oxidized groups such as Si–OH and Si-O-Si can be detected by the appearance and increase in two bands at 3400 cm^{-1} and 959 cm-1, and two bands at 1070 cm^{-1} and 1160 cm^{-1}, which correspond to: free OH, Si–OH stretching, the Si–O–Si “network” and the Si–O “cage” structure, respectively. The band at 2130 cm^{-1} associated to Si–H does not disappear but is sensitive to the

oxidation state of the Si atom and shifts to higer wavenumbers due to a higher oxidation state; this trend was previously reported for H-contaminated silicon dioxide.[160,175]

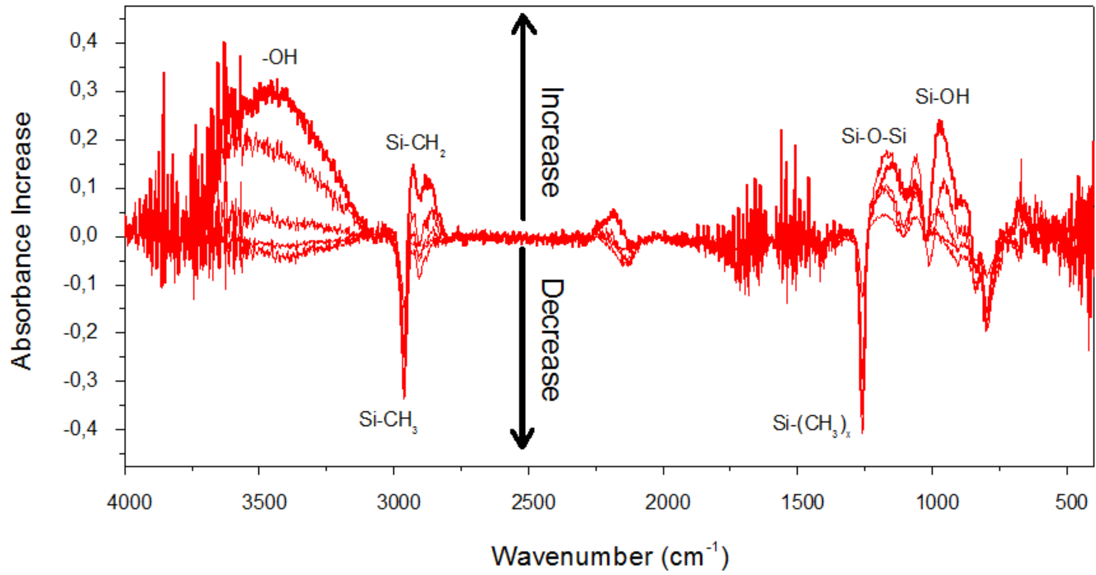

FIGURE 4.16. Differential FTIR spectra of oxygen-treated films with respect to the untreated film.

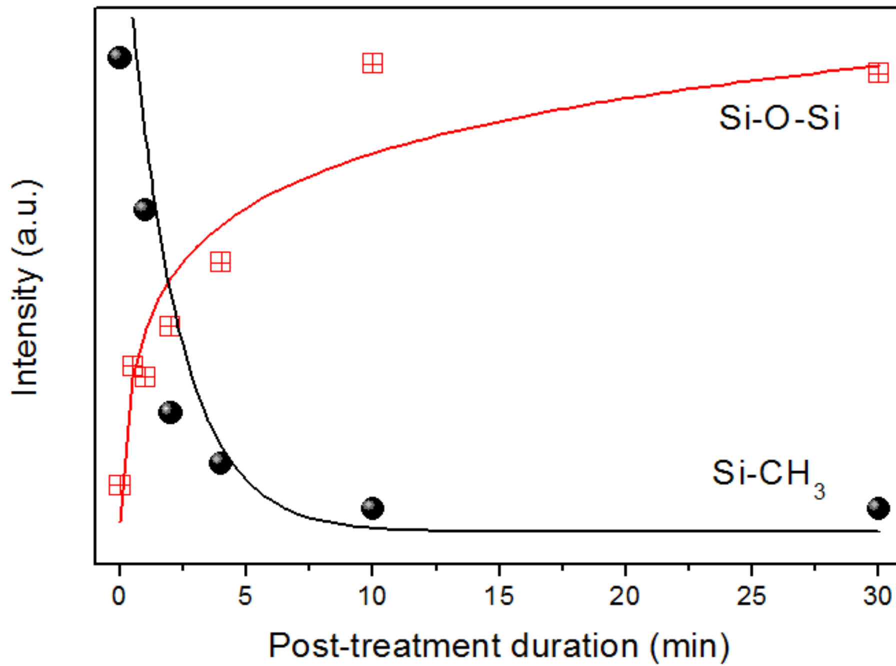

FIGURE 4.17. Evolution of Si-O-Si and $Si-CH_3$ band intensities with plasma treatment time.

Effect of oxygen pressure on the oxidized region

In order to investigate the effect of oxygen pressure on the modified region, the same group of medium-density ppHMDSO films from the time series were post-treated in an oxygen plasma at a fixed time of 10 min and at different total pressures of 0.05, 0.1, 0.2 and 0.3 mbar. Figure 4.18 shows the XPS depth profile for the oxygen concentration. There seems to be an optimal pressure range for maximum penetration around 0.1 to 0.2 mbar, but the differences are not as large as to exclude that the effect is only due to experimental variability. The reduction in the modified depth and in the oxidation degree at the surface observed with lower pressures could be easily related to the lower concentration of atomic oxygen and oxygen ions available to cleave organic groups; the slight decrease in penetration depth at higher pressures is more difficult to justify, but could be related to the lower energy of ions impinging on the surface, which could lead to a similar modification at the first surface layers but a decrease in the oxidation at the subsurface.[176]

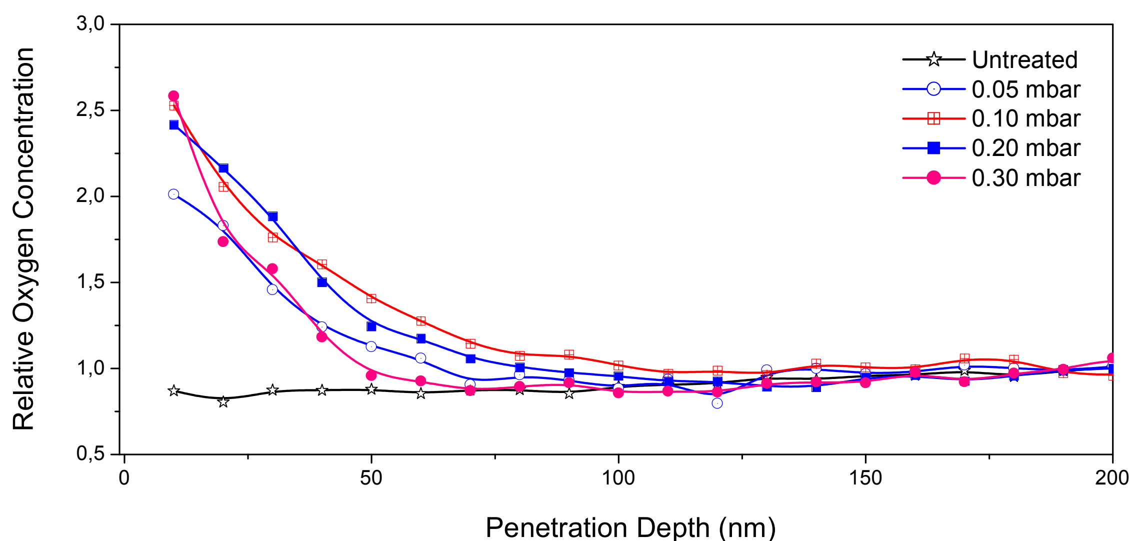

FIGURE 4.18. Depth profile for the relative concentration of oxygen with respect to the untreated region for a medium density ppHMDSO film post-treated in a DC oxygen plasma at different pressures.

Effect of film density on the oxidized region

The effect of film density was studied to confirm the assumption that density is one of the main parameters to analyze in order to explain the penetration depths of the treatments. Figure 4.19 shows two series of treatments effected on medium-density

(1.41 g/cm^3) and high-density films (1.71 g/cm^3). The penetration depth is substantially different between both treatments. In principle, the density and porosity of the films could explain most of the difference but it is not to be discarded that the closer distance to the cathode for the high density films produced an increase in the amount of sputtered aluminum which would be deposited as a high density aluminum oxide layer on top of the ppHMDSO film. This could have limited the diffusion of ions and reactive atoms into the inner bulk of the material.

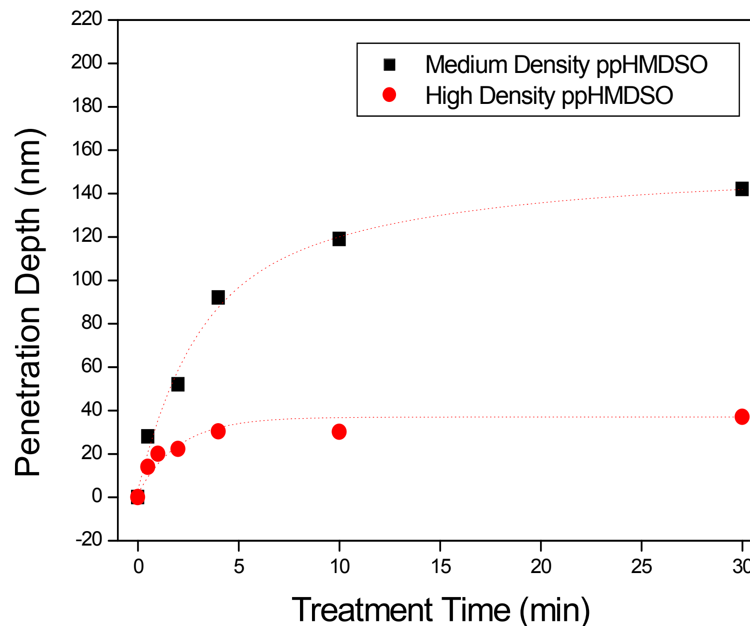

Figure 3.19. Medium- and high-density ppHMDSO films post-treated with different post treatment times.

Effect of type of plasma on the oxidized region

in our published work "*Comparison between continuous and microwave oxygen plasma*",[136] films obtained in a DC plasma and post-treated in the same DC plasma showed significantly lower penetration depths than films prepared in a MW plasma and post-treated therein. When XPS and FTIR spectra were analyzed, it was clear that the films deposited in the DC plasma had lower C content and higher density than the ones deposited in the MW reactor, for the chosen depostition parameters. DC ppHMDSO films were also denser and more oxidized prior to the post-treatment, because they had been deposited in the monomer-deficient regime, which promotes

fragmentation of the monomer molecule and cleavage of $–CH_3$ groups already during film growth. In order to clarify if the difference could be related to the plasma source or to the different densities of the films, additional films in the high density range were deposited only in a DC plasma and post-treated both in a DC and in a MW discharge. The analysis of these samples showed that the type of plasma post-treatment did not make a clear difference in the penetration depth, but could make a difference in surface properties such as roughness and wettability, due to the different ion densities and ion energies of both types of plasma.

4.3.3. Physico-chemical processes in plasma treatment of ppHMDSO films

The mechanisms involved in the oxygen or argon post-treatments of ppHMDSO films are similar to those existing in the oxygen plasma treatment of polydimethylsiloxane (PDMS) bulk polymer. While the latter has been studied extensively, in comparison, plasma treatment of ppHMDSO has received very limited attention since we first reported it.[133,136,152,157,158,177] Our focus was to study the functional properties of post-treated ppHMDSO films in order to explain how to tune the technological parameters to optimize different applications. Therefore, we have not conducted specific experiments neither employed analytical or simulation tools to explicitly elucidate these mechanisms.(23) Nonetheless, we have gathered and analyzed different published models and data to construct our own qualitative model to be consistent with our results.

From a physical perspective, the main species in the plasma that interact with the solid surface are the energetic ions, electrons and photons, which lose their energy into the film network either by collision (ions/electrons) or by absorption (photons). Electrons and photons play an additional role in the gas phase, where they create radicals and excited species by inelastic collisions. These neutral particles (radicals,

(23) Avalable tools can be used to analyze the plasma species and their energy and density in the gas phase, such as Lamgmuir probes, actinometry, in situ mass spectrometry, gas-phase FTIR, etc… Other tools can be used to analyze the radical species reacting within the film, e.g. magnetic ressonance; in addition, the real-time changes during plasma treatment can also be monitored by in situ ellipsometry, rutherford backscattering or in situ FTIR. Finally, simulation tools can be used to calculate the energy loss by ion collisions and the diffusion of neutrals, radicals and metastable species.

excited species) do not contribute significantly to the energy transfer to the film, but are the main drivers for the chemical reactions occurring thereafter.

Once part of the plasma energy has been transferred to the film, multiple reactive sites are generated, in addition to those already existing, and chemical reactions involving radicals, metastable and excited species acquire the leading role, which shifts the view to a chemical perspective. If the energy transferred by fast particles is above a certain threshold, sputtering of material will also occur. A physical model based on particle diffusion is usually employed to explain the apparent thickness of the modified region while a chemical model is used to explain its functional properties and (obviously) its chemical composition.

4.3.2.1. Physical model of film interaction with plasma species and its relation with penetration depth

A qualitative model to explain the physical modification of a plasma-treated surface needs to deal with all the possible energetic species in the plasma and how they could transfer their energy to the amorphous network in the film in order to create reactive sites (radicals, metastable, dangling bonds). The model needs to explain also how reactive atoms can diffuse through the film and be available for these newly created reactive sites or to any appropriate site where a chemical reaction may occur. Most authors attribute the leading role in plasma modification of polymers to ions and relate the extent of the treatment to different diffusion models. We will first discuss the possible role of electrons, followed by UV photons and ions; we will finally present a diffusion model for atomic oxygen, which is believed to be the main reactive species coming ‘from’ the plasma.

Electrons

The main role of electrons is to capture the energy from the electric field within the plasma, transform it into kinetic energy and transfer it by inelastic collisions to generate ions and additional electrons, and to dissociate molecules, -thus creating radicals-, or to promote atoms/molecules to excited states. On the contrary, the contribution of electrons arriving upon the surface of the film is to be neglected, other than their partial contribution to the increase on the sample temperature if it is placed at the grounded anode. Swiderek et al. compared plasma treatment, VUV

treatment and low-energy electron treatment on PDMS and condensed HMDSO coatings and concluded that modifications by electron bombardment are only significant for energies >500 eV,[164] which is two orders of magnitude higher than the average electron energy. There will be energetic electrons in the tail of the energy distribution function, but still far away from such high values. In addition to this, the electron density in an oxygen plasma is one order of magnitude lower than the amount of negative ions,[178] and if both were to reach the sample at the anode surface, the overall energy transfer by ions to the film would be much higher, indicating again that the interaction of electrons and the film can be mostly neglected.

UV photons

Photons are capable of direct absorption and breaking of intramolecular bonds, provided that their energy is greater than that of the target bond. Photons will penetrate the material until they are either absorbed or transmitted through. Therefore, the interaction is governed by the energy of the available photons, -which can be derived from the emission spectrum of the plasma-, the binding energy of main bonds and the absorption coefficient for the material. The energy of the main bonds is shown in Table 4.7, together with the equivalent maximum photon wavelength for photoablation of these bonds.

Bond	Binding Energy	Equivalent Photon Wavelength
Si-Si	3.39 eV	365 nm
Si-C	4.51 eV	275 nm
C-C	6.31 eV	196 nm
Si-H	3.09 eV	401 nm
C-H	3.49 eV	355 nm
Si-O	8.27 eV	150 nm

TABLE 4.7. Binding energies of main interatomic bonds in ppHMDSO[179,180] and equivalent photon wavelength.

The emission spectrum in Figure 4.20 shows that there is a small amount of energetic UV photons between 280 and 400 nm in both oxygen and air plasmas that can produce direct photoablation of Si-Si, SI-C , Si-H and C-H bonds. In addition, the absorption spectrum of ppHMDSO in Figure 4.21 shows that the absorption

coefficient α is rather low for these wavelengths. The intensity of photons reaching the surface of the film decreases exponentially within the depth of the film as:

$$I = I_0 e^{-\alpha x} \qquad (Equation\ 4.1)$$

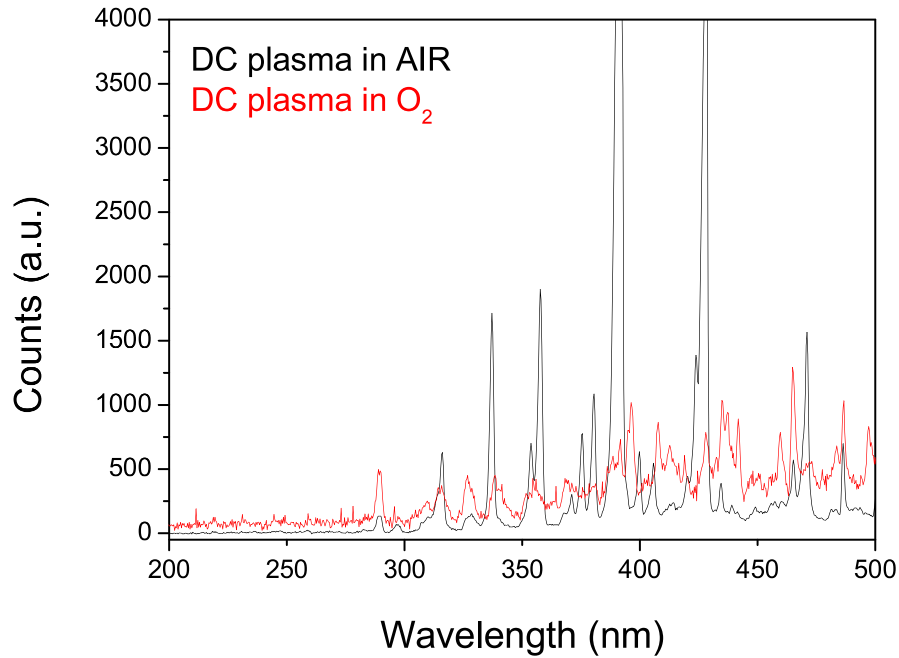

FIGURE 4.20. Emission Spectra of DC plasmas in Air and Oxygen.

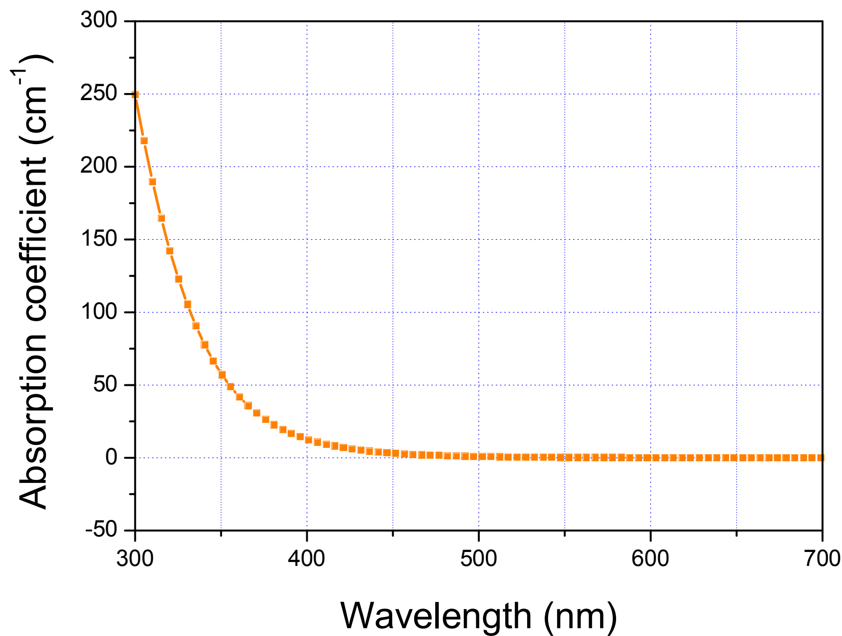

FIGURE 4.21. Absorption spectrum of ppHMDSO.

According to Eq 3.1, for a 400 nm thick ppHMDSO film the absorbed photons at a wavelength of 300 nm are only 1% of the incident ones. From an energetic balance point of view, assuming that 1) approximately the same energy is transferred by electron impact to ionization and excitation processes in the plasma, 2) that photon emission from excited atoms is isotropic in all directions, whereas ions are more efficiently directed by the electric field towards the substrate in a parallel plate discharge, and 3) that the absorption efficiency of UV photons in the spectral range of the plasma emission is rather low whereas the whole kinetic energy of an ion impinging upon the surface of the film is dissipated therein, we can conclude that photons contribute with much less energy input than ions to the chemical transformations occurring within the film.

Finally, although the extent of the modification exerted by photons can be rather small as compared to ions, it does account for a fraction of the changes, and the penetration depth of UV-induced modifications will be much higher than that for ions alone, as demonstrated by several works[181,182] and as expected by the absorption coefficient.

Ions

In addition to the hypothesis outlined before, most authors suggest that ions take the main role among energetic species in initiating the chemical reactions leading to plasma modification of polymers, and specifically of thin plasma polymer films.[152,157,159,161,183,184] The role of ions can be summarized in three mechanisms: first, ions supply energy to the film in order to break bonds and create reactive sites and organic radicals; second, ions can react with molecular groups in reactive sites within the film and remain incorporated (Si-O-Si, Si-OH bonds) or form volatile species (CO_2, H_2O). For non-reactive gases, such as Ar, only the first mechanism is possible; for reactive gases, such as O_2, both mechanisms are possible. Finally, in addition to the first two mechanisms, if the energy of ions is sufficiently high, the cascade of collisions generated by the arriving atom will also produce sputtering of recoiled atoms and particles at the surface. The energy of an ion arriving at the surface determines which of the aforementioned mechanisms is produced:

1) If $E_{diffusion} < E_{ion} < E_{bonds}$ the ion will diffuse through the film without creating additional reactive sites. The higher its energy, the faster it will diffuse with

respect to room temperature. The ion will slow down through collisions until it gets eventually thermalized, acquiring the same energy as the other atoms in the film, or until it is captured and reacts with a suitable site.

2) If $E_{threshold\ etching} < E_{ion} < E_{bonds}$ the ion can also loose its energy by destroying molecular bonds along its path within the film and creating radicals, dangling bonds and reactive sites.

3) If $E_{ion} > E_{threshold\ etching}$ the ion can lose most of its energy by producing sputtering of recoiled atoms at the surface, and also undergo paths 1) and 2) with the reamining energy.

The energy of ions arriving at the surface is dependent on the type of plasma and on the plasma parameters, specially on the floating potential and the voltage bias applied to the film, but also on pressure. With higher pressure, the density and the amount of neutrals (radicals, excited, metastable) arriving at the surface is increased, but the ion flux and the ion energy is reduced.[157] In order to estimate the energy of positive ions, the difference between the plasma potential and the floating potential of any surface is taken into account. For RF or MW plasmas, this energy is rather low, between 20 eV and 5 eV for a floating surface within the plasma, depending on the total pressure,[157] and no significant etching is expected to occur.

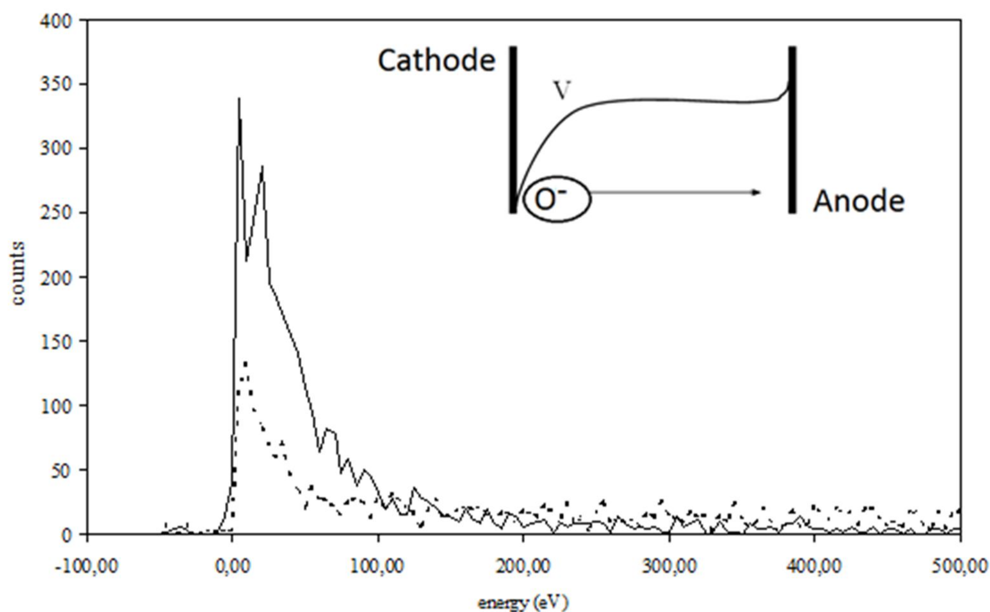

FIGURE 4.22. Voltage drop and energy distribution for the O^- ion in an O_2 DC plasma, at 0.05 mbar and 0.1 mbar (modified from [3008]), extracted from the anode by an orifice into a QMS. The energetic tail indicates that high energy ions exist and reach the anode.

For a DC plasma, positive ions will not reach the anode, but they can reach floating surfaces. Much more significantly, in a DC plasma with an electronegative gas such as oxygen the role of negative ions needs to be taken into account. The ionization reaction between an oxygen molecule and an energetic electron results in a positive ion ($O_2 + e^- \rightarrow O_2^+ + 2e^-$); negative ions are produced by the dissociation reactions of an oxygen molecule ($O_2 + e^- \rightarrow O^- + O$) and the attachment reactions between an oxygen atom and an electron ($O_2 + e^- \rightarrow O_2^-$). Since negative ions are generated in the cathode sheath of a DC discharge, they can acquire high energies and reach a substrate placed at the anode or floating within the plasma (see Figure 4.22),[178,185] whereas for RF and MW plasmas only positive ions reach the surfaces and negative ions cannot overcome the negative potential barrier, unless a bias is applied. The effect of high energetic ions has been previously assessed by Quadrupole Mass Spectrometry, by extracting the negative ions through an orifice at the anode.[63] In our study, QMS was not available, but an indirect evidence of the energy dissipated by negative ions at the anode surface was observed by measuring the high temperatures reached at the anode (>150° in 30 min). Supiot et al.[161] also observed the increase in temperature in a sample placed in the plasma afterglow after the arrival of energetic ions due to a high voltage bias applied; the temperature was not increased when the surface was unbiased. From the fact that a larger temperature increase at the grounded electrode is produced by an O_2 plasma as compared to an Ar plasma, we

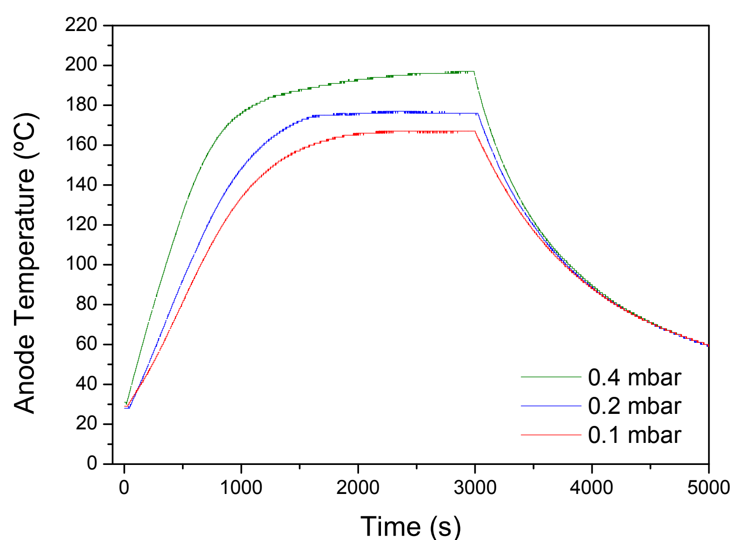

FIGURE 4.23. Anode temperature in a parallel plate DC O_2 plasma, at three different pressures: 0.4 mbar, 0.2 mbar, 0.1 mbar.

can conclude that not only electrons but also energetic negative ions bombarding the surface are responsible for the increase in temperature.[186]

The threshold for etching of SiO_2 has been measured to be around 35 eV[184] for any of the possible ions: Ar^+, O_2^+, O^-, O_2^-; the threshold for etching ppHMDSO is not documented, but should be somewhat lower, depending on the degree of crosslinking and film density. In fact, Hegemann et al. evaluated that the sputtering rate achieved by the Ar-ion gun in XPS for SiO_x-like films from HMDSO+O_2 could be up to 1.5 times smaller than for ppHMDSO films obtained from pure monomer,[168] which is a direct indication that the threshold for etching in both cases must be smaller than for SiO_2. We may therefore expect some amount of etching in DC plasma treated samples, whereas no significant etching is expected for RF or MW plasmas.

With respect to the penetration of energetic ions, we have simulated the interaction of ions and $SiO_xC_yH_z$ films for different film densities (1,2 – 1,9 g/cm^3), incident ion energy (25-1000 eV) and incident ion mass (Ar and O_2) with modern ion-matter interaction algorithms. Among several choices, SRIM: Stopping and Range of Ions in Matter, developed by Ziegler and coworkers[187] has been reported to give a most accurate match between simulated and experimental data.[188] Figure 4.24 shows an example of the ion trajectories for O^- ions with an incident energy of 500 eV for a ppHMDSO film with a density of 1.32 g/cm^3 on a Si substrate. Even such energetic atoms and the recoiled secondary atoms displaced from their original positions cannot penetrate to a distance larger than a few nanometers (about 10 nm) for the less dense films. Consequently, ion bombardment effects cannot explain alone the experimental evidence that chemical changes proceed much deeper into the film. Several works have arrived to the same conclusion and therefore have suggested that ion and atom diffusion have a higher impact than ion-surface energy transfer on the extent of the penetration of the plasma treatment.(24) In fact, Van Hest et al. clearly demonstrated that even in the afterglow, where the energy of ions is very low (1 eV), a ppHMDSO film can be oxidized efficiently, as far as sufficient O atoms or O- ions reach the surface and diffuse into the film.[152] Both O atoms and O^- ions are extremely

(24) As an example, the penetration depth of a H ion at 10 eV has been estimated in about 2 nm from data on amorphous hydrogenated carbon,[189,190] wheras the actual cross-linking induced depth for 10 eV ions reaches up to a depth of 10-20 nm.[191,192]

eager to bond to C, H and Si atoms, and will be able to react with reactive sites but, even most frequently, also with non-reactive sites.

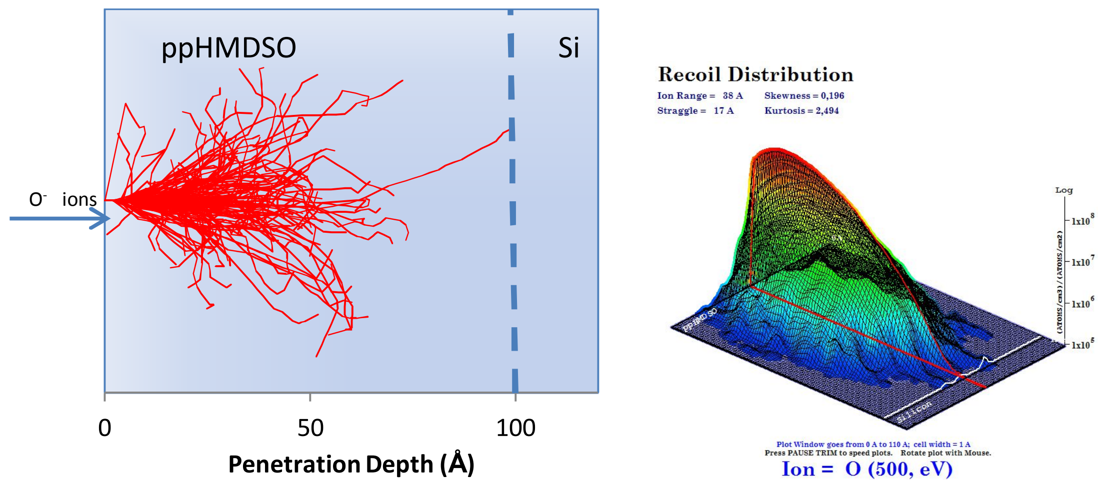

FIGURE 4.24. (LEFT) 2-D simulation of the scattering trajectories of 100 oxygen ions with an incident energy of 500 eV within a low-density ppHMDSO film. **(RIGHT)** Distribution for 1000 recoiled atoms.

Diffusion models

After showing that the modification effected by direct ion collision and the subsequent generation of reactive sites cannot explain alone the results which indicate that the oxidation treatment can proceed to a depth >100 nm, we will discuss if the mechanisms of ion and neutral diffusion could be compatible with these results.

Once an energetic ion has transferred all energy in excess of the lowest bond energy (Si-Si, 2.34 eV) to the atoms within the first nanometers beneath the surface, it cannot break any more bonds by inelastic collisions and it becomes a 'non-destructive' ion. These ions and neutral atoms do not have sufficient energy to generate sputtering or create reactive sites. Still, the kinetic energy of ions (around 0.1-2.3 eV) can be much higher than the thermal energy of atoms in the plasma or in the solid network (0.05 eV at 100°C). These ions will diffuse following a concentration gradient, from the ion density at the surface of the film towards the nule density at the interface of the film with the substrate. Diffusion will proceed until the atom has been captured in a bond and incorporated into the film, or the gradient has disappeared, or the atom has permeated through the whole thickness of the material. The main difference between a 'low-energy' O_2^+, O_2^- or O^- ion and a neutral O

atom is that the equivalent temperature for 1-2 eV ions is around 20-40 times higher than for a thermalized neutral atom (neutrals cannot gain energy from the electric fields), and therefore ion diffusion can be much faster than neutral diffusion; also the size is slightly different for anions, cations and neutrals and for monoatomic and diatomic ions, but for oxygen diffusion in SiO_2, size has been shown to have a small effect on the diffusion coefficient.[193]

Roberts et al.,[194] proposed four different paths for diffusion, depending on the width of the free space channel available for the atom or molecule to penetrate an apparently solid material, i.e. following IUPAC nomenclature:

- Macro-defects: pores, pinholes or cracks (width > 50 nm)
- Mesopore channels (width between 2 nm - 50 nm)
- Micropore defects (atomic interspace between 0.3 – 2.0 nm)
- Defect-free lattice (atomic interspace 0.2-0.3 nm)

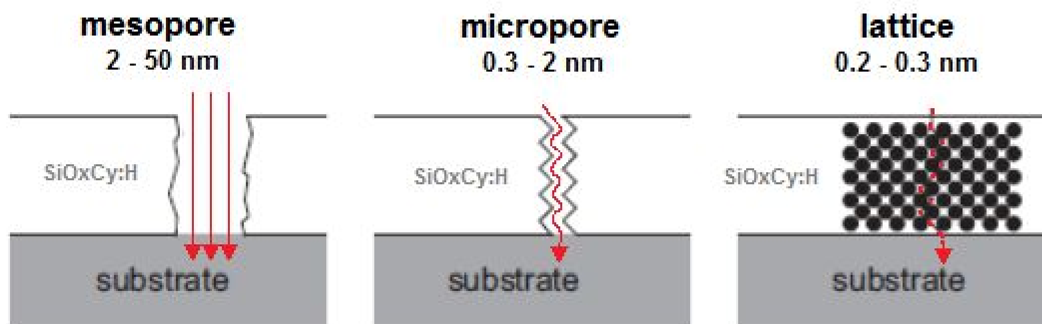

FIGURE 4.25. Representation of paths channeling the diffusion of atoms through the films.

For amorphous plasma-polymer films, the first mechanism is excluded, since the films are generally pinhole free and crack free. Mesopore channels and nanopore defects may exist, especially in grain boundaries of low density films that have been grown with a fast deposition rate under high-flow energy-deficient plasma conditions or in the afterglow, such as the one shown in Figure 4.26-left, without significant ion bombardment. For medium and high-density films, diffusion needs to proceed through vacancies in the disordered 3D network. It is reasonable to expect that the smaller the channel, the slower diffusion will proceed, but in low density films with larger channels and some degree of porosity, diffusion could be quite fast.

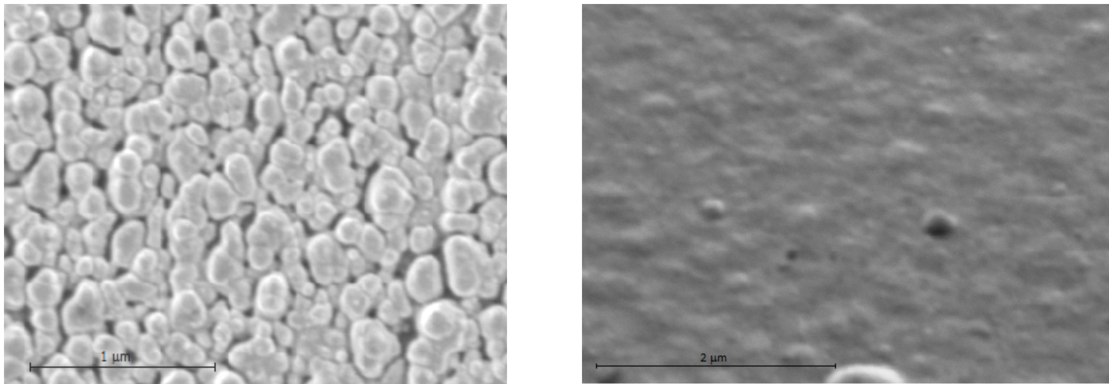

FIGURE 4.26. (LEFT) SEM image (normal incidence) showing the structure of a low density ppHMDSO film deposited under very high-flow energy-deficient plasma conditions in the near afterglow. The mesopore channels between grain boundaries can be easily distinguished. These channels accelerate diffusion of oxidizing species. **(RIGHT)** SEM image (45º tilt) showing the denser, channel free surface of a medium density ppHMDSO film deposited on a substrate placed at the anode, within the plasma and therefore submitted to ion bombardment during growth. The sample is tilted with the SEM chamber in order to enhance the topography of the surface, which would be otherwise undistinguishable at normal incidence.

When oxidation begins to develop at the surface and a SiO_x-like layer starts developing, the structure will get compacted and denser. Diffusion will sill proceed, though at a slower rate. Even in the case of a defect-free crystal structure, the activation energy required for an ion to diffuse is fairly low: in SiO_2 it has been calculated around 0,3 eV for molecular O_2 and 1.3 eV for atomic O, and, again, it should be lower for our amorphous less dense SiO_xC_y:H films, but still higher than the one for PDMS, which is around 0.2 eV.[193,195–197]

In order to estimate if diffusion of the oxygen atom and the oxygen anion can proceed fast enough in ppHMDSO films so that a depth around 100 nm can be reached in about 10-30 min, we will use a simple model and we will apply the diffusion laws by Fick. Fick's first law states that the flux of particles, j, entering an infinitesimal volume of material at a given position is proportional to the concentration gradient across that volume, where D is the diffusion coefficient:

$$j = -D\nabla c \qquad (Equation\ 4.2)$$

Fick's second law is derived from the first law by applying a mass balance through an infinitesimal volume element, and for a semi-infinite material with isotropic properties can be written as:

$$\frac{\partial C(x,t)}{\partial t} = D \cdot \frac{\partial^2 C}{\partial x^2} \qquad \textit{(Equation 4.3)}$$

If we assume that the concentrations of the O atom and the O^- ion at the surface of the film at x=0 are both constant magnitudes, C_0, throughout the plasma treatment duration, and we neglect that part of the O atoms will be lost due to reaction at reactive and non-reactive sites along their way to the deeper region of the film, equation X can be solved to produce the analytical solution of the concentration profile:

$$C(x,t) = C_0\left(1 - erf\left(\frac{x}{2\sqrt{Dt}}\right)\right) \qquad \textit{(Equation 4.4)}$$

Equation 4.4 is known as the Grube solution of diffusion. The value of $\sqrt{(D \cdot t)}$ represents the penetration depth at which the concentration of oxygen atoms/ions is half the concentration at the surface. We can normalize by the particle concentration at the surface to obtain the normalized concentration profile at any time; only the diffusion coefficient, D, for a given particle and material is unknown.

Diffusion coefficients are temperature dependent and follow an Arrhenius behavior with an apparent activation energy for diffusion, ΔE_D:

$$D = D_0 \cdot exp(-\Delta E_D / K_B T) \qquad \textit{(Equation 4.5)}$$

Since the energy of atoms and ions is quite different, Equation 3.5 implies that the diffusion of the more energetic oxygen ions will be faster than the diffusion of oxygen atoms. We cannot strictly transform the energy of ions to calculate an independent diffusion coefficient for ions because Equation 4.5 requires that the temperatures of the particle and the solid matrix be the same, but we can assume that energetic particles will diffuse faster than thermalized particles in any case.(25)

Published data is available for the activation energies and diffusion coefficients of oxygen in PDMS and SiO_2,[195–198] although the values can vary up to five orders of magnitude for SiO_2 depending on the exact composition, density and structure.

(25) For O^- ions with energies of 1eV and 2eV the equivalent temperatures would be 7700 K and 15400 K respectively, which is far beyond the melting point and boiling point of any substance. It is clear that the Arrhenius approximation does not hold for these temperatures, where the material ceases to be a solid network of atoms.

Oxygen diffusion proceeds much faster in PDMS and can be slowed down by many orders of magnitude by a defect-free SiO_2 barrier film. Table 4.8 displays the diffusion coefficients, activation energies and half-concentration penetration depths after 10 min diffusion for SiO_2[196] and PDMS.[197] From these data, it is clear that the difference of oxygen penetration between SiO_2 and PDMS is more than seven orders of magnitude. We can assume that the corresponding values for ppHMDSO films should be somewhere in between.

	Activation Energy (eV)	Diffusion coefficient D_0 (cm^2/s)	Diffusion coefficient D 25 ° C (cm^2/s)	$\sqrt{(D \cdot t)}$ (nm)
PDMS	0.207	1.02×10^{-5}	3.25×10^{-9}	13964
SiO_2	1.170	2.9×10^{-4}	5.90×10^{-24}	0,0006

TABLE 4.8. Activation energies and diffusion coefficients for PDMS[195,197] and SiO_2.[180][

We can calculate the apparent diffusion coefficient of ppHMDSO films by fitting Equation 4.4 to the depth profile of the increase in oxygen concentration with respect to the bulk of the film from experimental data measured by XPS, but only for those treatments that have not reached saturation. Figure 4.27 shows the oxygen depth profile for two different treatments, 120s and 240s DC plasma treatment in oxygen.

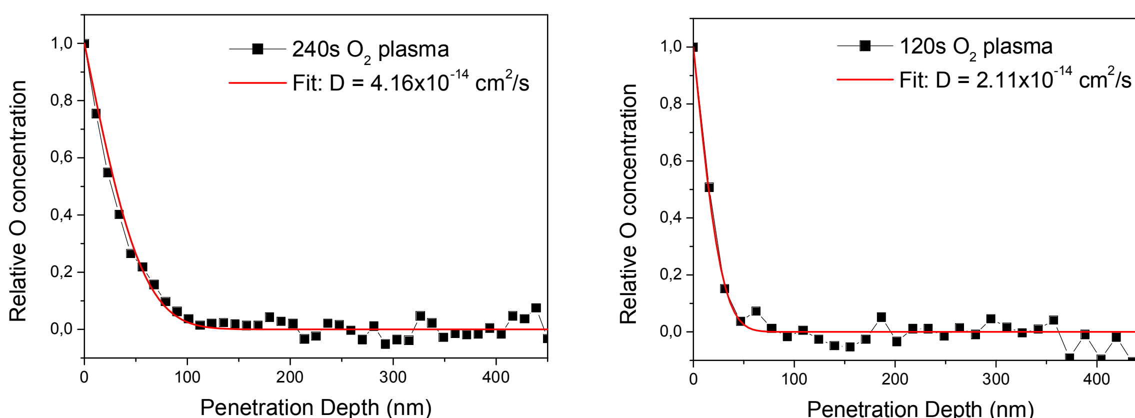

FIGURE 4.27. (LEFT) XPS depth profile for the normalized increase of O concentration with respect to the bulk of the film for a DC O_2 plasma treatment applied for 240s on a medium density ppHMDSO film. The red line indicates the fit for the Grube diffusion solution. **(RIGHT)** Equivalent data and fit for a 120s plasma treatment.

The diffusion coefficients thus obtained for ppHMDSO films are in the range 2×10^{-14} cm^2/s to 4×10^{-14} cm^2/s, which, lies mid way between the reported coefficients for PDMDS and SiO_2. Figure 4.28 shows the simulated depth profiles for the relative increase in atomic oxygen concentration due to diffusion for $D=3\times10^{-14}$ cm^2/s. The simulated penetration depths are of the same order of magnitude than those estimated by XPS, ellipsometry of FTIR, and thus we can conclude that diffusion is the governing physical mechanism that explains the penetration of the plasma treatment for reactive gases.

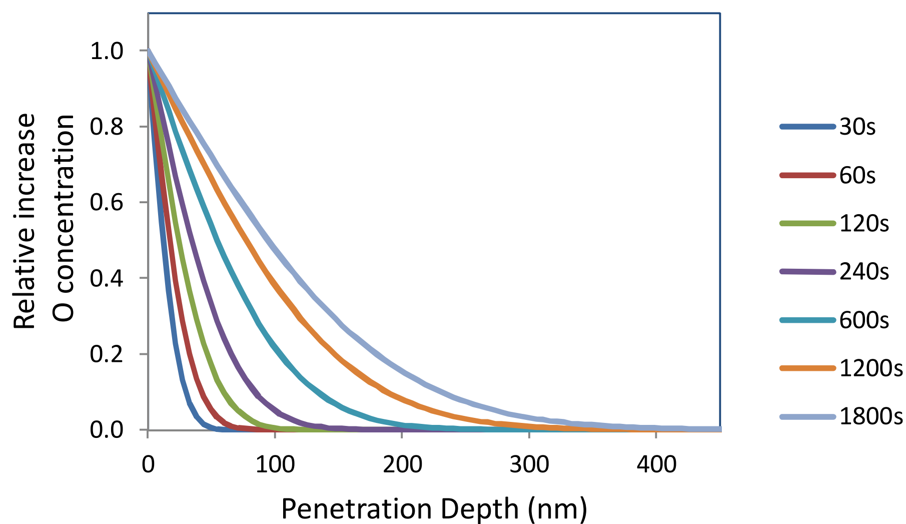

FIGURE 4.28. Simulated diffusion profiles for $D=3\times10^{-14}$ cm^2/s.

These diffusion coefficients and the corresponding penetration depths are only a first estimation, but a more accurate model should take into account the following processes:

- The fraction loss of diffusing atoms due to recombination with reactive sites in the film. The recombination may generate volatile species (CO_2, H_2O, $H_2C=O$) resulting from the combustion of organic groups, or oxygen incorporation to the film via Si-O-Si, Si-O-C or Si-OH bonds. Formation of volatile species will proceed faster and will not contribute to the XPS signal.
- The variation of the diffusion coefficient as the first layers of the film are oxidized, creating a barrier for further oxygen diffusion. This means that the diffusion coefficient is actually not constant, neither with depth nor with time.

- The porosity of the film (tortuosity can be neglected for thin films), if there are micro or nano-channels involved, which is only true for fast-grown films in the energy-deficient regime.

The first two effects (loss of oxygen atoms and development of a surface denser oxidized barrier) result in a slower diffusion than what would result in a homogeneous medium.(26)

On the contrary, porosity creates a faster equivalent diffusion than what would occur in a homogeneous film. Shamiryan et al. clearly demonstrated that after oxygen plasma treatment of a SiOxCy:H low-k film the penetration depth of the oxidized/carbon-depleted layer was much larger for a film with higher porosity.[199] Oszinda et al. reported that plasma treatments could remove carbon from the first 140 nm under the surface from a 25% porous SiOxCy:H film in just 60 s.[200] This could be reasonable since the diffusion coefficients reported for porous films are in the range 1×10^{-8} cm^2/s to 5×10^{-8} cm^2/s,[201] which is much faster than for non-porous films and even faster than for PDMS. Maex et al. proposed a method to measure the porosity of thin films by measuring the change in optical properties produced by the occupation of void volumes by toluene gas[202] and Hoyas et al. employed that method to confirm the reduction in porosity achieved by submitting the films to different plasma treatments.[201]

The previous discussion has been particularized for an oxygen plasma. For non-reactive gases, such as is the case for Ar treatments, all mechanisms remain valid, except for the fact that Ar^+ ions are not incorporated in the film by any kind of bond. They could be trapped for some time (implanted) by they would eventually diffuse to the surface and would be released to the atmosphere. In this case, the penetration depth is extremely difficult to determine, since the chemical modification and density change are minimum. If any modification could be detected deeper than the first 10 nm, it should not be attributed to Ar^+ ion diffusion, but should be necessarily related to reactive site generation by other means, which could only be possible by UV absorption and photodissociation of bonds.

In any case, the depth of penetration of ions is extremely difficult to match to a theoretical model. Ion bombardment effects in solids immersed in plasmas can

(26) Including these effects to obtain a more accurate estimation of diffusion coefficients is out of the scope of this thesis, but could be of practical importance for applications where the gas barrier properties of ppHMDSO films are sought.

penetrate much deeper than would be expected from Monte Carlo simulations of collision models. Some authors claim that it is effected by an increased athermal diffusion coefficient that can be explained by ever existing hydrogen ions moving deeper inside the bulk of the material and initiating additional reaction sites.[203,204]

From the XPS depth profiles, the amount of additional oxygen atoms incorporated to the film can be also estimated and compared to the amount of oxygen atoms in the film before the onset of the plasma treatment. This value is clearly related to the flux of oxygen atoms arriving at the surface and to the treatment time. The absolute amount of oxygen atoms per unit area in the untreated film can be calculated, step by step, through the following related magnitudes:

1) The stoichiometric formula $Si_xO_yC_zH_t$ for the untreated film, including H: the atomic formula derived by XPS for an untreated film is $SiO_{0.61}C_{1.89}$:H. Since H cannot be detected by XPS, we can approximately quantify it by considering that most of the H atoms will be linked to either Si (Si–H bonds) or C ($Si–CH_2$ and $Si–CH_3$ bonds) but none to O (–OH will be neglected) and assuming that a maximum of 1/10 Si atoms are bonded to H, and that 1/3 of H atoms bonded to C are in $–CH_2$ groups and the rest in $–CH_3$; we can obtain the relative amount of H as $[H] = [Si]\times 0.1 + 3\times[C]\times 2/3 + 2\times[C]\times 1/3$. The final formula thus calculated is $SiO_{0.61}C_{1.89}H_{5.13}$.
2) The average molecular weight, *M,* for the estimated stoichiometry: 65,57 g/mol.
3) The number of molecules per unit area, N_{molec}, given by $N_{molec} = N_A \times t \times D/M$, where N_A is Avogadro's number, *t* is the thickness of the film, *D* the density, *M* the estimated average molecular weight; thus: $N_{molec} = 5{,}45\times 10^{17}$ molecules/cm^2.
4) The number of oxygen atoms per unit area in the film, N_{oxygen}, prior to O_2 plasma treatment: $N_{oxygen} = 5{,}45\times 10^{17}$ molec/cm^2 $\times$ 0.61 atoms/molec = $3{,}33\times 10^{17}$ atoms/cm^2.
5) The normalized amount of XPS signal generated by electrons escaping from the oxygen atoms in arbitrary units:

$$I_{XPS} = \int_{t=0}^{t=450nm} i_{XPS}(t) \cdot dt$$

whence the integrated XPS signals for the treated and untreated films, $I_{XPS}^{untreated}$ and $I_{XPS}^{treated}$, can be calculated.

6) The amount of oxygen atoms incorporated into the film per unit area, assuming that the yield of X-ray photoelectrons is the same for the treated and untreated materials:

$$\Delta N_{Oxygen} = \frac{I_{XPS}^{treated} - I_{XPS}^{untreated}}{I_{XPS}^{untreated}} \times N_{Oxygen}^{unt}$$

Figure 4.29 shows the calculated amount of oxygen atoms incorporated to the film, ΔN_{oxygen}, as a function of the treatment time. For shorter treatment times, the amount of oxygen atoms incorporated increases almost linearly up to 600 seconds, at a constant rate of 1,3x10^{14} atoms/(s·cm^2). Following the same rationale the amount of carbon atoms removed from the film, can be calculated. Figure 4.29 also shows the total estimated amount of carbon atoms, which shows the inverse trend as for oxygen incorporation.

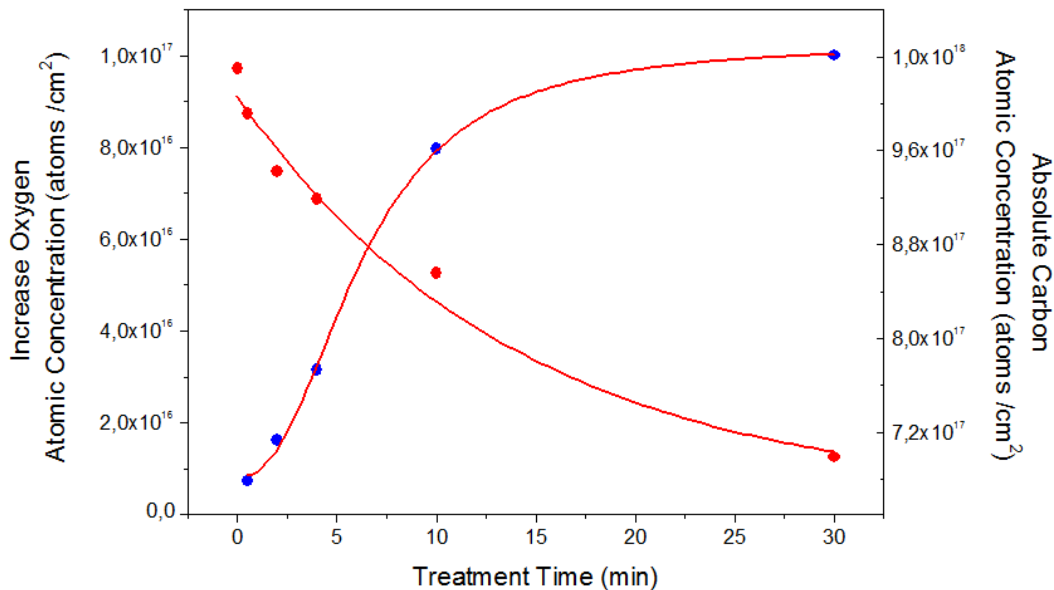

FIGURE 4.29. Increase in amount of Oxygen atoms relative to the untreated film and absolute amount of Carbon atoms as a function of treatment time.

According to these estimations, for each oxygen atom incorporated to the film 3.8 C atoms are removed in average. This is indicative of the fact that Si–O–Si bond formation proceeds slower than C removal. The flux of oxygen atoms arriving at the surface must be larger than the amount of atoms sticking to the film to create the

silica-liker layer, since part of them will be employed in the oxidation of organic species and removed as volatile combustion products (CO_2 and H_2O mainly).

4.3.2.2. Chemical reactions involved in the post-treatment of ppHMDSO

Argon plasma treatment

From the chemical perspective, modification of ppHMDSO films with inert gas plasmas such as argon is analog to the plasma modification of bulk polymers by inert gases, which was first described by Hansen and Schonhorn in 1966 under the acronym *CASING*, *Cross-linking by Activated Species of Inert Gas*. As mentioned before in this chapter, for bulk polymers it is easy to determine the amount of cross-linking, but for plasma polymers there is no standard method available. In the case of ppHMDSO, the main chemical mechanisms of cross-linking start with either H or CH_3 cleavage (Figure 4.30), when sufficient energy is provided by UV photons or Ar^+ ions, since C–H and Si–CH_3 bonds have the lowest binding energies (3.49 and 4.51 eV respectively).

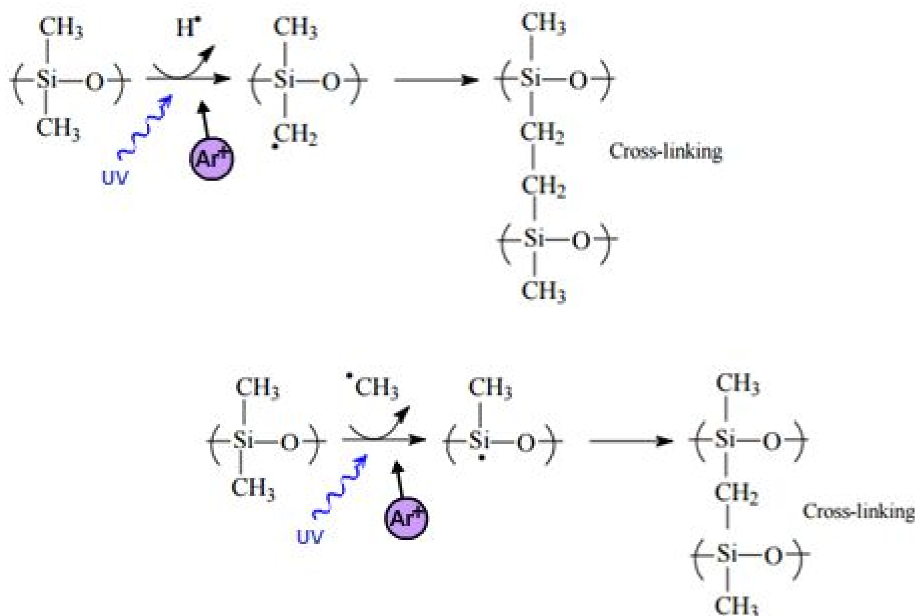

FIGURE 4.30. Main mechanisms of CASING in ppHMDSO.

Cross-linking is subsequently achieved by the formation of C–C bonds after –H removal from a methyl group, as in Si–CH_2–CH_2–Si bridges; Si–CH_2–Si bridges are also

possible after –H and $–CH_3$ removal; Si–Si bonds are in principle also possible but these require that one of the Si atoms is detached from all oxygens, which is much less frequent due to the high binding energy of the Si–O bond.

Evidence of additional cross-linking by Ar plasma treatments can be found in FTIR spectra. Figure 4.31 shows FTIR spectra for Ar plasma treatments of a low density ppHMDSO film at three different treatment times (10, 20 and 30 min). In this area, we can find the $–CH_3$ group asymmetric stretching at 1409 cm^{-1} and the scissor vibration of $Si–CH_2–Si$ at 1355 cm^{-1}.[133,136,145,158] The reduction in the concentration of CH_3 bonds is proportional to the increase in the concentration of CH_2-related peaks, specially the increase in the scissoring vibration. Precise quantitative analysis based upon these peaks would not be reliable since their intensity is rather small and the baseline correction is larger than the actual peaks, but qualitative analysis indicates that lengthier plasma treatments produce additional cross-linking to the pre-existing amount of bridges in the untreated film.

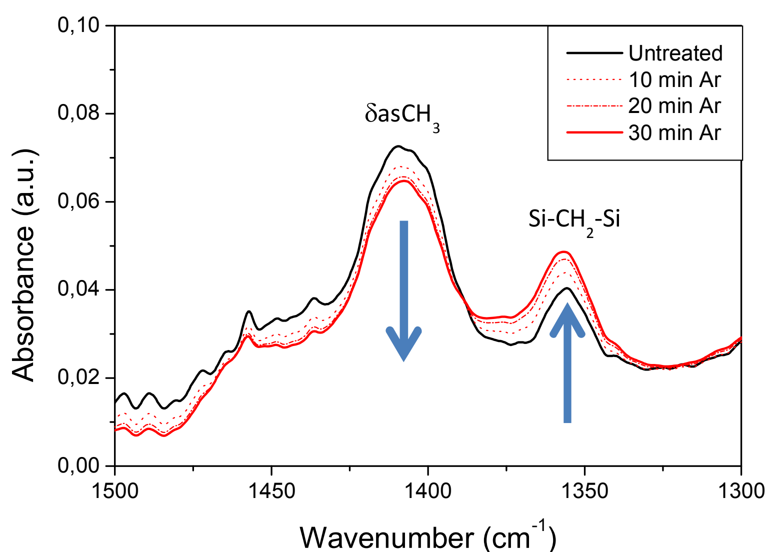

FIGURE 4.31. FTIR of Ar plasma treated ppHMDSO at different treatment times. The arrows indicate the increase of $Si–CH_2–Si$ bridges and the associated decrease of $Si–CH_3$ terminal groups.

In addition to cross-linking, some authors report that for plasma treatments in Ar a certain amount of oxidation by incorporation of carbonyl (C=O), carboxyl (HO-C=O) and hydroxyl (C-OH) groups at the surface is inevitable, even with the use of extremely pure inert gases. In principle, pure Ar treatment should be possible, but in practice it has been shown that for reasonable times of process, there is always a

certain amount of adsorbed water and oxygen at the reactor surface which desorbs during the plasma process, specially for reactors without a load lock, where all the surfaces are exposed to ambient atmosphere for insertion and removal of samples after each deposit. The desorbing gases can then contribute to a small fraction of the total pressure in the plasma and result in some oxidation.[133,169]

Oxygen plasma treatment

In Chapter 2, it was shown that the stability of ppHMDSO in air does not produce a permanent degradation or modification of the films, other than the reversible incorporation of physiadsorbed water (non-covalently linked). This means that at ambient temperatures molecular oxygen is obviously not capable of oxidizing the organic groups linked to the Si-O-Si backbone. Silicones are known to be stable in oxygen atmospheres up to 250°C and up to 400°C in vacuum.[205–207] At higher temperatures, combustion of silicone aerosols in oxygen flames produces SiO_2, CO_2 and H_2O, which are the same end products as for plasma deposition from HMDSO and O_2.

The energy provided by the oxygen plasma is employed in two different ways: first, it generates reactive species in the plasma by electron impact: O_2^*, O_2^+, O, O_2^- and O^-; secondly, it transfers energy to the atoms in the film by photon absorption and ion bombardment, which is mostly relaxed through cleavage of weaker bonded groups. Direct photoablation of groups by energetic photons is also possible.

Several reaction paths have been proposed for the oxidation of ppHMDSO films. Among them, condensation of silanol groups is the most widely accepted.[152,208–211] The presence of silanol groups is indicated in the FTIR spectra of oxygen plasma treated films, by a broad band clearly distinguished at 3200-3600 cm^{-1} and a weaker band corresponding to Si-OH stretching in the region 900 – 970 cm^{-1}, which is masked and overlapped with stronger bands. Van Hest et al. also suggest that direct oxidation by oxygen radicals of dangling bonds in Si is possible.[152] Finally, Waddell et al. reported that C=O-OH (carboxyl) groups can be temporarily created during UV irradiation of PDMS[212] and evolve to Si-OH by abstraction of formaldehyde. We have not found contribution of the carboxyl group in our FTIR spectra, and neither does it produce any signal in OES spectra, but some authors report that in-situ FTIR and QMS

analysis of the volatile gas species show molecular fragments compatible with this assumption.[208]

Figure 4.31 summarizes the reaction paths leading to the direct oxidation of Si and to the oxidation reactions of Si-H and Si-CH_3 groups with oxygen radicals resulting in silanol groups and followed by silanol condensation. No signs of other polar groups such as carbonyl or carboxyl has been found in the FTIR spectra of our samples and therefore, if existing, these groups must be formed in a very low amount.

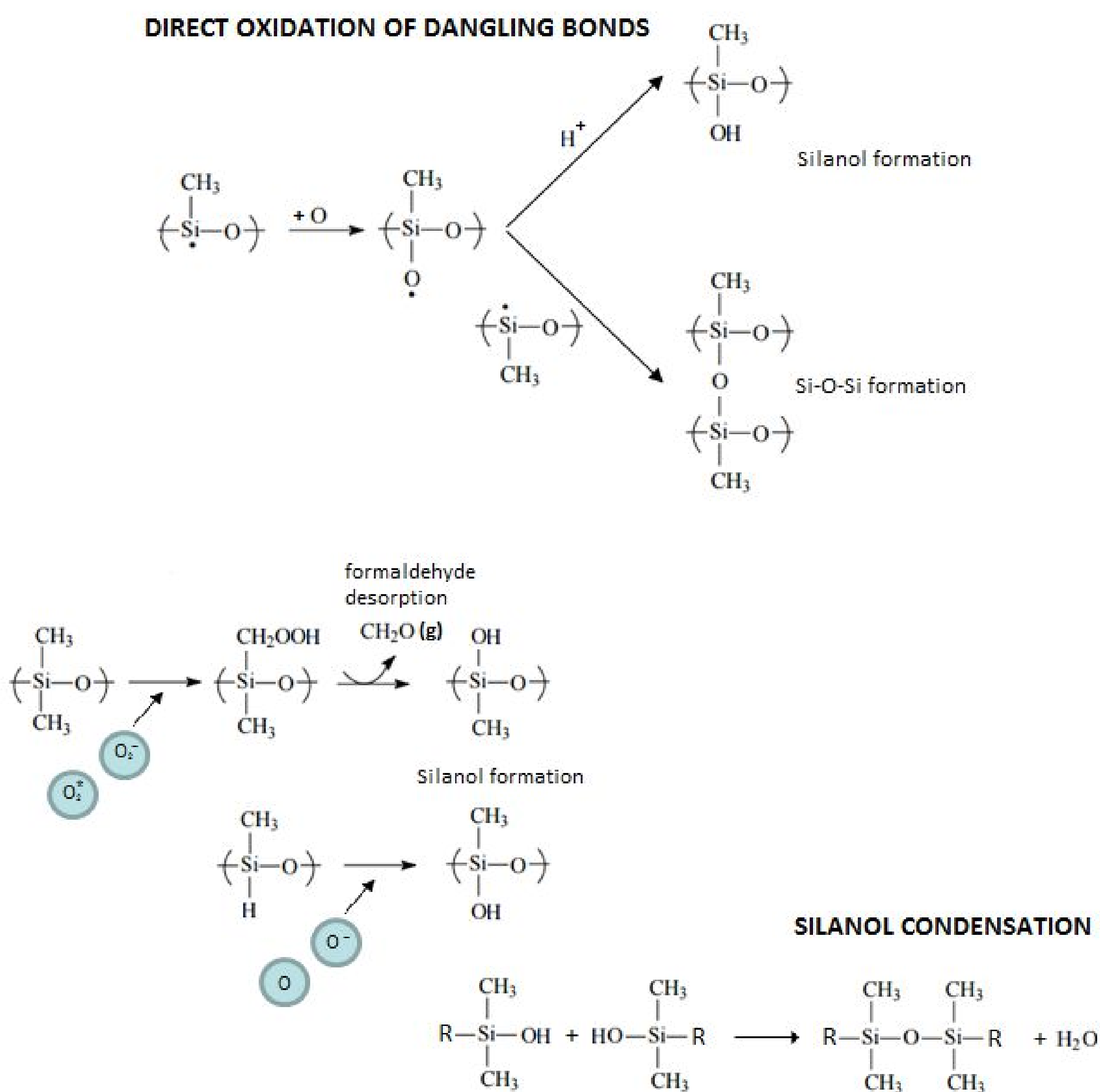

FIGURE 4.32. Chemical reactions leading to the oxidation of ppHMDSO films: oxidation of dangling bonds, formation of silanol groups, condensation of silanol groups.

4.3.4. Functional properties of plasma-treated PPHMDSO films

In previous sections we determined that plasma treatments in Ar or N_2 produce a slight increase in the cross-linking of the first few nanometers at and under the surface of the treated films, and some oxidation if contaminant traces of oxygen or water vapor are available to the plasma. In O_2 plasma treatments almost complete oxidation and carbon depletion is achieved at the surface of the film and partial oxidation of a region thicker than 100 nm below it. As a consequence, after these treatments the films are slightly densified and their properties should be shifted towards those of silica. The effects that these changes induce in the mechanical and hydrophobic properties of the films have been studied by measuring their hardness and wettability prior and after different plasma treatments.

4.3.4.1. Mechanical properties of plasma treated ppHMDSO films

We have assessed the improvement of hardness by different plasma treatments by measuring the load-unload nanoindentation displacement curves at applied loads below 1.0 mN. Several indenters were used: spherical, Berkovich and Corner-Cube. The Corner-Cube indenter proved to be the most sensitive to changes in the thin modified region of the films after plasma treatments, but we did not have a model to extract hardness values for this indenter. The partial unload method with spherical indenter was used to get a qualitatively measurement on the gradual change of hardness in the first 100 nanometers of the modified film.

Argon plasma-treated samples

Figure 4.33 shows the load unload-displacement curves at 0.35 mN and 0.50 mN maximum loads, as measured by the UMIS nanoindenter on medium-density ppHMDSO films modified in Ar plasmas for 10 and 30 min. The untreated ppHMDSO film is also shown as a reference. Under these conditions, the penetration depths of the indenters are limited to the first 125 nm for the Berkovic indenter and to 250 nm for the Corner Cube, which is still below the thickness of the films (450 – 500 nm), but well above 1/10 penetration/thickness criterion. This implies that the hardness values and Young's moduli obtained are affected to some extent by the properties of the substrate.[212] A reduction in the maximum penetration depth of the indenter and

in the slope of the loading curves is found for both indenters and both treatments, which is indicative of a higher hardness and elastic modulus than that of the untreated film. In addition, the residual penetration depth after unloading is slightly increased, which is related to a reduction in the elastic recovery rate when the surface is modified between an elastic-like behavior and a plastic-like behavior.

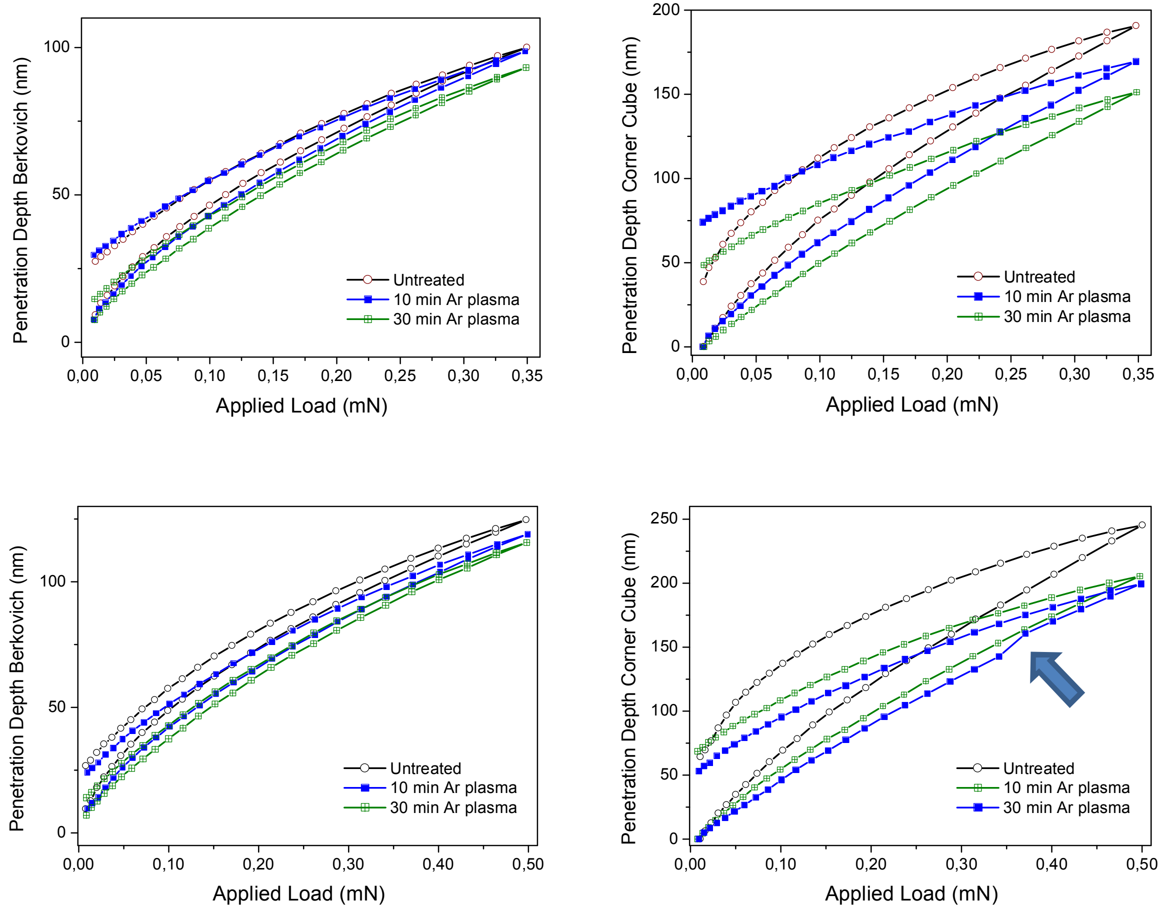

FIGURE 4.33. Load-unload displacement curves at 0.35 and 0.50 mN maximum applied force for untreated and Ar plasma-treated ppHMDSO films. **(LEFT)** Berkovich indenter. **(RIGHT)** Corner Cube indenter.

It is clear from the nanoindentation curves that the Corner Cube indenter produces a higher penetration depth, but at the same time it is more sensitive to small changes than the Berkovic one. In addition, a closer look at the displacement curves at 0.50 mN reveals a sudden change in the slope of the curve for the 30 min Ar plasma treatment sample which was not detected by the Berkovic indenter. This effect is also found in the plasma treatment of conventional polymers and is related to a discontinuity fracture of the interface between the modified region and the unmodified region.[124,132] The penetration depth at which the discontinuity is

detected is about 135 nm (indicated by a blue arrow in the figure). This value is consistent with the thickness of the modified region obtained in medium-density films for 30 minutes of treatment time in O_2 and it should be in the same range for equivalent treatment times in Ar, although the modified depth for non-reactive treatments cannot be measured by the techniques employed in our study, as shown earlier in this chapter. In any case, this discontinuity is a good indication that 30 min of Ar plasma in the experimental conditions employed is an excessive treatment time that generates an internal stress in the structure of the modified film, leading to fracture and possible adhesive failure, which would be detrimental for the mechanical performance in real-life applications. Table 4.9 summarizes the average penetration depth for the untreated, and Ar plasma-treated samples, for the Berkovic and Corner Cube indenters. Values for hardness and elastic recovery[(27)] are also shown.

AVERAGE PENETRATION DEPTH (CORNER CUBE INDENTER)			
APPLIED FORCE	**Untreated**	**10 min Ar**	**30 min Ar**
0.35 mN	187 nm	167 nm	152 nm
0.50 mN	249 nm	205 nm	196 nm
1.00 mN	370 nm	334 nm	328 nm
AVERAGE PENETRATION DEPTH (BERKOVICH INDENTER)			
0.35 mN	90 nm	89 nm	86 nm
0.50 mN	115 nm	109 nm	108 nm
1.00 mN	173 nm	172 nm	170 nm
HARDNESS / ELASTIC RECOVERY / ELASTIC MODULUS (BERKOVICH)			
HARDNESS	0.94 GPa	0.99GPa	1.03 GPa
ELASTIC RECOVERY	79.8%	56.3%	67.8%
ELASTIC MOD	16.4 GPa	17.6 GPa	18.6 GPa

TABLE 4.9. Summary of average maximum penetration depths, hardness and elastic recovery values for Ar plasma-treated ppHMDSO films.

[(27)] Each load-unload measurement is replicated several times at different spots to reduce the probabilty of indenting onto debris, which would produce false results. This allows to discard outlier measurements. Elastic recovery and hardness are calculated only for the Berkovich indenter as described in Chapter 2 – Experimental.

Oxygen plasma-treated samples

Figure 4.34 shows the load-unload displacement curves for a Corner Cube indenter measured at maximum applied loads of 0.35 and 0.50 mN on the following samples: an untreated medium-density ppHMDSO film, equivalent ppHDMSO films exposed to oxygen plasmas for 0.5, 1, 4, 10 and 30 min, and fused silica.

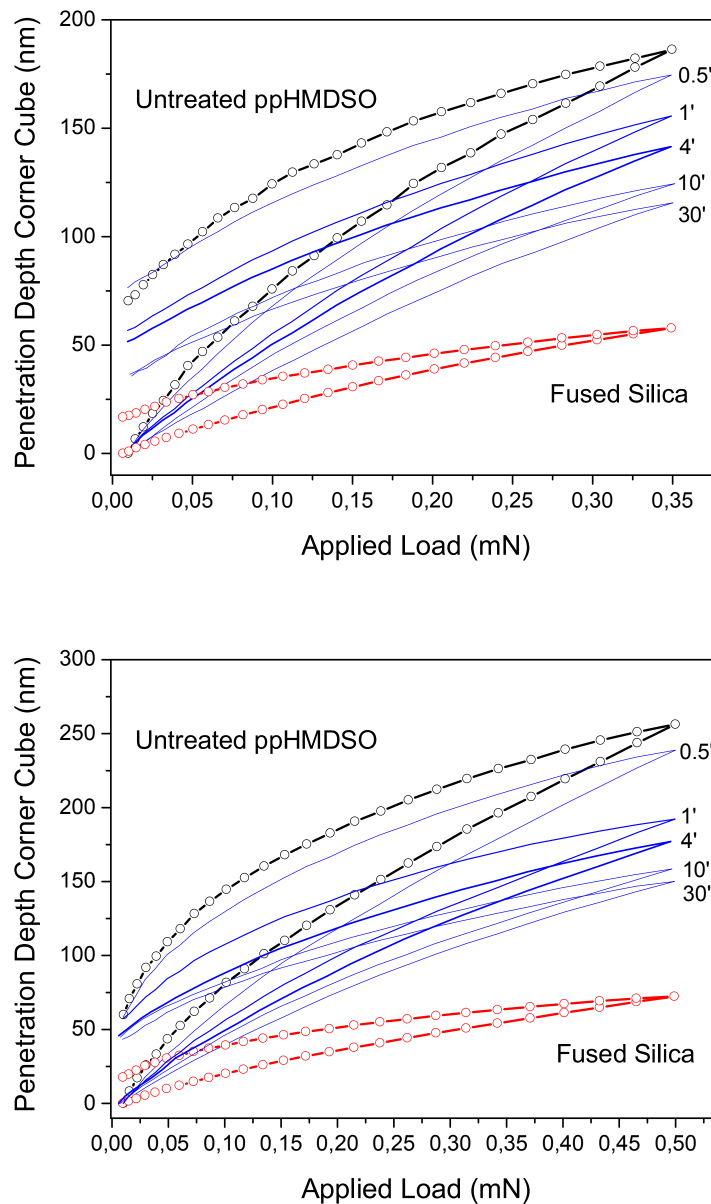

FIGURE 4.34. Load-unload displacement curves at 0.35 and 0.50 mN maximum applied force for untreated and O_2 plasma-treated ppHMDSO films. **(LEFT)** Berkovich indenter. **(RIGHT)** Corner Cube indenter.

For the same applied load, the maximum penetration depth decreases with increasing treatment time, which is consistent with an increasing thickness of the

silica-like modified region of the film. The reduction in penetration for treatments of 10 and 30 minutes is only of a few nanometers, which indicates that the plasma treatment tends to saturate and does not improve much further, even for longer treatment times. Table 4.10 shows the average maximum penetration depths, hardness values and elastic moduli for the same treatment times as in Ar plasma treatments in Table 4.9.

AVERAGE PENETRATION DEPTH (CORNER CUBE INDENTER)				
APPLIED FORCE	**Untreated**	**10 min O_2**	**30 min O_2**	**Silica**
0.35 mN	186 nm	124 nm	116 nm	58 nm
0.50 mN	256 nm	159 nm	150 nm	72 nm
1.00 mN	372 nm	220 nm	213 nm	123 nm
HARDNESS / ELASTIC RECOVERY / ELASTIC MODULUS (BERKOVICH)				
HARDNESS	0.93 GPa	1.90 GPa	2.21 GPa	8.74 GPa
ELASTIC REC	77.0%	71.7%	71.0%	73.7%
ELASTIC MOD	16.2 GPa	20.6 GPa	23.9 GPa	79.2 GPa

TABLE 4.10. Summary of average maximum penetration depths, hardness and elastic recovery values for O_2 plasma-treated ppHMDSO films and Silica.

It is worth noting that both oxygen and argon plasma modification increase the hardness of PPHMDSO films and at the same time maintain the high elastic recovery of the polymer-like structure. This can be explained by the fact that the modified layer does not comprise the whole film in depth and that a polymeric layer still remains underneath. Figure 4.35 shows the evolution of the estimated hardness as a function of the penetration depth for an spherical indenter of 1 μm nominal radius (real radius 0.8 μm according to SEM), during a load-unload cycle with partial unload at each sampling step. The hardness value at each step was calculated following the method by Swain and Field.[124,125] The values obtained by the partial unload method are slightly higher than for the load-unload method with a Berkovic indenter by the Oliver and Pharr method. This is probably due to the fact that the Berkovich indenter produces a different pressure profile and deformation of the film than the spherical

indenter, and therefore the contribution of the underlying material is different for both indenters. In fact, the tip of the Berkovich indenter is not perfect and can have an effective radius up to 10 μm, which is related to the lower penetration depths achieved with this indenter as compared to the spherical indenter. Moreover, the partial unload method achieves an estimation of local hardness of the film, -which is higher at the very surface and diminishes with depth-, whereas the load-unload method produces an effective hardness which is evaluated at maximum penetration. Nevertheless, the measurements with the partial unload technique are qualitatively illustrative of the substantial increase in hardness at the first 50-100 nm of the film after oxygen plasma treatment.

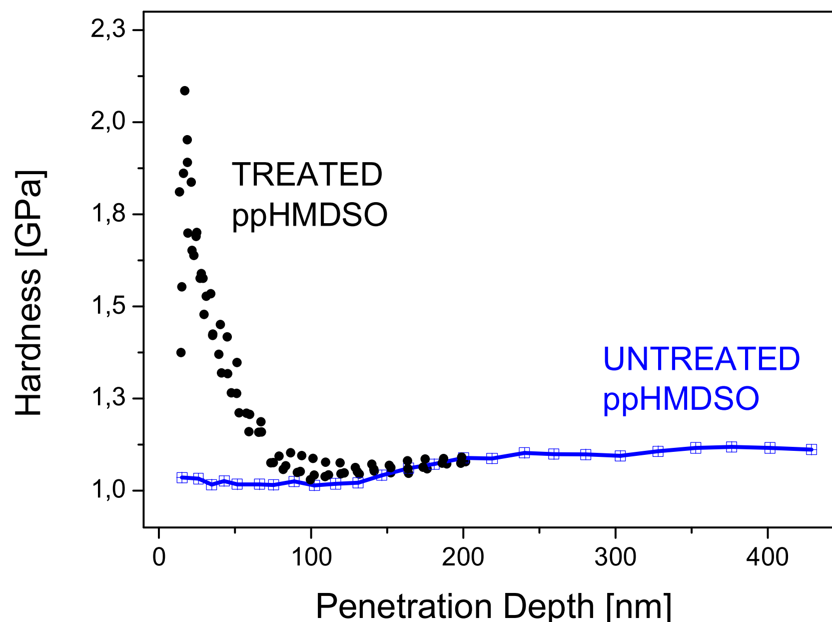

FIGURE 4.35. Elastic modulus as a function of indenter depth for a 10 min oxygen plasma treatment on a medium-density ppHMDSO film.

It has been shown that the hardness and elastic modulus of ppHMDSO films modified by oxygen plasma post-treatment is mid way between the initial properties of the unmodified film and those of fused silica. Since the film has graded properties and the penetration depth is a significant fraction of the total thickness, the effect of the substrate will be significant and the exact values obtained with the Berkovich indenter will depend on the total thickness of the film. In comparison with the

mechanical properties of films deposited from a mixture of O_2 and HMDSO and without a subsequent post-treatment, the properties of a 450-500 nm ppHMDSO film from 100% monomer post-treated for 10 min in an oxygen plasma would be equivalent to the addition of 15-30% of oxygen in the starting precursor mixture.

4.3.4.2. Surface properties: wettability and surface energy

Plasma treatment of polymers is established as a well-known technique for increasing the surface energy and wettability and render the surfaces of the polymers hydrophilic. Table 4.11 shows the values for the water static contact angle for different plasma treatments in Ar and O_2. The values of the contact angles follow two general trends: oxygen is more effective in reducing the contact angle than argon and higher treatment times result in lower contact angles.

	0.5 min	1.0 min	4.0 min	10 min	20 min	30 min
Argon Plasma	--	--	--	38°	36°	33°
Oxygen Plasma	44°	39°	36°	28°	23°	22°

TABLE 4.11. Static contact angle for water drops for samples with different plasma treatments.

We have previously shown that both plasma treatments, either in Ar or O_2, result in etching of organic groups and formation of Si-O-Si bridges and silanol groups. Silanol groups are highly polar groups and therefore increase the polar component of the surface energy. According to the XPS depth profiles, 4 min of oxygen plasma treatment should suffice to deplete the first layer completely of C atoms. FTIR shows that an additional amount of Si-OH bonds is formed with increasing treatment times, but FTIR integrates the complete thickness of the film, while surface energy and wettability only depend on the first 1-2 nm of material which must have been saturated of polar groups already at short times. Therefore, we believe that additional roughness created during extended ion bombardment by the plasma treatment contributes significantly to the effective decrease in the contact angle. Vallée[163] and Grundmeier[160] also reported that there is a clear relation between wettability and surface roughness in plasma-treated ppHMDSO films.

4.3.4.3. Aging of plasma-treated surfaces: hydrophobic recovery

For many applications (microfluidics, printing, adhesion, cell proliferation, etc.…), it is important to maintain the hydrophilic properties of a treated polymer surface over time. Unfortunately, this is not easy to achieve in conventional polymers, which recover their natural hydrophobic behavior in a few hours or days, at most. As an example, when the surface of PDMS is rendered hydrophilic by an Ar or O_2 plasma treatment it recovers its original hydrophobic nature in a time window that may vary from 15 min to 200 h, depending on the treatment. This would unacceptably limit the shelf-life of any commercial product employing such treatment, and therefore would restrain its use in many applications. The effect is commonly known as “hydrophobic recovery” and it is well-documented in the literature.

Reduction of hydrophobic recovery has been sought and partially achieved previously by different authors employing several processes:

1) Increase curing and cross-linking by thermal annealing,[213]
2) Grafting of hydrophilic groups on top of the polymer surface,
3) Deposition of a layer or multilayer of hydrophilic material,
4) Adding surfactants to the pre-polymer mixture before curing,[214]

We have studied and proposed our own solution, which can be classified within group 3. It consists in the plasma deposition of a ppHMDSO film on a PDMS substrate and ulterior post-treatment in an O_2 plasma. Among all possible coatings that could be deposited on PDMS, ppHMDSO shows the best chemical compatibility with the substrate.(28) To the best of our knowledge, this approach has not been previously described in the literature.

Hydrophobic recovery in plasma-treated ppHMDSO and PDMS

First in our study, the hydrophobic recovery of ppHMDSO films after O_2 and Ar DC plasma treatments in comparison to the hydrophobic recovery of PDMS substrates modified with the same plasma treatments was analyzed.

(28) HMDSO is the natural choice since it is the smallest molecule containing the repeating dimethylsiloxane -($(CH_3)_2$-Si-O-Si-$(CH_3)_2$)- unit in PDMS polymer and therefore the chemical compatibility between both materials is perfect.

FIGURE 4.36 shows the static contact angle for two different DC plasma treatments: Ar at 0.1 mbar for 10 min, and O_2 at the same conditions. These treatments were applied to medium density ppHMDSO films (1.52 g/cm^3) deposited onto Al-coated glass substrates, and to 1mm thick PDMS substrates (0.96 g/cm^3). The

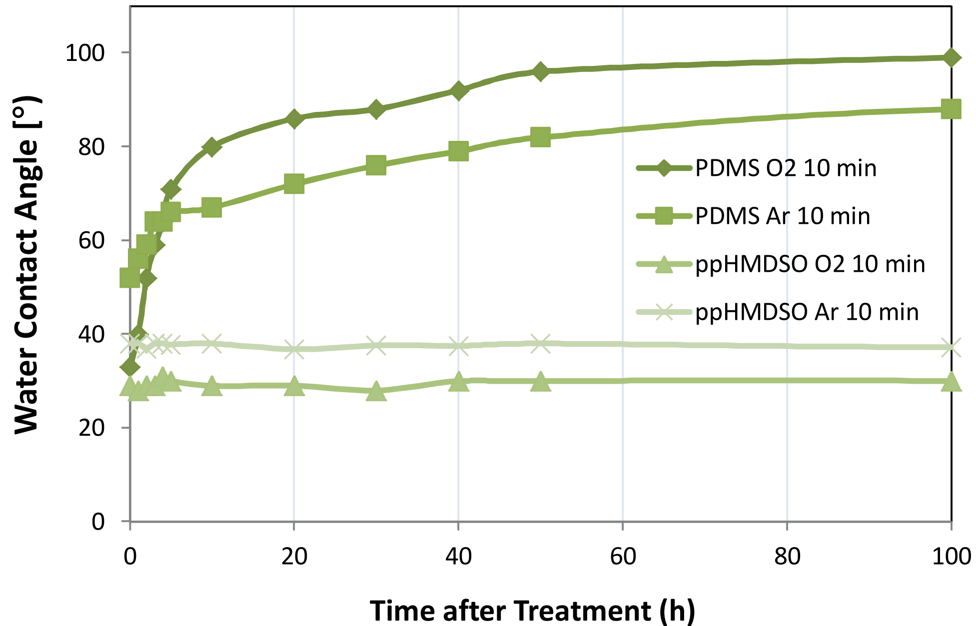

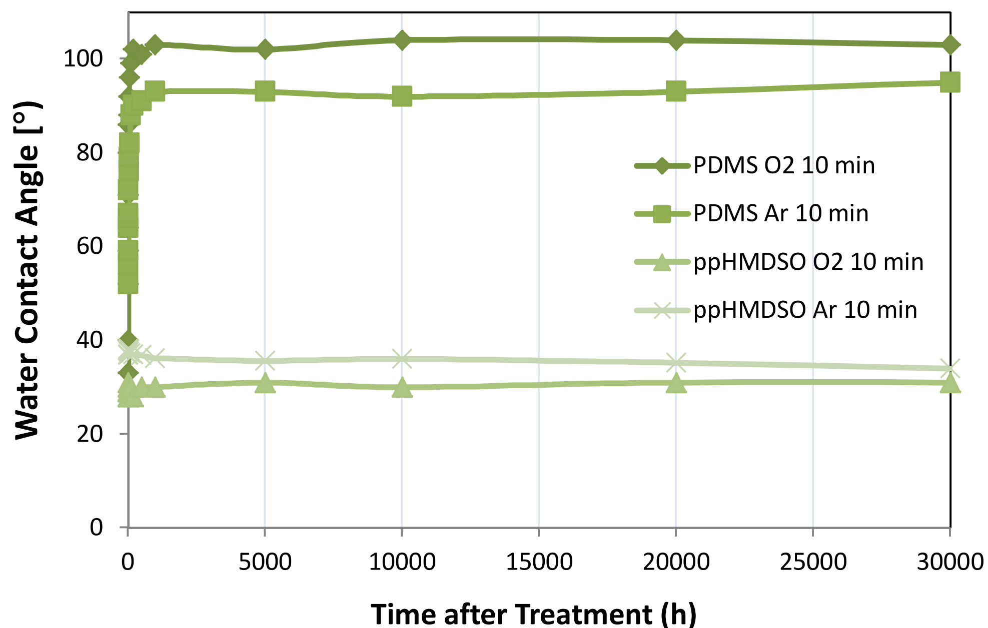

FIGURE 4.36. Hydrophobic recovery for oxygen plasma-treated PDMS, argon plasma-treated PDMS, oxygen plasma-treated ppHMDSO and argon plasma-treated ppHMDSO. (TOP) Hydrophobic recovery up to 100 h. (BOTTOM) Hydrophobic recovery up to 30.000 h.

treated samples were placed on the grounded electrode in a parallel plate DC configuration, as described in Chapter 2. The time series of measurements was extended for as long as 30.000 h (more than 3 years).

From this data it is clear that PDMS treated samples recovered their hydrophobic properties in a few hours, regardless of the treatment, whereas plasma treatment on ppHMDSO renders a hydrophilic surface which lasts at least several years. It is also interesting to notice that O_2 plasmas produce an initial larger reduction than Ar to the water contact angle in PDMS and ppHMDSO: 33° / 29° for O_2, and 52° / 38° for Ar, for PDMS and ppHMDSO respectively. Hydrophobic recovery is faster for the O_2-treated PDMS than for the Ar-treated one; O_2-treated ppHMDSO has no detectable recovery, whereas the Ar treated ppHMDSO film has a negative hydrophobic recovery, i.e., it is slightly more hydrophilic by the end of the experiment than at t=0, right after the treatment. In this case, the difference is very small (from 38° to 34°) and could be due to some additional amount of adsorbed water or to silanol groups formed at the surface during ambient exposure, although no significant change in the absorption bands of –OH groups (3200-3600 cm^{-1}) was detected by FTIR.

In order to understand these results, we need to put them in relation with other experimental studies and with a basic model explaining the mechanisms of hydrophobic recovery, although no studies on the hydrophobic recovery of Ar or O_2 plasma-treated ppHMDSO films have been reported in the literature so far. We will assume that the same fundamental mechanisms for hydrophobic recovery in bulk polymers apply to plasma deposited polymers, but considering the significant differences in density, cross-linking and oligomer content in each case.

With respect to PDMS, the fact that hydrophobic recovery is dependent on the treatment has been reported by several studies.[189–192] Truica-Marasescu et al.[189] concluded that UV-treated polymers suffer much less hydrophobic recovery than plasma-treated polymers, although the initial increase in surface energy may be slightly higher for plasma treatments. Hillborg[215,216] and Kim et al.[190,191] found that the most aggressive treatments generally produce a faster hydrophobic recovery. Battachariya et al.[192] showed that short or prolonged treatments will produce a surface with a higher contact angle than that of medium treatments. Bodas et al.[217] reported that the effect of the same plasma treatment on the hydrophobic recovery

was different for PDMS substrates polymerized with different additives. All these results are consistent with our findings and can be explained by applying the model established by Owen, Kim and Hillborg for hydrophobic recovery[189,191,218] to the different structure of the modified surfaces of PDMS and ppHMDSO produced by Ar and O_2 plasma treatments.

Mechanisms of hydrophobic recovery

The mechanisms leading to hydrophobic recovery are rather complex and Owen et al.[218] summarized them in five different hypothesis:

- Contamination of the surface by organic species during storage,
- Reorientation of polar groups from the surface to the bulk[219,220] or non-polar groups from the bulk to the surface ,
- Condensation of silanol groups at the surface,
- Loss of volatile oxygen-rich species contributing to the polar component of the surface energy to the atmposphere,
- Migration of low molar weight species (LMW) from the bulk to the surface

Depending on the starting PDMS material,[217] curing methods, type of treatment or storage condition[221] any of the aforementioned mechanisms may contribute to the hydrophobic recovery. For plasma-treated PDMS stored under clean conditions and atmospheric pressure, the most likely mechanisms are reduced to three: reorientation of polar groups, condensation of silanol groups and migration of LMW species to the surface, and most researchers believe the latter to be the predominant mechanism.[189–191,216,217,219,220,222] These high-mobility LMW species may have been present prior to the treatment (incompletely cured polymer) or created by the treatment itself by chain scission, but Kim et al. demonstrated that even after extracting all the pre-existing oligomers prior to plasma treatment, hydrophobic recovery still occurs due to the formation of new LMW species *during* plasma treatment.[191,222]

The theoretical mechanism of hydrophobic recovery is as follows: first, during plasma treatment the energetic species (photons, electrons and ions) destroy a multiplicity of bonds in their path from the surface to the inner bulk material. These

open bonds can recombine with neighboring sites and ions in different ways, creating new C-C , Si-Si or Si-C bonds (crosslinking); or Si-O, Si-OH, Si-O-Si bonds (oxidation); or just breaking parts of a longer chain (chain scission of oligomers, which occurs only for PDMS but not for ppHMDSO). If sufficient oxygen is available, oxidation will be the dominant mechanism, but as we proceed deeper away from the surface, the amount of oxygen will decrease and cross-linking and chain scission will be predominant.

A denser silica-like is formed on the outermost surface region of PDMS, while cross-linking and formation of oligomers and other LMW species occurs in the sub-surface region. Since the densities of PDMS, 0.97 g/cm^3, and silica, 2.2 g/cm^3, are substantially different, the densified region is tensioned and this can result in microcracks along the surface, as shown by Hillborg,[216] Bodas,[223] Waddell[181] and Williams,[183] and also in our previous work on PC.[132] LMW species diffuse to the surface in order to minimize the total free energy. As mentioned, these LMW species could be pre-existing (formed during the curing process of the polymer) or created by the plasma-treatment itself by chain scission. Depending on whether the densified layer presents cracks or pores, the diffusion of these LMW oligomers will be faster or slower, but whenever LMW species exist, they will slowly diffuse even through a dense low-defect silica layer.

It is important to notice that since the amount of trapped oligomers or radicals is very small in ppHMDSO, this mechanism does not play a role during aging after plasma treatment. In addition, the ppHMDSO subsurface is already cross-linked to a

	PDMS	ppHMDSO
Initial Density	**0,96 g/cm3**	**1,52 g/cm3**
Initial Cross-linking	**Very low**	**high**
Pre-trapped oligomers	**Medium**	**none**
Micro-cracks after pre-treatment	**Yes**	**No**
LMW species after pre-treatment	**Yes**	**No**

TABLE 4.12. Differences between plasma-treated PDMS and plasma-treated ppHMDSO.

much higher extent than the PDMS one, and the original densities are also different (0.96 g/cm^3 for PDMS, to 1.52 g/cm^3 for ppHMDSO), which reduces the stress created by further densification during plasma treatment. No cracks have been found by SEM in any of our plasma-treated ppHMDSO films.

These two mechanisms are illustrated in the schematic Figure 4.37, and the differences between plasma-treated PDMS and plasma-treated ppHMDSO are summarized in Table 4.12.

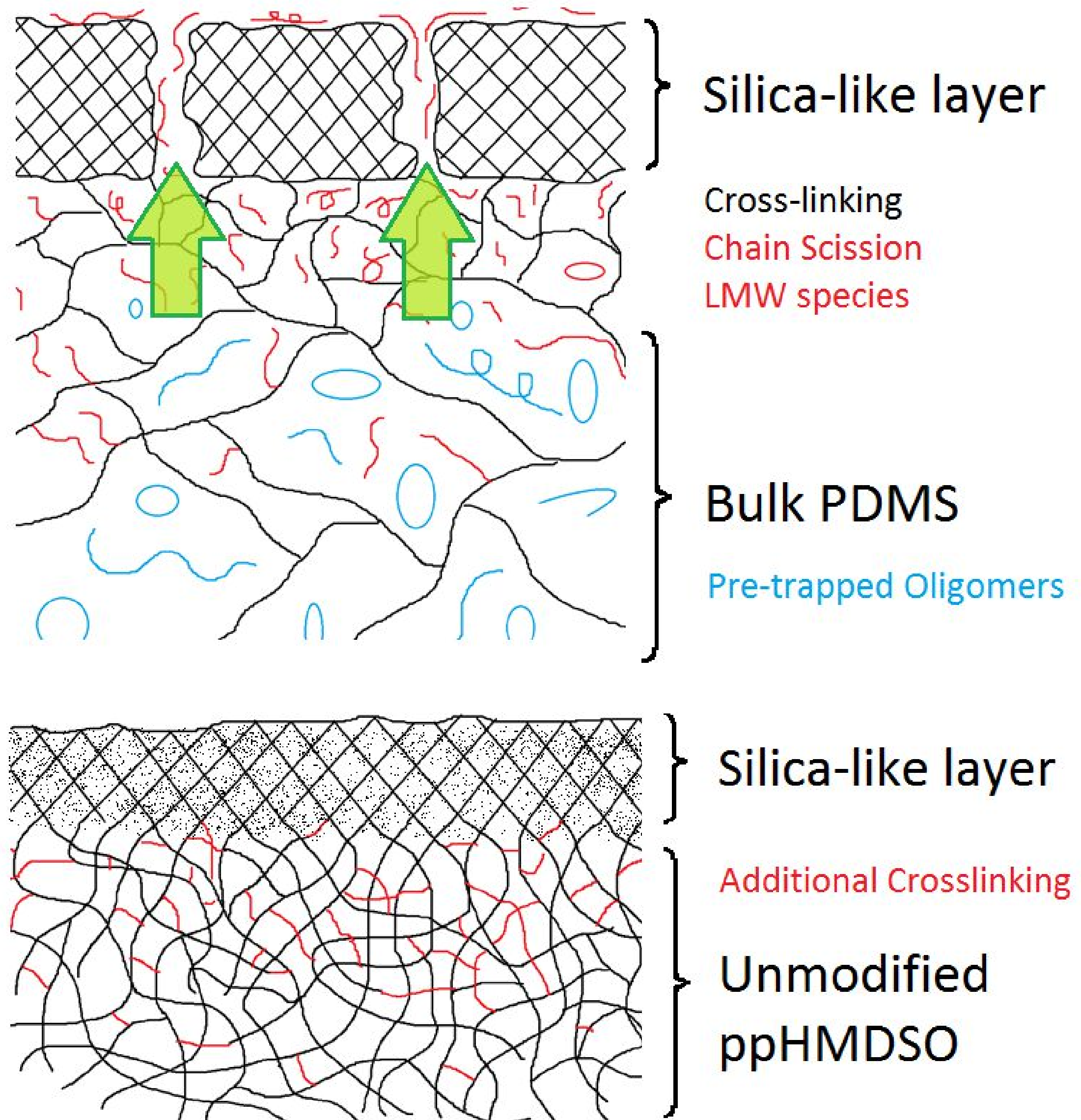

FIGURE 4.37. Schematic representation of the mechanism of hydrophobic recovery in PDMS (TOP) and ppHMDSO (BOTTOM). Green arrows indicate diffusion of LMW species –either preexisting or created by chain scission- through the pores and cracks of the silica-like hard layer in PDMS. In the case of ppHMDSO, the density of the silica-like layer is higher and free of cracks, and no significant amount of LMW species is created during plasma treatment.

Figure 4.37 is still valid for Ar treatments with sufficiently low background pressure (very low concentration of oxygen and water vapor). In this case the silica-like layer will be substituted by a modified surface region with higher crosslinking than the bulk. Some oxidation is unavoidable and a reduction in the carbon content is effected, but the surface cannot be considered a silica-like layer. The diffusion of oligomers through the layer itself is faster than for completely oxidized layers, but, in comparison, the reduction in porosity and crack density for the Ar treatments slows down the hydrophobic recovery. This is consistent with our results (Fig. 4.36) but also with results reported previously in the literature by Hillborg et al.[215] and Swiderek et al.[164] for Ar plasma treatments. As a summary, the following qualitative explanations can be given for our results:

- Hydrophobic recovery in plasma-treated PDMS samples is due to migration of LMW species from the inner bulk of the polymer to its surface, through pores and microcracks across the silica-like layer at the surface. These LMW species may be either pre-existing or created by the plasma treatment through chain-scission.
- The virtually hydrophobic-recovery-free surface of plasma-treated ppHMDSO is due to the lack of LMW species, which are neither pre-existing nor created during plasma treatment.
- Ar plasma treatments produce a hydrophilic surface with a higher surface energy and higher water contact angle than O_2 plasma treatments.
- Hydrophobic recovery in PDMS modified with Ar plasma treatments is slower than that of O_2 plasma treatments due to the lack of microcracks on the crosslinked region.

4.3.5.3. Long-lasting hydrophilic surface on PDMS by ppHMDSO deposition and O_2 plasma post-treatment

After demonstrating that the surface energy modification of a plasma-treated ppHMDSO film is extremely endurable, we tried to apply these properties to the versatile PDMS substrate. Hence, we deposited a ppHMDSO film on top of a PDMS substrate and effected an O_2 plasma post-treatment with the aim to achieve a long-lasting hydrophilic surface on top of the PDMS substrate. In order to minimize

bombardment of energetic species onto the PDMS substrates during deposition of the ppHMDSO film, which would generate additional LMW oligomers within the bulk PDMS, we placed two of the substrates in a semi-remote configuration, 20 mm below the electrodes and outside the glow discharge. Two additional substrates were placed within the plasma, on top of the surface of the grounded electrode. Prior to plasma polymerization, a short discharge in 0.1 mbar of Ar (for 10") was performed in order to activate the surface of PDMS and ease the adsorption of molecules to increase the starting growth rate of the plasma-polymer. A ppHMDSO film was then deposited in an HMDSO/Ar plasma (4:1) at 0.1 mbar total pressure for 6 min, and a subsequent O_2 plasma post-treatment at the same pressure was effected for 10 min. The chamber was vented and one of each type of substrates were removed from the reactor. The chamber was closed again and pumped down, and an additional 10 min of O_2 plasma treatment were effected on the remaining substrates.(29) In these conditions the thickness of the ppHMDSO films was around 400 nm for the PDMS substrates within the plasma and 250-300 nm for the PDMS substrates in a remote location.

Figure 4.38. and Table 4.13. show the evolution of the water contact angle with aging time, during storage in ambient atmosphere for 30.000 h (more than 2 years),

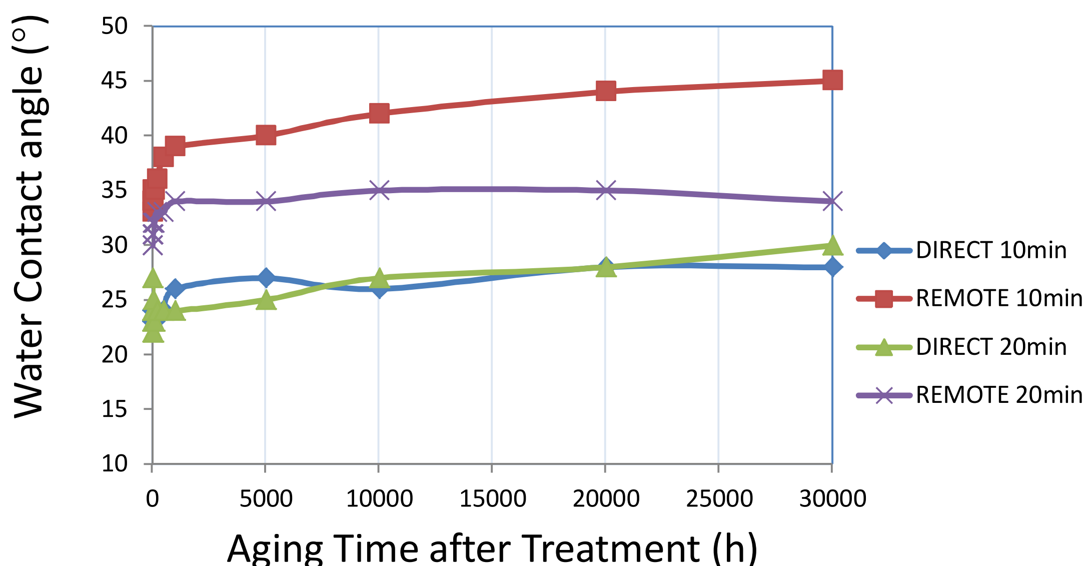

FIGURE 4.38. Hydrophobic recovery for O_2 plasma-treated ppHMDSO films on PDMS substrates, in a direct and remote location with respect to the plasma glow, for 10 and 20 min of plasma treatment.

(29) The corresponding detailed plasma cycle protocol can be found in Annex X / Chapter 2.

for the samples placed within the plasma (direct) and the samples placed downstream the plasma glow (remote), for 10 and 20 min of plasma post-treatment. All samples show an extremely low hydrophobic recovery, with the smaller recovery being for a 20 min treatment in a remote configuration and also by a 10 min treatment in a direct plasma.

	t = 0 h	t = 30.000 h
10 min O_2 Plasma - Direct	**28°**	**33°**
10 min O_2 Plasma - Remote	**34°**	**45°**
20 min O_2 Plasma - Direct	**23°**	**30°**
20 min O_2 Plasma - Remote	**31°**	**34°**

TABLE 4.13. Water static contact angles for different treatments on ppHMDSO/PDMS samples at t=0 and at t=30000h.

Contrary to the post-treatment of ppHMDSO films alone, in this case, none of the processes seem to eliminate the hydrophobic recovery completely. Surprisingly, the remote sample shows a superior performance with a lower hydrophobic recovery as compared to the direct configuration, despite having 33% less ppHMDSO film. Since the outer surface for plasma-treated ppHMDSO films on Al-coated glass and plasma-treated ppHMDSO films on PDMS is the same, the difference must be attributed to the substrate. This result supports the hypothesis that LMW oligomers from the PDMS substrate are capable of diffusing through the ppHMDSO and its oxidized surface, regardless of the thickness of the film and the silica-layer. The difference may not be detectable for short aging times (below 1000 h), but for longer times it can be. Therefore, migration of LMW species to the surface *IS* the dominating effect, even for the higher density and higher cross-linking barriers achieved by the plasma-polymerized coating. Since both denser layers and higher amount of LMWs are created by the same processes (i.e. bombardment by energetic species), a compromise between these two effects needs to be met by optimizing the

controllable parameters (treatment time, substrate position, gas pressure), in order to achieve the most endurable hydrophilic properties.

4.4. CONCLUSIONS

- Plasma post-treatments are an effective method to modify the surface properties of polymer-like ppHMDSO films. Oxygen plasma treatments achieve complete Carbon depletion and full oxidation of the surface in less than 10 min.

- Non-reactive plasma treatments with Ar or N2 do not achieve full oxidation of the surface, but rather enhance cross-linking.

- The penetration depth of the treatment is highly dependent on the treatment time and the density and porosity of the films. When high-density films are post-treated, the penetration depth is limited to a few tens of nanometers, whereas for medium and low density films, it can extend to more than 100 nm.

- The main mechanism for interpreting the evolution of the modified depth is diffusion of oxygen radicals, rather than ionic, electronic or UV absorption mechanisms.

- Plasma treatment outside the active zone of the plasma is also effective in creating a hydrophilic surface.

- The surfaces of plasma-treated ppHMDSO films are harder and more hydrophilic than the untreated ones.

- Hydrophobic recovery is not signifficant in plasma treated ppHMDSO films.

- Hydrophobic recovery can be greatly diminished in conventional PDMS polymer by depositing a ppHMDSO film and effecting an ulterior post-treatment in oxygen or argon plasmas.

- Plasma treatment of ppHMDSO films on PDMS substrates should be limited in time to less than 10 min if the sample is placed in the active plasma zone or 20 min if it is placed in the remote region.

CHAPTER 5

INDUSTRIAL APPLICATIONS

5.1. INTRODUCTION AND OBJECTIVES

This chapter is devoted to three examples of real industrial problems that have been studied and solved with plasma polymerized coatings or plasma treatments. Each of the coatings has been designed to maximize and make use of one specific property of PP-HMDSO films.

In the first example, the mechanical properties of SiO_x-like films are sought to enhance the surface hardness of a plastic part, in order to avoid scratches produced by normal use or cleaning. A major challenge in this case is the production of a thick coating with graded properties onto a soft plastic part while trying to avoid thermal damage on the part due to bombardment by energetic ions in the plasma.

In the second example, the low surface energy of PP-HMDSO films is used to modify and reduce the surface energy of a PMMA rotor which encloses a set of 120 reaction cuvettes. Each cuvette shares one wall with each of its two closest neighbors and a major cross-contamination problem was detected when some reaction mixtures were able to trespass from one cuvette to its neighbors, thus producing false results. The analysis of this effect showed that a capillary path was generated at the dihedral angle formed by the inner walls of the cuvettes, thus creating a fluidic communication between consecutive cuvettes. The reduction of the surface energy by a PP-HMDSO hydrophobic coating diminishes the capillary force and prevents fluidic communication between cuvettes. Due to the complexity of the geometry of the part to be coated, the major challenge in this case was two obtain a completely conformal coating that covered all the edges in all the cuvettes, to guarantee a 100% cross-contamination-free part, but with a thickness below 50 nm to avoid visible

interference fringes anywhere at the surface of the rotor, while avoiding thermal damage to the part during larger deposition times.

In the third example, the desired property was the chemical stability of PP-HMDSO, which creates a corrosion protective barrier in virtually any substrate. In this case, the part to be coated was a small metal shaft, which is one of the components of a high-speed miniaturized mixer employed in the homogenization of tissues and for the lysis of cells for ulterior DNA/RNA analysis. The problem to solve arises when the metal shafts get in contact with the corrosive chemical mixture, even for a short time. The chemicals contain highly corrosive agents, such as guanidinium isothiocianate or other chaotropic salts, combined with moderately high temperatures (up to 70ºC) and the impingement of high speed silica beads used to ‘crunch’ the cells and release their nucleic acids. Corrosion starts readily, and although the shaft itself is not greatly damaged, the metal ions released in the chemical mixture affect the nucleic acids and quickly degrade RNA, so as to make it unusable for downstream purification and detection. Again, the main difficulty is to obtain a uniform coating with no uncoated zones where the shaft is in contact with the reaction mixture.

5.2. APPLICATION I: ANTI-SCRATCH PROTECTIVE COATINGS ON ABS PLASTIC PROTECTORS FOR HOME SWITCHES

5.2.1. Description of the Problem

Plastic protectors for home switches are submitted to frequent manipulation with minimal care during daily use. Manufacturers of these products are increasingly challenged to produce more appealing designs, but also more rugged and abrasive resistant parts that will not be scratched or damaged by cleaning or actuation. These protectors are made of moldable plastics such as ABS (Acrylonitrile Butadiene Styrene).

Plastic protectors were supplied by a well-known electrical company in order to study the feasibility of applying plasma polymerization to increase the scratch resistance by a hard, adhered coating.

5.2.2. Protocol and results for plasma deposition of HMDSO on ABS

Different treatments were applied to plastic protectors molded from Polidux®-A300 ABS. The protectors were provided directly as molded, with no additional treatment. Since the geometry of the parts is basically flat, a parallel plate configuration was employed in all the tests to achieve maximum homogeneity for the thickness of the coating. The most difficult challenge was to avoid excessive heat dissipation by energetic ion bombardment on the surface to avoid thermal damage to the part.

Table 5.1.and Figure 5.1 show the parameters employed for deposition of the sample with the best performance. Two samples were located on the anode of a DC parallel plate plasma, 20 cm apart. One of the samples was lying flat parallel on top of the grounded anode (ref. ABS 541); the second one was supported perpendicularly to the grounded anode (ref. ABS 542). The samples were pre-treated with 30” Oxygen plasma to activate the surface; after that, the oxygen flow was stopped and 100% monomer was introduced. The plasma polymerization in pure HMDSO vapor was extended for 30 min. With these conditions, the temperature on the grounded anode

electrode reached 81°C, which is below the heat distortion temperature of ABS (107°C).

PARAMETER	VALUE
Source	**DC**
Geometry	**Plano Parallel**
Distance Anode-Electrode	**20 cm**
Substrate Position 1	**Perpendicular to the electrodes**
Substrate Position 2	**Parallel to the electrodes**
Background pressure	**0.008 mbar**
Monomer pressure	**0.210 mbar**
Monomer Flow	**30 sccm**
Power	**150 W**
Intensity	**75 mA**
Voltage	**2000 V**
Pre-treatment time	**30 s 100% Oxygen Plasma**
Deposition Time	**30 min 100% HMDSO Plasma**

TABLE 5.1. Values for the main parameters in the optimal configuration for the deposition of scratch-resistant transparent coatings in ABS protectors.

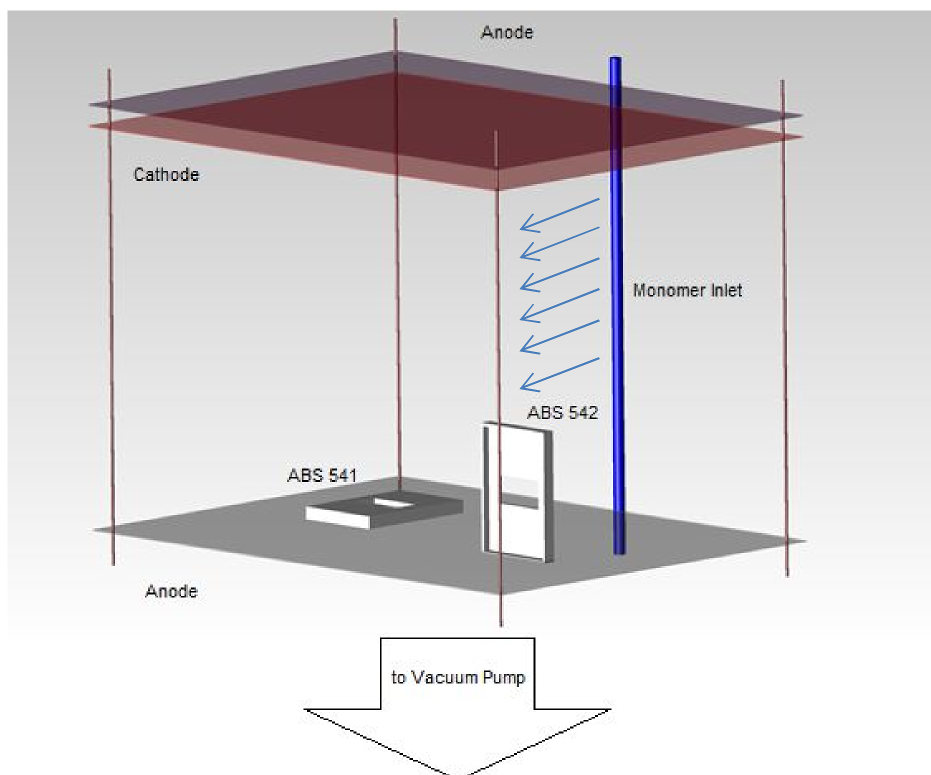

FIGURE 5.1. Geometry of the electrodes and location of the ABS parts on the anode. The monomer inlet distributes the gas flow by several orifices in a stainless steel tube, from the left side and into the plasma area.

Surprisingly, the parallel part and the perpendicular one produced completely different results, as shown in Figure 5.2: the parallel part was deformed and was coated by a brownish film, although the temperature at the anode had not reached the distortion temperature, whereas the perpendicular part was not damaged and was coated by a transparent film. Figure 5.2 also shows a previous sample (ABS 53) coated with the same parameters except for the flow of monomer and the total pressure, which was 15 sccm and 0.1 mbar. Clearly, the best appearance was achieved for sample ABS 542, which corresponded to the best conditions that we

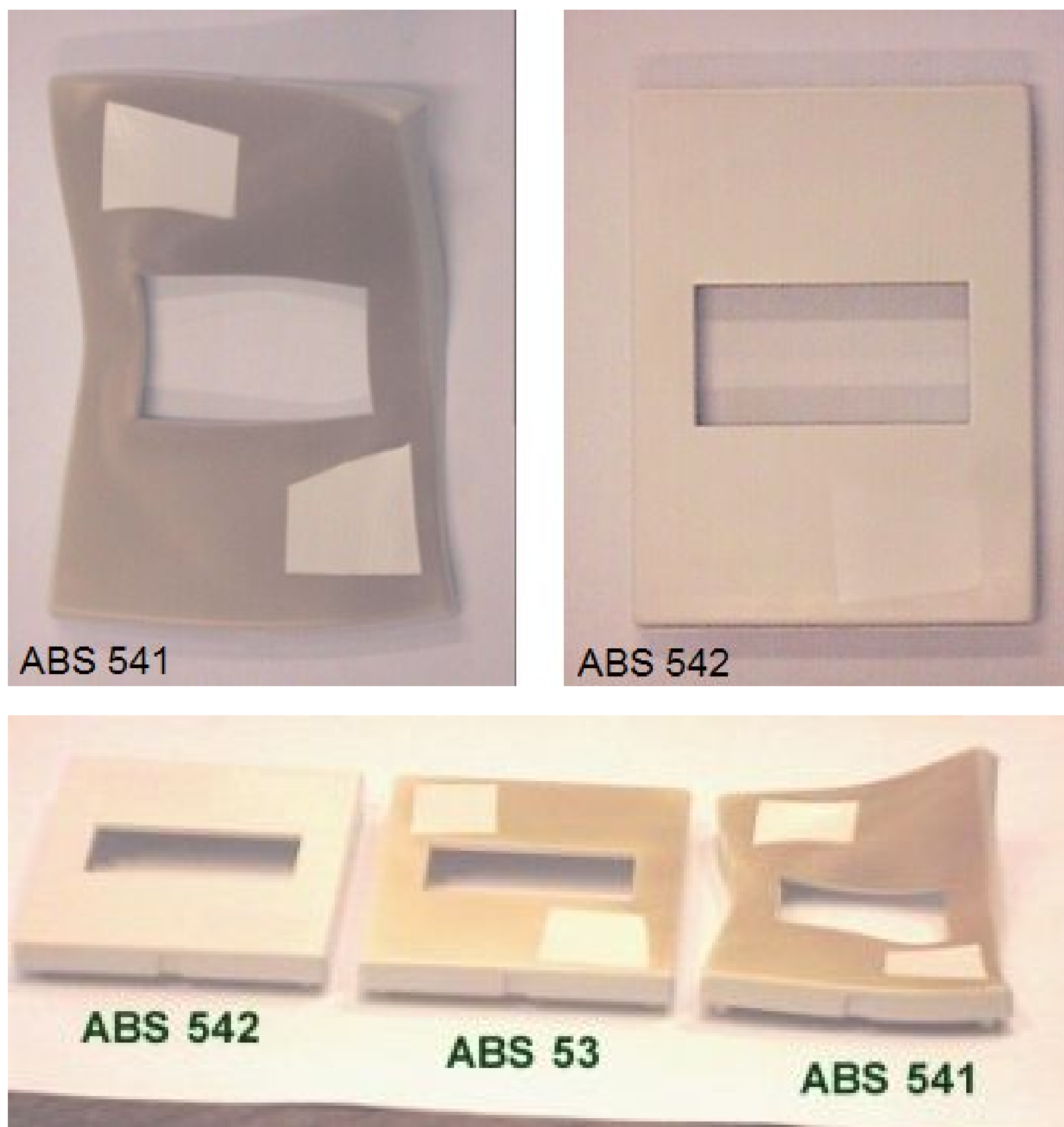

FIGURE 5.2. ABS protectors coated with different plasma parameters. ABS 542 corresponds to a perpendicular location with respect to the grounded anode; ABS 541 corresponds to the same deposit but in a parallel location on the grounded anode. ABS 53 is equivalent to ABS 541 but at half monomer flow and half total pressure.

could find in terms of part finish. The white uncoated areas were protected with adhesive kapton tape to allow a clear interface between the coated and uncoated material in order to evaluate the thickness and to perform comparative microscratch characterization to assess the improvement achieved by the as-deposited film.

5.2.3. Functional and structural characterization of the coating

The structural and functional properties of the coatings were analyzed from different perspectives: density, thickness uniformity, optical transmission and scratch resistance.

The thickness of the films was measured with mechanical profilometry across the edge of the uncoated area covered by the adhesive kapton tape to avoid deposition. The thickness was measured both in the ABS part and in glass slides placed in the equivalent positions on the anode[30] and proved to be homogeneous along several centimeters (Figure 5.3) and approximately the same for glass and ABS substrates:

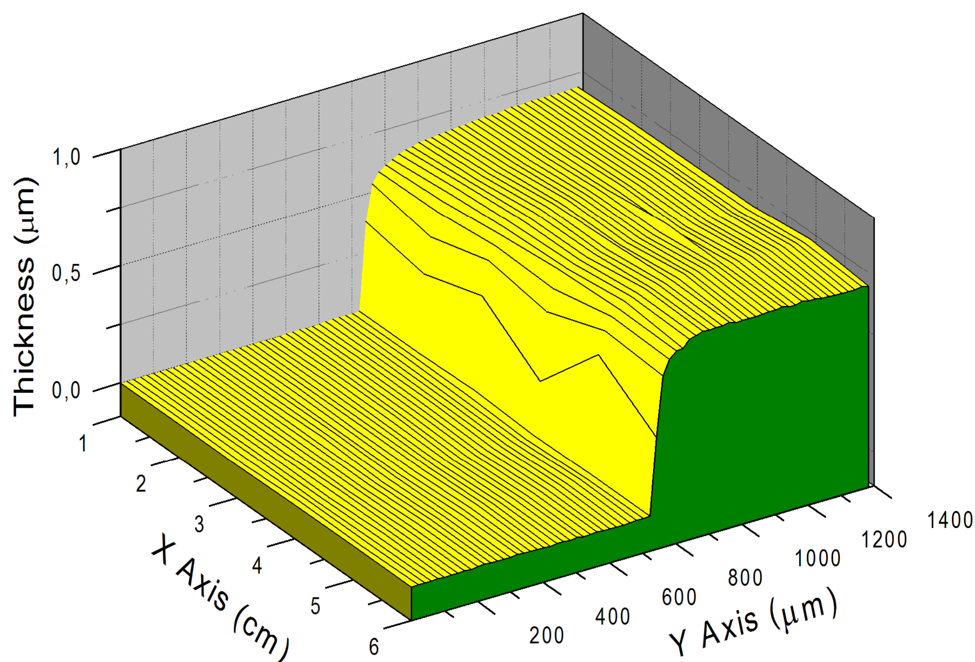

FIGURE 5.3. Thickness measurements at different locations along the step between the coated and uncoated areas allow to verify the good homogeneity of the film.

[30] Glass slides and Al-coated glass slides were used in all experiments conducted during this thesis since they are useful substrates for reliable measurements of thickness, UV-VIS transmittance and FTIR absorption measurements. Glass slides are pre-cleaned before the

550 - 680 nm, which is equivalent to a deposition rate of 18-23 nm/min for sample batch 54 and 250-300 nm for sample batch 53, at an equivalent deposition rate of 8-10 nm/min.

The density of the coatings was evaluated by weighting the ppHMDSO film on the glass slide probes as the difference in weight before and after plasma polymerization. Since the area of the glass slides was known, the density could be easily calculated. The measured densities were in the range 1.61 – 1.67 g/cm^3 for the sample batch 54 and 1.66-1.69 g/cm^3 for the sample batch 53.

The reflectance of the films in the UV-VIS and IR spectra were measured on the Al-coated glass slides and the results could be slightly different than for the perpendicular ABS substrate, due to the suspected difference in ion bombardment. The visible spectrum in Figure 5.4 shows some absorption towards the deep blue and near-UV range at 380-400 nm which maybe could be appreciated as a very faint yellowish color, but the overall transparency impression on the ABS substrate is satisfactory. Still, it is a quite large surface and some faint red-green interference colors could be detected due to small thickness differences over the whole part and specially at the edges.

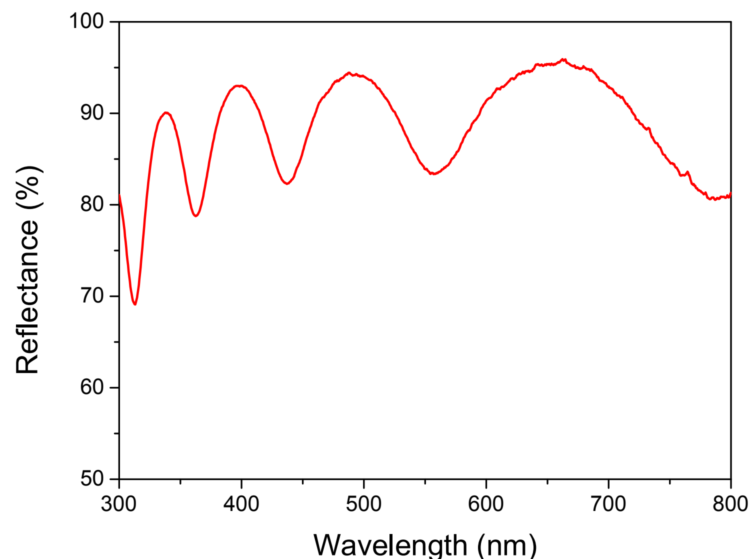

FIGURE 5.4. UV-VIS spectrum of the Al-coated glass slide in batch 54.

The reflectance FTIR spectrum shown in Figure 5.5 indicates that the film on the Al-coated glass substrate is not completely polymeric and most methyl groups have been etched already (band at 1260 cm^{-1}). Also a large OH band at 3200-3600 cm^{-1} is present. This fact is consistent with the relatively high density measured and it is also probably related to the high ion bombardment to which the glass substrate is submitted on the anode. It is to be expected that the ABS sample located perpendicularly to the anode would not suffer the same amount of bombardment and that more organic groups could still be found on that sample.

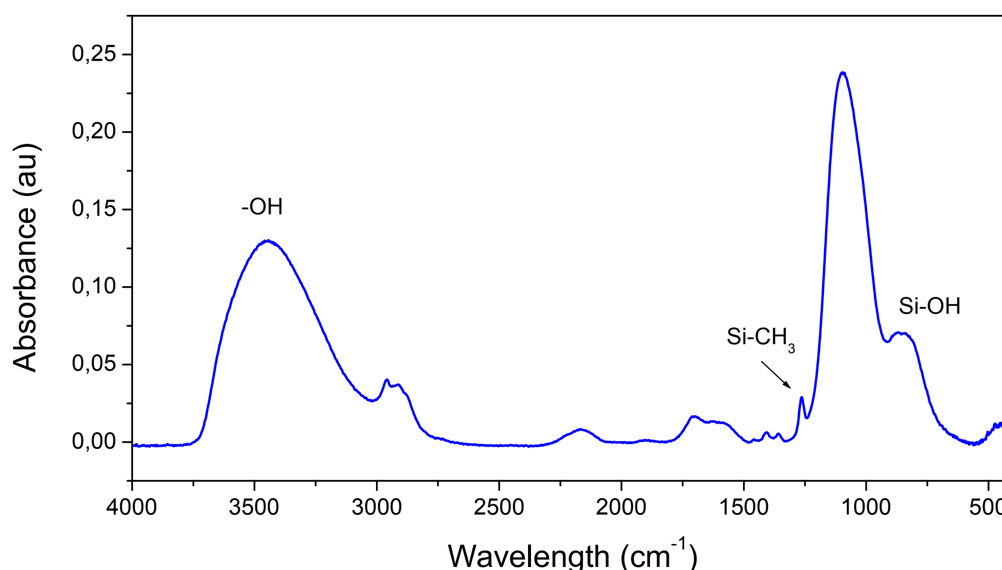

FIGURE 5.5. FTIR absorption spectrum of batch 54 showing a medium degree of oxidation, as indicated by the low methyl (Si-CH_3) peak and the large silanol (Si-OH) and adsorbed OH bands.

In order to asses the real functionality of the protective ppHMDSO coating, a microscratch test was performed with a 200 μm radius diamond tip at a constant load of 500 mN, in a path that transited across the limit between the treated and untreated areas in the ppHMDSO coated ABS plastic part. The friction force and the topography of the track were analyzed and the results are shown in Figure 5.6. For ppHMDSO-coated ABS, the friction coefficient drops to less than half of that for the uncoated ABS. In addition, the groove created by the diamond tip is reduced substantially, both in width and depth and is less visible for the ppHMDSO-coated ABS.

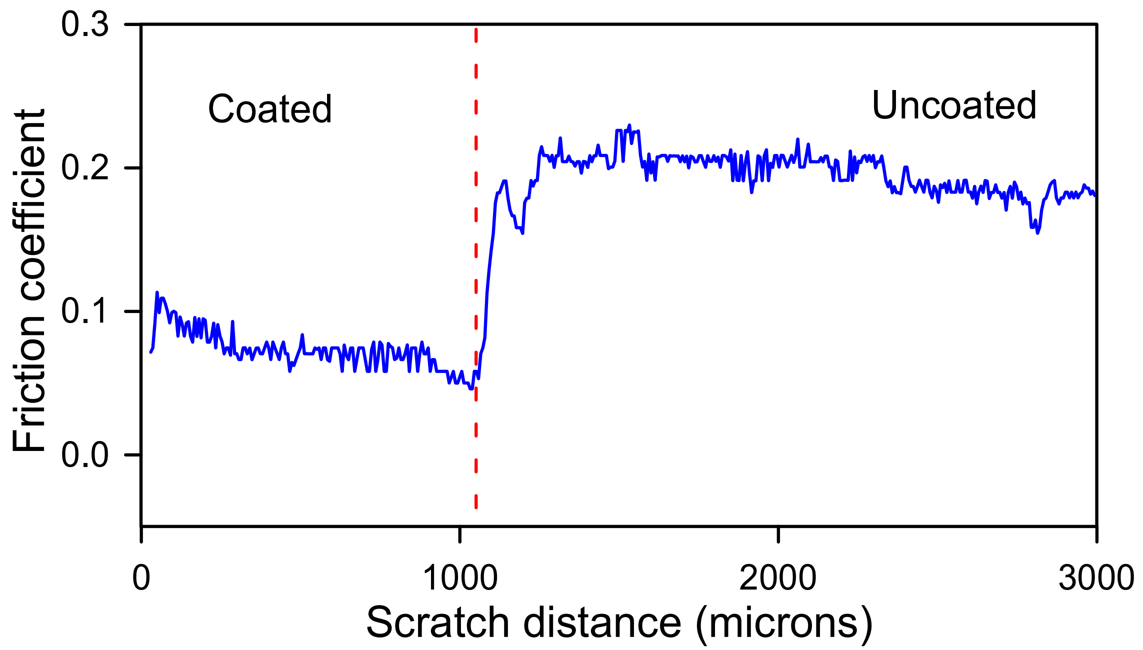

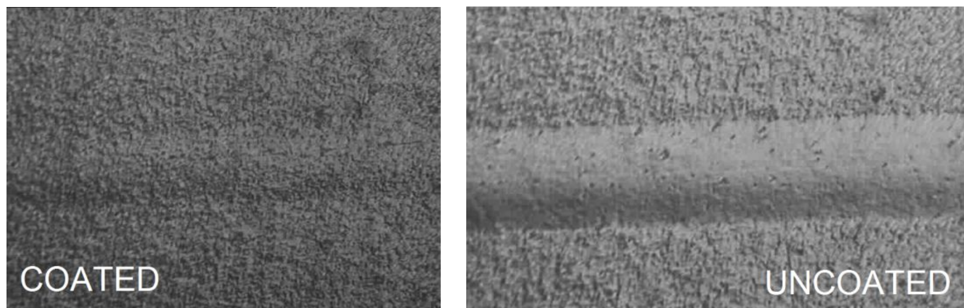

Coated ABS	Uncoated ABS
Scratch width: **51.4 µm**	Scratch width: **76.4 µm**
Scratch Depth: **9.6 µm**	Scratch width: **23.1 µm**

FIGURE 5.6. Microscratch test across the transition between uncoated ABS and ppHMDSO-coated ABS. The friction coefficient, groove width and groove depth are significantly reduced.

Finally, the microhardness of the coated and uncoated substrate was measured by nanoindentation with a Berkovich indenter. Figure 5.7. shows the load-unload displacement curve for the uncoated ABS and the ppHMDSO-coated ABS. The penetration of the indenter at 1mN load for the uncoated ABS is almost twice the depth indented in the ppHMDSO-coated ABS. Even more significantly, the residual penetration after unloading shows a clear plastic behavior for the uncoated ABS, with an elastic recovery of only 54% , whereas for ppHMDSO-coated ABS the elastic recovery is higher than 90%, which is extremely good.

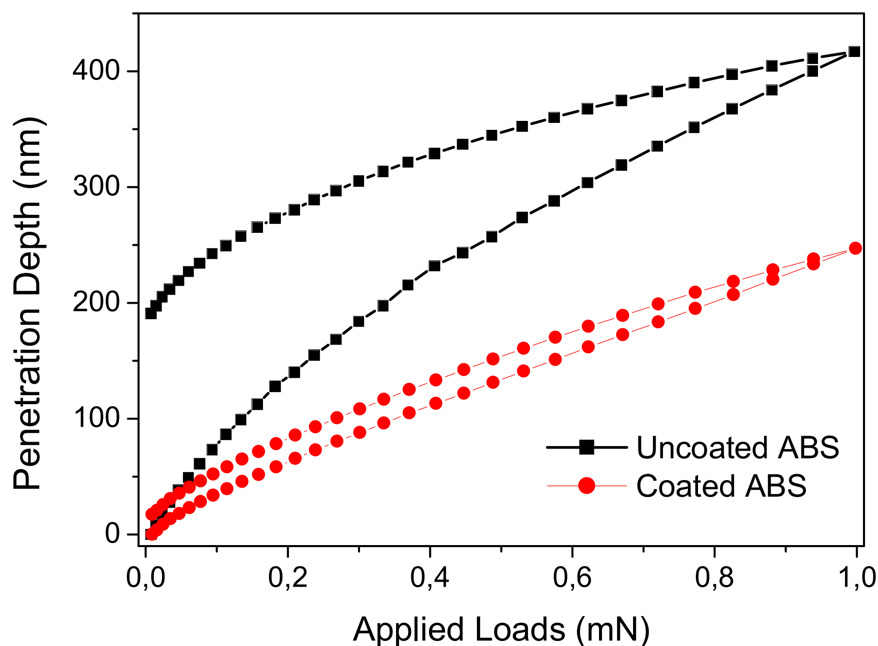

FIGURE 5.7. Load-unload nanoindentation displacement curves for uncoated and ppHMDSO-coated ABS substrates.

5.2.4. Final remarks and conclusions

Although the results for the nanoindentation and scratch tests look very promising, the films prepared with the proposed approach are still too thin for real-life applications. Additional work was started to pursue coatings in the range 3-10 μm on plastic substrates without excessive thermal load to the parts and within reasonable processing times. This cannot be done in a DC plasma and should be done necessarily in a different reactor, optimized for higher deposition rates in the afterglow configuration

5.3. APPLICATION II: HYDROPHOBIC, LOW SURFACE-ENERGY COATING ON PMMA REACTION CUVETTES TO AVOID CROS-CONTAMINATION

5.3.1. Description of the Problem

Barcelona based company in the field of In Vitro Diagnostics (IVD) designs and manufactures a family of clinical chemistry analyzers and a large portfolio of reagents, with customer laboratories spread worldwide in more than 100 countries. In the origin of this application lies a complaint issued by a customer laboratory arguing that some combinations of test profiles could result in falsely elevated concentrations of critical analytes, thus leading to a wrongful interpretation by the physician. This could support an inappropriate medical decision on the treatment and eventually harm the patient whose blood had been tested.

First statement by the complaining laboratory included very little information: the contaminated test was CK-MB, a cardiac marker employed for the determination of possible myocardial infarction.(31) An investigation needed to be conducted to assess the scope of the reported problem, including the frequency and combination of possible false results, and to understand the root cause in order to find a cost-effective solution applicable to a product that was already in the market, worldwide. Therefore, the question reached the R&D Department of the company.

5.3.2. Description of the system and initial inputs

The basic workflow of a clinical chemistry analyzer is quite simple: predefined volumes of sample and reagent are pipetted by metal probes from their original vials into a reaction cuvette, the mixture is incubated at 37°C for a set time and a series of optical measurements is taken to generate a kinetic curve of absorbance vs time, from where the concentration or activity of a certain analyte can be calculated. The pipetting probes are washed and rinsed between any pipetting operation to minimize any possible cross-contamination. The reactions take place in any of the 120 reaction

(31) An elevated CK-MB can only be produced after the muscular fibers of the heart have been damaged or destroyed by lack of blood supply. The destruction of the heart's cells releases the CK-MB enzyme and therefore it is a strong indication of heart stroke. Until the arrival of the more specific and sensitive biomarker Troponin I, CK-MB was considered as the gold standard of clinical chemistry to aid in the detection of heart stroke.

wells (or reaction cuvettes) that are defined within a single injection molded plastic part, the rotor of cuvettes (see Fig. 5.8). Each cuvette shares two walls with its closest neighbors (clockwise and anticlockwise) and can hold up to 800 μL, but most reactions require only between 200 μL and 450 μL. The rotors are molded in poly(methylmethacrylate), PMMA, since it is a cheap transparent moldable plastic with sufficient transmission down to the UVA range of the spectrum (320 nm – 400 nm), and 40% of clinical chemistry tests are measured by photometry at 340 nm. All wells are scanned sequentially every 15 seconds by a single light beam, hence the rotor needs to spin in order to expose each cuvette for a small time window to allow the photometric measurement to take place.

FIGURE 5.8. PMMA injection-molded rotors comprising 120 reaction cuvettes for clinical chemistry photometric tests.

Analysis of the log files(32) from the instruments that performed the inaccurate tests showed that CK-MB tests were usually made in combination with Cholesterol tests (which makes sense, since myocardial infarction is frequently accompanied by an elevated cholesterol level in the patient's blood) and sometimes with Creatinine tests.

(32) "Log files" are text records that register all the operations performed by an instrument in order to allow the Technical Service, Product Support or the R&D teams to easily review all information related to any investigation on the performance of the system.

Therefore, initially the focus was set on Cholesterol, Creatinine and CK-MB reagents to detect a possible cross-contamination between any combination of these reagents.

5.3.3. Reproducing the problem: cross-contamination protocols

In order to detect a cross-contamination from one test to another (always as pairs of tests) a predefined alternated sequence of suspect tests applied as replicates to the same sample is executed, in search of anomalous results. For example, a possible sequence of execution for tests A and B suspected to have a cross-contamination could be:

$$A_1\text{-}A_2\text{-}A_3\text{-}A_4\text{-}A_5\text{-}B_1\text{-}A_6\text{-}B_2\text{-}A_7\text{-}B_3\text{-}A_8\text{-}B_4\text{-}A_9\text{-}B_5\text{-}B_6\text{-}B_7\text{-}B_8\text{-}B_9$$

The reference values for uncontaminated A and B tests are taken as the mean value of the replicates performed at the beginning and the end of the sequence, without any possible interaction between each other, i.e.:

$A_{\text{uncontaminated}}$ = mean (A_1-A_2-A_3-A_4), $B_{\text{uncontaminated}}$ = mean(B_6-B_7-B_8-B_9)

Similarly, the mean values of the replicates which were executed after a different test, and therefore susceptible to be contaminated, are calculated, i.e.:

$A_{\text{contaminated}}$ = mean (A_6-A_7-A8-A_9), B contaminated = mean(B_1-B_2-B_3-B_4)

If $A_{\text{contaminated}}$ is significantly different[33] than $A_{\text{uncontaminated}}$, it is established that B is a contaminant technique over A; conversely, if $B_{\text{contaminated}}$ is significantly different than $B_{\text{uncontaminated}}$, then A is a contaminant technique over B. Mutual contamination is very rare, but has been found occasionally.

Generally, cross-contaminations produced when a contaminating reagent is pipetted before the contaminated one are due to the carry-over transfer of contaminant traces at the walls of the pipetting probes, even after washing the probe between reagents. These are normally 'chemical' in nature, which means that some components of reagent A can react with the components of reaction B even at very small concentrations (1:10.000 or 1:100.000) of contaminant. Consequently, when a chemical cross-contamination is detected, it usually affects all the replicates that have been in contact with the contaminant reagent. Individual values for A_6, A_7, A_8, A_9 or

[33] "Significantly different" is an arbitrary criterion defined as a threshold of decision. Usually, a 10% difference is considered as a cross-contamination, but a more general rule, the threshold is assigned to be 3 times the standard deviation of the replicates for the uncontaminated test.

B_1, B_2, B_3, B_4 should all be quite different from $A_{uncontaminated}$ or $B_{uncontamiated}$, if a 'normal' cross-contamination was to be found.

These and other sequences were executed with different combinations (CK-MB against Cholesterol and Creatinine) with unclear results. Contaminations occurred much less frequently than expected, but they did occur from time to time. Surprisingly, after conscious examination of all the results, in this case the key point was found not to be the sequence of execution of pipetting operations, but the sequence of disposition in the rotor of cuvettes, and even so, the same disposition did not always produce the expected contamination. Additional tests were performed to exclude the possibility of a chemical contamination during pipetting operations by the analyzer and these confirmed that the contamination was randomly produced, somehow, by transfer of small amounts of reagents from one cuvette to the adjacent ones *after* being dispensed into the reaction cuvettes, but never *before* dispensation.

By manually pipetting these reagents in different sequences into the reaction cuvettes in the rotor the effect of liquid transfer was confirmed by color development in transparent reagents (CK-MB or water) contaminated with traces of colored ones (Calcium or Creatinine) in adjacent cuvettes (Figure 5.9). The change in color increased with time, thus confirming that the contamination proceeded after dispensing and, clearly, only the reagents and the cuvettes could take a part in the mechanism, but not the analyzer.

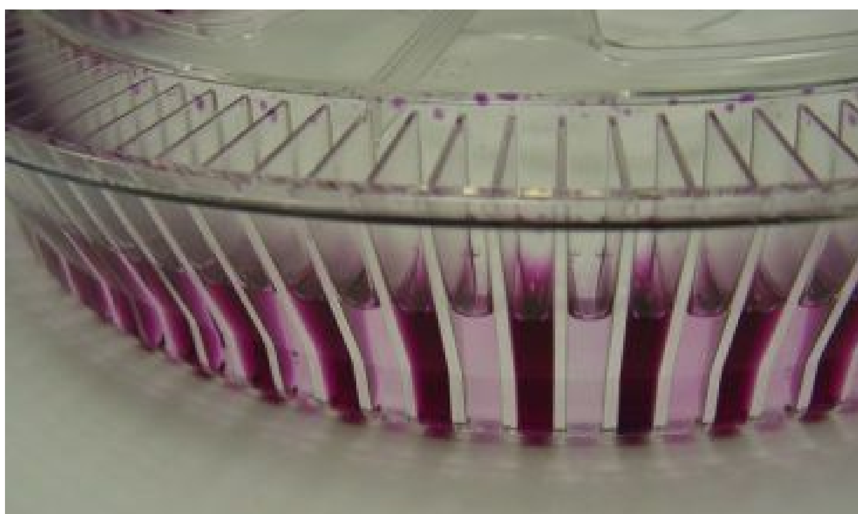

FIGURE 5.9. Sequence of reagents manually dispensed to verify cross-contamination between adjacent cuvettes, after a few minutes.

5.3.4. Migration of reagents and root source of the problem

The focus was therefore switched onto a phenomenon not noticed before during development and validation of the product: the migration of reagents between cuvettes.

Different theories could explain the effect and were all put to test:

- Pinholes at the walls between cuvettes;
- Adsorption by PMMA and migration through the walls;
- Spillage due to centrifugal force during measurement at the analyzer;
- Capillarity at the edges of the walls.

A thorough inspection of the parts excluded any possibility of pinholes, and although PMMA is known to have some degree of water adsorption, this is not to be considered within the timeframe of a test, since lengthiest techniques such as CK-MB take a maximum of 15 min for completion and most tests are finished in less than 10 min; water adsorption and migration trough solid walls are mechanisms that require rather hours or days to produce any macroscopic effect;, accidental spillage from one cuvette to another due to the centrifugal force acting on the liquids during rotor spin was discarded, both by test and theory, since the acceleration and velocity of the rotor during the tests are too small and the volume of filling of the cuvettes is less than 40%.

A closer look at contaminated wells revealed that, at the dihedral angles defined by their walls, a microchannel was created that allowed the free surface of some liquids to raise much further than the apparent meniscus of the bulk of the liquid, by capillary action (Figure 5.10).

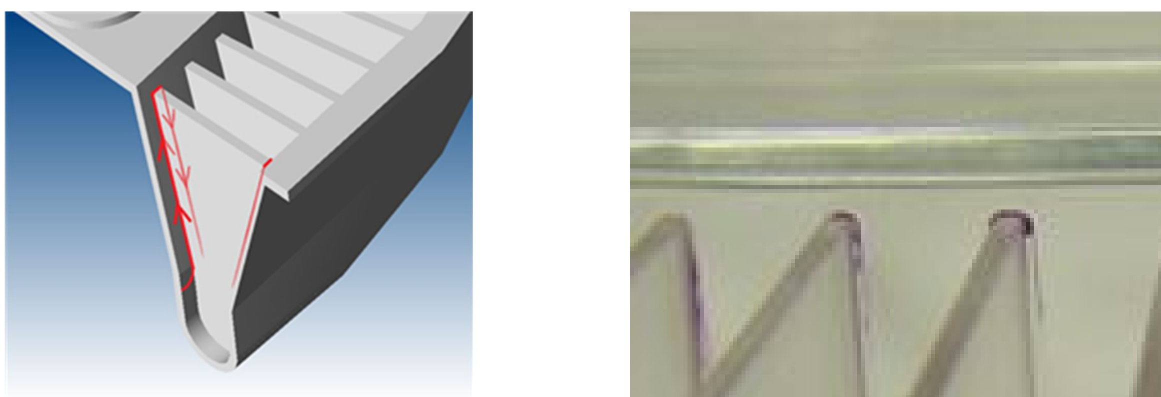

FIGURE 5.10. Capillary flow path created along the walls of the cuvettes to allow liquid transfer following the Concus-Finn condition. **(LEFT)** Schematic drawing. **(RIGHT)** magnified detail of actual traces of reagent overcoming the walls of the cuvettes.

The liquids could eventually overcome the top of the wall that separates the wells and start descending into the adjacent well until it finally met the neighboring reaction, thus contaminating it. A bibliographic search on the topic of capillary forces and meniscus evolution at dihedral surfaces showed that a mathematical formulation had been derived by Concus and Finn, back in 1969.[224] They concluded that there are only two possible scenarios for the behavior of the liquid free-surface in a wedge with smooth walls: either the liquid raises infinitely (no equilibrium free-surface exists) or it raises only to a certain height. These two possibilities are limited by the simple equation known as the Concus-Finn condition, which is a fundamental law in microfluidics:

$$\alpha + \gamma < \tfrac{1}{2}\pi$$

where α is the semiangle of the dihedral angle defined by the walls and γ is the contact angle of the liquid on the surface. If the condition is met, the liquid raises indefinitely; if not, it stops after a certain height (see Figure 5.11). In our case, for the

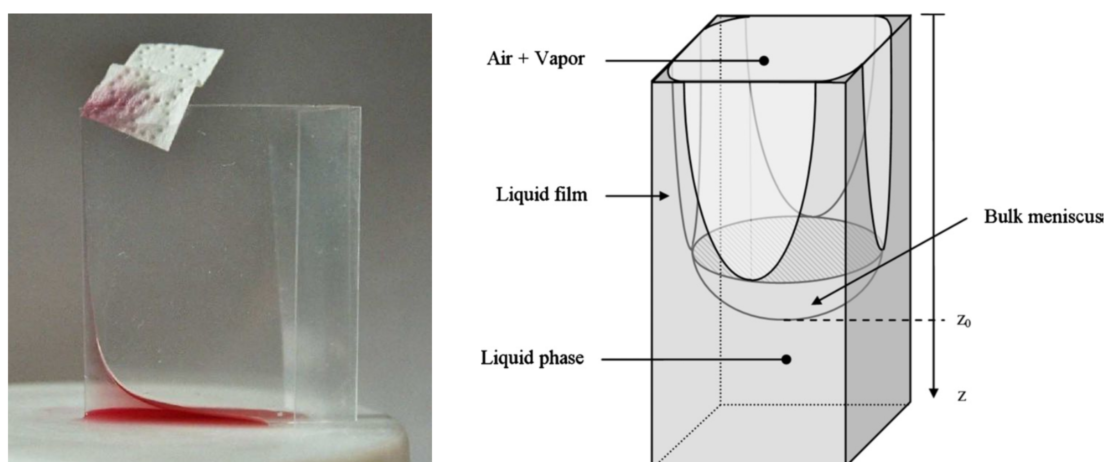

FIGURE 5.11. Capillary flow in a wedge surface. **(LEFT)** The red liquid verifys the Concus-Finn condition and therefore is capable of raising up to the absorbent paper. **(RIGHT)** Capillary flow at the corners of a square cuvette. From [ref 2. Capillary surfaces in wedge domains; Depinning of evaporating liquid films in square capillary tubes: Influence of corners' roundedness]

geometry defined by the cuvettes, α = 45° and the CF condition takes the form: γ < 45° (see Fig. 5.12). Therefore, it was necessary to consider the contact angles of each reagent on PMMA to predict if a certain liquid was a candidate to trespass from one cuvette to the neighboring ones by creating a fluidic path as indicated by red arrows in Figure 5.10.

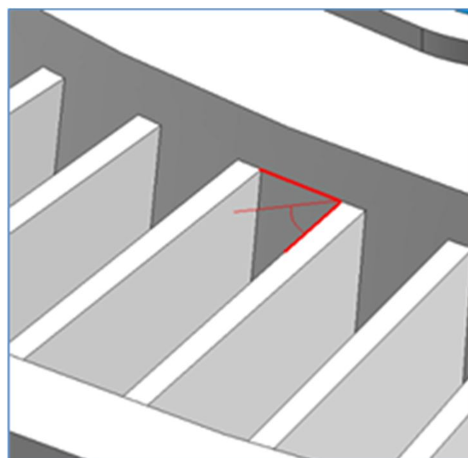

FIGURE 5.12. Geometry of the dihedral surface created between the walls of the cuvette. Here, the wedge is 90° and the semiangle of the wedge is 45°; therefore, the Concus-Finn condition requires that γ < (90° - 45°), for an infinitely raising liquid.

There are two additional remarks to be made: the Concus & Finn condition does not have any implications on the height of the meniscus or the velocity of the moving fluid; it also does not consider evaporation of liquid throughout the liquid path. In reality, the situation is much different for a 0° contact angle liquid than for a 35° contact angle liquid, since the former moves faster, whereas the latter moves slowly and suffers from increased evaporation, which leads to a change in density and viscosity and eventually to a stop in the liquid front. A complete analysis of the dynamics of capillary flow in a wedge can be found in Refs.[225,226]

After this theoretical analysis, all reagents in the company's portfolio were tested according to the following criteria: contact angle on PMMA and migration velocity.

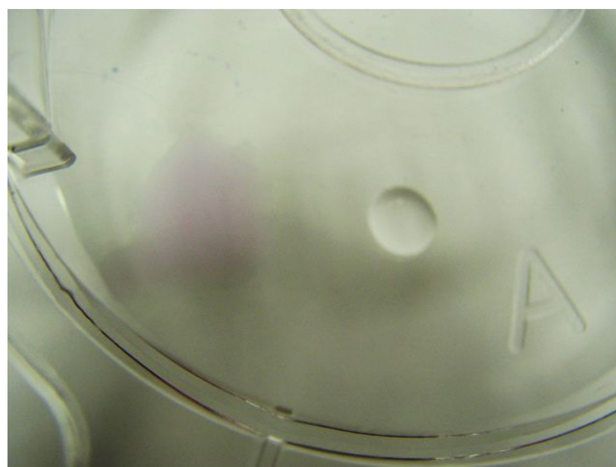

FIGURE 5.13. Surface wetting of PMMA by two different reagents: Calcium, on the left, spreads readily and has a 0° contact angle, whereas Phosphorus, on the right, maintains the droplet form, with a contact angle of 9°.

Figure 5.13 illustrates a qualitative contact angle test on PMMA. It is performed by placing 5μL of reagent on the surface of the rotor; the contact angle can be then estimated from a digital image and a suitable software package.

Contact angle and migration ability of different reagents

The results showed that the reagents could be classified in four different groups (Table 5.2):

- GROUP 1: reagents with contact angle $\gamma > 45°$, do not migrate at all.
- GROUP 2: reagents with contact angle $45° > \gamma > 15°$, show a very slow upwards progress of the meniscus at the wedge surface; usually the liquid is evaporated before it gets to the top of the cuvette and does not progress any further.
- GROUP 3: reagents with contact angle $15° > \gamma > 0°$, show a moderately rapid upwards progress of the meniscus at the wedge surface, which can reach the top of the cuvette in 10-30 min.
- GROUP 4: reagents with contact angle (0°), show a fast progress of the meniscus, which can reach the top of the cuvette in less than 10 min.

GROUP 1	GROUP 2	GROUP 3	GROUP 4
$\gamma > 45°$	$45° > \gamma > 15°$	$15° > \gamma > 0°$	$\gamma = 0°$
ALT	ALBUMIN	TOTAL BILIRUBINE	CALCIUM AR
ALP-AMP	AMILASE EPS	FERROZINE IRON	TOTAL CHOLESTEROL
ALP-DEA	TOTAL PROTEIN	PHOSPHORUS	CREATININE
DIRECT AMILASE	TRIGLYCERIDGES	DIRECT LDL CHOLESTEROL	MAGNESIUM
AST	URIC ACID		
DIRECT BILIRUBINE	DIRECT HDL CHOLESTEROL		
CK			
CK-MB			
gGT			
GLUCOSE			
LDH			
PROTEIN IN URINE			
UREA-UV			
LATEX TURBIDIMETRY			
LATEX-FREE TURBIDIMETRY			

TABLE 5.2. Contact angle of different reagents as measured on the surface of a PMMA rotor.

The results from Table 5.2 were easily correlated to the composition of the different reagents. A close look at the different formulations would reveal that the

addition of different amounts of detergents or alcohols was responsible for the low surface tension and low contact angle. Consequently, it was concluded that reagents in group 4 should have the largest concentration of tensioactives by far.

Ability to contaminate of a migrating reagent

Even if a certain reagent has a very low surface tension and can easily migrate from one cuvette to another, its capacity to affect the optical measurement in the neighboring reaction[34] depends on the amount of liquid that can be transferred to the adjacent cuvette and on the absorption of the contaminating reagent at the wavelength of measurement of the contaminated one. The attention was further closed on Creatinine and Calcium as contaminant candidates, since these reagents have an extremely high absorbance peak (Table 5.3)[35] and therefore, small amounts of these reagents would produce a detectable increase of the absorbance of a neighboring reaction, if contaminated. Not surprisingly, these reagents were among the initial suspects detected in the logs of the original claim.

	CALCIUM	CREATININE
Wavelength (nm)	Absorbance (Abs)	Absorbance (Abs)
340	3.02	215
405	2.67	145
505	5.90	0.48
560	7,63	<0.10
600	2.68	<0.10
635	0.80	<0.10
670	0.24	<0.10

TABLE 5.3. Absorbance at different wavelengths of Calcium and Creatinine reagents. The wavelengths are selected for their use in different tests.

The extent of the effect of optical contamination by a certain volume of any reagent can be calculated with a simple proportional rule, since the absorbance due to molecular chromophores is an additive magnitude. The following expression holds for the total absorbance of a mixture AB of two liquids A and B at a given wavelength:

[34] Only the optical contamination is considered, since the chemical effect depends on the formulation and it was considered to be neglectable for all reagents in group 4.

[35] In fact, the absorbances are so high that they can only be measured by diluting the reagents 1:10 or 1:100 in order to produce solutions within the measuring range of most spectrophotometers.

$$ABS_{AB} = (V_A*ABS_A + V_B*ABS_B) / (V_A+V_B),$$

where V_A and V_B are the initial volumes of the different liquids; ABS_A and ABS_B are the absorbances (always at constant conditions: wavelength and optical path length). The absolute and relative errors due to the contamination are:

$$ERR \approx V_A / (V_A+V_B)*ABS_A$$

$$ERR\ (\%) \approx V_A/V_B*(ABS_A / ABS_B - 1)*100$$

Since most techniques have a sensitivity of 0.050 to 0.200 Abs for normal samples or samples in the low concentration range, a small amount of Creatinine could very easily produce a falsely elevated result, and to less extent, also Calcium. For example, 1μL of Creatinine in 300uL of CK-MB would produce an increase in absorbance of 0.714 Abs which would be falsely identified as a sample with a CK-MB concentration indicating myocyte destruction and therefore possibly diagnosed as myocardial infarction

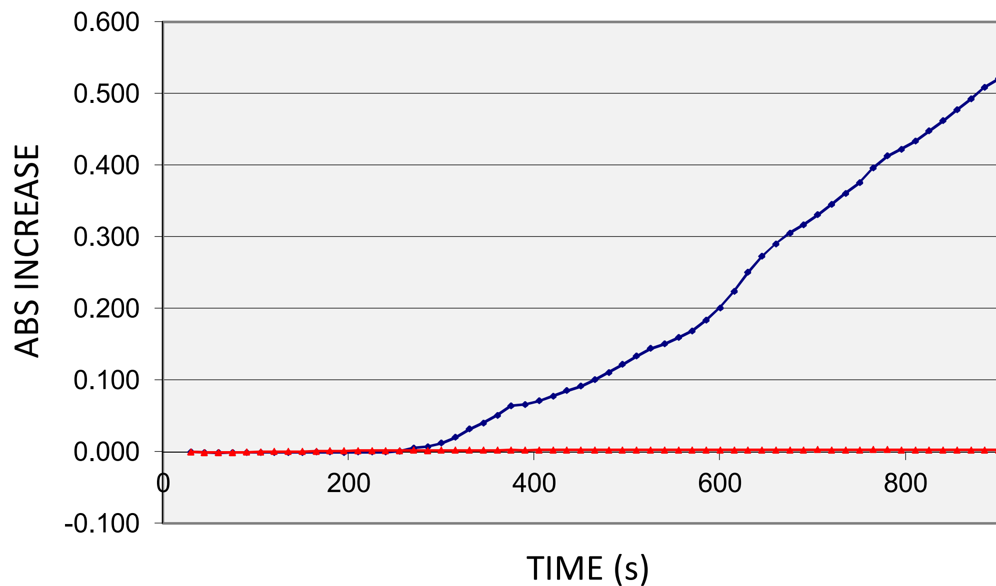

FIGURE 5.14. Contaminated (BLUE) and Uncontaminated (RED) CK-MB replicates from a negative sample. A small amount of Creatinine reagent produces a falsely elevated result that could lead to an incorrect diagnosis of heart attack. In this case, the trace of contaminant is quantified to be only around 0.8μL.

5.3.5. Strategies to solve the problem

Once a clear knowledge of the nature of the problem was available, implementing a solution to avoid the migration effect of contaminating reagents could be realized by different approaches:

1) Changing the geometry of the cuvettes by avoiding any sharp wedges.
2) Molding the part with a plastic polymer of lower surface energy.
3) Modifying the surface of the PMMA rotor to diminish its surface energy.
4) Changing the formulation of all problematic reagents in order to increase their surface tension.

Approach 1) was the most desirable since it would completely prevent the migration effect. A new geometry had to be defined with a sufficiently large radius to be applied to any corner or dihedral surface, without affecting the optical windows of the cuvettes; after that, the time needed to produce the mold and validate the part would take no less than 8 months, while more than 10.000 rotors per month were already in production.

Approach 2), switching materials in a complicated molded part, is not always as easy as it seems and has some potential drawbacks: all the injection parameters have to be optimized again, including costly fluidic simulations for the flow of melted plastic and filling of the mold; cooling rates and shrinkage of the part are material dependent and need to be assessed again; new sink marks or defects due to incomplete filling of some features may have to be corrected; there is always a risk of mold damage if the new parts get stuck (which would have been catastrophic for the Company's ability to deliver pending orders); and finally, even if the same mold could be used, the possible candidate materials to replace PMMA were very limited due to the following requirements:

- lower surface energy than PMMA, which is around 41-46 mJ/m^2;
- comparable or better optical transmittance at the UVA-VIS range;
- good dimensional stability and good mechanical performance to avoid sink marks or scratches in the optical window during molding and also during user manipulation (since many customers wash and reuse the rotors several times);

- good chemical stability to hold liquids such as alcohols, acids, bases, buffers and detergents commonly employed in the formulation of biochemistry reagents;
- low cost, since the rotor is a bulky part and the cost of the raw material could result in an unacceptable cost increase.

Approach 3) could be implemented in two different ways, both leading to a modification of the surface energy: additive processes or non-additive processes. An additive process would require the deposition of a thin conformal coating with a low surface energy, for example by plasma polymerization of HMDSO; a non-additive process would imply the modification or removal of polar groups on the surface of PMMA, since the largest contribution to its surface energy is given by the polar component due to groups such as carbonyl and carboxyl.[227]

Approach 4) required a thorough review of the formulations of at least Group 4 reagents to generate an equivalent composition for each reagent with a lower surface energy. This would imply a huge effort in terms of regulatory approval to demonstrate an equivalent performance of the modified reagents, and it would be a lengthy process, as well.

With all these key points in mind, it was decided to undertake only approaches 1) and 3) in parallel, i.e.: a change in the geometry of the cuvettes and perform a surface modification, both by additive and non-additive processes. Approach 2) was discarded due to the high cost of the only feasible material (COC). Approach 4) was discarded because it was reagent dependent, would have a high regulatory impact and would not solve the problem for good.

5.3.5.1. Geometry modification: rounded corners

As mentioned before, in order to completely solve the problem and avoid the capillary-driven flow along the corners of the cuvettes, a modification in the geometry of the cuvettes had to be undertaken. The aim was to impede capillary rise even for reagents with 0° contact angle by applying a certain radius to the dihedral angles

formed by the walls, and therefore fail to meet the Concus-Finn condition.(36) It was crucial to estimate the minimum radius that would safely prevent capillary raise without modifying the geometry in excess, since large radii would create thick walls that would produce sink marks close to the optical windows of the cuvettes, where the measurements take place, and that could produce unexpected results in certain tests(37). Also, the modification needed to be made on solid grounds, since the effect of the new geometry could not be assessed until 6-8 months later, when first sample parts from the new molds would be available, and a failure to solve the problem would represent a huge loss in time and materials costs.(38)

There are a few physical and mathematical derivations for the problem of capillary rise of liquids in wedges and in slightly rounded wedges.[226,228] Scott, Sander and Norbury demonstrated that even a little rounding of corners has a dramatic effect on reducing the liquid rise in the corner.[228] When the contact angle θ is fixed, a corresponding critical (maximum) roundedness for every corner can be identified above which no spontaneous flow can take place.[225] Unfortunately, no clear analytical expression can be found to express this relation in a simple way and the estimates need to be computed. A calculation for several rounded corners on a wedge shows that small radii of a fraction of the characteristic capillary length d are sufficient to greatly diminish the capillary height at the corner. Since the characteristic capillary length d of a liquid is given by:

$$d = \left(\frac{\sigma}{\rho \cdot g}\right)^{1/2}$$

where σ and ρ are the surface tension and the density of the liquid, and g is the acceleration of gravity, for aqueous solutions with a large amount of tensioactive (where σ may be as low as 20-25 mJ/m^2) d is usually in the range 1.4 to 1.6 mm. Table 5.4 shows the estimated height of the liquid column at the contact line for a 45°

(36) Everyday experience confirms that liquids do not raise infinitely in a rounded glass or plastic tube, regardless of the liquid contained in it.

(37) Turbidimetry techniques, for example, are very sensitive to changes in the paths followed by the optical rays in the beam. This is due to the fact that these tests are not based on molecular absorption (colorimetry) but on light scattering, where the angles formed by the different rays have to be controlled with excellent precission.

(38) As a quick reference, the cost of a single-cavity mold with a difficult geometry, with mirror-like polishing for optical measurements in 240 windows (120 front+120 rear) and dimensional accuracy (since the pathlength of the cuvette depends on the precision of the mold) would be in excess of 100 k€.

wedge (22.5° semiangle) normalized by the capillary length (from Ref. [228]). As an example, applying a radius of 0.5 *d* (0.7 - 0.8 mm) would reduce the infinite rise of a highly wetting liquid (1° contact angle) down to 2.65 *d* (4.2 mm). The geometry of the cuvettes allows a nominal distance of 8 mm from the surface of maximum volume of liquid for any reagent to the top of its confining wall,[(39)] so that a meniscus height of 4.2 mm should be on the safe side. Besides, the estimation of the radius is based on a calculation for a 45° wedge, whereas the cuvettes in the rotor are defined by a 90° wedge. Since a smaller angle generates a larger capillary effect, the radius that eliminates the infinite capillary effect in a smaller angle wedge should also eliminate it in a larger one.

Contact Angle	R_c=0	R_c=0.10	R_c=0.25	R_c=0.50	R_c=1
85 °	0.366	0.269	0.220	0.179	0.143
80 °	0.751	0.541	0.440	0.357	0.285
75 °	1.606	0.816	0.660	0.535	0.428
70 °	29.43	1.096	0.898	0.711	0.567
65 °	56.42	1.384	1.100	0.886	0.706
60 °	82.06	1.688	1.321	1.060	0.844
45 °	∞	2.798	1.989	1.562	1.236
30 °	∞	4.732	2.684	2.031	1.593
10 °	∞	8.078	3.648	2.549	1.971
5 °	∞	8.756	3.833	2.614	2.025
1 °	∞	9.009	3.904	2.650	2.043

Table 5.4. Estimated height of the liquid column at the contact line for a 45° wedge (22.5° semiangle) for different rounded corners with dimensionless radius R_c normalized by the characteristic capillary length for different contact angles (from Ref. [228]).

5.3.5.2. Surface modification of PMMA by additive process: PP-HMDSO hydrophobic coating

As demonstrated in Chapter 3, PP-HMDSO films can be produced with a very high water contact angle, around 100-110°, and a correspondingly low surface energy around 26 mJ/m^2, with excellent adhesion and high deposition rates on almost any kind of substrate. Consequently, it could be a good option in order to create a stable

[(39)] Geometrical estimation by considering the geometry of the cuvette and a volume of filling liquid of 450 μL without capillary effects ($\gamma = \pi/2$)

hydrophobic coating onto the PMMA surface. A first analysis of the requirements of a suitable functional coating for the application was made and the technological parameters for initial tests were chosen accordingly. Tables 5.5.a,b,c show the main requirements for the coating and the corresponding plasma parameters.

FILM REQUIREMENTS	
WATER CONTACT ANGLE	> 100°
SURFACE ENERGY	< 30 mJ/m^2
THICKNESS	20-50 nm

PLASMA REQUIREMENTS	
INDUCED SUBSTRATE TEMPERATURE	< 50 °C
FRAGMENTATION OF MONOMER	LOW

TECHNOLOGICAL PARAMETERS	
PRESSURE	0.100 mbar
POWER	50 W
SOURCE	RF
ELECTRODE GEOMETRY	Parallel plates
POSITION	immediate afterglow
FLOW RATE HMDSO	10 sccm
FLOW RATE Ar	1 sccm
DEPOSITION TIME	30 s
SURFACE PRE-TREATMENT	None

Table 5.5.a.b.c. Requirements specified for the deposition of a ppHMDSO films with hydrophobic properties on a large PMMA part.

The rationale behind the choice of parameters was as follows:

Low surface energy is achieved by preserving the structure of the HMDSO monomer as much as possible. To that end, setting the plasma parameters in an energy-deficient regime, i.e. low DC or RF power and high flow of monomer, results in low fragmentation of the monomer. The monomer molecules will suffer less energetic collisions by electron impact, thus avoiding major scission of $-CH_3$ groups, which provide the hydrophobic behavior.

To minimize any damage to the PMMA rotors, a DC plasma with an afterglow configuration was chosen and the parts were placed 30 mm below the plasma zone (see Figure 5.5). RF is preferred to DC because the plasma is more stable and the temperature increase on the sample is reduced. The choice of the afterglow location is for the same reason. Gas flows were chosen to be 40 sccm of HMDSO and 5 sccm of Ar and the total pressure was set at 0.300 mbar. Ar was added in order to slightly increase the plasma density, the amount of reactive species, and therefore the deposition rates, but only at a low proportion to avoid excessive monomer fragmentation. Ar and HMDSO were initially fed from the top of the chamber. Different electrode geometries were tested, seeking for the most uniform, conformal

and transparent coating. Deposition time was fixed at 30”, according to growth rates

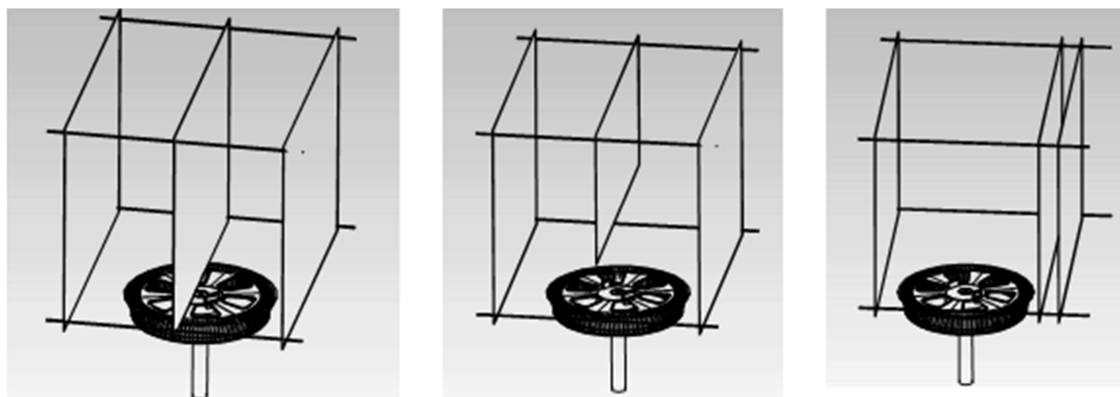

FIGURE 5.15. Different parallel plate electrode configuration for afterglow plasma deposition on PMMA rotors. The configuration in the middle produces the best results in therms of film homogeneity.

in afterglow configuration, which are between 50-100 nm/min, for 100W. Since surface energy is a surface property to which only a few nanometers of the material contribute, just a very thin coating is required in order to reduce capillarity. Due to the 3D geometry of the part, it was not feasible to produce a coating with homogeneous thickness, but the goal was to produce conformal coatings of 10-50 nm (maximum thickness variation within same coating) with good adhesion. Thicker coatings would also eliminate the capillarity problem, but they would generate uncontrolled interference fringes which would affect the visible aesthetic appearance of the rotor. Deposition times also had to be kept to a minimum in order to reduce bombardment by highly energetic species in the plasma onto the PMMA surface. This could result in undesired effects such as a slightly yellowish surface, or a temperature increase which could deform the part.[(40)] Glass slides were placed together with the PMMA rotors to verify the thickness of the coatings and their contact angle in different liquids.[(41)]

Cross-contamination tests in ppHMDSO-coated cuvettes

Figures 5.16 and 5.17 show some images illustrating the functional improvement of the hydrophobic behavior of the surfaces after 30 s of plasma deposition of

[(40)] As shown in the previous application: “Anti-scratch protective coatings on ABS plastic parts”

[(41)] Although for very thin films, the initial stages of growth depend on the material, and therefore thickness on glass is only to be considered as an approximate reference of thickness on PMMA.

ppHMDSO. Figure 5.16 shows two glass slides with and without the ppHMDSO coating. Two drops of 5μL of Ca (purple) and CK-MB (transparent) reagents were

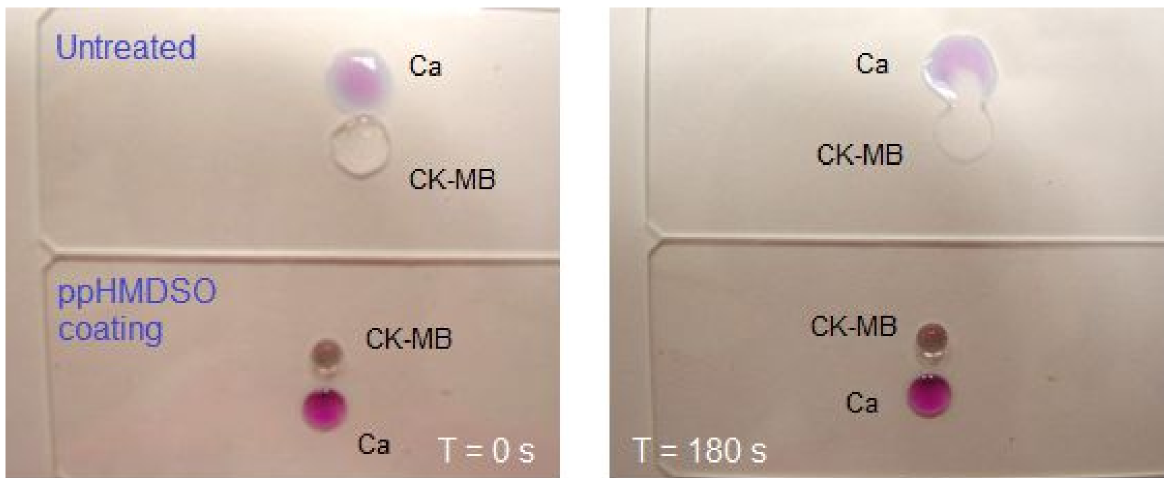

FIGURE 5.16. Evolution of the liquid surface at t=0 and t=180 s of two drops of Ca and CK-MB reagents dispensed in close proximity on untreated glass (top slide) and ppHMDSO-coated glass (bottom slide).

dispensed in close proximity and the evolution was observed. After 3 min, both drops have already contacted and start interdiffusing on the untreated glass-slide, whereas the treated glass-slide leaves the free-surface of the liquids stable until all liquid evaporates.

Figure 5.17 shows the same reagents deposited on the flat surface top of the reactor of cuvettes showing that the same effect is achieved by the ppHMDSO coating

FIGURE 5.17. Assesment of the improvement in hydrophobic behavior of ppHMDSO-coated rotor (RIGHT) as compared to an untreated rotor (LEFT) by depositing 5μL of Ca and CK-MB reagents.

on PMMA. Coated rotors are more hydrophobic than the untreated ones.

The thickness of the ppHMDSO coatings, as measured on the glass slides was around 60-70 nm, but the thickness measured by cutting different parts of the rotors indicated that whereas on the flat surface on top of the rotor the thickness was similar to the value measured on glass, within the wells it was much lower and very difficult to measure. In some samples we found thicknesses of 10-20 nm inside the wells, but hardly reproducible. In some cases, the step created by the coating was not detectable, but in all cases the samples were more hydrophobic than bare untreated PMMA.

The functionality of the coated rotors was tested and compared to the functionality of the untreated rotors in order to verify that the migration of problematic reagents could be avoided by the coating. A series of intercalated negative reactions where run combining Creatinine and CK-MB reagents and the number and position of reaction wells were the “false positive” curves appeared was measured as the figure of merit to assess the progress. Figures 5.18 and 5.19 show the results for an untreated rotor and for a ppHMDSO coated rotor respectively. The coated rotor is a best case, where the deposition time was increased to 90”, and the thickness on the flat top surface was 190-200 nm. For these two runs, the results show that the occurrence of falsely elevated concentrations is 58% for the untreated rotor and 5% for the coated rotor.

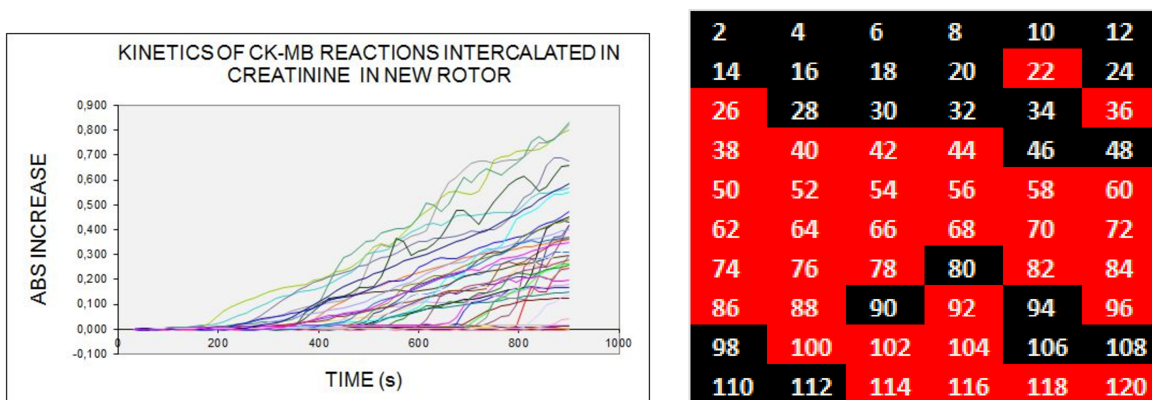

FIGURE 5.18. (LEFT) Kinetic Curves of CK-MB negative reactions intercalated between Creatinine reactions in a new rotor. **(RIGHT)** Creatinine-contaminated CK-MB reactions are identified in red; uncontaminated reactions are identified in black. A cross-contamination occurs within 15 min in 35 out of 60 cuvettes, i.e. in 58% of the replicates.

It was not possible to find conditions in the afterglow that would eliminate completely the contamination with less than 1 min of deposit. With higher treatment times, it was possible to ensure complete coverage but the thickness deposited on flat optical surfaces was too high and affected the measurements of the analyzer at 340 nm;[42] interference fringes also developed.

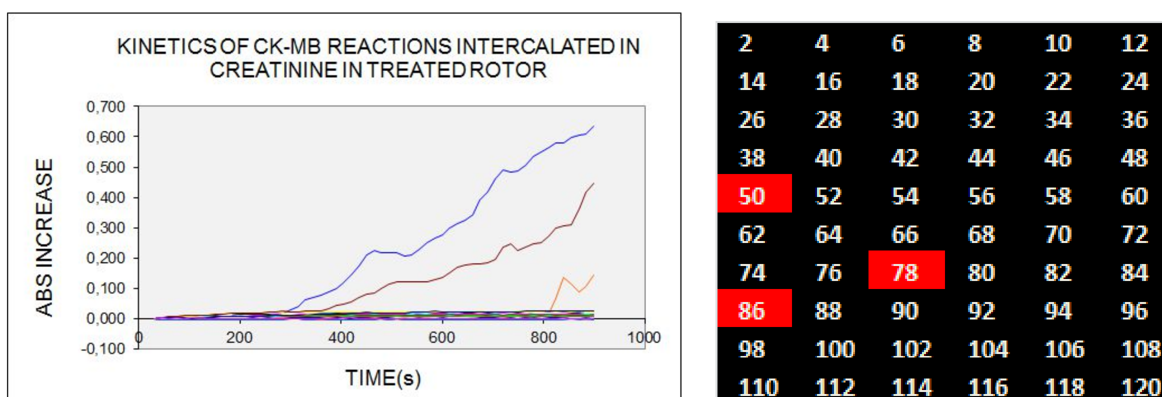

FIGURE 5.19. (LEFT) Kinetic Curves of CK-MB negative reactions intercalated between Creatinine reactions in an HMDSO coated rotor. **(RIGHT)** Creatinine-contaminated CK-MB reactions are identified in red; uncontaminated reactions are identified in black. A cross-contamination occurs within 15 min in 3 out of 60 cuvettes, i.e. in only 5% of the replicates.

We believe that the complex geometry of the rotor and the inefficient transport inside the cuvettes of radicals and monomer fragments leading to the growth of the polymer do not allow to obtain full coverage of all surfaces in the rotor with short deposition times. To this aim, the dihedral wedges of the cuvettes are extremely challenging to coat, and clearly the deposited films were not 100% conformal. Still, we expected that the coating on the top edge of the walls would be sufficient to stop liquid overflow from any cuvette to the neighboring one. This was true for most wells but some were not effectively coated as to completely eliminate the probability of cross-contamination between neighboring reactions.

[42] The absorbance of the film is multiplied by almost a factor of 4 because both sides of each wall are covered by the film and thus the light path is transmitted four times through ppHMDSO films, twice for the entrance into the reaction cuvette and twice for the exit.

5.3.6. Conclusions and final decision

Analysis of the cross-contamination found between neighboring reactions in the cuvettes of a clinical chemistry analyzer demonstrated that the root source of the problem was the flow of low surface tension reagents by capillarity along the dihedral edges of the PMMA cuvettes. We assayed the deposition of a low surface energy coating by plasma polymerization of HMDSO in energy-deficient conditions in the afterglow of a RF plasma. The results showed that depositing a ppHMDSO coating on top of the PMMA rotor of cuvettes was possible and reduced the frequency of cross-contaminations between reagents with very low surface tension. Unfortunately, a homogeneous conformal film was not possible within short deposition times, which resulted in a residual probability of cross-contamination. The procedure was not scalable, i.e. it had to be performed rotor by rotor, i.e. one rotor per each plasma cycle. The Company decided to employ a chemical modification procedure(43) which was cheaper and scalable to bridge the time span necessary for the fabrication of a new mold with rounded corners.

(43) The final process was based on a series of chemical treatments in liquid reagents and a final rinse in deionized water. The protocol finally employed is not disclosed in this thesis.

CONCLUSIONS

- Plasma polymerization of hexamethyldisiloxane can be successfully achieved in a DC plasma reactor provided that the reactor, anode and cathode surfaces are clean in order to avoid arcing. Plasma polymerization in the direct configuration can be sustained up to 60 min if these conditions are met. Polymer-like films have been grown to thickness up to 3 μm. Higher thickness may be possible but the plasma is highly instable when the dielectric film grows thick on the electrodes.

- Deposition rates are highly dependent on the composite parameter, Y. Higher values of Y result in higher deposition rates. Deposition rates up to 200 nm/min have been achieved for short deposition times, but these rates decrease with time as the intensity of the glowing plasma is diminished by the isolating film growing on all surfaces.

- Conformal films are achieved more easily at higher pressures, where the mean free-path of the molecules is smaller and the gas behaves like a fluid.

- Uniform films with static substrates are achieved more easily at lower pressures, where the mean-free path of the molecules is higher and the interactions in the gas phase smaller, and in a parallel plate electrode configuration.

- Loss of transparency with a characteristic milky appearance is produced by scattering of globular like structures incorporated in the growing film. This can happen due to ultra-fast polymerization rates in the energy-deficient regime and at higher pressures. The same effect is observed when local glows are generated near the substrates due to arcing or plasma instability.

- At very high pressures and high powers, powders can be generated in the gas phase.

- The properties of DC ppHMDSO thin films are dependent on many different operational parameters (pressure, residence time of molecules, deposition time, starting gas mixture composition, power, electrodes surface area, geometry, substrate location) but the most important parameter is the composite parameter, Y=W/(M*F), which relates de energy available per monomer molecule, and allows to define three regimes: monomer-deficient regime, transition-regime and energy-deficient regime

- The character of the films may be varied from polymer-like to inorganic-like by varying the composite parameter and the relative amount of oxygen in the precursor mixture. Polymer-like films with high C/Si and low O/Si ratios are mainly produced in the energy-deficient regime and at low oxygen concentrations; inorganic-like films with low C/Si and high O/Si rations are obtained in the monomer-deficient regime and at high oxygen concentrations.

- The addition of oxygen results in the deposition of silica-like films in any regime, but it is more efficient in the high energy regime. Silica-like films can be obtained at oxygen/monomer ratios of 1.0 - 1.5, but they can only be grown up to 300 nm in thickness.

- Inorganic films grown at high Y values are generated by cleavage of organic groups, which can be produced in the gas phase or by ion/solid interaction, due to ion-bombardment during film growth. When the cleavage of organic groups and high fragmentation of the monomer are produced already in the

gas phase by electron impact or charge exchange, inorganic films will develop independently of the location of the substrate. Films with inorganic-like properties can be also obtained by locating the substrates in high ion bombardment locations, especially at or in proximity to the cathode.

- In the monomer deficient regime, monomer molecules are highly fragmented. Films grown in the monomer deficient region have lower organic content, due to cleavage of methyl groups; hence their refractive index is lower and their hardness and elastic modulus higher.

- Plasma post-treatments are an effective method to modify the surface properties of polymer-like ppHMDSO films in order to obtain graded films.

- Oxygen plasma treatments achieve complete Carbon depletion and full oxidation of the surface in less than 10 min. Non-reactive plasma treatments with Ar or N2 do not achieve full oxidation of the surface, but rather enhance cross-linking.

- The penetration depth of the treatment is highly dependent on the treatment time, and the density and porosity of the films. When high-density films are post-treated, the penetration depth is limited to a few tens of nanometers, whereas for medium and low density films, it can extend to more than 100 nm.

- The main mechanism for interpreting the evolution of the modified depth is diffusion of oxygen radicals, rather than ionic, electronic or UV absorption mechanisms.

- Plasma treatment outside the active zone of the plasma is also effective in creating a hydrophilic surface.

- The surfaces of plasma-treated ppHMDSO films are harder and more hydrophilic than the untreated ones.

- Hydrophobic recovery is not significant in plasma treated ppHMDSO films due to their intrinsic higher cross-linking, as compared to conventional bulk polymers.

- Hydrophobic recovery can be greatly diminished in conventional PDMS polymer by depositing a ppHMDSO film and effecting an ulterior post-treatment in oxygen or argon plasmas.

- Plasma treatment of ppHMDSO films on PDMS substrates should be limited in time to less than 10 min if the sample is placed in the active plasma zone or 20 min if it is placed in the remote region.

- DC Plasma polymerization of HMDSO proves to be a simple and feasible technology with applicability to solve multiple industrial problems, provided that the required thicknesses of the films are within the limitations of the technique.

BIBLOGRAPHY

1. Ohring, M. Materials science of thin films. *Acad. Press San Diego* (2001).
2. Mattox, D. The Foundations of Vacuum Coating Technology. *Noyes Publ. Norwich USA* (2003).
3. Edison, T. Art of Plating One Material on Another. *US Pat. 526147* (1894).
4. Faraday, M. Researches in Electricity. *Lond. UK* (1844).
5. Langmuir, I. The interaction of electron and positive ion space charges in cathode sheaths. *Phys. Rev.* **33,** 954–989 (1929).
6. Staudinger, H. Über polymerisation. *Berichte Dtsch. Chem. Ges. B Ser.* **53,** 1073– 1085 (1920).
7. Yasuda, H. Plasma polymerization. *Acad. Press Orlando USA* (2012).
8. Grill, A. Cold plasma in materials fabrication. *Wiley-IEEE Press* (1994).
9. Boehnig, H. Fundamentals of plasma chemistry and Technology. *Technomic Publ. Companay Lanc.* (1998).
10. Martin, P. Handbook of deposition technologies for films and coatings: science, applications and technology. *Elsevier Burlingt. USA* (2009).
11. Fridman, A. & Kennedy, L. Plasma physics and engineering. *Taylor Francis N. Y.* (2004).
12. von Engel, A. Ionized Gases. *Am. Institure Phys. N. Y. USA* (1994).
13. Yu, Q., Huang, C. & Yasuda, H. Glow characterization in direct current plasma polymerization of trimethylsilane. *J. Polym. Sci. Part Polym. Chem.* **42,** 1042–1052 (2004).
14. Yasuda, H. Some important aspects of plasma polymerization. *Plasma Process. Polym.* **2,** 293–304 (2005).
15. Goodman, J. The formation of thin polymer films in the gas discharge. *J. Polym. Sci.* **44,** 551–552 (1960).
16. Inagaki, N. Plasma surface modification and plasma polymerization. *Technocmic Publ. Lancaste USA* (1996).
17. Hegemann, D., Hossain, M., Körner, E. & Balazs, D. J. Macroscopic description of plasma polymerization. *J. Phys. Appl. Phys.* **46,** (2007).
18. Hegemann, D. Macroscopic investigation of reaction rates yielding plasma polymer deposition. *J. Phys. Appl. Phys.* **46,** 1–7 (2013).
19. Friedrich, J. Mechanisms of plasma polymerization–reviewed from a chemical point of view. *Plasma Process. Polym.* **8,** 783–802 (2011).

20. Willliams, T. & Hayes, M. Polymerization in a glow discharge. *nature.com* **209,** 769–773 (1966).

21. Haller, I. & White, P. Polymerization of butadiene gas on surfaces under low energy electron bombardment. *J. Phys. Chem.* **67,** 1784–1788 (1963).

22. Westwood, A. Glow discharge polymerization—I. Rates and mechanisms of polymer formation. *Eur. Polym. J.* **7,** 363–375 (1971).

23. Thompson, L. & Mayhan, K. The plasma polymerization of vinyl monomers. I. The design, construction, and operation of an inductively coupled plasma generator and preliminary studies with nine monomers. *J. Appl. Polym. Sci.* **16,** 2291–2315 (1972).

24. Kobayashi, H., Bell, A. & Shen, M. Formation of an amorphous powder during the polymerization of ethylene in a radio-frequency discharge. *J. Appl. Polym. Sci.* **17,** 885–892 (1973).

25. Carchano, H. Gas-discharge polymerization. *J. Chem. Phys.* **61,** 3634 (1974).

26. Tibbitt, J., Jensen, R., Bell, A. & Shen, M. A model for the kinetics of plasma polymerization. *Macromolecules* **10,** 647–653 (1977).

27. Ivanov, S., Fakirov, S. & Svirachev, D. Radio-frequency gas-discharge polymerization of ethylene and acetylene. *Eur. Polym. J.* **14,** 611–617 (1978).

28. Yasuda, H. Glow discharge polymerization. *Thin Film Process.* **16,** 199–293 (1978).

29. Yasuda, H. & Yasuda, T. The competitive ablation and polymerization (CAP) principle and the plasma sensitivity of elements in plasma polymerization and treatment. *J. Polym. Sci. Part Polym. Chem.* **38,** 943–953 (2000).

30. Yasuda, H. Luminous Chemical Vapor Deposition and Interface Engineering. *Marcel Dekker N. Y. USA* (2005).

31. Lommatzsch, U. & Ihde, J. Plasma Polymerization of HMDSO with an Atmospheric Pressure Plasma Jet for Corrosion Protection of Aluminum and Low-Adhesion Surfaces. *Plasma Process. Polym.* **6,** 642–648 (2009).

32. Esteve, J. *et al.* Protective coatings for Al metallizations obtained by plasma polymerization. in (ed. Fulton, M. L.) 120–128 (2000). doi:10.1117/12.404758

33. Török, T., Urbán, P. & Lassú, G. Surface cleaning and corrosion protection using plasma technology. *Int J Corros Scale Inhib* **4,** 116–124 (2015).

34. Vautrin-Ul, C., Roux, F., Boisse-Laporte, C., Pastol, J. L. & Chausse, A. Hexamethyldisiloxane (HMDSO)-plasma-polymerised coatings as primer for iron corrosion protection: influence of RF bias. *J. Mater. Chem.* **12,** 2318–2324 (2002).

35. Bour, J. *et al.* Different Ways to Plasma-Polymerize HMDSO in DBD Configuration at Atmospheric Pressure for Corrosion Protection. *Plasma Process. Polym.* **5,** 788–796 (2008).

36. Fracassi, F. *et al.* Application of plasma deposited organosilicon thin films for the corrosion protection of metals. *Surf. Coat. Technol.* **174,** 107–111 (2003).

37. Angelini, E., Grassini, S., Rosalbino, F., Fracassi, F. & d'Agostino, R. Electrochemical impedance spectroscopy evaluation of the corrosion behaviour of Mg alloy coated with PECVD organosilicon thin film. *Prog. Org. Coat.* **46,** 107–111 (2003).

38. Bardon, J. *et al.* Deposition of Organosilicon-Based Anticorrosion Layers on Galvanized Steel by Atmospheric Pressure Dielectric Barrier Discharge Plasma. *Plasma Process. Polym.* **4,** S445–S449 (2007).

39. Petit-Etienne, C., Tatoulian, M., Mabille, I., Sutter, E. & Arefi-Khonsari, F. Deposition of SiOχ-Like Thin Films from a Mixture of HMDSO and Oxygen by Low Pressure and DBD Discharges to Improve the Corrosion Behaviour of Steel. *Plasma Process. Polym.* **4,** S562–S567 (2007).

40. Vassallo, E., Cremona, A., Laguardia, L. & Mesto, E. Preparation of plasma-polymerized SiO x-like thin films from a mixture of hexamethyldisiloxane and oxygen to improve the corrosion behaviour. *Surf. Coat. Technol.* **200,** 3035–3040 (2006).

41. Fernandes, J. C. S. *et al.* Plasma-polymerised coatings used as pre-treatment for aluminium alloys. *Surf. Coat. Technol.* **154,** 8–13 (2002).

42. Grünwald, H. *et al.* Better aluminium mirrors by integrating plasma pretreatment, sputtering, and plasma polymerization for large-scale car headlight production. *Surf. Coat. Technol.* **111,** 287–296 (1999).

43. Del Frari, D. *et al.* Hybrid layers deposited by an atmospheric pressure plasma process for corrosion protection of galvanized steel. *J. Nanosci. Nanotechnol.* **10,** 2611–2619 (2010).

44. Miyachi, H., Ikebukuro, K., Yano, K., Aburatani, H. & Karube, I. Single nucleotide polymorphism typing on DNA array with hydrophobic surface fabricated by plasma-polymerization technique. *Biosens. Bioelectron.* **20,** 184–189 (2004).

45. Hayakawa, T., Yoshinari, M. & Nemoto, K. Characterization and protein-adsorption behavior of deposited organic thin film onto titanium by plasma polymerization with hexamethyldisiloxane. *Biomaterials* **25,** 119–127 (2004).

46. Mutlu, M., Mutlu, S., Boyaci, I. H., Alp, B. & Piskin, E. High-linearity glucose enzyme electrodes for food industries: preparation by a plasma polymerization technique. (1998).

47. Prasad, G. R. *et al.* PECVD of biocompatible coatings on 316L stainless steel. *Surf. Coat. Technol.* **200,** 1031–1035 (2005).

48. Bayram, C. *et al.* In vitro biocompatibility of plasma-aided surface-modified 316L stainless steel for intracoronary stents. *Biomed. Mater.* **5,** 055007 (2010).

49. Tang, L., Wu, Y. & Timmons, R. B. Fibrinogen adsorption and host tissue responses to plasma functionalized surfaces. *J. Biomed. Mater. Res.* **42,** 156–163 (1998).

50. Malmsten, M., Muller, D. & Lassen, B. Sequential adsorption of human serum albumin (HSA), immunoglobulin G (IgG), and fibrinogen (Fgn) at HMDSO plasma polymer surfaces. *J. Colloid Interface Sci.* **193,** 88–95 (1997).

51. Gandhiraman, R. P., Daniels, S. & Cameron, D. C. A Comparative Study of Characteristics of SiOxCyHz, TiOx and SiO-TiO Oxide-Based Biocompatible Coatings. *Plasma Process. Polym.* **4,** S369–S373 (2007).

52. Jankowski, P., Ogonczyk, D., Kosinski, A., Lisowski, W. & Garstecki, P. Hydrophobic modification of polycarbonate for reproducible and stable formation of biocompatible microparticles. *Lab. Chip* **11,** 748–752 (2011).

53. Gandhiraman, R. P. *et al.* Interaction of Plasma Deposited HMDSO-Based Coatings with Fibrinogen and Human Blood Plasma: The Correlation between Bulk Plasma, Surface Characteristics and Biomolecule Interaction. *Plasma Process. Polym.* **7,** 411–421 (2010).

54. Shahidi, S., Ghoranneviss, M., Wiener, J., Moazzenchi, B. & Mortazavi, H. Effect of Hexamethyldisiloxane (HMDSO)/Nitrogen Plasma Polymerisation on the Anti Felting and Dyeability of Wool Fabric. *Fibres Text. East. Eur.* 116–119 (2014).

55. Kayaoğlu, B. K. & Öztürk, E. Imparting hydrophobicity to natural leather through plasma polymerization for easy care effect. *Fibers Polym.* **14,** 1706–1713 (2013).

56. Kale, K. H., Palaskar, S. & Bhat, N. V. Effect of plasma polymerization of hexamethyldisiloxane on polyester / cotton blended fabrics properties. *AATCC Rev. Mag. Text. Dye. Print. Finish. Ind.* **12,** 53–60 (2012).

57. Kale, K. H. & Palaskar, S. Atmospheric Pressure Plasma Polymerisation of Hexamethyldisiloxane for Imparting Water Repellency to Cotton Fabric. *Text. Res. J.* 0040517510385176 (2010).

58. Sariisik, M., Kilic, B., Cireli Aksit, A. & Mutlu, M. Surface modification and characterization of cotton and polyamide fabrics by plasma polymerization of hexamethyldisilane and hexamethyldisiloxane. *Int. J. Cloth. Sci. Technol.* **21,** 137–145 (2009).

59. Dai, X. J., Church, J. S. & Huson, M. G. Pulsed plasma polymerization of hexamethyldisiloxane onto wool: Control of moisture vapor transmission rate and surface adhesion. *Plasma Process. Polym.* **6,** 139–147 (2009).

60. Rombaldoni, F. *et al.* The effects of HMDSO plasma polymerization on physical, low-stress mechanical and surface properties of wool fabrics. *AUTEX Res. J.* **8,** 77–83 (2008).

61. Sarmadi, A. M., Ying, T. H. & Denes, F. HMDSO-plasma modification of polypropylene fabrics. *Eur. Polym. J.* **31,** 847–857 (1995).

62. Hegemann, D. Plasma polymerization and its applications in textiles. *Indian J. Fibre Text. Res.* **31,** 99–115 (2006).

63. Höcker, H. Plasma treatment of textile fibers. *Pure Appl. Chem.* **74,** 423–427 (2002).

64. Ji, Y. Y., Chang, H. K., Hong, Y. C. & Lee, S. H. Water-repellent improvement of polyester fiber via radio frequency plasma treatment with argon/hexamethyldisiloxane (HMDSO) at atmospheric pressure. *Curr. Appl. Phys.* **9,** 253–256 (2009).

65. Palaskar, S., Kale, K. H., Nadiger, G. S. & Desai, A. N. Dielectric barrier discharge plasma induced surface modification of polyester/cotton blended fabrics to impart water repellency using HMDSO. *J. Appl. Polym. Sci.* **122,** 1092–1100 (2011).

66. López-Barrea, J. A., Pimentel-Tinoco, O. G., Olayo-Valles, R., Morales-Corona, J. & Olayo, R. Water permeability of quarry stone superficially modified by plasma polymerization of hexamethyldisiloxane at atmospheric pressure. *J. Coat. Technol. Res.* **11,** 661–664 (2014).

67. Balastikova, R. *et al.* Protection of Archaeological Artefacts by Deposition of Parylene and SiOx Thin Films.

68. Krcma, F. *et al.* Application of low temperature plasmas for the treatment of ancient archaeological objects.

69. Al Tarazi, S. *et al.* Deposition of SiO x layer by plasma-enhanced chemical vapor deposition for the protection of silver (Ag) surfaces. *Radiat. Eff. Defects Solids* **169,** 217–224 (2014).

70. Zanini, S. *et al.* Wood coated with plasma-polymer for water repellence. *Wood Sci. Technol.* **42,** 149–160 (2008).

71. Kuzminova, A. *et al.* From super-hydrophilic to super-hydrophobic surfaces using plasma polymerization combined with gas aggregation source of nanoparticles. *Vacuum* **110,** 58–61 (2014).

72. Foroughi Mobarakeh, L., Jafari, R. & Farzaneh, M. Superhydrophobic surface elaboration using plasma polymerization of hexamethyldisiloxane (HMDSO). in *Advanced Materials Research* **409,** 783–787 (Trans Tech Publ, 2012).

73. Rats, D., Martinu, L. & Von Stebut, J. Mechanical properties of plasma-deposited SiO x N y coatings on polymer substrates using low load carrying capacity techniques. *Surf. Coat. Technol.* **123,** 36–43 (2000).

74. Taeschner, K., Bartzsch, H., Frach, P. & Schultheiss, E. Scratch resistant optical coatings on polymers by magnetron-plasma-enhanced chemical vapor deposition. *Thin Solid Films* **520,** 4150–4154 (2012).

75. Rzad, S. J., Conley, D. J. & Reed, C. W. *Method of preparing UV absorbant and abrasion-resistant transparent plastic articles*. (Google Patents, 1992).

76. Hegemann, D., Brunner, H. & Oehr, C. Deposition rate and three-dimensional uniformity of RF plasma deposited SiO x films. *Surf. Coat. Technol.* **142-144,** 849–855 (2001).

77. Nowling, G. R. *et al.* Chamberless plasma deposition of glass coatings on plastic. *Plasma Sources Sci. Technol.* **14,** 477 (2005).

78. Barrell, Y. *et al.* Expanding thermal plasma for fast deposition of scratch-resistant SiC x H y O z films. *Surf. Coat. Technol.* **180,** 367–371 (2004).

79. Hegemann, D., Vohrer, U., Oehr, C. & Riedel, R. Deposition of SiO x films from O 2/HMDSO plasmas. *Surf. Coat. Technol.* **116,** 1033–1036 (1999).

80. Xiao, Z. G. & Mantei, T. D. Plasma-enhanced deposition of hard silicon nitride-like coatings from hexamethyldisiloxane and ammonia. *Surf. Coat. Technol.* **172,** 184–188 (2003).

81. Trunec, D. *et al.* Deposition of hard thin films from HMDSO in atmospheric pressure dielectric barrier discharge. *J. Phys. Appl. Phys.* **43,** 225403 (2010).

82. Benıtez, F., Martınez, E. & Esteve, J. Improvement of hardness in plasma polymerized hexamethyldisiloxane coatings by silica-like surface modification. *Thin Solid Films* **377,** 109–114 (2000).

83. Benıtez, F., Martınez, E., Galan, M., Serrat, J. & Esteve, J. Mechanical properties of plasma deposited polymer coatings. *Surf. Coat. Technol.* **125,** 383–387 (2000).

84. Deilmann, M., Thei\s s, S. & Awakowicz, P. Pulsed microwave plasma polymerization of silicon oxide films: Application of efficient permeation barriers on polyethylene terephthalate. *Surf. Coat. Technol.* **202,** 1911–1917 (2008).

85. Kim, K.-S. & Cho, D.-L. Improvement of barrier property of LDPE food packaging film by plasma polymerization. *Polym. Korea* **32,** 38–42 (2008).

86. Deilmann, M., Grabowski, M., Thei\s s, S., Bibinov, N. & Awakowicz, P. Permeation mechanisms of pulsed microwave plasma deposited silicon oxide films for food packaging applications. *J. Phys. Appl. Phys.* **41,** 135207 (2008).

87. Schneider, J. *et al.* Development of plasma polymerised SiOx barriers on polymer films for food packaging applications. *Plasma Process. Polym.* **4,** S155–S159 (2007).

88. Creatore, M., Palumbo, F., d'Agostino, R. & Fayet, P. RF plasma deposition of SiO 2-like films: plasma phase diagnostics and gas barrier film properties optimisation. *Surf. Coat. Technol.* **142,** 163–168 (2001).

89. Plog, S., Schneider, J., Walker, M., Schulz, A. & Stroth, U. Investigations of plasma polymerized SiO x barrier films for polymer food packaging. *Surf. Coat. Technol.* **205,** S165–S170 (2011).

90. Schneider, J. *et al.* Silicon oxide barrier coatings deposited on polymer materials for applications in food packaging industry. *Plasma Process. Polym.* **6,** S700–S704 (2009).

91. Guermat, N., Bellel, A., Sahli, S., Segui, Y. & Raynaud, P. Plasma Polymerization of Hexamethyldisiloxane and Tetraethoxysilane Thin Films for Humidity Sensing Application. in *Defect and Diffusion Forum* **354,** 41–47 (Trans Tech Publ, 2014).

92. Boscher, N. D. *et al.* Atmospheric pressure plasma polymerisation of metalloporphyrins containing mesoporous membranes for gas sensing applications. *Surf. Coat. Technol.* **234,** 48–52 (2013).

93. Weichart, J. & Müller, J. Plasma polymerization of silicon organic membranes for gas separation. *Surf. Coat. Technol.* **59,** 342–344 (1993).

94. Janča, J. & Sodomka, L. Plasma-polymerised organosiloxane thin films as selective gas sensors. *Surf. Coat. Technol.* **98,** 851–854 (1998).

95. Radeva, E. Thin plasma-polymerized layers of hexamethyldisiloxane for acoustoelectronic humidity sensors. *Sens. Actuators B Chem.* **44,** 275–278 (1997).

96. Bruno, P., Cicala, G., Corsi, F., Dragone, A. & Losacco, A. M. High relative humidity range sensor based on polymer-coated STW resonant device. *Sens. Actuators B Chem.* **100,** 126–130 (2004).

97. Guo, S., Rochotzki, R., Lundström, I. & Arwin, H. Ellipsometric sensitivity to halothane vapors of hexamethyldisiloxane plasma polymer films. *Sens. Actuators B Chem.* **44,** 243–247 (1997).

98. Schartel, B., Kühn, G., Mix, R. & Friedrich, J. Surface Controlled Fire Retardancy of Polymers Using Plasma Polymerisation. *Macromol. Mater. Eng.* **287,** 579–582 (2002).

99. Horrocks, A. R., Nazaré, S., Masood, R., Kandola, B. & Price, D. Surface modification of fabrics for improved flash-fire resistance using atmospheric pressure plasma in the presence of a functionalized clay and polysiloxane. *Polym. Adv. Technol.* **22,** 22–29 (2011).

100. Farag, Z. R. *et al.* Deposition of thick polymer or inorganic layers with flame-retardant properties by combination of plasma and spray processes. *Surf. Coat. Technol.* **228,** 266–274 (2013).

101. Zeinab R. F. Mohamed. Synthesis and Characterization of Fire-Retardant Layers onto Polyolefin Substrates. (2014).

102. Costantino, G., Zeik, D. B. & Clarson, S. J. Improvement of the adhesion of silicone to aluminum using plasma polymerization. *J. Inorg. Organomet. Polym.* **4,** 425–430 (1994).

103. Debnath, S. *et al.* Chemical surface treatment of ultrahigh molecular weight polyethylene for improved adhesion to methacrylate resins. *J. Appl. Polym. Sci.* **96,** 1564–1572 (2005).

104. Pihan, S. A., Tsukruk, T. & Förch, R. Plasma polymerized hexamethyl disiloxane in adhesion applications. *Surf. Coat. Technol.* **203,** 1856–1862 (2009).

105. Cho, B.-H., Han, G.-J., Oh, K.-H., Chung, S.-N. & Chun, B.-H. The effect of plasma polymer coating using atmospheric-pressure glow discharge on the shear bond strength of composite resin to ceramic. *J. Mater. Sci.* **46,** 2755–2763 (2010).

106. Leiber, J., Michaeli, W., Telgenbüscher, K. & Stollenwerk, M. UV protecting layers on PVC made by plasma polymerization. *J. Vinyl Technol.* **15,** 57–61 (1993).

107. Mandlik, P. *et al.* A single-layer permeation barrier for organic light-emitting displays. *Appl. Phys. Lett.* **92,** 103309 (2008).

108. Kuo, C.-F. J., Lan, W.-L., Chang, Y.-C. & Lin, K.-W. The preparation of organic light-emitting diode encapsulation barrier layer by low-temperature plasma-enhanced chemical vapor deposition: a study on the \hbox {SiO}_\mathrm{x}\hbox {N}_\mathrm{y} film parameter optimization. *J. Intell. Manuf.* 1–13 (2014). doi:10.1007/s10845-014-0893-8

109. Lee, S., Kang, Y.-J., Jung, S., Kim, J.-K. & Kim, D.-G. Plasma-Deposited $SiO_x C_y H_z$ Barrier Coatings for Organic Device Encapsulation. *Jpn. J. Appl. Phys.* **52,** 076001 (2013).

110. Aceros, J. *et al.* Polymeric packaging for fully implantable wireless neural microsensors. *Conf. Proc. Annu. Int. Conf. IEEE Eng. Med. Biol. Soc. IEEE Eng. Med. Biol. Soc. Annu. Conf.* **2012,** 743–746 (2012).

111. Li, Y.-S. *et al.* Single-layer organic–inorganic-hybrid thin-film encapsulation for organic solar cells. *J. Phys. Appl. Phys.* **46,** 435502 (2013).

112. Martinu, L. & Poitras, D. Plasma deposition of optical films and coatings: A review. *J. Vac. Sci. Technol. A* **18,** 2619–2645 (2000).

113. Schulz, U. Review of modern techniques to generate antireflective properties on thermoplastic polymers. *Appl. Opt.* **45,** 1608–1618 (2006).

114. Goldstein, J. *et al. Scanning Electron Microscopy and X-Ray Microanalysis: A Text for Biologists, Materials Scientists, and Geologists*. (Springer Science & Business Media, 2012).

115. Egerton, R. F., Li, P. & Malac, M. Radiation damage in the TEM and SEM. *Micron* **35,** 399–409 (2004).

116. Koenig, J. L. *Spectroscopy of polymers*. (Elsevier, 1999). at <http://books.google.es/books?hl=es&lr=&id=SoPVc77xN5wC&oi=fnd&pg=PP1&dq=Spectroscopy+of+polymers%E2%80%9D,+Koenig&ots=KNrGnzJQHm&sig=NMTeOcnkYbD_qG5M_Sk-uPH5448>

117. Urban, M. W. *Attenuated total reflectance spectroscopy of polymers: theory and practice*. (American Chemical Society, 1996). at <http://www.bcin.ca/Interface/openbcin.cgi?submit=submit&Chinkey=180036>

118. Abeles, F. Optical properties of very thin films. *Thin Solid Films* **34,** 291–302 (1976).

119. Hass, G. & Waylonis, J. E. Optical Constants and Reflectance and Transmittance of Evaporated Aluminum in the Visible and Ultraviolet. *J. Opt. Soc. Am.* **51,** 719 (1961).

120. Forouhi, A. R. & Bloomer, I. Optical properties of crystalline semiconductors and dielectrics. *Phys. Rev. B* **38,** 1865 (1988).

121. Oliver, W. c. & Pharr, G. m. An improved technique for determining hardness and elastic modulus using load and displacement sensing indentation experiments. *J. Mater. Res.* **7,** 1564–1583 (1992).

122. Fischer-Cripps, A. C. & Mustafaev, I. *Introduction to contact mechanics*. (Springer, 2000). at <http://link.springer.com/content/pdf/10.1007/978-0-387-68188-7.pdf>

123. Martínez Fraiz, E. Caracterització mecànica i tribològica de materials en capa fina. (PhD Dissertation, Universidad de Barcelona, Barcelona, España, 2000).

124. Swain, M. V. & Menčík, J. Mechanical property characterization of thin films using spherical tipped indenters. *Thin Solid Films* **253,** 204–211 (1994).

125. Field, J. S. & Swain, M. V. Simple predictive model for spherical indentation. *J. Mater. Res.* **8,** 297–306 (1993).

126. Kaelble, D. H. Dispersion-polar surface tension properties of organic solids. (1970). at <http://www.tandfonline.com/doi/abs/10.1080/0021846708544582>

127. Owens, D. K. & Wendt, R. C. Estimation of the surface free energy of polymers. *J. Appl. Polym. Sci.* **13,** 1741–1747 (1969).

128. Van Ooij, W., Eufinger, S. & Guo, S. DC Plasma polymerization of hexamethyldisiloxane. *Plasma Chem. Plasma Process.* **24,** (1997).

129. Eufinger, S., Van Ooij, W. J. & Conner, K. D. DC-Plasma Polymerization of Hexamethyldisiloxane Part II. Surface and Interface Characterization of Films Deposited on Stainless-steel Substrates. *Surf. Interface Anal.* **17,** 127–154 (1996).

130. Guo, S. & Van Ooij, W. Kinetics of DC discharge plasma polymerization of hexamethyldisiloxane and pyrrole. *Plasmas Polym.* **3,** 1–21 (1998).

131. Durrant, S., Mota, R. & De Moraes, M. Plasma polymerized hexamethyldisiloxane: discharge and film studies. *Vacuum* **47,** 187–192 (1996).

132. Benıtez, F., Martınez, E., Galan, M., Serrat, J. & Esteve, J. Mechanical properties of plasma deposited polymer coatings. *Surf. Coat. Technol.* **125,** 383–387 (2000).

133. Benıtez, F., Martınez, E. & Esteve, J. Improvement of hardness in plasma polymerized hexamethyldisiloxane coatings by silica-like surface modification. *Thin Solid Films* **377-378,** 109–114 (2000).

134. Esteve, J. *et al.* Protective coatings for Al metallizations obtained by plasma polymerization. *Proc. SPIE - Int. Soc. Opt. Eng.* **4094,** 120–128 (2000).

135. Benitez, F., Esteve, J. & Galan, M. SiOx - SiNx Functional Coatings by PECVD of Organosilicon Monomers Other Than Silane. *Soc. Vac. Coaters 45th Annu. Tec. Conf. Proc.* 280–285 (2002).

136. Clergereaux, R. *et al.* Comparison between continuous and microwave oxygen plasma post-treatment on organosilicon plasma deposited layers: Effects on structure and properties. *Thin Solid Films* **515,** 3452–3460 (2007).

137. Flamm, D., Auciello, O. & d'Agostino, R. Plasma deposition, treatment, and etching of polymers. *Acad. Press Lond.* (1990).

138. Biederman, H. Plasma polymer films. *Imp. Coll. Press Lond.* (2004).

139. Eofinger, S., Van Ooij, W. J. & Ridgway, T. H. DC plasma-polymerization of pyrrole: Comparison of films formed on anode and cathode. *J. Appl. Polym. Sci.* **61,** 1503–1514 (1996).

140. Yin, Y., Bilek, M., McKenzie, D., Boswell, R. W. & Charles, C. Microarcing instability in RF PECVD plasma system. *Surf. Coat. Technol.* **198,** 379 – 383 (2005).

141. Li, K., Gabriel, O. & Meichsner, J. Fourier transform infrared spectroscopy study of molecular structure formation in thin films during hexamethyldisiloxane decomposition in low pressure rf discharge. *J. Phys. Appl. Phys.* **37,** 588−594 (2004).

142. Vautrin-Ul, C. *et al.* Plasma-polymerized coatings using HMDSO precursor for iron protection. *Prog. Org. Coat.* **38,** 9–15 (2000).

143. Sahli, S., Segui, Y., Moussa, S. & Djouadi, M. Growth, composition and structure of plasma-deposited siloxane and silazane. *Thin Solid Films* **217,** 17–25 (1992).

144. Sahli, S., Segui, Y., Ramdani, S. & Takkouk, Z. Rf plasma deposition from hexamethyldisiloxane-oxygen mixtures. *Thin Solid Films* **250,** 206–212 (1994).

145. Rau, C. & Kulisch, W. Mechanisms of plasma polymerization of various silico-organic monomers. *Thin Solid Films* **249,** 28–37 (1994).

146. Alexander, M., Jones, F. & Short, R. Radio-frequency hexamethyldisiloxane plasma deposition: a comparison of plasma-and deposit-chemistry. *Plasmas Polym.* **2,** 277–299 (1997).

147. Walkiewicz-Pietrzykowska, A., Cotrino, J. & González-Elipe, A. R. Deposition of thin films of SiOxCyH in a surfatron microwave plasma reactor with hexamethyldisiloxane as precursor. *Chem. Vap. Depos.* **11,** 317–323 (2005).

148.Heyner, R. & Marx, G. High power deposition and analytics of amorphous silicon carbide films. *Thin Solid Films* **258,** 14–20 (1995).

149.Lamendola, R., d'Agostino, R. & Fracassi, F. Thin film deposition from hexamethyldisiloxane fed glow discharges. *Plasmas Polym.* **2,** 147–164 (1997).

150.Yasuda, H. & Hirotsu, T. Distribution of polymer deposition in plasma polymerization. III. Effect of discharge power. *J. Polym. Sci. Part Polym. Chem.* **16,** 313–326 (1978).

151.Yasuda, H. & Hirotsu, T. Distribution of polymer deposition in plasma polymerization. II. Effect of reactor design. *J. Polym. Sci. Part Polym. Chem.* **16,** 2587–2592 (1978).

152.Van Hest, M., Klaver, A., Schram, D. C. & van de Sanden, M. C. M. Argon–oxygen plasma treatment of deposited organosilicon thin films. *Thin Solid Films* **449,** 40–51 (2004).

153.Walker, M. *et al.* Silicon oxide films from the Plasmodul®. *Vacuum* **57,** 387–397 (2000).

154.Schwarzer, N. Coating design due to analytical modelling of mechanical contact problems on multilayer systems. *Surf. Coat. Technol.* **133-134,** 397–402 (2000).

155.Hegemann, D., Brunner, H. & Oehr, C. Plasma treatment of polymers to generate stable, hydrophobic surfaces. *Plasmas Polym.* **6,** 221–235 (2001).

156.Mano, T., Sugiyama, O. & Nakayama…, H. Nanostructure and composition of carbon/silicon graded film produced by ionization-assisted deposition. *Jpn. J. Appl. Phys.* **44,** 5807–5810 (2005).

157.Granier, A. *et al.* Mechanisms Involved in the Conversion of ppHMDSO Films into SiO2-Like by Oxygen Plasma Treatment. *Plasma Process. Polym.* **3,** 365–373 (2006).

158.Radeva, E., Georgieva, V., Lazarov, J., Gadjanova, V. & Tsankov, D. PLASMA POLYMERIZED HEXAMETHYLDISILOXANE THIN FILMS FOR NO2 GAS SENSOR APPLICATION. *Dig. J. Nanomater. Biostructures* **9,** 459 – 466 (2014).

159.Kondoh, E., Asano, T. & Nakashima…, A. Effect of oxygen plasma exposure of porous spin-on-glass films. *J. Vac. Sci. Technol. B* **18,** 1276 (2000).

160.Grundmeier, G., Thiemann, P., Carpentier, J., Shirtcliffe, N. & Stratmann, M. Tailoring of the morphology and chemical composition of thin organosilane microwave plasma polymer layers on metal substrates. *Thin Solid Films* **449,** 61–71 (2004).

161.Supiot, P., Vivien, C. & Granier…, A. Growth and modification of organosilicon films in PECVD and remote afterglow reactors. *Plasma Process. Polym.* **3,** 100–109 (2006).

162.Wang, Y., Kumar, R., Zhou, X., Pan, J. & Chai, J. Effect of oxygen plasma treatment on low dielectric constant carbon-doped silicon oxide thin films. *Thin Solid Films* **473,** 132– 136 (2005).

163.Vallee, C. *et al.* Chemical etching of thin SiO x C y H z films by post-deposition exposure to oxygen plasma. *Appl. Surf. Sci.* **138–139,** 57–61 (1999).

164. Swiderek, P. *et al.* Modification of Polydimethylsiloxane Coatings by H2 RF Plasma, Xe2* Excimer VUV Radiation, and Low-Energy Electron Beams. *Macromol. Mater. Eng.* **297,** 1091–1101 (2012).

165. ASTM D2765 – 11 - Standard Test Methods for Determination of Gel Content and Swell Ratio of Crosslinked Ethylene Plastics.

166. Rivière, J. & Myhra, S. Handbook of surface and interface analysis: methods for problem-solving. *CRC Press Boca Raton FL* (2009).

167. Oechsner, H. Thin film and depth profile analysis. *Springer Heidelb.* (2013).

168. Hegemann, D., Schütz, U., U & Oehr, C. RF-Plasma Deposition of SiOx and a-C:H as Barrier Coatings on Polymers. *N Plasma Process. Polym. Eds R Agostino P Favia C Oehr M R Werth. Wiley-VCH Verl. GmbH Co KGaA Weinh. FRG* (2005).

169. Foerch, R., McIntyre, N., Sodhi, R. N. S. & Hunter, H. Nitrogen plasma treatment of polyethylene and polystyrene in a remote plasma reactor. *J. Appl. Polym. Sci.* **40,** 1903–1915 (1990).

170. Forouhi, A. & Bloomer, I. Optical properties of crystalline semiconductors and dielectrics. *Phys. Rev. B* **38,** 1965 (1988).

171. Launer, P. J. Infrared Analysis of Organosilicon Compounds: Spectra-Structure Correlations. *"Silicone Compd. Regist. Rev. B Arkles Ed Petrarch Syst.* (1987).

172. Rojas, S., Modelli, A., Wu, W. & Borghesi…, A. Properties of silicon dioxide films prepared by low-pressure chemical vapor deposition from tetraethylorthosilicate. *J. Vac. Sci. Technoogy B* **8,** 1177 (1990).

173. Liu, Y. *et al.* A study on Si nanocrystal formation in Si-implanted SiO2 films by x-ray photoelectron spectroscopy. *J. Phys. Appl. Phys.* **36,** 97–100 (2003).

174. Alexander, M., Short, R., Jones, F., Michaeli, W. & Blomfield, C. J. A study of HMDSO/O 2 plasma deposits using a high-sensitivity and-energy resolution XPS instrument: curve fitting of the Si 2p core level. *Appl. Surf. …* **137,** 179–183 (1999).

175. Borghesi, A., Sassella, A., Pivac, B. & Zanotti, L. SiH bonding configuration in SiO x: N, H films deposited by chemical vapor deposition. *Solid State Commun.* **100,** 657 (1996).

176. Zajickova, L., Subedi, D., Bursikova, V. & Veltruska, K. Study of argon plasma treatment of polycarbonate substrate and its effect on film deposition. *Acta Phys. Slovaca* **53,** 489 – 504 (2003).

177. Radeva, E. Structure of Thin Plasma Polymer Films on the Base of Hexamethyldisiloxane. *Bulg. J. Phys.* **40,** 208–213 (2013).

178. Stoffels, E. *et al.* Negative ions in a radio-frequency oxygen plasma. *Phys. Rev. E* **51,** 2425 (1995).

179. Lopata, E. S. & Felts, J. T. Method of plasma enhanced silicon oxide deposition - (Ref: US005904952A). (1993).

180. Walsh, R. Bond dissociation energies in organosilicon compounds. *Tech. Note Dep. Chem. Univ. Read.* (1998).

181. Waddell, E., Shreeves, S., Carrell, H. & Perry…, C. Surface modification of Sylgard 184 polydimethylsiloxane by 254 nm excimer radiation and characterization by contact angle goniometry, infrared spectroscopy, atomic force and scanning electron microscopy. *Appl. Surf. Sci.* **254,** 5314–5318 (2008).

182. Holländer, A., Wilken, R. & Behnisch, J. Subsurface chemistry in the plasma treatment of polymers. *Surf. Coat. Technol.* **116-119,** 788–791 (1999).

183. Williams, R., Wilson, D. & Rhodes, N. Stability of plasma-treated silicone rubber and its influence on the interfacial aspects of blood compatibility. *Biomaterials* **25,** 4659–4673 (2004).

184. Meeks, E. *et al.* Modeling of SiO2 deposition in high density plasma reactors and comparisons of model predictions with experimental measurements. *J. Vac. Sci. Technol A* **16,** 554 (1998).

185. Kim, J., Kim, G., Chung, T. H., Yeom, G. Y. & Kwon, K. H. Characterization of an oxygen plasma by using a langmuir probe in an inductively coupled plasma. *J. Korean Phys. Soc.* **38,** 259–263 (2001).

186. Makrinich, G. & Fruchtman, A. Heat flux measurements and plasma composition. *J. Appl. Phys.* **100,** 093302 (2006).

187. Ziegler, J., Ziegler, M. & Biersack, J. SRIM–The stopping and range of ions in matter (2010). *Nucl. Instrum. Methods Phys. Res. Sect. B* **268,** 1818–1823 (2010).

188. Kondyurin, A. & Bilek, M. Ion beam treatment of polymers: application aspects from medicine to space. *2nd Ed. Elsevier Amst.* (2014).

189. Truica-Marasescu, F., Guimond, S., Jedrzejowski, P. & Wertheimer, M. R. Hydrophobic recovery of VUV/NH 3 modified polyolefin surfaces: Comparison with plasma treatments in nitrogen. *Nucl. Instrum. Methods Phys. Res. Sect. B Beam Interact. Mater. At.* **236,** 117–122 (2005).

190. Kim, J., Chaudhury, M. & Owen, M. Modeling hydrophobic recovery of electrically discharged polydimethylsiloxane elastomers. *J. Colloid Interface Sci.* **293,** 364–375 (2006).

191. Kim, J., Chaudhury, M., Owen, M. & Orbeck, T. The mechanisms of hydrophobic recovery of polydimethylsiloxane elastomers exposed to partial electrical discharges. *J. Colloid Interface Sci.* **244,** 200–207 (2001).

192. Bhattacharya, S., Datta, A., Berg, J. M. & Gangopadhyay, S. Studies on surface wettability of poly (dimethyl) siloxane (PDMS) and glass under oxygen-plasma treatment and correlation with bond strength. *J. Microelectromechanical Syst.* **14,** (2005).

193. Hoshino, T., Hata, M., Neya, S. & Nishioka…, Y. Diffusion of molecular and atomic oxygen in silicon oxide. *Jpn. J. Appl. Phys.* **42,** Number 6A (2003).

194. Roberts, A., Henry, B. & Sutton…, A. Gas permeation in silicon-oxide/polymer (SiO x/PET) barrier films: role of the oxide lattice, nano-defects and macro-defects. *J. Membr. Sci.* **208,** 75–88 (2002).

195. Cox, M. & Dunn, B. Oxygen diffusion in poly (dimethyl siloxane) using fluorescence quenching. I. Measurement technique and analysis. *J. Polym. Sci. Part Polym. Chem.* **24,** 621–636 (1986).

196. Nuccio, L. Diffusion of small molecules in amorphous SiO2: effects on the properties of the material and on its point defects. *PhD Thesis*

197. Markov, D., Lillie, E., Garbett, S. P. & McCawley, L. J. Variation in diffusion of gases through PDMS due to plasma surface treatment and storage conditions. *Biomed. Microdevices* **16,** 91–96 (2014).

198. Nascimento, M. F. & Dutra Zanotto, E. Diffusion processes in vitreous silica revisited. *Phys. Chem. Glas. Eur. J. Glass Sci. Tech B* **48,** 201–217 (2007).

199. Shamiryan, D., Baklanov, M. R., Vanhaelemeersch, S. & Maex, K. Comparative study of SiOCH low-k films with varied porosity interacting with etching and cleaning plasma. *J. Vac. Sci. Technol. B* **20,** 1923 (2003).

200. Oszinda, T. *et al.* Improved characterization of Fourier transform infrared spectra analysis for post-etched ultra-low-κ SiOCH dielectric using chemometric methods. *J. Vac. Sci. Technol. B* **27,** 521 (2009).

201. Hoyas, A., Schuhmacher, J. & Whelan…, C. Effect of plasma treatments on a low-k dielectric polymer surface. *J. Vac. Sci. Technoly B* **23,** 1551 (2005).

202. Maex, K. *et al.* Low dielectric constant materials for microelectronics. *J. Appl. Phys.* **93,** 8793 (2003).

203. Galdikas, A. & Pranı͡avichı͡us, L. Interaction of ions with condensed matter. *Nova Sci. Publ. N. Y.* (2000).

204. Oehrlein, G., Tromp, R., Tsang, J., Lee, Y. H. & Petrillo, E. J. Near-Surface Damage and Contamination after CF 4/H 2 Reactive Ion Etching of Si. *J. …* **132,** 1441 (1985).

205. Thermal properties of silicones. *Blustar Silicones Wwwbluestarsiliconescom*

206. Radhakrishnan, T. New method for evaluation of kinetic parameters and mechanism of degradation from pyrolysis–GC studies: thermal degradation of polydimethylsiloxanes. *J. Appl. Polym. Sci.* **73,** 441–450 (1999).

207. Hanu, L., Simon, G. & Cheng, Y. Thermal stability and flammability of silicone polymer composites. *Polym. Degrad. Stab.* **91,** 1373–1379 (2006).

208. Segui, Y. & Raynaud, P. Deposition of Silicon containing films and FTIR diagnostics. *'Plasma Polym. Films' Ed Hynek Biederman Imp. Coll. Press Lond.* (2004).

209. Stout, P. J. & Kushner, M. J. A Monte Carlo Simulation of Surface Kinetics During Plasma Enhanced Chemical Vapor Deposition of SiO2 using O2/TEOS Chemistry. *J. Vac. Sci. Technol. A* **11,** 2562 (1993).

210. Kim, M. T. Deposition kinetics of silicon dioxide from tetraethylorthosilicate by PECVD. *Thin Solid Films* **360,** 60–68 (2000).

211.Rhallabi, A. & Turban, G. Study of the early stage of SiO2 growth by a TEOS-O-2 plasma mixture using a three-dimensional MonteCarlo model. *J. Vac. Sci. Technol. A* **19,** 743 (2001).

212.Fischer-Cripps, A. C. A review of analysis methods for sub-micron indentation testing. *Vacuum* **58,** 569–585 (2000).

213.Nguyen, L. Minimizing Hydrophobic Recovery of Polydimethylsiloxane after Oxygen Plasma Treatment. *PhD Thesis Mt. Holyoke* (2014).

214.Madadi, H. & Casals-Terré, J. Long-term behavior of nonionic surfactant-added PDMS for self-driven microchips. *Microsyst. Technol.* **19,** 143–150 (2013).

215.Hillborg, H. Loss and recovery of hydrophobicity of polydimethylsiloxane after exposure to electrical discharges. *KTH Stockh. Swed.* (2001).

216.Hillborg, H. *et al.* Crosslinked polydimethylsiloxane exposed to oxygen plasma studied by neutron reflectometry and other surface specific techniques. *Polymer* **41,** 6851–6863 (2000).

217.Bodas, D., Rauch, J. & Khan-Malek, C. Surface modification and aging studies of addition-curing silicone rubbers by oxygen plasma. *Eur. Polym. J.* **44,** 2130–2139 (2008).

218.Owen, M. J., Gentle, T. M., Orbeck, T. & Williams, D. E. Polymer surface dynamics. *N. Y. Plenum* 101 (1998).

219.Tóth, A. *et al.* Oxidative damage and recovery of silicone rubber surfaces. I. X-ray photoelectron spectroscopic study. *J. Appl. Polym. Sci.* **52,** 1293–1307 (1994).

220.Occhiello, E., Marola, R., Garbassi, F., Humphrey, P. & Johnson, D. On the aging of oxygen plasma-treated polydimethylsiloxane surfaces. *J. Colloid …* **137,** 11–24 (1990).

221.Lawton, R., Price, C., Runge, A., Doherty, W. J. & Saavedra, S. Air plasma treatment of submicron thick PDMS polymer films: effect of oxidation time and storage conditions. *Colloids Surf. Physicochem. Eng. Asp.* **253,** 213–215 (2005).

222.Kim, J., Chaudhury, M. & Owen, M. Hydrophobic recovery of polydimethylsiloxane elastomer exposed to partial electrical discharge. *J. Colloid Interface Sci.* **226,** 231–236 (2000).

223.Bodas, D. & Khan-Malek, C. Hydrophilization and hydrophobic recovery of PDMS by oxygen plasma and chemical treatment—An SEM investigation. *Sens. Actuators B Chem.* **123,** 368–373 (2007).

224.Concus, P. & Finn, R. On the behavior of a capillary surface in a wedge. *Proc. Natl. Acad. Sci.* **63,** 292–299 (1969).

225.Chen, Y. & Weislogel…, M. Capillary-driven flows along rounded interior corners. *J. Fluid Mech.* **556,** 225–271 (2006).

226.Chauvet, F., Duru, P. & Prat, M. Depinning of evaporating liquid films in square capillary tubes: Influence of corners' roundedness. *Phys. Fluids 1994-Present* **22,** 112–113 (2010).

227.Lu, X. *et al.* A simple approach for fabricating a superhydrophobic surface based on poly (methyl methacrylate). *J. Adhes. Sci. Technol.* **22,** 1841–1852 (2008).

228. Scott, C., Sander, G. & Norbury, J. Computation of capillary surfaces for the Laplace–Young equation. *Q. J. Mech. Appl. Math.* **60,** 1–12 (2005).

LIST OF ACRONYMS (1/2)

ABS *Acrylonitrile Butadiene Styrene*

ATR *Attenuated Total Reflectance*

CASING *Cross-linking by Activated Species of Inert Gas*

CAP *Competitive Ablation and Polymerization*

CFD *Computational Fluid Dynamics*

DC *Direct Current*

DSA *Drop Shape Analyzer*

EDX *Energy-Dispersive X-Ray*

EPO *European Patent Office*

FTIR *Fourier-Transform InfraRed*

HMDSO *Hexamethyldisiloxane*

HMDSZ *Hemxamethyldisilazane*

IUPAC *International Union of Pure and Applied Chemistry*

LVDT *Linear Variable Differential Transformer*

MFC *Mass Flow Controller*

MSDS *Material Safety Data Sheet*

MW *MicroWave*

OES *Optical Emission Spectroscopy*

PLC *Programmable Logic Controller*

ppHMDSO *PlasmaPolymerized Hexamethyldisiloxane*

PDMS *PolyDimethylsiloxane*

PC *PolyCarbonate*

PMMA *PolyMethylMethacrylate*

PVD *Physical Vapor Deposition*

PECVD *Plasma-Enhanced Chemical Vapor Deposition*

QMS *Quadrupole Mass Spectrometry*

RF *Radio Frequency*

RSGP *Rapid Step-Growth Polymerization*

SCCM *Standard Cubic Centimeters per Minute*

SEM *Scanning Electron Microscopy*

SRIM *Stopping and Range of Ions in Matter*

LIST OF ACRONYMS (2/2)

TEOS Tetraethoxysilane

TEM *Transmission Electron Microscopy*

UV *Ultraviolet*

XPS *X-Ray Photoelectron Spectroscop*